

AD-A085 258

LOCKHEED-GEORGIA CO MARIETTA

F/6 20/4

ACQUISITION AND APPLICATION OF TRANSONIC WING AND FAR-FIELD TES--ETC(U)

MAR 80 B L HINSON, K P BURDGES

F49620-78-C-0068

UNCLASSIFIED

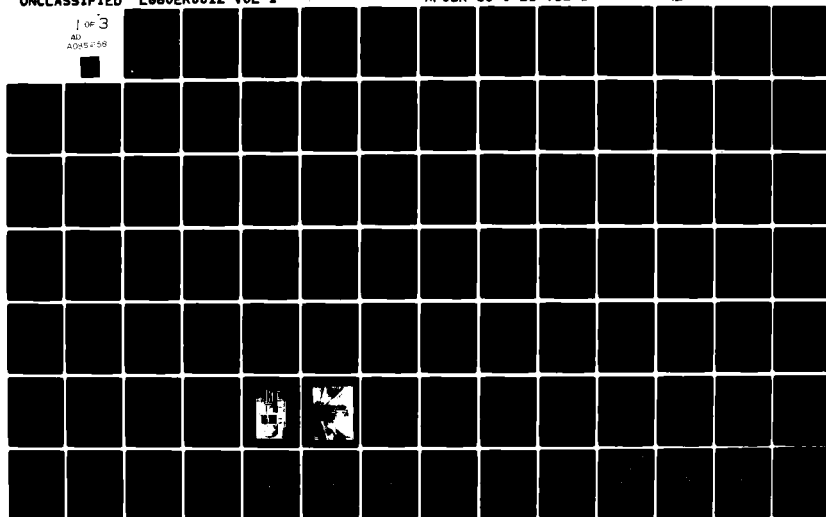
L680ER0012-VOL-1

AFOSR-80-0421-VOL-1

NL

1 OF 3

AD  
A085 258



AFOSR-TR- 80-0421

LEVEL

AFOSR-TR-80-

259

12

ACQUISITION AND APPLICATION OF TRANSONIC  
WING AND FAR-FIELD TEST DATA FOR THREE-  
DIMENSIONAL COMPUTATIONAL METHOD EVALUATION

By

B. L. Hinson and K. P. Burdges

LOCKHEED-GEORGIA COMPANY  
86 South Cobb Drive  
Marietta, Georgia 30063

DTIC  
JUN 10 1980

March 1980

Final Report

May 1978 - August 1979

Approved for public release; distribution unlimited

80 6 9 1 68

Prepared For

AIR FORCE OFFICE OF SCIENTIFIC RESEARCH  
Bolling Air Force Base, D. C. 20332

ADA 085258

FILE COPY

UNCLASSIFIED

SECURITY CLASSIFICATION OF THIS PAGE (When Data Entered)

REPORT DOCUMENTATION PAGE		READ INSTRUCTIONS BEFORE COMPLETING FORM
1. REPORT NUMBER <b>AFOSR-TR-80-0421</b>	2. GOVT ACCESSION NO. <b>AD-A085258</b>	3. RECIPIENT'S CATALOG NUMBER
4. TITLE (and Subtitle) <b>ACQUISITION AND APPLICATION OF TRANSONIC WING AND FAR-FIELD TEST DATA FOR THREE-DIMENSIONAL COMPUTATIONAL METHOD EVALUATION</b>	5. TYPE OF REPORT & PERIOD COVERED <b>Final Report May 1978 - Aug 1979</b>	6. PERFORMING ORG. REPORT NUMBER <b>LG80ER0012-VOL-1</b>
7. AUTHOR(s) <b>B. L. Hinson K. P. Burdges</b>	8. CONTRACT OR GRANT NUMBER(s) <b>F49620-78-C-0068</b>	9. PROGRAM ELEMENT, PROJECT, TASK AREA & WORK UNIT NUMBERS <b>61102F17 2307/A1</b>
10. PERFORMING ORGANIZATION NAME AND ADDRESS <b>LOCKHEED CORPORATION Lockheed-Georgia Company Marietta, Georgia 30063</b>	11. CONTROLLING OFFICE NAME AND ADDRESS <b>Air Force Office of Scientific Research/NA Bolling Air Force Base, D. C. 20332</b>	12. REPORT DATE <b>Mar 1980</b>
13. MONITORING AGENCY NAME & ADDRESS (if different from Controlling Office) <b>(12216)</b>	14. SECURITY CLASS. (of this report) <b>UNCLASSIFIED</b>	15. DECLASSIFICATION/DOWNGRADING SCHEDULE
16. DISTRIBUTION STATEMENT (of this Report) <b>Approved for public release; distribution unlimited.</b>		
17. DISTRIBUTION STATEMENT (of the abstract entered in Block 20, if different from Report)		
18. SUPPLEMENTARY NOTES		
19. KEY WORDS (Continue on reverse side if necessary and identify by block number) <b>Aircraft Aerodynamics Subsonic and Transonic Flow Computational Aerodynamics Wind-Tunnel Testing</b>		
20. ABSTRACT (Continue on reverse side if necessary and identify by block number) <b>A comprehensive program to acquire high Reynolds number transonic experimental data on three advanced technology wings of aspect ratio from 2.8 to 8.0, specifically for evaluation of three-dimensional computational methods, was accomplished. The wings were tested over a wide range of conditions isolated wings and in the presence of a simple fuselage in high, mid, and low wing configurations on a unique test apparatus in the Lockheed-Georgia</b> <div style="text-align: right;">(Continued)</div>		

DD FORM 1 JAN 73 1473 EDITION OF 1 NOV 65 IS OBSOLETE

UNCLASSIFIED

SECURITY CLASSIFICATION OF THIS PAGE (When Data Entered)

UNCLASSIFIED

SECURITY CLASSIFICATION OF THIS PAGE(When Data Entered)

20. ABSTRACT (Continued)

compressible flow wind tunnel. The unique test apparatus included provisions for removal of the wind tunnel boundary layer and measurements of far-field pressures for evaluation of wind tunnel wall interference. A unique technique for evaluation of wind tunnel wall interference was developed and applied to the data. Selected three-dimensional transonic computational methods were compared with the test data. A full potential code, FLO-22, was found to give excellent agreement with experiment for all three wings, while a small disturbance solution provided acceptable agreement only for the high aspect ratio wing.

UNCLASSIFIED

SECURITY CLASSIFICATION OF THIS PAGE(When Data Entered)

## FOREWORD

This report was prepared by the Lockheed-Georgia Company for the Air Force Office of Scientific Research, Bolling AFB, D. C. The research associated with Wings A and B was performed under Contract No. F49620-78-C-0068. The AFOSR Program Monitor was Dr. James D. Wilson. The research activity associated with Wing C was performed under Lockheed's Internal Research and Development Program and has been included in this report for completeness.

Computer time for the code evaluations was provided on the NASA-Ames Research Center CDC 7600 computer, through the Applied Computational Aerodynamics Branch, Dr. W. F. Ballhaus, Branch Chief.

AIR FORCE OFFICE OF SCIENTIFIC RESEARCH (AFOSR)  
NOTICE OF TRANSMITTAL TO IAC  
This technical report has been reviewed and is  
approved for distribution in accordance with AFM 100-12 (7b).  
Distribution is unlimited.  
A. D. BROSE  
Technical Information Officer

## SUMMARY

A comprehensive program to acquire transonic experimental data specifically for evaluation of current three-dimensional computational methods was accomplished. Three advanced technology wings of aspect ratios from 2.8 to 8.0 were tested at high Reynolds number using a unique semispan test apparatus in the Lockheed-Georgia Compressible Flow Wind Tunnel. The unique test apparatus included provisions for removal of the wind tunnel boundary layer and measurements of far-field pressures for evaluation of wind tunnel wall interference. The wings were tested in an isolated configuration and also in the presence of a simple fuselage in high, mid, and low wing positions. Comprehensive pressure and force measurements were obtained on the three wings from subcritical flow conditions up to drag rise conditions. A unique technique for evaluation of transonic wind tunnel wall interference was developed and applied to the test data. Particular attention was given to documentation of all information necessary for simulation of the experiment in 3-D theoretical computations.

The data were used to evaluate three selected three-dimensional transonic computational methods: the Bailey-Ballhaus extended small-disturbance (non-conservative/fully-conservative) code; the Jameson-Caughey full-potential, non-conservative code, FL0-22; and the Jameson-Caughey full-potential, fully-conservative code, FL0-27. Fully conservative solutions were found to give poorer agreement with measurements than non-conservative solutions. The FL0-22 code was found to give excellent agreement with experiment for all three wings, while the small-disturbance code provided acceptable agreement only for the high aspect ratio, low-sweep configuration.

The effect of viscosity was assessed by including an iterated two-dimensional strip boundary layer solution in the FL0-22 analysis. The difference between viscous and inviscid solutions was small.

SEARCHED	INDEXED	SERIALIZED	FILED
MAR 1971			
FBI - NEW YORK			
A			

# TABLE OF CONTENTS

	Page
SYMBOLS . . . . .	ix
1. INTRODUCTION AND BACKGROUND . . . . .	1
2. WING DESIGN . . . . .	4
2.1 Introduction . . . . .	4
2.2 Wing A Design Procedure . . . . .	5
2.3 Wing B Design Procedure . . . . .	6
2.4 Wing C Design Procedure . . . . .	6
3. APPARATUS . . . . .	8
3.1 Models . . . . .	8
3.1.1 Wings . . . . .	8
3.1.2 Fuselage . . . . .	8
3.2 Test Facility . . . . .	8
3.3 Instrumentation . . . . .	9
3.4 Data Reduction . . . . .	10
3.4.1 Balance Data . . . . .	10
3.4.2 Pressure Data . . . . .	11
3.4.3 Machine Plotting . . . . .	11
4. TESTS AND METHODS . . . . .	12
4.1 Test Conditions . . . . .	12
4.2 Transition . . . . .	12
5. TEST RESULTS . . . . .	14
5.1 Test Techniques . . . . .	14
5.1.1 Boundary layer removal system . . . . .	14
5.1.2 Tunnel calibrations . . . . .	14
5.1.3 Force balance evaluation . . . . .	15
5.1.4 Fuselage/wing seal . . . . .	15

	Page
5.2 Wing A Test Results . . . . .	15
5.2.1 Force data . . . . .	15
5.2.2 Pressure data . . . . .	16
5.2.3 Fuselage effects . . . . .	16
5.3 Wing B Test Results . . . . .	17
5.3.1 Force data . . . . .	17
5.3.2 Pressure data . . . . .	17
5.3.3 Fuselage effects . . . . .	18
5.4 Wing C Test Results . . . . .	18
5.4.1 Force data . . . . .	18
5.4.2 Pressure data . . . . .	19
5.4.3 Fuselage effects . . . . .	19
5.5 Detailed Experimental Data . . . . .	20
6. WIND TUNNEL WALL INTERFERENCE . . . . .	21
6.1 Review of Current Methods . . . . .	21
6.1.1 Inclusion of wall interference in code correlations . .	21
6.1.2 Correction of tunnel data to free-air conditions . . .	22
6.2 Development of New Computational Method . . . . .	23
6.2.1 Method formulation . . . . .	23
6.2.2 Computing blockage correction using the new method . .	25
6.3 Application of New Method . . . . .	25
7. EVALUATION OF TRANSONIC COMPUTATIONAL METHODS . . . . .	28
7.1 Description of Methods . . . . .	28
7.1.1 Bailey-Ballhaus code . . . . .	28
7.1.2 FLO-22 code . . . . .	28
7.1.3 FLO-27 code . . . . .	28
7.2 Code Convergence . . . . .	29
7.3 Code Correlations . . . . .	31
7.3.1 Wing A - High aspect ratio, low speed . . . . .	31
7.3.2 Wing B - Moderate aspect ratio and sweep . . . . .	32
7.3.3 Wing C - Low aspect ratio, high sweep . . . . .	33
7.3.4 Evaluation of correlations . . . . .	34



	Page
8. CONCLUSIONS . . . . .	36
9. REFERENCES . . . . .	38
APPENDIX A - THREE-DIMENSIONAL TRANSONIC CODE CORRELATIONS . . . . .	150
APPENDIX B - EXPERIMENTAL DATA . . . . .	206

## SYMBOLS

AR	wing aspect ratio, $b^2/S$
b	wing span
C	streamwise local chord of wing
$C_D$	drag coefficient
$C_L$	lift coefficient
$C_M$	pitching-moment coefficient about quarter chord of MAC
$C_p$	pressure coefficient
M	freestream Mach number
MAC	mean aerodynamic chord of wing
$R_N$	Reynolds number based on freestream conditions and MAC
S	wing planform area
x	streamwise coordinate measured from wing leading edge
y	spanwise coordinate measured from plane of symmetry
z	coordinate normal to WRP
$\alpha$	angle of wing reference plane relative to tunnel axis
$\theta$	wing section local incidence angle relative to WRP
$\lambda$	wing taper ratio, $C_t/C_r$
$\Lambda'$	wing sweep angle
$\eta$	span station, $y/(b/2)$
$\phi$	perturbation velocity potential
$\tau$	wind tunnel wall porosity

### Subscripts:

L	lower surface
LE	leading edge

M	measured
r	wing root
t	wing tip
TE	trailing edge
U	upper surface

Abbreviations:

CFWT	Lockheed Compressible Flow Wind Tunnel
WRP	wing reference plane

## 1. INTRODUCTION AND BACKGROUND

Since the original work of Bailey and Ballhaus in the early 1970's, significant advancements have been made in the development of computational methods for analyzing the transonic flow about isolated wings and simple wing-body combinations. Table 1 lists some of the methods which are readily available and are widely used in this country. These methods differ from one another in the complexity of the governing equations and boundary conditions, computational grids, finite-difference schemes, and solution algorithms.

The simplest problem formulation is the classical small disturbance (CSD) Bailey-Ballhaus code, while the most complex formulation is the Jameson-Caughey full potential equation method (FPE). Experience has shown that when similar grids are used and solutions are converged to roughly the same tolerance, the extended small disturbance formulations (ESD) require about twice the computation time as the CSD. Furthermore, depending upon the particular FPE formulation, the FPE codes require considerably more computation time than the ESD.

Unfortunately, ESD is known to be needed to compute flows with swept shocks, and FPE is believed to be required when accurate solutions near the leading edge are required and/or when shock waves are more than moderately swept. Other questions such as the need for fully conservative relaxation (FCR) instead of non-conservative relaxation (NCR) and the accuracy required of viscous corrections remain to be answered. Since additional complexities result in increased costs of solutions, clearly the simplest method which yields satisfactorily accurate results for the problem at hand should be used.

The accuracies and computational efficiencies of the methods listed in Table 1 can best be determined by a systematic comparison with reliable experimental data. The comparisons must all be performed on the same computer system, and variables such as number of surface grid points and convergence criteria must be considered.

The major obstacle to performing such an evaluation is the paucity of reliable experimental data suitable for code correlation. Most of the transonic test data which are available are unsuitable for inviscid transonic code correlation because of one or more of the following test-related problems:

- o Low test Reynolds number
- o Lack of transition information
- o Wind-tunnel wall interference
- o Flow spillage and an induced spanwise flow on splitter-plate mounted configurations
- o Interaction of wind-tunnel wall boundary-layer with floor-mounted wings
- o Limited pressure data.

Furthermore, many of the data are unsuitable because either (1) the model incorporated old wing-design technology, or (2) the model is a complex wing-body-component configuration which cannot be properly modeled in the codes.

To alleviate the above situation, a comprehensive research program was initiated in 1978 to:

- (1) Acquire a set of quality correlation-tailored, transonic test data for a series of isolated advanced technology wings and simple wing-body combinations which would serve as a standard for future method evaluations.
- (2) Utilize these data to initiate the evaluation of selected 3-D transonic codes.

These objectives have been accomplished by first designing, fabricating and testing three advanced technology wings (both isolated and in the presence of a body in high, mid, and low-wing positions) in the Lockheed-Georgia Company high Reynolds number wind-tunnel using a unique test apparatus. The test procedure is shown to eliminate most of the inherent problems associated with previous tests of this type. Finally, these data are then compared with theoretical results from the Bailey-Ballhaus ESD code, the Jameson-Caughey FPE finite-difference method (FLO-22), and the Jameson-Caughey FPE finite-volume method (FLO-27).

This report contains the results of this investigation. The first section of the report is a detailed discussion of the experimental program, including model design, test facility, test procedures, and instrumentation. A novel approach which uses measured wind-tunnel wall pressures for taking wall-interference effects into account in code correlation is described in the second section. The next section is devoted to a comparison of calculated results using advanced 3-D transonic codes with the experimental data. Finally, conclusions are drawn relative to the quality of the data and its applicability for transonic code correlation, the adequacy of the wall-interference corrections, and the accuracy and efficiency of the evaluated codes.

## 2. WING DESIGN

### 2.1 Introduction

The philosophy adopted in this program with regard to wing design was:

(1) To use proven design techniques to obtain wings which are not necessarily optimized, but which produce well-behaved flow fields. Such flow fields are required for an unambiguous correlation of theory with experiment.

(2) To use wings which are geometrically simple. This not only simplifies the task of applying surface boundary conditions in the computational methods, but also makes test model fabrication easier.

(3) To cover the range of practical concepts from transports to fighters.

The planform configurations for the correlation wings are shown in figure 1. The configurations are referred to as Wings A, B, and C. Wing A planform is representative of an advanced transport aircraft concept while Wing B planform is typical of a high performance fighter.

Wing C was designed to serve as a multi-purpose test article; particularly for acquiring boundary layer test data to support other programs as well as for correlating potential flow codes. As such, it represents a compromise (with respect to the strength and extent of viscous effects) between these requirements. The planform of Wing C is characteristic of a supersonic-cruise, transonic-maneuver fighter.

To minimize model fabrication costs, only root and tip control stations were defined for the three wings, with wing coordinates at other spanwise stations defined by linear loft between the root and tip. The overall geometric characteristics of the three semispan wing models are summarized in Table II.

Details of the design of each of the three wings will now be discussed in separate subsections.

## 2.2 Wing A Design Procedure

Wing A is a transport-type wing defined by two control stations at the root and tip. It has an aspect ratio (AR) of 8, and quarter chord sweep of  $25^\circ$ . The root and tip sections are 12% thick. Wing A was designed to incorporate state-of-the-art supercritical airfoil technology. However, because of the requirement of simplified geometries for the purpose of code correlation, the complicated glove-type planform which is typical of advanced supercritical wings was not used.

The wing root and tip sections were developed by first establishing a mid-wing subcritical pressure distribution consistent with advanced supercritical airfoil technology. The mid-wing design pressure distribution was then incremented for root and tip effects obtained from the Lockheed version of the Hess panel program (ref. 14). These incremented pressure distributions for the root and tip were then used in an inverse program to produce the actual root and tip section geometry. The resulting wing was analyzed using both the subcritical panel program and the Bailey-Ballhaus small disturbance transonic code (ref. 4). Results for the subcritical case are shown in figure 2, which shows the constant sweep isobar pattern obtained by this design procedure.

At transonic speeds the wing shock pattern obtained from the transonic small disturbance code can be seen in figures 3 and 4. The shock pattern follows the constant isobar sweep pattern obtained at subcritical speeds, except in the vicinity of the wing root. The Mach number normal to the shock was less than 1.2 at all points on the wing, so the design was expected to perform well. The airfoil sections used to define the wing are shown in figure 5. Actual root and tip nondimensional ordinates are given in Table III.



### 2.3 Wing B Design Procedure

Wing B is a fighter type wing with aspect ratio 3.8, designed for transonic cruise. This wing is defined by root and tip sections and has a quarter-chord sweep of  $30^\circ$ . The root and tip sections are 6% thick and were designed using supercritical airfoil technology for cruise conditions at  $M = .9$ . The subcritical isobar pattern obtained on Wing B using the panel program is shown in figure 6. The swept isobar pattern is expected to produce, during cruise, a shock with a sweep matching the wing mid-chord sweep. Pressure distributions from an analysis of the wing using the Bailey-Ballhaus small disturbance transonic program are shown in figure 7 at  $M = 0.86$ . This code shows that the wing supercritical flow pattern is dominated by a shock that is completely unswept. This discrepancy in predictions of shock sweep by the subcritical isobar technique and the transonic small disturbance code is one question to be resolved by the test of Wing B.

In order to keep the geometry simple, the supercritical wing glove and fillet have not been incorporated into the design. Figure 8 shows the root, mid-wing, and tip airfoil sections in a rigged position. Wing B non-dimensional section ordinates are given in Table IV.

### 2.4 Wing C Design Procedure

Wing C was designed using two existing computer codes: a numerical optimization program based on the Method of Feasible Directions (ref. 15) and an aerodynamic analysis program based on a relaxation solution of the 3-D full-potential equation, FL0-22 (ref. 10).

The initial design effort was directed toward the more conventional approach of drag minimization at a single-point design condition of  $M = 0.85$  and  $C_L = 0.5$ . Various perturbation shape functions were used to modify the ordinates of the root and tip sections, as well as wing twist and incidence. Although this approach did result in significant reductions in drag from the

starting wing geometry, the final optimized wing pressure distribution was less than desirable. This resulted primarily from neglecting viscous effects in the aerodynamic analysis code. Since the inclusion of viscous effects in the analysis would result in a prohibitive increase in computation time, an alternative approach was sought.

A unique design-to-pressure distribution approach was selected. The design objective of this case was to minimize the RMS deviation between the computed surface pressure distribution and a design pressure distribution by appropriate modifications to the wing geometry.

Figure 9 shows the final "optimized" pressure distributions at the design conditions as predicted by FL0-22. The airfoil contours at the root and tip are depicted in figure 10, and Table V gives the airfoil section ordinates.

### 3. APPARATUS

#### 3.1 Models

3.1.1 Wings. - The three semispan wing models were each machined from a solid billet of 17-4PH stainless steel by a numerically controlled milling machine. The models were hand-finished to a tolerance of  $\pm 0.05$  mm (.002 in.). Actual model coordinates were measured at several stations by a precision measuring machine, and compared to lofted coordinates used to define the wing. Each wing had a total of 160 static pressure orifices located in chordwise rows at 5 span stations. The actual measured locations of the static pressure ports are included in Table VI. The upper surface pressure orifices were installed by drilling completely through the wing so that all tube routing could be done on the wing lower surface. This instrumentation technique leaves the upper surface completely free of tube routing channels which can cause irregularities in curvature.

3.1.2 Fuselage. - The fuselage used in these tests was a simple shape, having an elliptical forebody and afterbody with a constant section in the wing region. The three different center-sections were required for each wing to allow testing in high, mid and low-wing position. The three portions of the fuselage were all mounted to a 1.3 cm (.5 in.) thick plate. A sketch of the fuselage is shown in figure 11.

#### 3.2 Test Facility

The general arrangement of the Lockheed Compressible Flow Wind Tunnel (CFWT) is shown in figure 12. The tunnel is of the blow-down type, exhausting directly to the atmosphere. The air storage capability is  $368 \text{ m}^3$  (13,000  $\text{ft}^3$ ) at 413 dynes/ $\text{cm}^2$  (600 psia). A sleeve-type control valve accurately maintains the settling chamber stagnation pressure at selected pressure less than or equal to the 172 dynes/ $\text{cm}^2$  (250 psia) maximum at a mass flow rates less than 1089 kg/sec (2400 lb/sec). The test section is 50.8 cm (20.0 in.) wide by 71.2 cm (28.0 in.) high by 183 cm (72.0 in.) long and is enclosed

in a 3.7 m (12.0 ft.) diameter plenum chamber. The top and side walls of the three-dimensional test section have variable porosity capability (from 0 to 10 percent), obtained by sliding two parallel plates with .635 cm (.250 in.) diameter holes slanted 60 degrees from the vertical. The bottom wall, where the model is mounted, is not porous. The model is mounted on a five-component balance located in the floor. The balance and model rotate together on a turntable to vary angle of attack. A bleed duct is located 53.6 cm (21 in.) ahead of the balance centerline to remove the wind tunnel boundary layer. The boundary layer bleed system has an independent control valve and exhausts to atmosphere through a separate pipe system. The main features of the test apparatus are illustrated in the photograph of figure 13. A more detailed description of the facility may be found in reference 16.

### 3.3 Instrumentation

Instrumentation for this test program consists of a five-component strain gauge balance to measure model aerodynamic forces. One hundred and sixty surface pressure taps were installed in the wing at five spanwise stations as summarized in figure 14. Six far-field pressure rails, each containing 31 static pressure taps, were mounted on the tunnel walls as shown in figure 13 and detailed in figure 15. The far-field measurements were extended to the symmetry plane by a row of fourteen streamwise pressure taps along the tunnel floor on each side of the model. These pressure orifices were displaced 5.08 cm (2.0 in.) inward from the tunnel sidewalls.

Measurements of the static pressures on the wing surface and the wall rails were made using electronically actuated pressure scanning valves. The full-scale range of the quarter percent accuracy Statham pressure transducers in the scanning valves were selected to provide maximum accuracy for the wind tunnel conditions tested (wall rails  $\pm 12.5$  psi and airfoil pressures  $\pm 50$  psi). CEC force balance pressure transducers were used in conjunction with CEC servo amplifiers to provide a precise measurement of the atmospheric pressure, stagnation pressure, and test section static pressure to 0.05% of the 250 psi capacity. These transducers allow

determination of the test section Mach number to an accuracy of  $\pm 0.002$  at the highest stagnation pressure.

Angle of attack was measured with a calibrated potentiometer operated by the angle-of-attack drive mechanism.

The balance used to measure forces on the model was designed and built by Lockheed-California. It is a strain gauge five-component temperature compensated balance designed to the following load capacities:

Normal force	$\pm 750$ lbs.
Axial force	$\pm 75$ lbs.
Pitching moment	$\pm 1800$ in. lb.
Rolling moment	$\pm 6000$ in. lb.
Yawing moment	$\pm 600$ in. lb.

Design accuracy of the balance is 1/4% of design load and 1/2% of applied load. To produce the most accurate data, the test Reynolds number was chosen such that the highest Mach-Alpha point of the test matrix corresponded to a design load condition for the balance. Raw pressure and balance data were recorded on magnetic tape utilizing the CFF high speed data acquisition system. The data acquisition system consists of a Lockheed Electronics Company MAC-16 computer and associated peripheral equipment. The raw data was reduced to coefficient form with a TI-990 computer. Machine plots were made on a Calcomp 765 plotter.

### 3.4 Data Reduction

3.4.1 Balance data. - The force balance data were acquired by taking one hundred samples over a one second time span. The average of the 100 samples was reduced to pounds of force and inch pounds of moment by multiplying the five measured values by the calibration matrix. The resulting measurements were converted to conventional coefficient form using the tunnel conditions at the time the force measurements were made.

3.4.2 Pressure data. - All static pressure measurements from the wing and far-field rails were reduced to standard coefficient form using instantaneous tunnel conditions at the time each pressure was measured. Pressure coefficients for each spanwise station were numerically integrated to determine a local lift coefficient. Plots of span load distribution were made using the local lift coefficients obtained from the pressure integrations.

3.4.3 Machine plotting. - A plot routine was developed for the UNIVAC 1106 computer to generate machine plots of the pressure data on a CALCOMP 765 plotter. Sample plots for each wing are shown in the Test Results section. The plots consisted of chordwise pressure plots for each wing station, a summary of the wing pressures on a pseudo-three dimensional plot of the wing planform, span load distribution, and plots of the far-field pressure data.

## 4. TESTS AND METHODS

### 4.1 Test Conditions

The three wings were tested over a wide range of conditions to provide data at off-design as well as design conditions. Tests were conducted at nominal unit Reynolds numbers ranging from 43 to 52 million per meter (14 to 17 million per foot). The test Reynolds number based on mean aerodynamic chord was nominally 6 million for Wing A and 10 million for Wings B and C. Although the wind tunnel was capable of much higher unit Reynolds numbers, the actual test values were limited by the capacity of the wing force-balance.

The angle of attack and tunnel Mach number were varied over a wide range: from zero-lift to above design values and subcritical speeds through drag-rise, respectively.

Most of the wind tunnel testing was conducted at a fixed wall porosity of 4% because previous tests in the CFWT had indicated this value would provide minimum wall interference effects. However, in order to properly assess the effect of wind-tunnel wall interference, each of the wings was tested over a range of wall porosities varying from 3 to 6%.

High, mid, and low-wing/fuselage configurations were tested for all three wings over a limited matrix of conditions. A complete summary of test conditions for the three wings is presented in Table VII.

### 4.2 Transition

For the unit Reynolds numbers of these tests, experience with the CFWT facility indicates that significant regions of laminar flow would exist on a smooth model. Therefore, to fix transition and to eliminate the uncertainties of the transition location, a transition strip was applied to each model. The transition strips were applied to both the upper and lower

surface and were located and sized according to the guidelines of reference 17. The strips were thus located a fixed distance from the leading edge equal to 5% of the mean aerodynamic chord. The grit consisted of .058 mm (.0023 in.) diameter glass beads, set in a lacquer fixative. The width of the strips were constant at 1.2 mm (.05 in.).



## 5. TEST RESULTS

### 5.1 Test Techniques

Since the primary objective of this program is to establish a set of benchmark data suitable for evaluations of theoretical codes, considerable effort was expended to evaluate those aspects of the test techniques which could affect the quality of the results.

5.1.1 Boundary layer removal system. One unique aspect of the test facility used in this test program was the bleed system used to remove the wind tunnel boundary layer ahead of the model (fig. 13). An investigation was conducted to determine the sensitivity of the model data to boundary layer bleed rate. The operational procedure used in all of the testing was to set the bleed rate so that the static pressures measured at the leading edge of the flat plate which formed the top of the bleed duct did not indicate any angle-of-attack loading. The correct bleed-valve setting for most testing was found to be around 60% full-open.

Sensitivity of the force data to the bleed system is shown in figure 16, which summarizes the effect of bleed-valve position on  $C_L$ ,  $C_D$ , and  $C_m$  as measured by the balance. The lines faired through the data have been adjusted for the small differences in Mach number and lift coefficient between the runs. On the basis of these data, it was concluded that the bleed system had a large effect on the balance data when the valve was nearly closed, but once the valve was half open, the results were not sensitive to small differences in bleed valve setting.

5.1.2 Tunnel calibrations. Prior to installation of the models, the Lockheed-Georgia CFWT was calibrated by installing a static pipe along the tunnel centerline. The pipe extended from the settling chamber through the test section into the tunnel diffuser. Static pressure orifices located along the pipe were used to determine the Mach number through the tunnel test section. The test section configuration was the same as would be used when the model was installed, in that the bleed system as well as the far-field

static pressure rails were installed. The tunnel Mach number distribution was found to be uniform as shown in figure 17.

5.1.3 Force balance evaluation. - The force balance used for these tests was calibrated prior to the conduct of the tests. However, as a further check, an evaluation of the repeatability of the balance was made midway during test. Figure 18 shows repeatability of measurements obtained with this balance. It appears that lift and drag repeat quite well. Pitching moment shows a little more scatter, but is felt to be acceptable.

5.1.4 Fuselage/wing seal. - The wing/fuselage configurations were tested with the fuselage non-metric. The fuselage center-shells were cut out so that the wing could fit through the fuselage with a nominal gap of .76 mm (.030 in.). Wing C, the Lockheed IRAD wing, was tested first with the wing/fuselage gap unsealed. It was found that a significant amount of flow was passing from the wing lower surface to the upper surface through the fuselage cavity. Figure 19 shows a comparison of the wing pressure distribution before and after a foam seal was added to the wing/fuselage gap, with clean wing data included for reference. The effect of the seal is modest in absolute terms. As a result of these tests, Wing A and B fuselage configurations were run with a foam seal in place, but Wing C data was not re-run.

## 5.2 Wing A Test Results

5.2.1 Force data. - The force data obtained from balance readings is shown in figures 20 through 22. As is customary, these data have not been corrected for wind tunnel wall effects. The  $C_L$  versus  $\alpha$  curves shown in figure 20 vary systematically: As Mach number increases, the slope becomes steeper in the mid- $C_L$  range. At the higher Mach numbers, the data becomes nonlinear at both high and low values of lift coefficient, reflecting the effect of supercritical flow on the wing. The pitching moment ( $C_L$  vs.  $C_M$ ) curves shown in figure 21 are seen to vary systematically but are generally nonlinear. The drag polars ( $C_D$  versus  $C_L^2$ ) show a systematic variation with Mach number, but is nonlinear, even at low Mach number. This is caused by

the fact that the balance forces were resolved about the flight-axis coordinates without including the effect of wind tunnel wall interference on the angle of attack. This effect is discussed in the section on wind tunnel wall interference. A summary plot of  $C_D$  versus Mach number is shown in figure 23 for various values of lift coefficient. The drag-rise Mach number for this wing occurs at about  $M = .82$  for a lift coefficient of .4 to .5. This is a reasonable level of performance for an advanced technology transport wing.

5.2.2 Pressure data. - Figures 24 through 29 show the distribution of pressures on the wing at various Mach numbers for a constant angle of attack of  $3^\circ$ . This corresponds to a lift coefficient in the range from .45 to .53 depending on Mach number. The constant-isobar pressure distribution at  $M = .62$  (fig. 24) is typical for an advanced supercritical wing. (The third pressure port at the  $\eta = .95$  station is apparently not reading correctly because of the transition grit strip.) As Mach number is increased to .76 (fig. 25), the strong leading-edge suction peak develops into a supercritical flow region terminated by a shock wave which follows the constant-isobar sweep line. This shock pattern continues up to  $M = .78$  as shown in figure 26. However, at  $M = .80$  (fig. 27) a root lambda-shock develops at the inboard station. The back leg of the lambda shock moves aft and outboard at  $M = .82$  as shown in figure 28. This condition represents the design point for the wing as evidenced by good supercritical airfoil pressure distributions at the various stations, and no evident separation. The condition of  $M = .82$  and  $\alpha = 3^\circ$  is also the beginning of drag rise as indicated by the force data. A further increase in Mach number to  $M = .84$  (fig. 29) results in the beginning of trailing-edge type shock-induced separation at the  $\eta = .7$  station where the wing local lift coefficient reaches a maximum on the wing.

A summary of the shock pattern obtained from the pressure distributions is shown in figure 30.

5.2.3 Fuselage effects. - Wing A was tested with three fuselage configurations. Pressure measurements are shown in figure 31 comparing the wing pressures at  $M = .82$  without a fuselage to wing pressures at the same Mach number in the presence of a fuselage where the wing is mounted as a mid-wing

configuration. The change in pressure distribution shows that the main effect of the fuselage is to move the reflection plane (which was represented by the tunnel floor) outboard by approximately the radius of the fuselage. This is clearly seen in figure 34 which shows the wing-shock pattern for the clean wing and the wing/fuselage configurations at  $M = .82$ .

Similar results were obtained for both a high wing and low wing configuration as shown in figures 32 and 33. In general it can be seen that the effect of the fuselage is strongest on the upper surface wing pressures for the low wing configuration. The impact of the fuselage was more severe on the lower surface pressures for the high wing configuration.

### 5.3 Wing B Test Results

5.3.1 Force data. - The force data obtained from balance readings for Wing B is shown in figures 35 through 37. The lift data shown in figure 35 are linear with an increasing slope as Mach number is increased. The pitching moment data in figures 36 show the wing to have a large negative value of pitching moment at zero lift and the  $C_M$  vs  $C_L$  curves are generally nonlinear. At the highest Mach number tested,  $M = .94$  the pitching moment becomes quite large as the supersonic flow regions expands over the aft portion of the wing. Drag polars for various Mach numbers are shown in figure 37.

A cross plot of drag vs Mach number at constant lift is shown in figure 38. The beginning of drag rise occurs at about  $M = .90$  to  $.92$  at all lift coefficients, which indicates that this wing performs well and is representative of an advanced supercritical wing.

5.3.2 Pressure data. - Pressure data measured at five spanwise stations on Wing B for various Mach numbers and an angle of attack of  $3^\circ$  are shown in figures 39 through 44. At  $M = .7$  the pressure distribution shown in figure 39 is typical of a supercritical wing, having a high suction peak at the leading edge, and a large amount of aft loading due to the trailing edge camber. As Mach number is increased to  $.85$  (fig. 41), the wing develops a

supersonic region with a shock following the constant percent-chord isobar pattern of the original design.

Figure 42 shows the wing pressures at  $M = .90$  where the leading edge shock has pulled back on the outer portions of the wing giving a sweep-angle greater than local constant percent-chord line sweep. An aft shock develops as well, producing a typical lambda shock pattern. The aft leg of the lambda pattern is nearly normal to the freestream. The aft shock grows stronger and a third shock forms at the  $\eta = .8$  station at  $M = .91$  (fig. 43). The third shock merges with the aft leg of the lambda shock at  $M = .93$  as shown in figure 44. The wing is into drag rise condition at  $M = .93$  even though there is no noticeable separation on the wing.

5.3.3 Fuselage effects. - Comparisons of the wing pressure distribution with and without a fuselage present are shown in figures 46 through 48. Data are presented for high, mid and low-wing configurations at  $M = .90$  and an angle of attack of  $4^\circ$ . The effect of the fuselage is primarily to move the lambda shock pattern on the wing outboard by a distance of approximately one body radius. The aft shock tends to move further back on the high wing case and least on the low wing case. There is a significant reduction in strength of the aft shock at the inboard station for all three fuselage configurations. There appears to be a reduction in trailing edge pressure recovery due to the fuselage over-velocity which is most pronounced on the low wing configuration. A summary of the wing shock patterns for the three fuselage configurations is shown in figure 49.

## 5.4 Wing C Test Results

5.4.1 Force data. - The force data obtained on Wing C are summarized in figures 50 through 52. The lift data shown in figure 50 are very linear with angle of attack, even at the highest transonic speeds. The pitching moment vs lift coefficient curves are generally linear. This wing has a large negative pitching moment at zero lift which is caused by the aft loading type airfoils used in the wing. The drag data for Wing C is shown

in figure 52. A summary plot of drag vs Mach number is presented in figure 53. The drag-rise Mach number for this wing is about .87 to .88 at the design lift coefficient.

5.4.2 Pressure data. - The pressure data obtained from five spanwise rows of pressure taps on Wing C at Mach numbers from .7 to .9 at an angle of attack of  $5^\circ$  are shown in figures 54 through 60. The difference in design technique between this wing and Wing B can be clearly seen by comparing the Mach = .7 pressure distributions. Wing B has a much higher suction peak than Wing C. As Mach number is increased to .80, a region of supersonic flow begins to develop on the outboard portion of the wing as shown in figure 55. At a Mach number of .84 (fig. 56), a strong shock has developed at the  $\eta = .9$  station. The tip shock continues to be the dominant feature of the wing pressure distribution at all Mach numbers up to .9 as shown in figures 57 through 60. At  $M = .9$  the wing pressure distribution exhibits a lambda shock pattern near the tip.

A summary of the wing shock pattern obtained from these pressure data is shown in figure 61.

5.4.3 Fuselage effects. - Comparisons of the wing pressure distribution with and without a fuselage present are shown in figures 62 through 64. Data are presented for high, mid, and low-wing configurations, respectively at  $M = .90$  and an angle of attack of  $5^\circ$ . It should be noted that the fuselage center-shell covered the inboard row of pressure orifices. The overall effect of the fuselage on this wing flow is similar to that observed for Wings A and B; that is, to move the wing reflection plane outboard by approximately the fuselage radius. However, for Wing C the sensitivity of the flow to wing-fuselage position is small, with only modest differences in wing pressure distributions observed for the three wing/fuselage configurations.

Wing C does not have significant supercritical flow in the inboard regions, so a shock movement is not apparent at the  $\eta = .3$  station. However, the presence of the fuselage causes a shift in pressure similar to the

centerline "kink effect" often seen on wings at subcritical conditions, namely the leading edge suction pressures are suppressed while the suction pressures are increased toward the trailing edge. A summary of the wing shock pattern for the three fuselage configurations is shown in figure 65.

#### 5.5 Detailed Experimental Data

To facilitate use of these data for future code correlations, a significant portion of the experimental pressure data have been machine plotted and published in a separate volume in Appendix B. The plots include wing three-dimensional pressure plots, local section pressure plots, and span load distributions for all wing and wing/fuselage configurations. Also included in Appendix B are instructions for obtaining a complete set of data on magnetic tape.

## 6. WIND TUNNEL WALL INTERFERENCE

### 6.1 Review of Current Methods

Transonic wind tunnel wall interference is the least understood aspect of transonic testing. Researchers have attempted to minimize the effects of wall interference by reducing model-to-tunnel size ratio, using ventilated tunnel walls, and, more recently, by developing adaptive wall wind tunnels. Notwithstanding these efforts, interference effects at transonic speeds can still be quite large, and without proper understanding and evaluation can result in uncertainty in the quality of the test data. These uncertainties must be resolved before wind-tunnel data can be used for code correlations and for predictions of free-air aerodynamics.

6.1.1 Inclusion of wall interference in code correlations. If test data are to be used to correlate theoretical methods, as in the present investigation, the effects of transonic wall interference must be well understood and taken into account in the correlations. In this way the adequacy of the mathematical models (governing equations, boundary conditions, solution algorithms, etc.) used in the theoretical methods can be properly evaluated.

A generally applicable method for treating transonic wind tunnel wall interference in three-dimensional calculations has not yet been developed. The usual procedure has been to apply conventional wall-interference correction methods which are based on linearized subsonic theory. This procedure, however, has been found to be generally inadequate for a quantitative assessment of wall interference at transonic speeds.

Recently, nonlinear method development has received increased attention. Chan (ref. 18) has developed a perturbation technique based on the transonic small-disturbance equation for two-dimensional flow. Murman (ref. 19) included a theoretical model for ventilated wind tunnel walls directly into a transonic airfoil analysis program. Three-dimensional, nonlinear methods are just now being developed. Shankar, et. al. (ref. 20) report on the



development of a method for treating wall interference in solid and free-jet tunnels.

A major weakness in all of the above (linear and nonlinear) methods is the use of the classical homogeneous wind-tunnel wall boundary condition. This model is a simplified linear approximation of a complex viscous-flow process. The exact nature of the flow through a porous wall is not well understood; but it is considered to be highly nonlinear, depending upon the boundary layer development on the wall, the pressure field induced by the model, and whether there is inflow or outflow through the wall. As a result, methods employing this model have been useful only in providing qualitative estimates of wind tunnel wall interference.

A more exact approach to evaluation of wind tunnel wall effects is to measure the flow-field properties on control surfaces near the wind-tunnel walls, but outside of the complex viscous flow region, and introduce the measured values directly into the computational method as far-field boundary conditions. Comparisons of computations based on free-air far-field boundary conditions and computations based on measured far-field boundary conditions then gives a precise, quantitative assessment of the wind tunnel wall interference. This new method for evaluation of wall interference will be developed in Section 6.2.1 of this report.

6.1.2 Correction of tunnel data to free-air conditions. - Kemp (ref. 21) proposed the concept of "correctable interference," whereby there exists a range of flow conditions for which wind tunnel wall interference effects can be treated by a simple adjustment in freestream Mach number and angle of attack. This concept has been supported two-dimensionally by the experimental work of Blackwell (ref. 22) and analytically by Murman (ref. 23). The validity of this concept, however, has not been investigated to date for three-dimensional flows.

The new method to be developed in the next section will be applied to the test data acquired herein to quantify the effects of wall interference

and establish the validity of simple corrections to Mach number and angle of attack.

## 6.2 Development of New Computational Method

A unique procedure has been developed to include wind tunnel walls in three-dimensional transonic flow calculations. The new method is based upon the Bailey-Ballhaus ESD transonic code (ref. 4). The primary reason for the selection of this code is that the finite Cartesian grid used in the code is amenable to the inclusion of measured wind tunnel wall pressures in the solution process. The explicit inclusion of measured wind tunnel wall pressures as outer Dirichlet boundary conditions is the essential feature of the solution process. This procedure eliminates the need for a theoretical model for the wall boundary condition, and thus ensures that the true nonlinear character of the porous walls are properly taken into account. This procedure is similar to that of Kemp (ref. 24) and Stahara (ref. 25). Kemp imposed measured boundary conditions to solve for the flow about two-dimensional airfoils while Stahara followed a similar approach to model flow about axisymmetric, nonlifting bodies in ventilated wind tunnels.

6.2.1 Method formulation. - The formulation of the procedure for incorporating measured boundary conditions in the nonlinear transonic theory is illustrated in figure 66 and described in detail in the following paragraphs.

A rectangular computational boundary is established around the wing as shown in figure 66. The top, bottom, and side planes approximate the locations of the porous wind tunnel walls. The boundary conditions near the upper and lower walls are determined by integrating static pressure distributions which were measured during the test:

$$\phi(x,y,z) = -\frac{1}{2} \int_{x_0}^x c_{pM}(\xi,y,z) d\xi + \phi(x_0,y,z) \quad (1)$$

where  $\phi_x$  has been replaced by  $-C_p/2$  in keeping with small disturbance theory. The wall-induced perturbations on the side plane is assumed to be sufficiently small such that the disturbance potential can be approximated by an asymptotic far-field solution of the small-disturbance transonic equation given by Klunker (ref. 26). The downstream boundary is assumed to be sufficiently far removed from the model that the streamwise perturbation velocity vanishes, that is,  $\phi_x = 0$ , at the downstream boundary. The usual symmetry conditions,  $\phi_y = \phi_{xy} = 0$ , are applied on the plane of symmetry.

The perturbation potential at the upstream boundary,  $\phi(x_0, y, z)$  requires special treatment. It can be shown that for small flow-inclination angles at the upstream boundary,

$$\phi(x_0, y, z) = \int_{z_0}^z \alpha(x_0, y_0, \zeta) d\zeta + \int_{y_0}^y \beta(x_0, \eta, z) d\eta + \phi_0 \quad (2)$$

where  $\alpha$  and  $\beta$  are the upflow and crossflow inclination angles, respectively.

Furthermore, if the flow angles at the upstream boundary are expressed as combinations of the free-air values and wall-induced perturbations to the free-air values, then

$$\phi(x_0, y, z) = \phi_{FF}(x_0, y, z) + \int_{z_0}^z \delta\alpha(x_0, y_0, \zeta) d\zeta + \int_{y_0}^y \delta\beta(x_0, \eta, z) d\eta \quad (3)$$

where  $\phi_{FF}$  is the free-air far-field potential. These wall-induced upwash and crossflow distributions at the upstream boundary,  $\delta\alpha$  and  $\delta\beta$ , are regarded as small quantities but their impact on the solution may be quite significant. These terms represent the lift interference contributions, and their effect is approximately equivalent to that produced by a change in angle of attack or sideslip in a free-air solution. Therefore, the approach used herein is to ignore the sideslip correction,  $\delta\beta$ , and to approximate the  $\delta\alpha$  integral by a simple adjustment in the angle of attack. The angle-of-attack correction,  $\Delta\alpha$ , is found by matching computed and measured upper and lower surface

pressures in the leading edge region where the pressures are very sensitive to angle of attack.

The  $\Delta\alpha$  approximation in the method could be eliminated by extending the far-field pressure measurements sufficiently far upstream into the unventilated section of the tunnel where the wall-induced angularity is zero. The  $\delta\alpha$  and  $\delta\beta$  integrals over the upstream boundary would then vanish.

6.2.2 Computing blockage correction using the new method. The new method provides a means for assessing the validity of applying a simple Mach number increment to the test data to correct for tunnel blockage. To do this, theoretical solutions are first computed using measured wind-tunnel wall boundary conditions and the corrected angle of attack. Next, free-air solutions are computed while varying Mach number to produce the best match with the tunnel solution. If the differences in the tunnel and free-air solutions are sufficiently small, the data are considered correctable and a simple adjustment of Mach number can be made to remove tunnel wall blockage effects from the test data.

Results discussed in the following section show that such a correction procedure is possible.

### 6.3 Application of New Method

A comparison of the theoretical free-air and measured pressure distributions on the control surfaces above and below Wing A is presented in figure 67. A comparison is presented at the wing design condition using angles of attack which have been adjusted to give approximately the same lift coefficient. Differences in the measured wind-tunnel pressures and the computed free-air pressures are relatively small, indicating that the wall-induced interference effects are small in this case. The theoretical calculations do not account for the effects of the viscous layer over the wing or in the wake. It is felt that by matching lift the primary effects of viscosity on the far-field pressures is taken into account. The effect of

neglecting displacement surface effects on the wing is important only near the wing. The effect of the wing viscous wake, however, which is also neglected, is probably more significant in the far-field.

When the experimental far-field pressures (fig. 67) are incorporated as boundary conditions in the transonic code, the effect on the computed wing surface pressures are as shown in figure 68(a). The broken line corresponds to the free-air conditions noted in figure 67 while the dashed line is the result of specifying experimental far-field pressures. The interference effect of the tunnel walls is indeed small, resulting in a forward shift in the shock location of approximately 5% chord and a general depression of the upper surface suction level.

To investigate the correctability of the "tunnel" data with regard to wall interference, the theoretical free-air solution was recomputed while varying freestream conditions to obtain the best possible match of the uncorrected tunnel pressures. Figure 68 shows that for a simple correction of  $\Delta M = -0.005$  to the freestream Mach number, the free-air pressure distribution at the corrected conditions and the pressure distribution in the tunnel closely agree. The good agreement for the complete wing, shown in figure 68(b), indicates that the effect of spanwise variations in tunnel Mach number is negligible.

Thus, it has been shown that for Wing A the test data obtained in the wind-tunnel at the conditions noted can be reinterpreted to free-air conditions at a corrected Mach number which is approximately 0.005 less than the wind tunnel test Mach number.

Similar analyses have been conducted for Wings B and C. Figure 69 illustrates the differences between the theoretical free-air and experimental pressures at the tunnel walls for Wing B near its design conditions. The differences are very similar to those observed for Wing A. The effect of wall interference on the wing pressures [fig. 70(a)] is also similar; forward displacement of the shock and a decrease in the upper surface suction level. A correction of approximately -0.005 in Mach number was

found to provide the best simulation of wall interference effects [fig. 70(a)]. The correctability of the tunnel data to free air with a simple Mach number correction is not quite as good as for Wing A. The major discrepancy is the upper surface suction level which cannot be improved by an  $\alpha$  adjustment since the lower surface agreement would then suffer.

The results of the wall interference investigation for Wing C at its design conditions are presented in figures 71 and 72. Again the wind tunnel data can be corrected to free air by an adjustment of  $-0.005$  in Mach number.

To obtain an indication of the range of conditions over which the data for the three wings are correctable, an analysis of Wing C at a tunnel Mach number well above its design conditions was conducted (fig. 73). A larger Mach number correction is now required, but the match in the tunnel and corrected free air pressure distributions is still excellent. This result implies the correctability of off-design data for all three wings.

The salient conclusion of this study is that the concept of correctable interference in three-dimensional transonic flow is indeed valid. Furthermore the wind tunnel test data obtained in this investigation can be corrected to equivalent free-air conditions by simple adjustments in Mach number and angle of attack. Near the design conditions for the three correlation wings investigated herein, a small constant adjustment of  $\Delta M = -.005$  is sufficient to remove the effect of blockage interference from the test data. The effect of lift interference is accounted for by adjusting the model angle of attack until the upper and lower surface pressure level in the nose region matches the theoretical free-air values.

## 7. EVALUATION OF TRANSONIC COMPUTATIONAL METHODS

An evaluation of several transonic calculation procedures will be made and discussed in this section. First, a brief description is presented of the methods selected for evaluation. Next, the convergence characteristics and numerical efficiency of the selected codes will be discussed. Finally, the results of the calculations will be compared with experimental data for Wings A, B, and C and conclusions drawn.

### 7.1 Description of Methods

The three-dimensional transonic computational methods selected for evaluation in this program are:

1. The Bailey-Ballhaus extended small disturbance (ESD) code (ref. 4).
2. The Jameson-Caughey full-potential equation (FPE), non-conservative relaxation (NCR) method, FL0-22 (ref. 10).
3. The Jameson-Caughey FPE fully-conservative relaxation (FCR) method, FL0-27 (ref. 12).

Each of the codes solve a type-dependent finite-difference approximation to the governing equations by an iterative relaxation process. Another common feature of the methods is the use of successive grid refinement to speed convergence.

7.1.1 Bailey-Ballhaus code. - The Bailey-Ballhaus code solves a modified or extended small disturbance approximation of the full potential equation. Linearized wing boundary conditions are applied in the wing reference plane. The embedded grid scheme of Boppe (ref. 6) is followed in which a fine skewed inner grid (enclosing the wing) is embedded within a crude Cartesian outer grid. The outer computational grid is finite with

boundary conditions given by the Klunker asymptotic far-field expansion (ref. 26).

The version of the Bailey-Ballhaus code used in this study was modified at Lockheed by incorporating automatic grid generation routines which provided grid-stretching capability. This produced smooth, highly dense grids in regions with large gradients, with smooth stretching toward the grid boundaries.

The Bailey-Ballhaus program is formulated using both non-conservative and fully-conservative differencing. The desired form is selected by the user.

7.1.2 FL0-22 code. - The Jameson-Caughey FL0-22 program is a production code capable of treating the flow about yawed or swept wings. The method solves a quasi-linear (nonconservative) form of the full potential equation which has been explicitly transformed to a boundary conforming coordinate system. The coordinate system is generated by a sequence of numerical shearing transformations, and a simple square-root mapping about a point inside the wing leading edge. This results in a desirable concentration of grid points in the nose region, but the simple shearing, however, results in a spanwise decrease in the number of computational grid points on the wing.

7.1.3 FL0-27 code. - The Jameson-Caughey FL0-27 program is a pilot code capable of treating the flow about an isolated yawed or swept wing, or one mounted on an infinite circular cylinder. A finite-volume scheme is used to difference the full potential equation in conservative form. The analysis of FL0-27 is based on a numerical calculation of the required transformation derivatives at each grid point in the computational region. Thus, in principle, the method can be adapted to treat configurations of arbitrary geometric complexity simply by providing the Cartesian coordinates of each mesh point. This flexibility is achieved at the expense of an increase in computation time and some loss in accuracy because the transformation coefficients must be calculated numerically for each relaxation cycle.



In the present version of the program, the computational grid is generated by a sequence of global mappings which are similar to those used explicitly in FL0-22. The main difference (for isolated wings) is that in FL0-27 the wing chord is covered by the same number of grid points at every span station.

## 7.2 Code Convergence

Since solution cost is an important consideration in the selection of a computational method, a study was conducted to assess the relative computational efficiency of the selected codes by comparing computation times required for solution convergence. For this purpose, convergence was established from an examination of the time-history of the wing pressure distributions. The solution for Wing A at its design conditions of  $M=0.82$  and  $\alpha = 1.5^\circ$  was arbitrarily chosen as the test case; however, the results should also apply for either of the other wings at other transonic conditions.

The results of this investigation are presented in figures 74, 75, and 76, which show the variation in the wing pressure distributions (at two span stations) with iteration number for the three evaluated codes. The iteration number,  $n$ , refers to the number of relaxation cycles on the final (finest) grid only. The solution for the Bailey-Ballhaus code (fig. 74) was achieved by first completing 50 iterations on an initial coarse grid (5,000 points), then interpolating the results to start the solution on the fine embedded grid system. The FL0-22 solution history shown in figure 75 was preceded by 50 iterations on a crude grid ( $48 \times 6 \times 8$  mesh cells) followed by 50 iterations on a medium grid ( $96 \times 12 \times 16$  cells). A similar procedure was followed for execution of the FL0-27 code - 100 iterations on a  $40 \times 4 \times 8$  grid and 100 iterations on a medium  $80 \times 8 \times 16$  grid.

The pressure distribution histories indicate that convergence was obtained after approximately 200 iterations of the Bailey-Ballhaus code, 50 to 100 iterations of FL0-22, and 200 iterations of FL0-27. The corresponding computation times, and other grid features, are summarized in Table VIII. The solution time for the conservative FL0-27 code is approximately twice that

for the nonconservative FL0-22 code and about five times the required CPU time for the Bailey-Ballhaus small disturbance code. (The convergence characteristics were essentially the same for both the FCR and NCR solutions of the Bailey-Ballhaus program.)

No systematic attempt was made to optimize the convergence characteristics or grid structures of the programs, but adjustments in convergence-related input parameters were made when appropriate. It should be noted that attempts to improve upon the convergence characteristics shown for FL0-27 were generally unsuccessful, usually resulting in solution divergence.

### 7.3 Code Correlations

In this section experimental data are compared with theoretical solutions for the three wings. First, nonconservative relaxation (NCR) inviscid solutions generated using the FL0-22 FPE and the Lockheed version of the Bailey-Ballhaus ESD codes are compared with experimental data. Next, fully-conservative relaxation (FCR) inviscid results computed using FL0-27 FPE and Bailey-Ballhaus ESD are correlated. Finally, viscous effects are assessed from results obtained using the FL0-22 code coupled with an iterated two-dimensional boundary layer and conclusions are drawn.

All calculations were made for isolated wings in free-air conditions using Mach numbers and angles of attack corrected according to the technique described in Section 6.3. The corrected  $\alpha$  was obtained using FL0-22 calculations.

Only summary plots are presented and discussed in this section. Detailed results of the correlations may be found in Appendix A.

7.3.1 Wing A - High aspect ratio, low sweep. - Computed Wing A inviscid nonconservative FPE and ESD solutions are compared with experiment in figures 77(a) and 77(b), respectively. The agreement between FPE and experiment is surprisingly good in view of the fact that the boundary layer was neglected in the calculations. The only serious discrepancies between

theory and experiment are in the aft portion of the wing where the calculations over-predict the airfoil loading.

The ESD results also are in good agreement with experiment, but not as good as the FPE solution. The ESD results over-predict the airfoil aft loading to about the same extent as did the FPE calculations. However, unlike the FPE results, the ESD solutions misses the weak (supersonic to supersonic) oblique leading-edge shock and mis-predicts the plateau pressure gradient upstream of the outboard shock wave. The failure to properly capture the leading edge shock is characteristic of small disturbance formulations and primarily due to the relatively large shock sweep.

Using the  $\alpha$  selected from the full potential NCR correlations, FCR solutions were generated using FLO-27 FPE and Bailey-Ballhaus ESD codes. Comparisons with experiment are summarized in figure 78. Comparison of these results with the NCR solutions shown in figure 77 shows that FCR solutions result in the expected aft shift in shock location from the NCR shock position and in increase in strength. Otherwise, the FCR solutions are very similar to NCR results.

In order to assess the magnitude of viscous effects, calculations were performed with viscous displacement-surface effects included in the full potential NCR solution. The angle of attack was again adjusted to match experimental and calculated pressures in the nose region. Viscous calculations performed in this manner are compared with experiment in figure 79. These data show that full-potential NCR calculations using an iterated 2-D boundary layer result in excellent agreement with experiment. Not only are the shock waves properly computed, but the aft loading is corrected predicted. Thus, the inclusion of a simple strip boundary layer within the calculations improves the agreement between measured and computed lift over that resulting from inviscid solutions.

7.3.2 Wing B - Moderate aspect ratio and sweep. - Both FPE and ESD nonconservative solutions are compared with experimental data for Wing B in

figure 80. Here, the good agreement between FL0-22 solutions and experiment is evident, as is the relatively poor agreement between ESD results and experiment. The ESD method fails to capture the weak leading edge shock, and positions the trailing edge shock too far aft at the wing root. The spurious ESD tip pressures are probably attributable to the lack of coarse grid resolution at the tip. This is a fundamental problem with the grid embedding scheme.

A calculation was performed to investigate the sensitivity of the ESD solution to grid density in the leading edge region, with the aim of improving the shock capture characteristics. The number of grid points in the forward 10-percent chord was doubled from the default value of 7 per surface to 14. The resulting calculation did show a modest increase in the leading edge suction peak, but the "shock" was still badly smeared, to the point being almost indiscernible.

Figure 81 contains the comparisons of FPE and ESD conservative solutions with Wing B experimental data. The use of FCR with inviscid solutions causes a degradation in the correlations as evidenced by a comparison of figures 80 and 81. The degradation is primarily manifested in the too-far aft positioning of the shock wave in the FCR calculations.

The inclusion of a boundary layer in the FL022 solution process produces excellent agreement between theory and experiment. Figure 82 shows that the only failure of the numerical results is the excessive smearing of the computed leading edge shock wave. This failure might be avoided by the use of a more closely spaced grid. Of note in these results is the good prediction of aft loading, and the close agreement between predicted and measured lift.

7.3.3 Wing C - Low aspect ratio, high sweep. - Figure 83 compares FPE and ESD nonconservative solutions with Wing C experimental data. Although the correlation is not quite as good as it was for Wings A and B, FL022 solutions are in fair agreement with experiment. The major differences between theory and experiment occur near the tip and may be due to vortex

roll-up which is not modeled in the theory. On the other hand, the ESD solution is a poor representation of experiment. This failure is really not surprising because as wing sweep increases, some of the nonlinear cross-flow terms which were neglected in the formulation become important.

Fully-conservative relaxation does not improve the agreement between theory and experiment for Wing C, as evidenced by figure 84. In this case, FCR actually caused a deterioration of the quality of the FPE results, and did nothing to improve the ESD solutions.

The inclusion of viscous effects in the FL0-22 calculation (fig. 85) results in only marginal improvement in the correlation (cf. figs. 83 and 85). In fact, the effect of viscosity (within the framework of a displacement surface concept) is very small, as evidenced by the slight .01 decrease in lift coefficient at the fixed angle of attack. Almost all of the lift lost is attributable to the forward movement and slightly increased smearing of the shock.

7.3.4 Evaluation of correlations. - Although the previous correlations do not by any means constitute an indepth evaluation of the computational methods, a number of salient conclusions can be drawn from these limited correlations:

1. Full potential solutions are uniformly in better agreement with experiment than small disturbance results.
2. Inviscid nonconservative solutions more closely predict measured pressures than fully conservative solutions.
3. The FL0-22 code coupled with a 2-D boundary layer program provides very accurate predictions of isolated wing pressures for all three wings, but some deterioration in quality is evident for the highly swept, low aspect ratio wing.

4. Extended small disturbance results can be considered adequate only for the high aspect ratio, moderately swept wings.

## 8. CONCLUSIONS

A comprehensive program was formulated and conducted for the specific purpose of acquiring test data suitable for current and future three-dimensional transonic code correlations. High-quality test data was acquired for three advanced technology wings by using a unique test apparatus and by devoting careful attention to details of the experiment. The data have been used in preliminary evaluations of three selected transonic computational methods. The salient conclusions to be drawn from this research are:

1. The unique test apparatus designed to remove the wind tunnel boundary layer ahead of the semispan wing model was found to eliminate uncertainties about interaction of the wind tunnel boundary layer with the model.
2. All three wings tested in this program performed well with aerodynamic characteristics representative of state-of-the-art supercritical wing technology. In particular, the isolated wing and wing-body data exhibit all of the complex transonic flow features needed to thoroughly evaluate computational methods.
3. Fuselage effects on wing pressures were obtained and found to represent a movement of the reflection plane outboard to the fuselage side.
4. The measurement of far-field pressures provides a means for assessing transonic wind tunnel wall interference effects without assumptions concerning the nature of the flow through the porous wall.
5. In this investigation wall interference effects were found to be small for test conditions in the range of interest; furthermore, the test data could be corrected to free-air conditions by simple adjustments in Mach number and angle of attack.
6. The full potential, non-conservative solutions (FLO-22) provided excellent agreement with data for all three wings, while the small disturbance code was acceptable only for the transport wing.

7. Nonconservative formulations more closely predicted measured pressures than conservative formulations.



## 9. REFERENCES

1. Ballhaus, W. F. and Bailey, F. R.: Numerical Calculation of Transonic Flow About Swept Wings. AIAA Paper 72-677, June 1972.
2. Bailey, F. R. and Ballhaus, W. F.: Relaxation Methods for Transonic Flow About Wing-Cylinder Combinations and Lifting Swept Wings. *Lecture Notes in Physics*, Vol. 19, Springer-Verlag, 1972.
3. Ballhaus, W. F.: Some Recent Progress in Transonic Flow Computations. VKI Lecture Series on Computational Fluid Dynamics, March 1976.
4. Ballhaus, W. F.; Bailey, F. R.; and Frick, J.: Improved Computational Treatment of Transonic Flow About Swept Wings. NASA CP-2001, Nov. 1976.
5. Mason, W.; Mackenzie, D. A.; Stern, M. A.; and Johnson, J. K.: A Numerical Three-Dimensional Viscous Transonic Wing-Body Analysis and Design Tool. AIAA Paper 78-101, Jan. 1978.
6. Boppe, C. W.: Calculation of Transonic Wing Flows by Grid Embedding. AIAA Paper 77-207, Jan. 1977.
7. Boppe, C. W.: Computational Transonic Flow About Realistic Aircraft Configurations. AIAA Paper 78-104, Jan. 1978.
8. Boppe, Charles W.: Towards Complete Configurations Using an Embedded Grid Approach. NASA CR-3030, July 1978.
9. Jameson, Antony: Iterative Solution of Transonic Flows Over Airfoils and Wings, Including Flows at Mach 1. *Commun. Pure & Appl. Math.*, Vol. XXVII, No. 3, May 1974, pp. 238-309.
10. Jameson, Antony; and Caughey, D. A.: Numerical Calculation of the Transonic Flow Past a Swept Wing. C00-3077-140, ERDA Math. & Comput. Lab., New York Univ., June 1977 (also available as NASA CR-153297).
11. Caughey, D. A.; and Jameson, Antony: Numerical Calculation of Transonic Potential Flow About Wing-Fuselage Combinations. AIAA Paper 77-677, June 1977.
12. Jameson, Antony; and Caughey, D. A.: A Finite Volume Method for Transonic Potential Flow Calculations. AIAA Paper 77-635, June 1977.
13. McLean, J. D.; and Randall, J. L.: Computer Program to Calculate Three-Dimensional Boundary Layer Flows Over Wings with Wall Mass Transfer. NASA CR-3123, May 1979.
14. Hess, J. L.: Calculation of Potential Flow About Arbitrary Three-Dimensional Lifting Bodies, McDonnell-Douglas Report No. MDC J5679-01, Oct. 1972.

15. Vanderplaats, Garret N.: CONMIN - A Fortran Program for Constrained Function Minimization. NASA TM X-62282, 1973.
16. Pounds, G. A.; and Stanewsky, E.: The Research Compressible Flow Facility. Lockheed-Georgia Company ER-9219, 1967.
17. Braslow, Albert L.; and Knox, Eugene C.: Simplified Method for Determining of Critical Height of Distributed Roughness Particles for Boundary Layer Transition at Mach Numbers from 0 to 5. NACA TN 4363, 1958.
18. Chan, Y. Y.: A Perturbation Theory of Two-Dimensional Transonic Wind Tunnel Wall Interference. NAE LR-598, April 1979.
19. Murman, E. M.: Computation of Wall Effects in Ventilated Transonic Wind Tunnels. AIAA Paper 72-1007, September 1972.
20. Shankar, V.; Malmuth, N. D.; and Cole, J. D.: Computational Transonic Design Procedure for Three-Dimensional Wings and Wing-Body Combinations. AIAA Paper 79-0344, January 1979.
21. Kemp, W. B. Jr.: Toward the Correctable-Interference Transonic Wind Tunnel. Proc. AIAA 9th Aerodynamic Testing Conference, June 1976.
22. Blackwell, J. A.: An Empirical Correction for Wind Tunnel Wall Blockage in Two-Dimensional Transonic Flow. AIAA Paper 78-806, April 1978.
23. Murman, E. M.: A Correction Method for Transonic Wind Tunnel Wall Interference. AIAA Paper 79-1533, July 1979.
24. Kemp, W. B. Jr.: Transonic Assessment of Two-Dimensional Wind Tunnel Wall Interference Using Measured Wall Pressures. NASA CP-2045, Part 2, March 1979.
25. Stahara, S. S.; and Spreiter, J. R.: A Transonic Wind Tunnel Interference Assessment - Axisymmetric Flows, AIAA Paper 79-0208, January 1979.
26. Klunker, E. B.: Contribution to Methods for Calculating the Flow About Thin Lifting Wings at Transonic Speeds - Analytical Expressions for the Far Field. NASA TN D-6530, 1971.

TABLE 1. CURRENT THREE-DIMENSIONAL TRANSONIC FLOW METHODS

METHOD	CSD	ESD	FPE	NCR	FCR	MGE	BL	BODY	COMMENTS
Bailey-Ballhaus #0	✓			✓					Original code (ref. 1,2)
Bailey-Ballhaus #3A		✓		✓	✓	✓		✓	Current (ref. 3,4)
Bailey-Ballhaus/FDL		✓		✓	✓	✓	✓	✓	Weak interaction (ref. 5)
Boppe/LRC #1		✓		✓		✓			Multiple Wings (ref. 6)
Boppe/LRC #2		✓		✓		✓		✓	Wing-Fuselage (ref. 7,8)
Jameson-Caughey FLO-22			✓	✓					Skewed or arrow wings (ref. 9,10)
Jameson-Caughey FLO-25			✓		✓			✓	Quasi-conservative (ref. 11)
Jameson-Caughey FLO-27			✓		✓				Finite-volume (ref. 12)
Jameson-McLean/LRC			✓		✓		✓		3-D Boundary layer (ref. 13)

Code:

CSD/ESD	Classical/Extended Small Disturbance
FPE	Full Potential Equation
NCR/FCR	Non-Conservative/Fully Conservative Relaxation
MGE	Multiple Grid Embedding
BL	Boundary Layer
BODY	Wing-Body Capability

TABLE II. - WING MODEL GEOMETRY

	WING		
	A	B	C
AR	8.0	3.8	2.6
$\lambda$	0.4	0.4	0.3
$\Lambda_{C/4}$ , deg.	25.0	30.0	38.4
$\theta_r$ , deg.	2.76	2.50	2.38
$\theta_t$ , deg.	-2.04	-4.00	-5.79
$(t/c)_r$ , %	12.0	6.0	7.0
$(t/c)_t$ , %	12.0	6.0	11.0
$S/2$ , cm <sup>2</sup> (in <sup>2</sup> )	528.0 (81.8)	530.0 (82.1)	523.0 (81.0)
$b/2$ , cm (in.)	45.7 (18.0)	31.8 (12.5)	26.1 (10.26)
$C_r$ , cm (in.)	16.51 (6.50)	23.88 (9.40)	30.83 (12.14)
$C_t$ , cm (in.)	6.60 (2.60)	9.55 (3.76)	9.25 (3.64)
MAC, cm (in.)	12.26 (4.825)	17.71 (6.974)	21.95 (8.642)
$Y_{MAC}$ , cm (in.)	19.59 (7.714)	13.60 (5.355)	10.68 (4.206)

TABLE III. - WING A NONDIMENSIONAL AIRFOIL ORDINATES.

ROOT SECTION			TIP SECTION	
X/C	Z <sub>U</sub> /C	Z <sub>L</sub> /C	Z <sub>U</sub> /C	Z <sub>L</sub> /C
.00000	.00000	.00000	.00000	.00000
.00241	.00952	-.00800	.00788	-.00899
.00961	.01758	-.01578	.01697	-.01588
.02153	.02431	-.02205	.02557	-.02141
.03806	.03018	-.02822	.03305	-.02589
.05904	.03496	-.03432	.03984	-.02964
.08427	.03857	-.04055	.04610	-.03320
.11349	.04136	-.04684	.05172	-.03659
.14645	.04364	-.05309	.05658	-.03990
.18280	.04554	-.05889	.06067	-.04296
.22221	.04704	-.06391	.06401	-.04562
.26430	.04807	-.06772	.06665	-.04775
.30866	.04864	-.07031	.06859	-.04922
.35486	.04874	-.07126	.06983	-.04992
.40245	.04835	-.07094	.07036	-.04964
.45099	.04736	-.06882	.07021	-.04802
.50000	.04574	-.06540	.06943	-.04460
.54901	.04345	-.06008	.06799	-.03923
.59755	.04062	-.05349	.06591	-.03238
.64514	.03726	-.04548	.06311	-.02478
.69134	.03353	-.03695	.05956	-.01710
.73570	.02958	-.02838	.05504	-.00997
.77779	.02554	-.02034	.04948	-.00381
.81720	.02153	-.01323	.04295	.00099
.85355	.01767	-.00734	.03585	.00423
.88651	.01410	-.00283	.02874	.00596
.91573	.01087	.00016	.02206	.00617
.94096	.00806	.00168	.01618	.00522
.96194	.00574	.00195	.01134	.00357
.97847	.00382	.00142	.00745	.00155
.99039	.00237	.00048	.00481	-.00003
.99759	.00124	-.00043	.00285	-.00146
1.00000	.00080	-.00080	.00207	-.00207

TABLE IV. - WING B NONDIMENSIONAL AIRFOIL ORDINATES

ROOT SECTION			TIP SECTION	
X/C	Z <sub>U</sub> /C	Z <sub>L</sub> /C	Z <sub>U</sub> /C	Z <sub>L</sub> /C
.00000	.00000	.00000	.00000	.00000
.00241	.00617	-.00528	.00507	-.00606
.00961	.01181	-.00895	.00972	-.01066
.02153	.01649	-.01198	.01401	-.01408
.03806	.01991	-.01511	.01770	-.01691
.05904	.02268	-.01839	.02110	-.01951
.08427	.02517	-.02111	.02421	-.02161
.11349	.02737	-.02333	.02700	-.02325
.14645	.02925	-.02503	.02949	-.02439
.18280	.03075	-.02618	.03168	-.02492
.22221	.03191	-.02691	.03360	-.02498
.26430	.03277	-.02705	.03522	-.02446
.30866	.03330	-.02669	.03654	-.02344
.35486	.03346	-.02582	.03762	-.02180
.40245	.03325	-.02458	.03847	-.01967
.45099	.03258	-.02287	.03905	-.01689
.50000	.03155	-.02070	.03933	-.01361
.54901	.03013	-.01768	.03922	-.00950
.59755	.02842	-.01376	.03882	-.00396
.64514	.02639	-.00985	.03799	.00042
.69134	.02417	-.00615	.03669	.00474
.73570	.02178	-.00316	.03491	.00814
.77779	.01925	-.00109	.03258	.01020
.81720	.01660	.00003	.02962	.01087
.85355	.01388	.00043	.02608	.01026
.88651	.01116	.00043	.02211	.00867
.91573	.00865	.00032	.01793	.00651
.94096	.00644	.00012	.01379	.00417
.96194	.00459	-.00021	.00991	.00196
.97847	.00308	-.00055	.00674	.00036
.99039	.00196	-.00082	.00445	-.00138
.99759	.00130	-.00102	.00305	-.00227
1.00000	.00109	-.00109	.00259	-.00257

TABLE V. - WING C NONDIMENSIONAL AIRFOIL ORDINATES.

ROOT SECTION			TIP SECTION	
X/C	Z <sub>U</sub> /C	Z <sub>L</sub> /C	Z <sub>U</sub> /C	Z <sub>L</sub> /C
.00000	.00000	.00000	.00000	.00000
.00241	.00708	-.00622	.00598	-.00827
.00961	.01521	-.00991	.01428	-.01277
.02153	.02241	-.01268	.02237	-.01580
.03806	.02811	-.01558	.03013	-.01813
.05904	.03267	-.01860	.03780	-.02020
.08427	.03634	-.02109	.04534	-.02181
.11349	.03911	-.02310	.05272	-.02303
.14645	.04098	-.02464	.05993	-.02385
.18280	.04205	-.02569	.06682	-.02417
.22221	.04245	-.02635	.07315	-.02412
.26430	.04238	-.02645	.07852	-.02359
.30866	.04188	-.02608	.08252	-.02262
.35486	.04096	-.02522	.08492	-.02110
.40245	.03969	-.02401	.08560	-.01912
.45099	.03800	-.02233	.08455	-.01654
.50000	.03603	-.02018	.08191	-.01346
.54901	.03375	-.01719	.07791	-.00956
.59755	.03127	-.01354	.07284	-.00502
.64514	.02857	-.00943	.06691	-.00013
.69134	.02578	-.00572	.06030	.00411
.73570	.02292	-.00275	.05324	.00732
.77779	.02001	-.00071	.04602	.00926
.81720	.01706	.00041	.03889	.00985
.85355	.01411	.00077	.03203	.00921
.88651	.01122	.00054	.02565	.00766
.91573	.00853	.00012	.01984	.00562
.94096	.00617	-.00029	.01470	.00341
.96194	.00421	-.00056	.01036	.00130
.97847	.00272	-.00057	.00692	-.00033
.99039	.00167	-.00070	.00455	-.00163
.99759	.00103	-.00079	.00316	-.00242
1.00000	.00082	-.00082	.00270	-.00268

TABLE VI. - WING PRESSURE ORIFICE LOCATIONS.

(a) Wing A

UPPER SURFACE					
ETA	.15	.3	.5	.7	.95
X/C	0.0000	0.0000	0.0000	0.0000	0.0000
	.0193	.0180	.0185	.0175	.0196
	.0480	.0467	.0459	.0514	.0480
	.0975	.0968	.0975	.0958	.0929
	.1471	.1474	.1479	.1463	.1440
	.1967	.1971	.1956	.1964	.1930
	.2478	.2465	.2458	.2442	.2434
	.2982	.2963	.2962	.2956	.2959
	.3471	.3463	.3461	.3465	.3438
	.3981	.3971	.3752	.3955	.3940
	.4465	.4465	.4466	.4438	.4426
	.4970	.4777	.4965	.4952	.4948
	.5475	.5468	.5459	.5451	.5419
	.5972	.5965	.5972	.5940	.5945
	.6467	.6463	.6468	.6442	.6442
	.6769	.6965	.6956	.6946	.6930
	.7471	.7475	.7455	.7444	.7437
	.7981	.7963	.7965	.7944	.7941
	.8478	.8464	.8458	.8450	.8417
	.8934	.8967	.8960	.8951	.8930
	.9490	.9467	.9458	.9449	.9416
	1.0000	1.0000	1.0000	1.0000	1.0000
LOWER SURFACE					
	0.0000	0.0000	0.0000	0.0000	0.0000
	.0471	.0470	.0453	.0440	.0472
	.0976	.0989	.0948	.0965	.0946
	.1976	.1975	.1954	.1949	.1954
	.2974	.2962	.2952	.2931	.2954
	.3970	.3968	.3952	.3938	.3967
	.4973	.4964	.4952	.4942	.4952
	.5972	.5948	.5955	.5951	.5968
	.6976	.6921	.6954	.6964	.6973
	.7967	.7964	.7953	.7961	.7912
	.8983	.8985	.8979	.9014	.9017
	.9472	.9497	.9522	.9476	.9201
	1.0000	1.0000	1.0000	1.0000	1.0000



TABLE VI. - Continued.

(b) Wing B

UPPER SURFACE					
ETA	.216	.4	.6	.8	.95
(X/C)	0.0000	0.0000	0.0000	0.0000	0.0000
	.0197	.0208	.0189	.0187	.0217
	.0497	.0503	.0495	.0483	.0497
	.0992	.1003	.0993	.0989	.1005
	.1495	.1507	.1492	.1483	.1496
	.1993	.2001	.1995	.1995	.1993
	.2496	.2509	.2487	.2490	.2500
	.2995	.3002	.2999	.2982	.3001
	.3495	.3504	.3496	.3495	.3504
	.3997	.4009	.3991	.3994	.4006
	.4493	.4502	.4497	.4493	.4503
	.4976	.5001	.4997	.4995	.5000
	.5488	.5501	.5492	.5485	.5499
	.5993	.6001	.5997	.5985	.5997
	.6495	.6503	.6493	.6486	.6500
	.6994	.7004	.6992	.6995	.7001
	.7492	.7505	.7494	.7489	.7498
	.7993	.8000	.7988	.7987	.8015
	.8493	.8507	.8497	.8490	.8512
	.8993	.9010	.9007	.9009	.9005
	.9492	1.0000	.9513	1.0000	.9515
	1.0000		1.0000		1.0000
LOWER SURFACE					
	0.0000	0.0000	0.0000	0.0000	0.0000
	.0503	.0500	.0520	.0500	.0521
	.1013	.1000	.1012	.0973	.1012
	.2008	.2004	.2005	.1981	.1992
	.3012	.2999	.2999	.2981	.3010
	.4011	.3999	.3999	.3974	.4003
	.6012	.4999	.5003	.4986	.4997
	.8010	.5997	.5990	.5968	.5992
	.8998	.6997	.6995	.6985	.6992
	1.0000	.8005	.7994	.7968	.7980
		.9016	.8933	.8961	.8916
		.9518	.9480	.9452	.9548
		1.0000	1.0000	1.0000	1.0000

TABLE VI. - Concluded.  
(c) Wing C

UPPER SURFACE					
ETA	.1	.3	.5	.7	.9
(X/C)	0.0000	0.0000	0.0000	0.0000	0.0000
	.0196	.0196	.0188	.0186	.0181
	.0501	.0499	.0505	.0489	.0447
	.1000	.0997	.0995	.0990	.0980
	.1500	.1501	.1497	.1494	.1488
	.2000	.1995	.1997	.1989	.1974
	.3001	.2496	.2497	.2498	.2498
	.3505	.2997	.2995	.2997	.2989
	.4002	.3496	.3501	.3489	.3491
	.4505	.4005	.4005	.4000	.4001
	.5003	.4498	.4495	.4490	.4483
	.5502	.5001	.5000	.5004	.4983
	.6003	.5510	.5496	.5507	.5500
	.6502	.6002	.5996	.5994	.6000
	.7002	.6504	.6500	.6506	.6494
	.7501	.7004	.7005	.6998	.6993
	.8005	.7505	.7500	.7496	.7502
	.8504	.8003	.8003	.7996	.8000
	.9001	.8503	.8505	.8497	.8520
	.9506	.9005	.9008	.9005	1.0000
	1.0000	.9502	.9509	.9501	
		1.0000	1.0000	1.0000	
LOWER SURFACE					
	0.0000	0.0000	0.0000	0.0000	0.0000
	.0484	.0483	.0488	.0491	.0485
	.0996	.0996	.0995	.0991	.1008
	.2001	.1995	.1995	.1991	.2000
	.2995	.3002	.3001	.3001	.3000
	.3996	.4004	.4006	.3991	.4004
	.5004	.5010	.5002	.4999	.5019
	.6010	.6001	.6007	.5999	.6002
	.7003	.7009	.7013	.7019	.7003
	.8007	.8014	.8006	.8018	.8006
	.9004	.9006	.8961	.8979	.9006
	.9486	.9518	.9451	.9508	1.0000
	1.0000	1.0000	1.0000	1.0000	

TABLE VII. - SUMMARY OF TEST CONDITIONS

(a) Wing A

$M_\alpha$	.62	.72	.76	.78	.80	.82	.84
-2	○ ○ ○ □ ◇ △	○	○	○ ○ ○ ○ ○ ○ ○ ○	○ ○ ○ ○ ○ ○ ○ ○	○ ○ ○ ○ ○ ○ ○ ○	○ ○ ○ ○ ○ ○ ○ ○
-1	○ ○ ○ ○ ○ □ ◇ △	○	○	○ ○ ○ ○ ○ ○ ○ ○	○ ○ ○ ○ ○ ○ ○ ○	○ ○ ○ ○ ○ ○ ○ ○	○ ○ ○ ○ ○ ○ ○ ○
0	○ ○ ○ ○ ○ □ ◇ △	○	○	○ ○ ○ ○ ○ ○ ○ ○	○ ○ ○ ○ ○ ○ ○ ○	○ ○ ○ ○ ○ ○ ○ ○	○ ○ ○ ○ ○ ○ ○ ○
1	○ ○ ○ ○ ○ □ ◇ △	○	○	○ ○ ○ ○ ○ ○ ○ ○	○ ○ ○ ○ ○ ○ ○ ○	○ ○ ○ ○ ○ ○ ○ ○	○ ○ ○ ○ ○ ○ ○ ○
2	○ ○ ○ ○ ○ □ ◇ △	○ ○ ○ ○ ○ ○ ○ ○	○ ○ ○ ○ ○ ○ ○ ○	○ ○ ○ ○ ○ ○ ○ ○	○ ○ ○ ○ ○ ○ ○ ○	○ ○ ○ ○ ○ ○ ○ ○	○ ○ ○ ○ ○ ○ ○ ○
3	○ ○ ○ ○ ○ □ ◇ △	○	○	○ ○ ○ ○ ○ ○ ○ ○	○ ○ ○ ○ ○ ○ ○ ○	○ ○ ○ ○ ○ ○ ○ ○	○ ○ ○ ○ ○ ○ ○ ○
4	○ ○ ○ ○ ○ □ ◇ △	○	○	○ ○ ○ ○ ○ ○ ○ ○	○ ○ ○ ○ ○ ○ ○ ○	○ ○ ○ ○ ○ ○ ○ ○	○ ○ ○ ○ ○ ○ ○ ○
5	○ ○ ○ ○ ○ □ ◇ △						
$c_L = .45$	○ ○ ○ ○ ○ □ ◇ △				○	○ ○ ○ ○ ○ ○ ○ ○	○ ○ ○ ○ ○ ○ ○ ○

○	CLEAN WING,	$\tau = 4\%$	☐	HIGH WING,	$\tau = 4\%$
□	CLEAN WING,	$\tau = 3\%$	⊖	MID WING,	$\tau = 4\%$
◇	CLEAN WING,	$\tau = 5\%$	⊖	LOW WING	$\tau = 4\%$
△	CLEAN WING,	$\tau = 6\%$			

TABLE VII.- Continued

(b) Wing B

$\alpha$	M	.70	.75	.80	.82	.84	.85	.86	.88	.90	.91	.92	.94
-2		$\circ\circ\phi\Omega$ $\square\Delta$					$\circ\phi\Omega$			$\circ\phi\Omega$ $\square\Delta$		$\circ\phi\Omega$	
-1		$\circ\phi\Omega$ $\square\Delta$					$\circ\phi\Omega$			$\circ\phi\Omega$ $\square\Delta$		$\circ\phi\Omega$	
0		$\circ\phi\Omega\circ$ $\square\Delta$	$\circ$	$\circ$	$\circ$		$\circ\phi\Omega\circ$	$\circ$		$\circ\phi\Omega\circ$ $\square\Delta$	$\circ$	$\circ\phi\Omega\circ$	$\circ$
1		$\circ\phi\Omega\circ$ $\square\Delta$	$\circ$	$\circ$	$\circ$	$\circ$	$\circ\phi\Omega\circ$	$\circ$		$\circ\phi\Omega\circ$ $\square\Delta$	$\circ$	$\circ\phi\Omega\circ$	$\circ$
2		$\circ\phi\Omega\circ$ $\square\Delta$	$\circ$	$\circ$	$\circ$	$\circ$	$\circ\phi\Omega\circ$	$\circ$	$\circ$	$\circ\phi\Omega\circ$ $\square\Delta$	$\circ$	$\circ\phi\Omega\circ$	$\circ$
3		$\circ\phi\Omega\circ$ $\square\Delta$	$\circ$	$\circ$	$\circ$	$\circ$	$\circ\phi\Omega\circ$	$\circ$	$\circ$	$\circ\phi\Omega\circ$ $\square\Delta$	$\circ$	$\circ\phi\Omega\circ$	$\circ$
4		$\circ\phi\Omega\circ\phi\Omega$ $\square\Delta$	$\circ\phi\Omega\circ\phi\Omega$	$\circ\phi\Omega\circ\phi\Omega$	$\circ\phi\Omega\circ\phi\Omega$	$\circ\phi\Omega\circ\phi\Omega$	$\circ\phi\Omega\circ\phi\Omega$	$\circ\phi\Omega\circ\phi\Omega$	$\circ\phi\Omega\circ\phi\Omega$	$\circ\phi\Omega\circ\phi\Omega$ $\square\Delta$	$\circ\phi\Omega\circ\phi\Omega$	$\circ\phi\Omega\circ\phi\Omega$	
5		$\circ\phi\Omega\circ$ $\square\Delta$	$\circ$	$\circ$	$\circ$	$\circ$	$\circ\phi\Omega\circ$	$\circ$	$\circ$	$\circ$			
$C_L = .0$		$\circ$	$\circ$	$\circ$	$\circ$	$\circ$	$\circ$	$\circ$	$\circ$	$\circ$		$\circ$	$\circ$
$C_L = .5$		$\circ$ $\square\Delta$	$\circ$	$\circ$	$\circ$	$\circ$	$\circ$	$\circ$	$\circ$	$\circ$ $\square\Delta$			

$\circ$  CLEAN WING,  $\tau = 4\%$

$\square$  CLEAN WING,  $\tau = 3\%$

$\diamond$  CLEAN WING,  $\tau = 5\%$

$\Delta$  CLEAN WING,  $\tau = 6\%$

$\circ$  HIGH WING,  $\tau = 4\%$

$\phi$  MID WING,  $\tau = 4\%$

$\Omega$  LOW WING,  $\tau = 4\%$

TABLE VII. - Concluded

(c) Wing C

$\alpha$	M	.70	.75	.80	.82	.84	.85	.86	.88	.90
0		○ ◇ △	○ ◇ △	○ ◇ △	○ ◇ △	○ ◇ △	○ ◇ △	○ ◇ △	○ ◇ △	○ ◇ △
1		○ ◇ △	○ ◇ △	○ ◇ △	○ ◇ △	○ ◇ △	○ ◇ △	○ ◇ △	○ ◇ △	○ ◇ △
2		○ ◇ △	○ ◇ △	○ ◇ △	○ ◇ △	○ ◇ △	○ ◇ △	○ ◇ △	○ ◇ △	○ ◇ △
3		○ ◇ △	○ ◇ △	○ ◇ △	○ ◇ △	○ ◇ △	○ ◇ △	○ ◇ △	○ ◇ △	○ ◇ △
4		○ ◇ △	○ ◇ △	○ ◇ △	○ ◇ △	○ ◇ △	○ ◇ △	○ ◇ △	○ ◇ △	○ ◇ △
5		○ ◇ △	○ ◇ △	○ ◇ △	○ ◇ △	○ ◇ △	○ ◇ △	○ ◇ △	○ ◇ △	○ ◇ △
6		○ ◇ △	○ ◇ △	○ ◇ △	○ ◇ △	○ ◇ △	○ ◇ △	○ ◇ △	○ ◇ △	○ ◇ △
7		○ ◇ △	○ ◇ △	○ ◇ △	○ ◇ △	○ ◇ △	○ ◇ △	○ ◇ △	○ ◇ △	○ ◇ △
$C_L = .5$		○ ◇ △	○ ◇ △	○ ◇ △	○ ◇ △	○ ◇ △	○ ◇ △	○ ◇ △	○ ◇ △	○ ◇ △

○ CLEAN WING,  $\tau = 4\%$

□ CLEAN WING,  $\tau = 3\%$

◇ CLEAN WING,  $\tau = 5\%$

△ CLEAN WING,  $\tau = 6\%$

○ HIGH WING,  $\tau = 4\%$

◇ MID WING,  $\tau = 4\%$

△ LOW WING,  $\tau = 4\%$

TABLE VIII. GRID FEATURES AND COMPUTING TIMES OF EVALUATED CODES

Code	Wing Chordwise Grid Points	Wing Spanwise Grid Points	Total Field Points	Approximate CPU Min. (CDC 7600)
Bailey- Ballhaus 3A	37	25	41,000	6
FLO-22	61 (Root) 40* (Tip)	21	159,000	15
FLO-27	51	21	90,000	30

\*Wing A. Value dependent upon wing taper ratio.

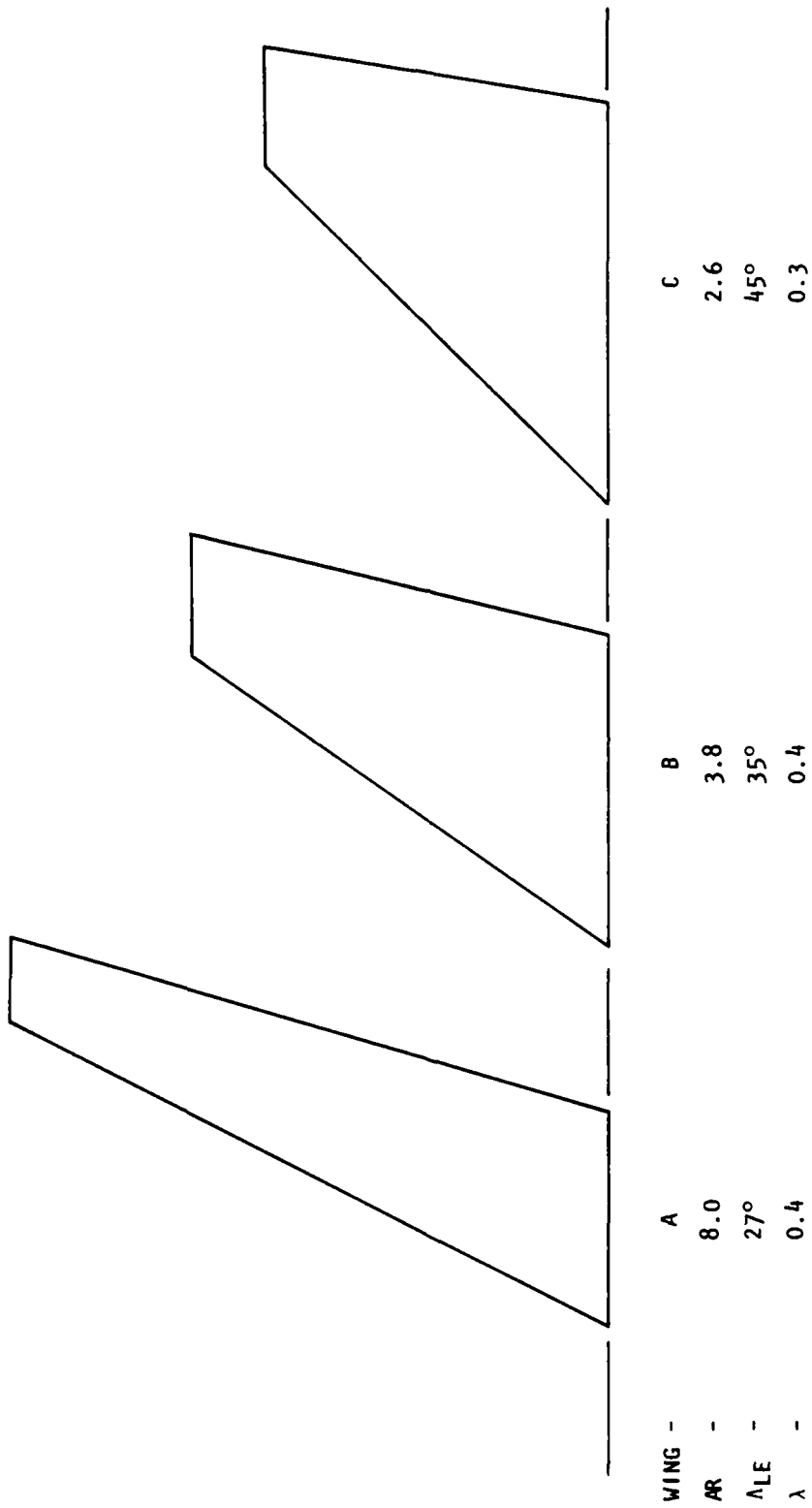


Figure 1. - Planform of correlation wings.

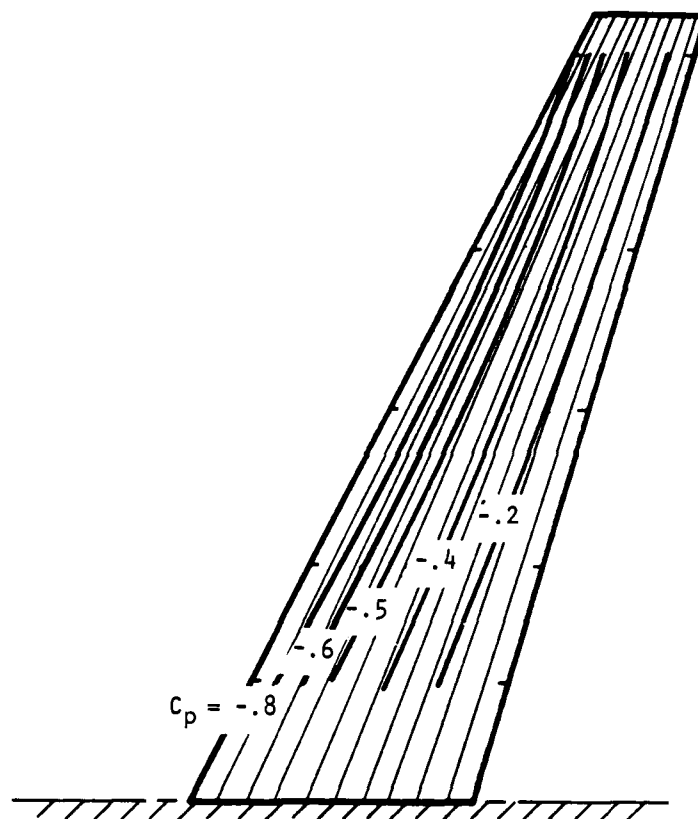


Figure 2 . - Wing A isobar pattern at  $M = .62$



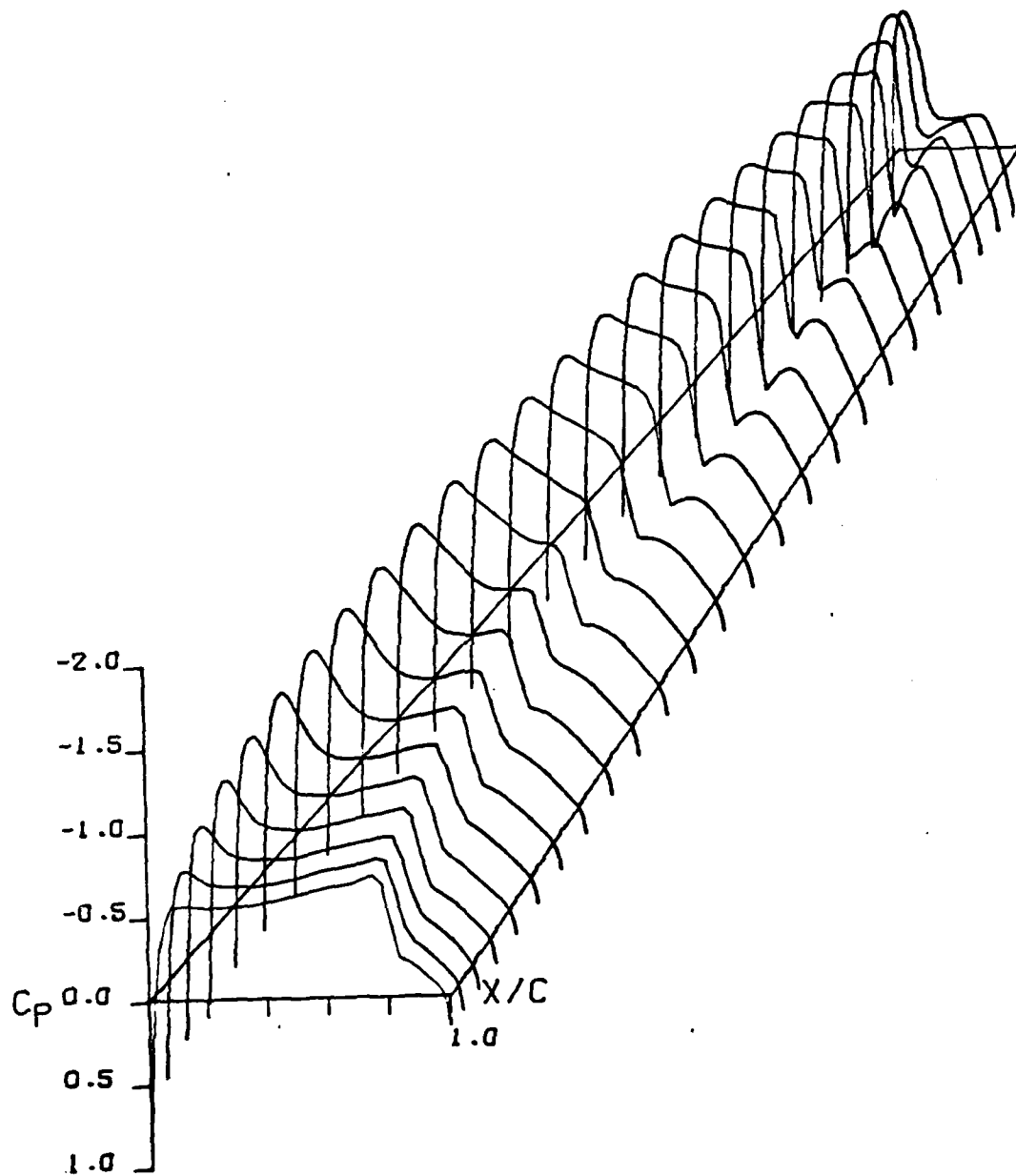


Figure 3 . - Wing A theoretical pressure distribution at  $M = .82$ ,  $\alpha = 1.5$

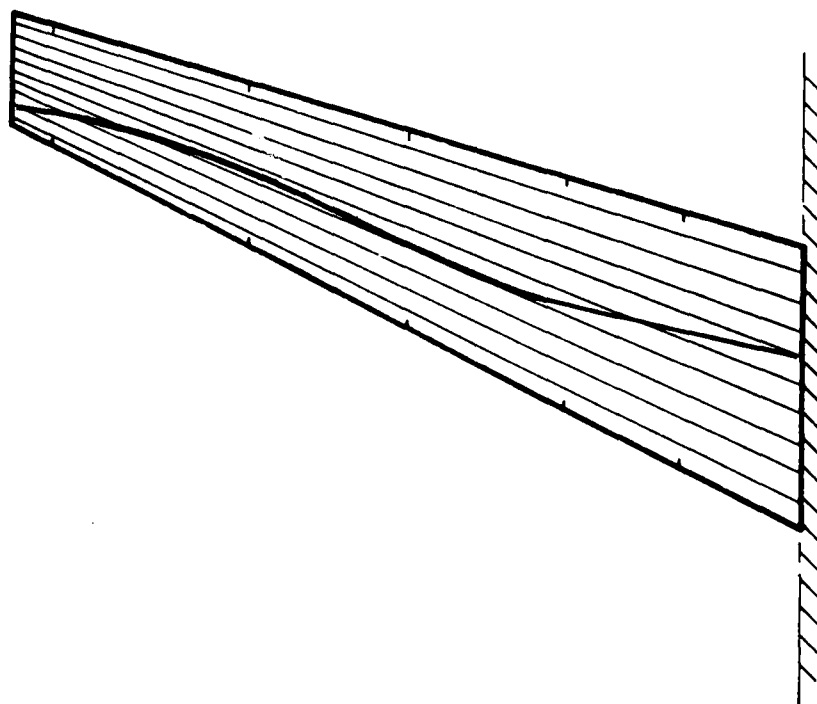


Figure 4 . - Theoretical Wing A shock pattern at  $M = .82$ ,  $\alpha = 1.5^\circ$ .

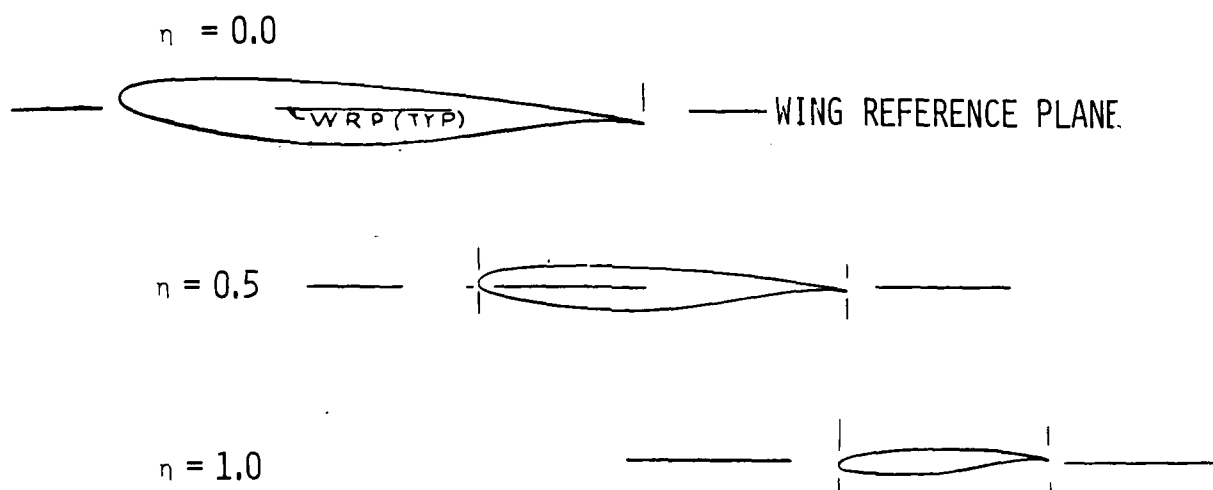


Figure 5 . - Wing A airfoil sections in rigged position

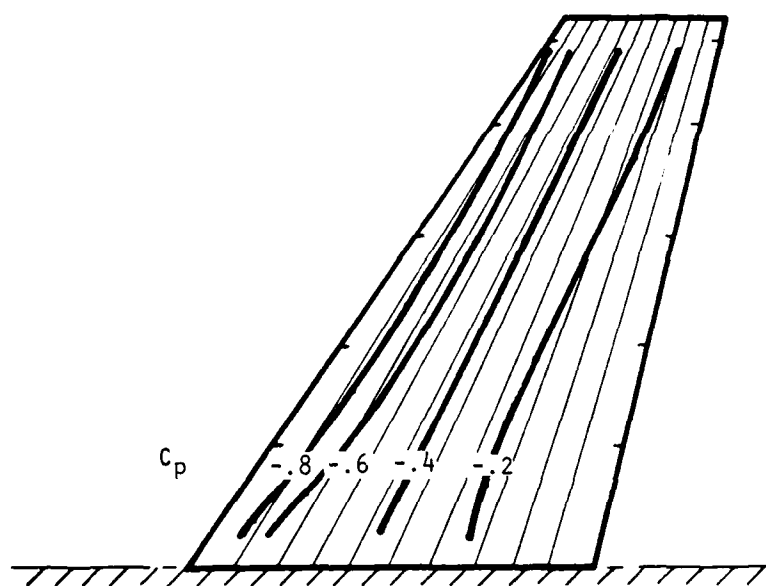


Figure 6. - Wing B isobar pattern at  $M = 0.6$ .

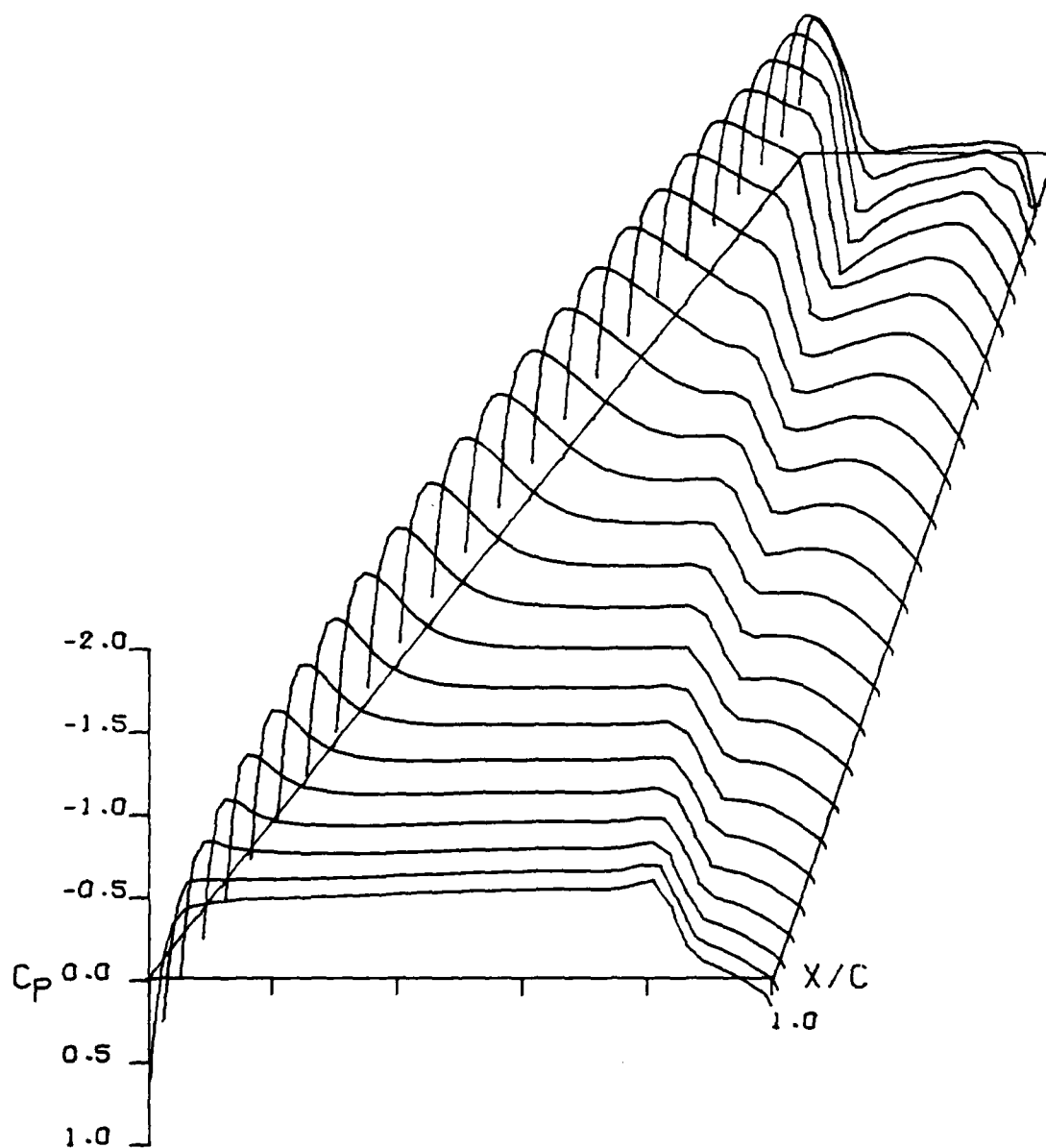


Figure 7 . - Wing B theoretical pressure distribution at  $M = .86$ ,  $\alpha = 5.0^\circ$

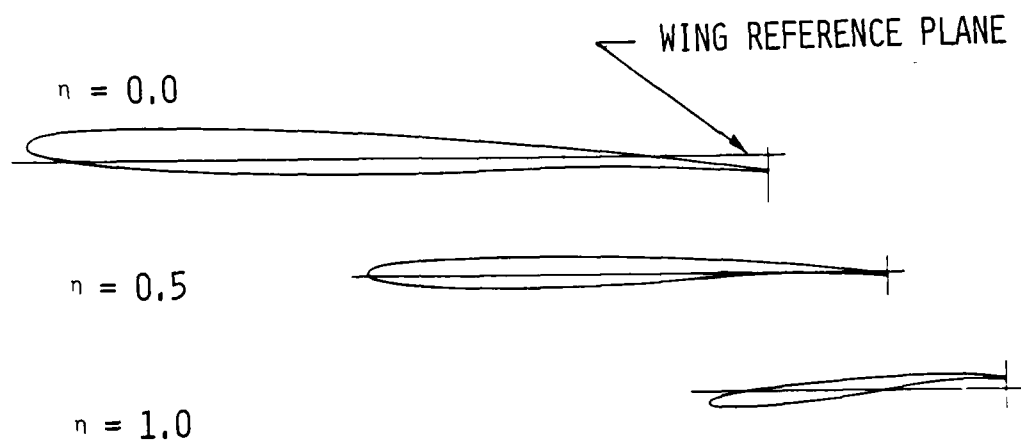


Figure 8 . - Wing B airfoil sections in rigged position

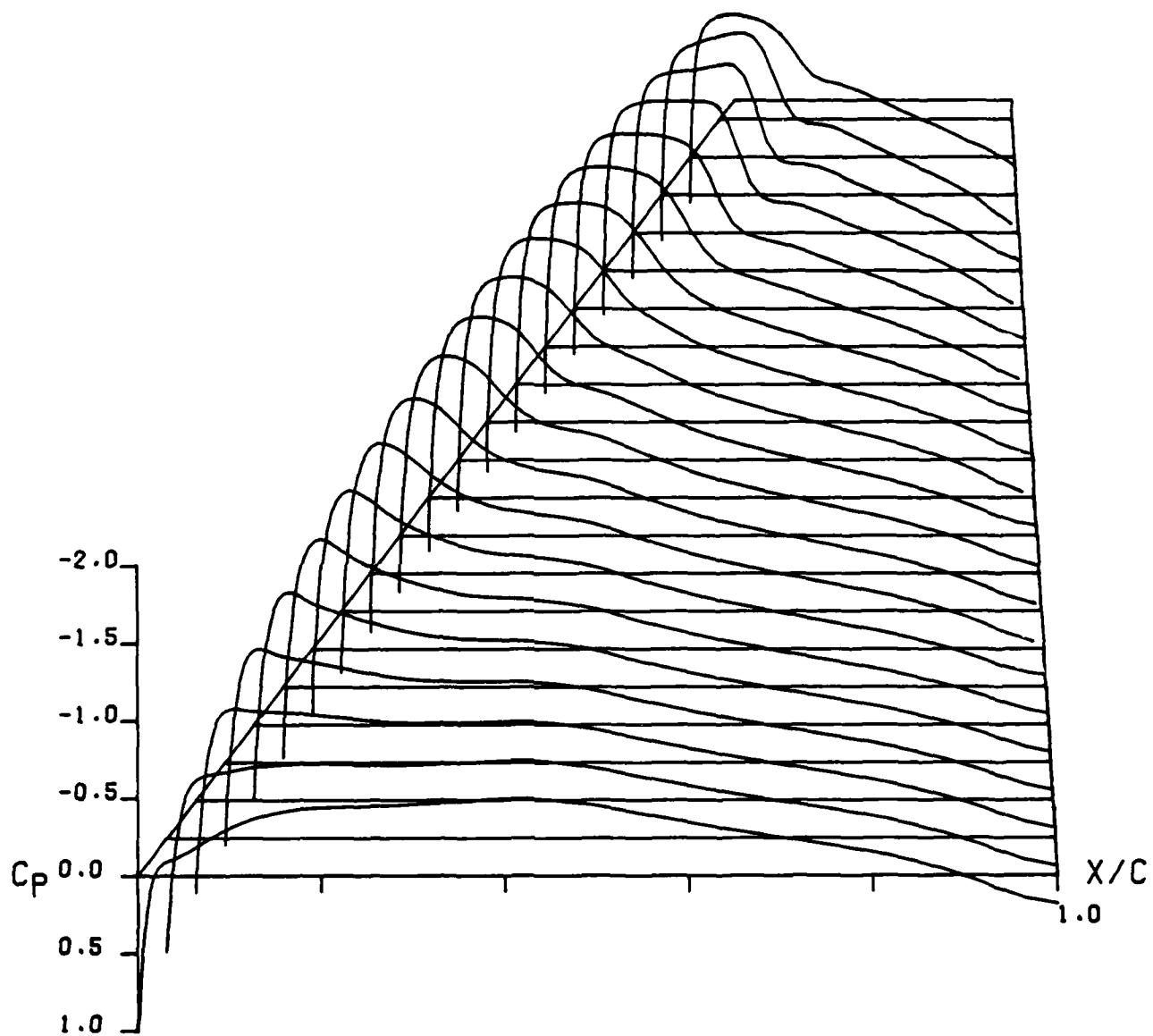


Figure 9 . - Upper surface design pressure distribution for Wing C;  
 $M = .85$ ,  $\alpha = 5.0^\circ$

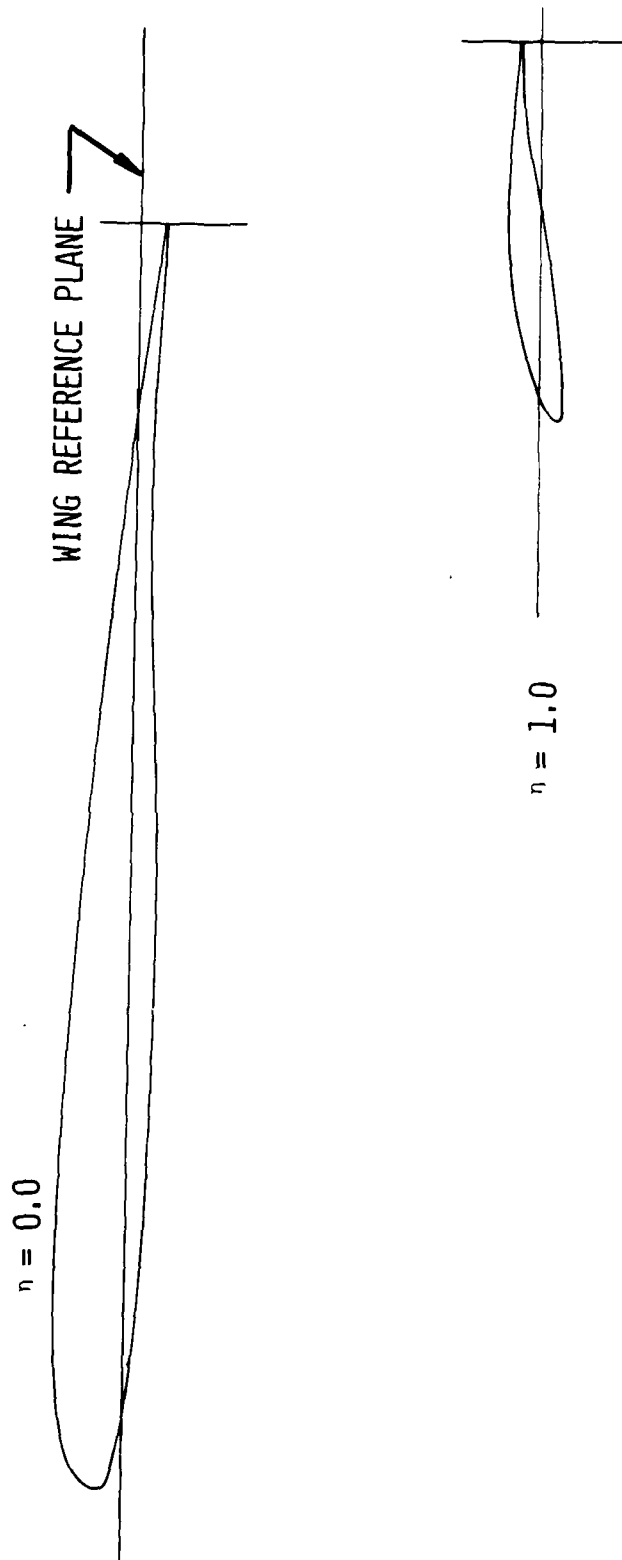


Figure 10. - Wing C airfoil sections in rigged position



WING	$x'$
A	6.599 (2.598)
B	9.543 (3.757)
C	12.324 (4.852)

BODY RADIUS 4.45 (1.75)

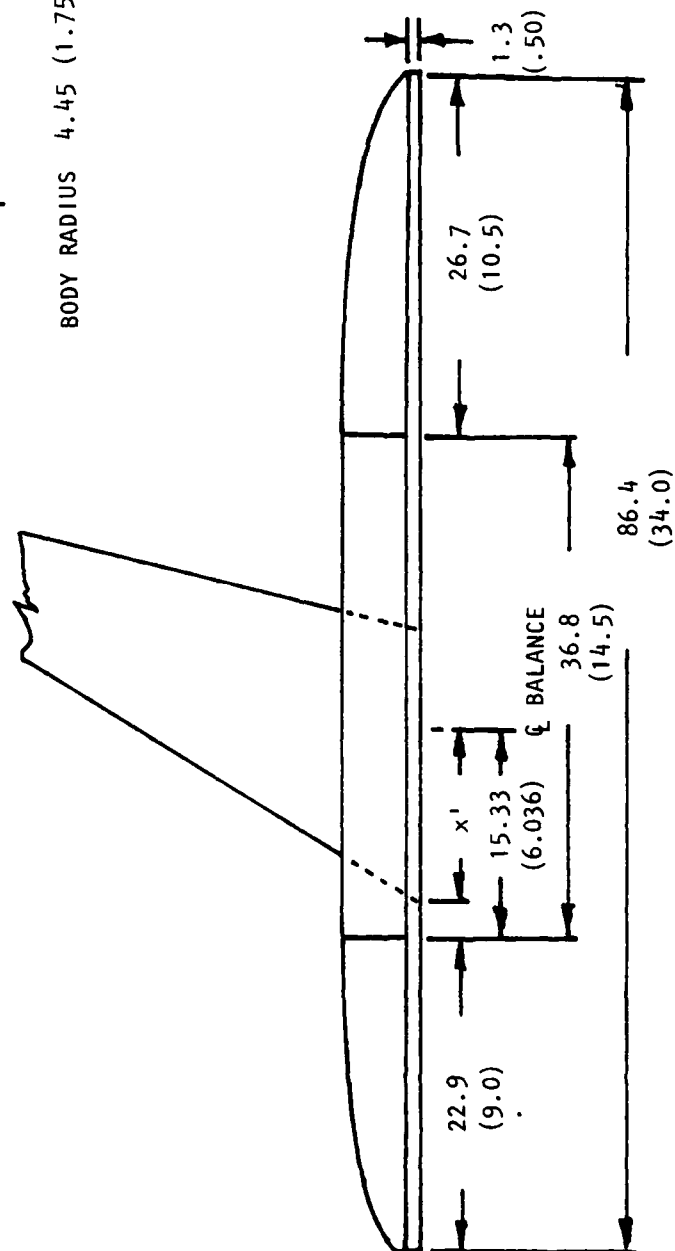


Figure 11 . - Fuselage geometry - cm (in.).

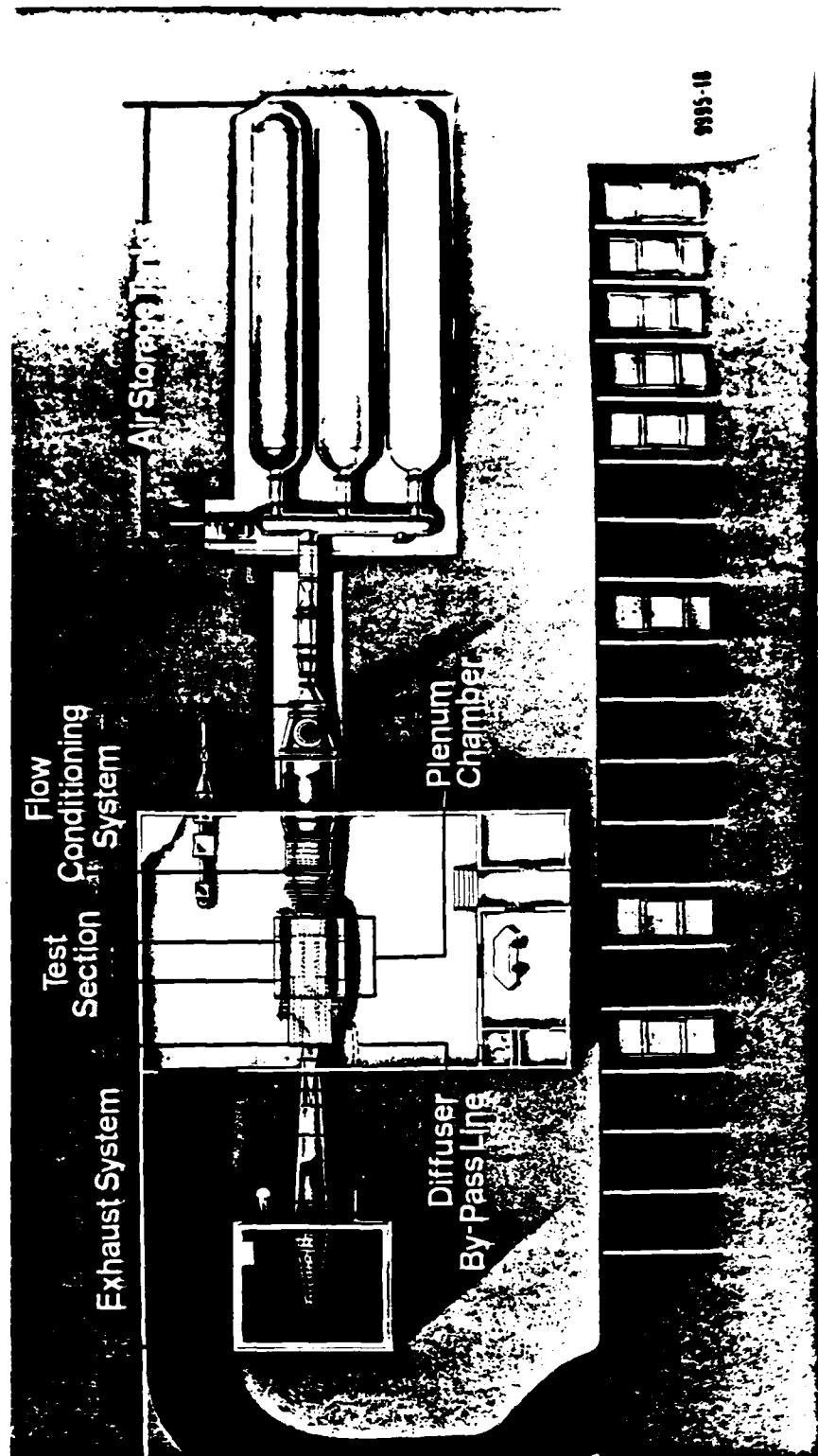


Figure 12. - Lockheed-Georgia Compressible Flow Wind-Tunnel

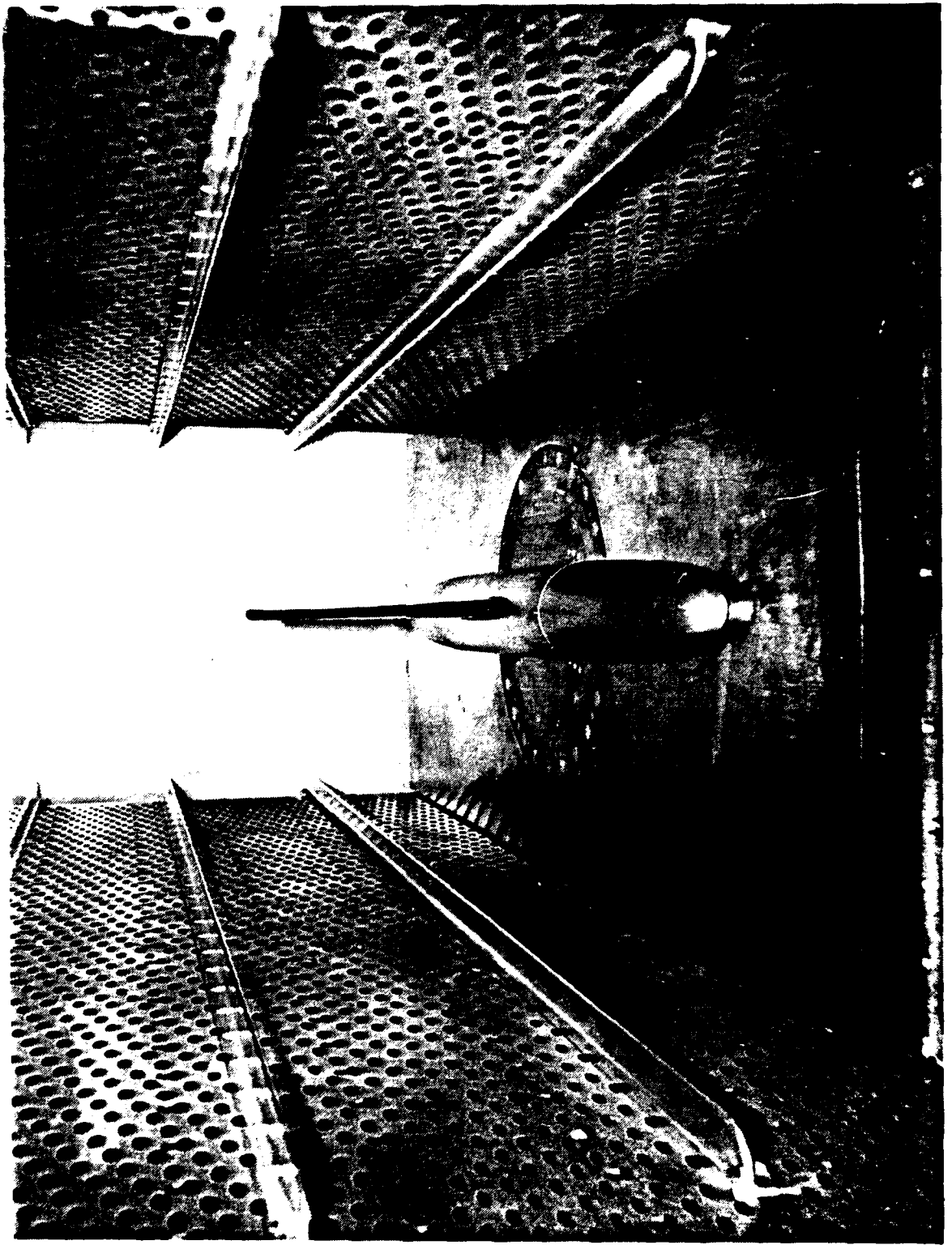


Figure 13 . - Wing C with fuselage installed in the Lockheed CFWT.

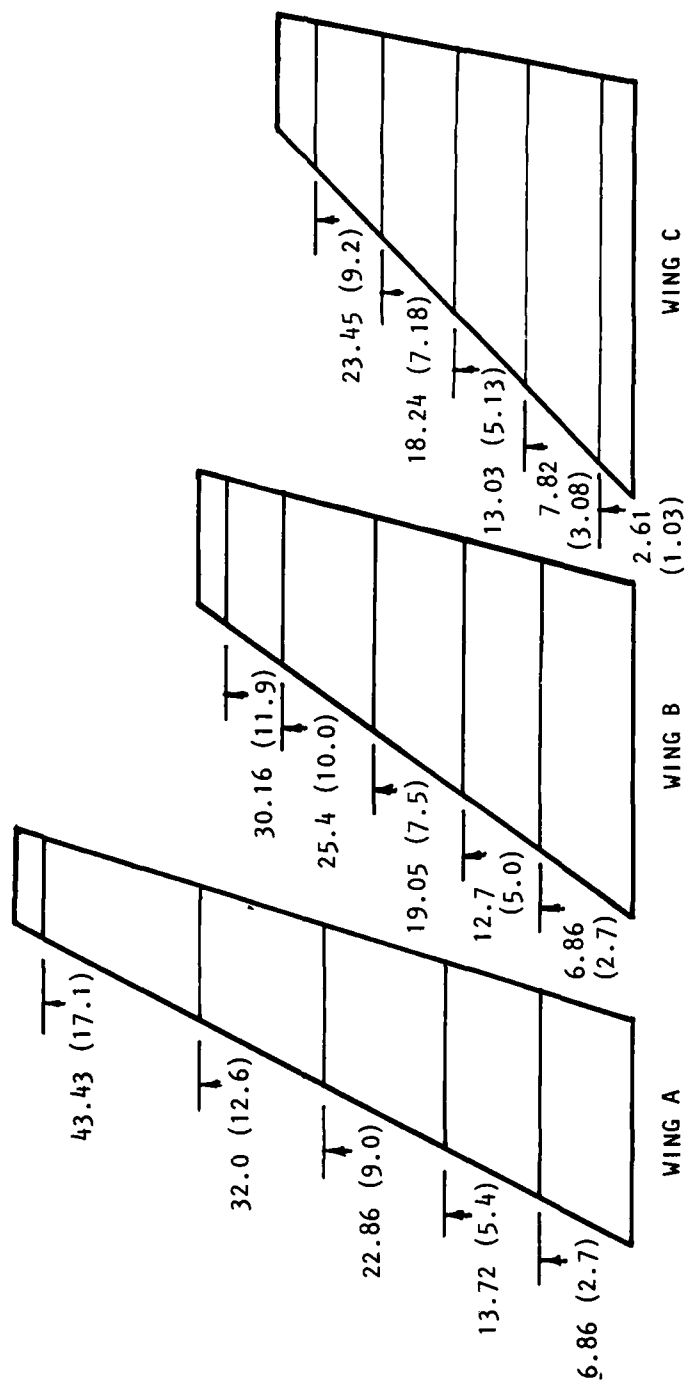


Figure 14 . - Model wing pressure orifice locations - cm (inches).

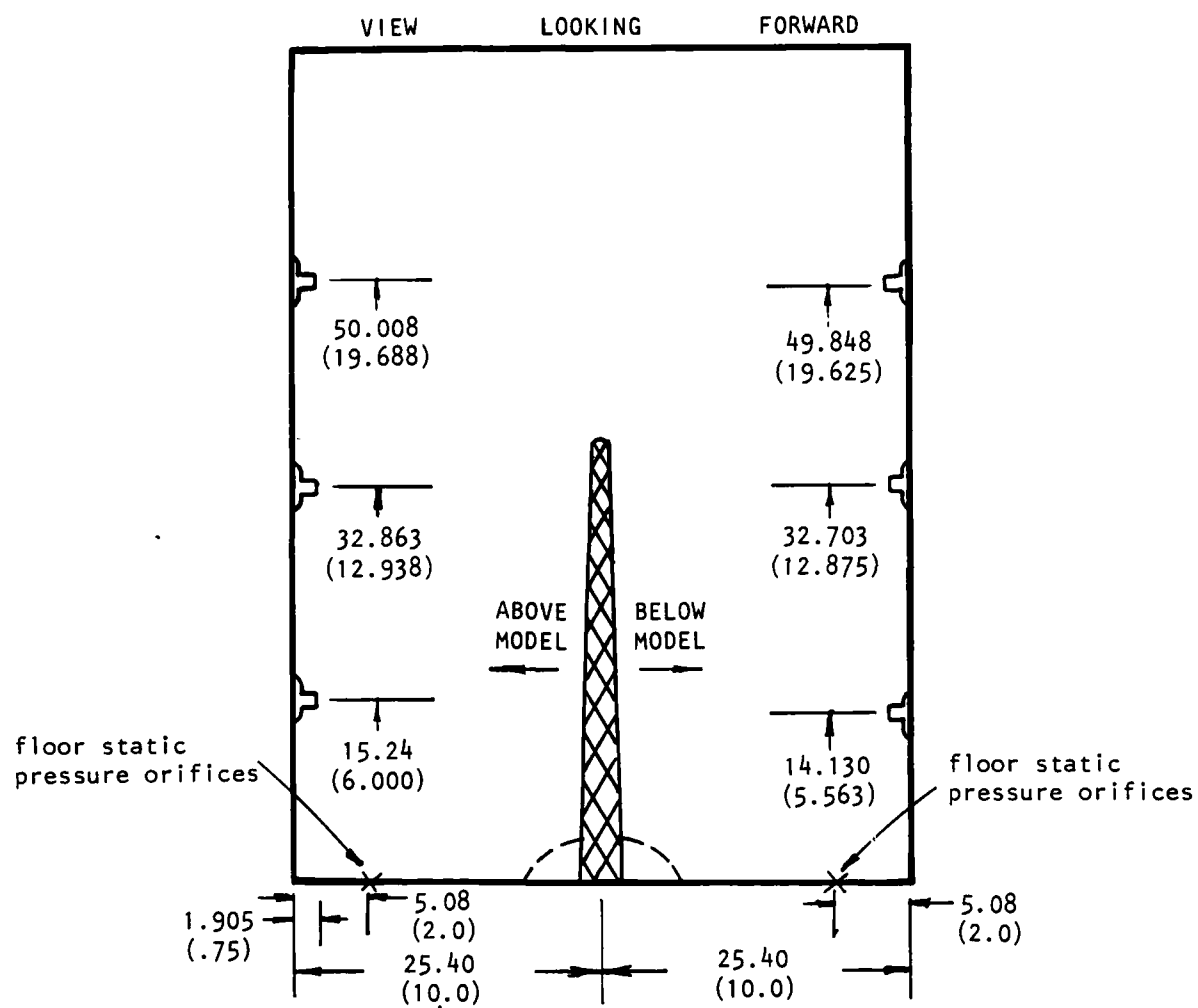


Figure 15 . - Far-field rail locations - cm (inches).

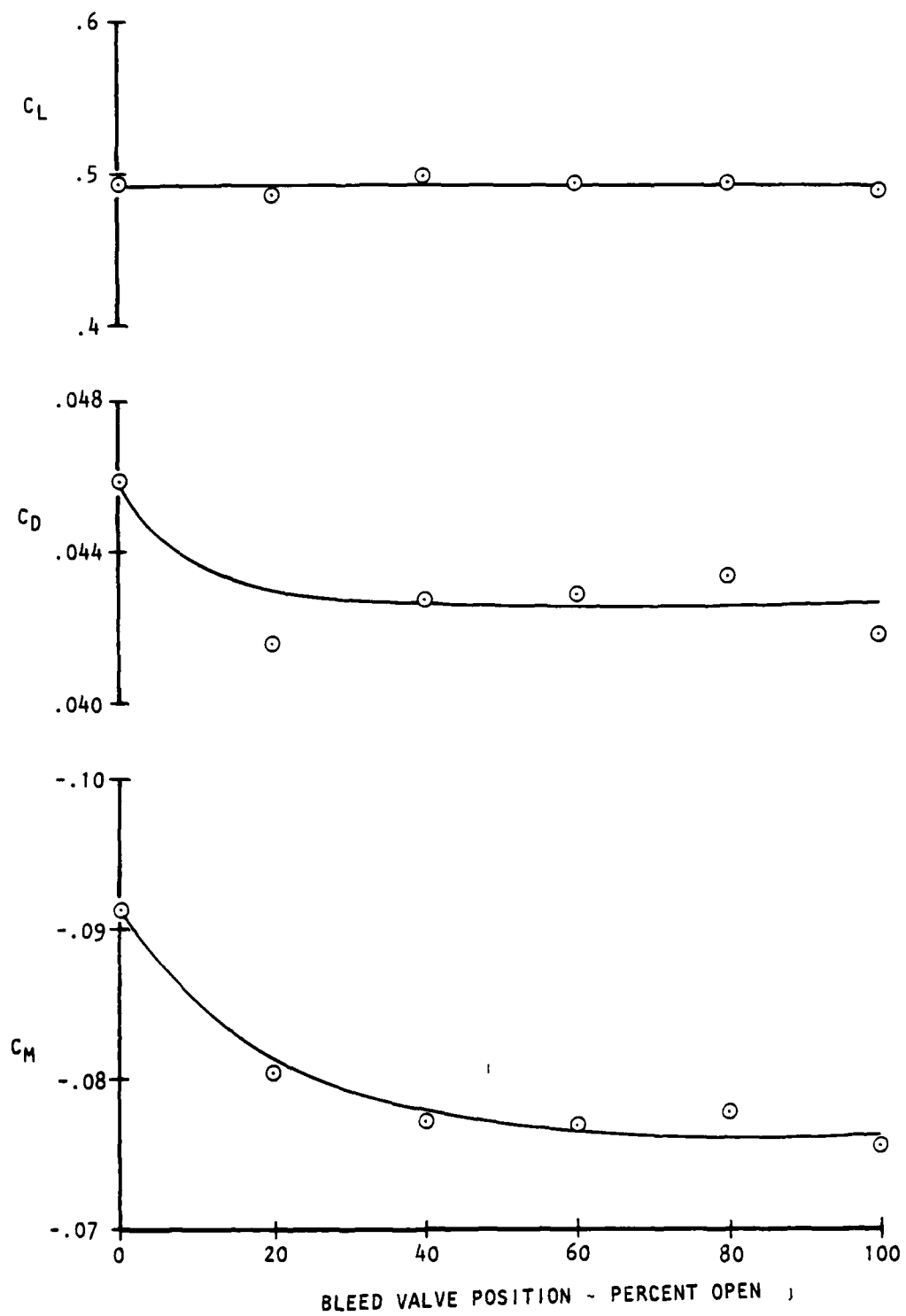
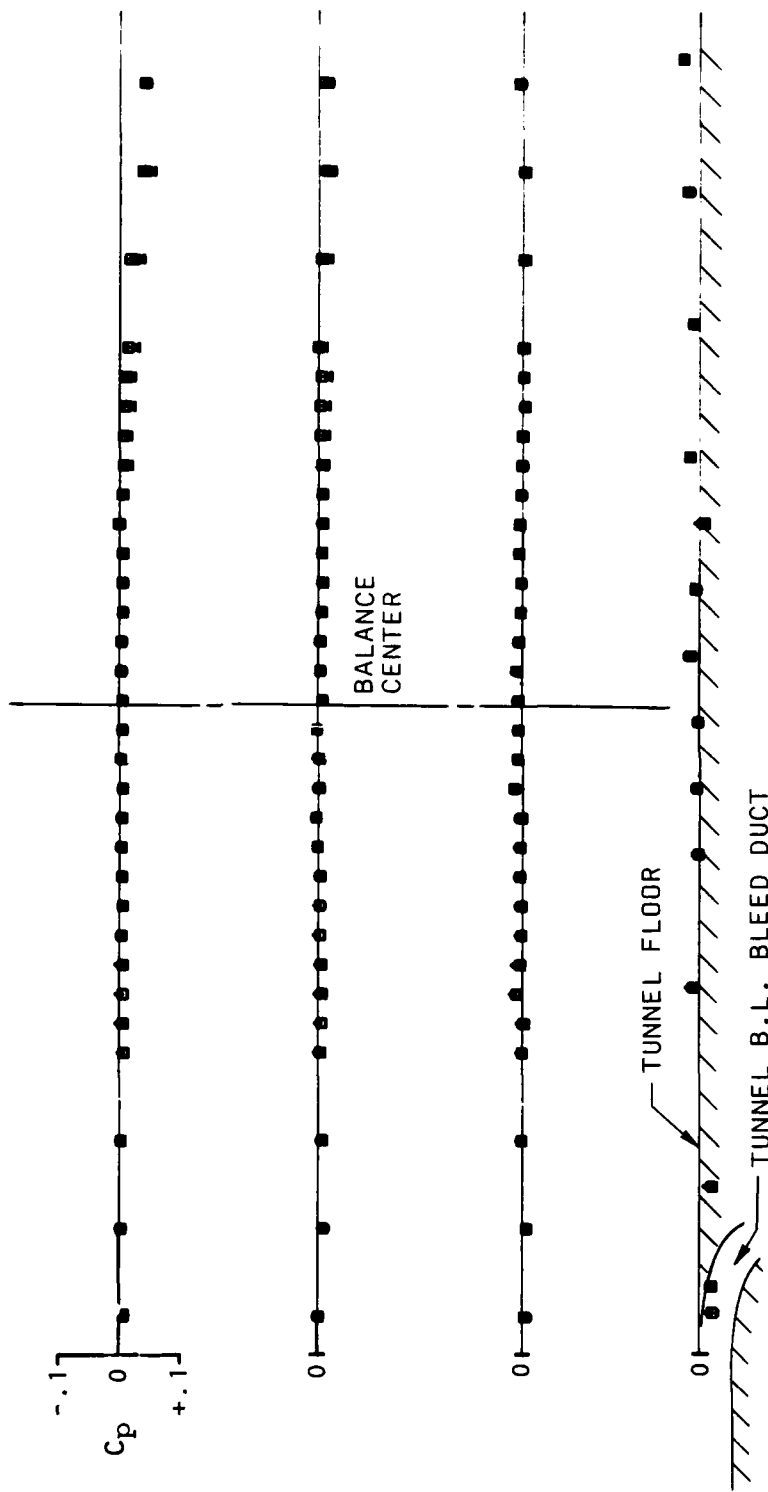


Figure 16 . - Effect of tunnel boundary layer bleed system on Wing C forces;  
 $M = .85$ ,  $\alpha = 5^\circ$ .

SYM	RUN	MACH	TAU	BLEED
□	307	0.8051	4.94	58.1
○	308	0.8042	3.91	58.0
▲	309	0.8023	2.98	58.0

UPPER POROUS WALL

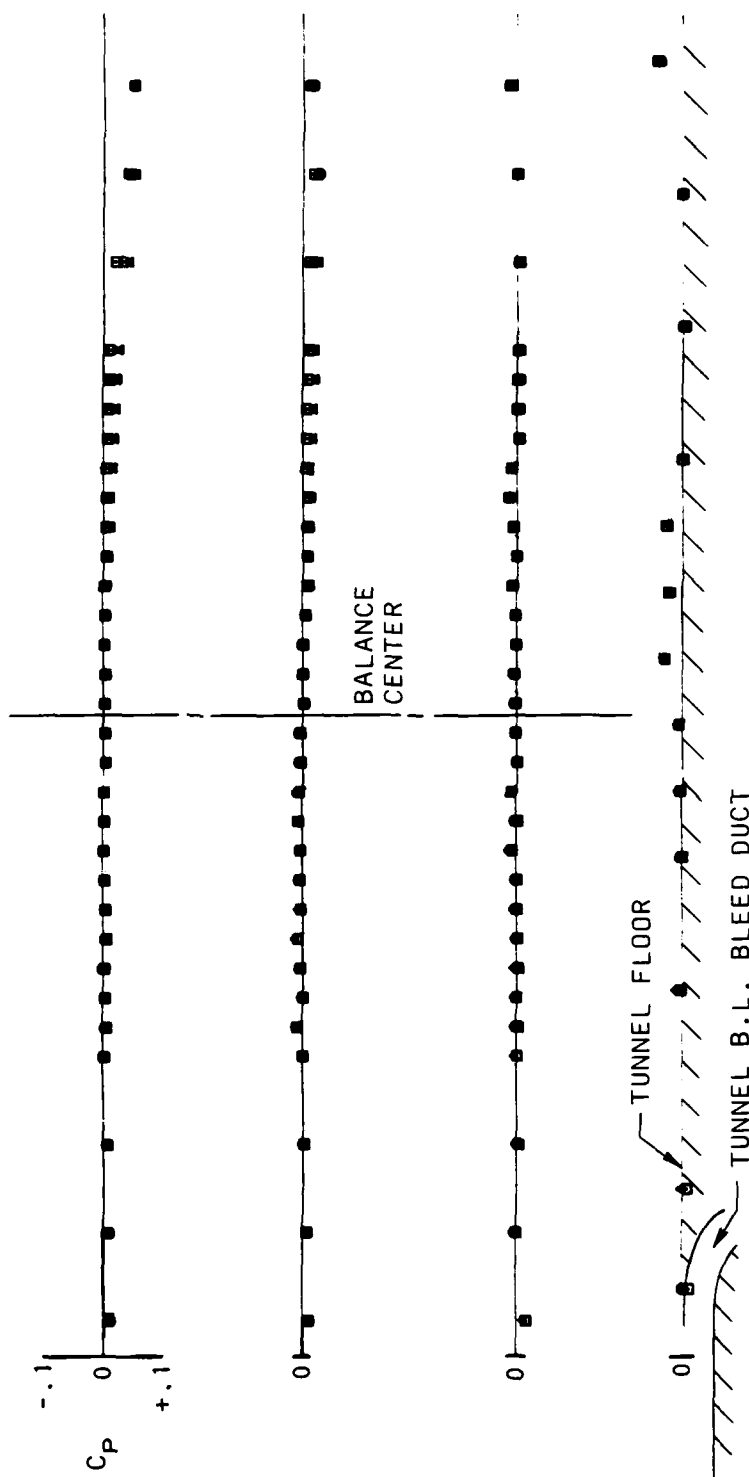


(a) Above Model (left wall)

Figure 17. - Calibration of floor static pressure orifices and far-field rails.

SYM	RUN	MACH	TAU	BLEED
□	307	0.8051	4.94	58.1
○	308	0.8042	3.91	58.0
△	309	0.8023	2.98	58.0

UPPER POROUS WALL



(b) Below Model (right wall)

Figure 17. - Concluded



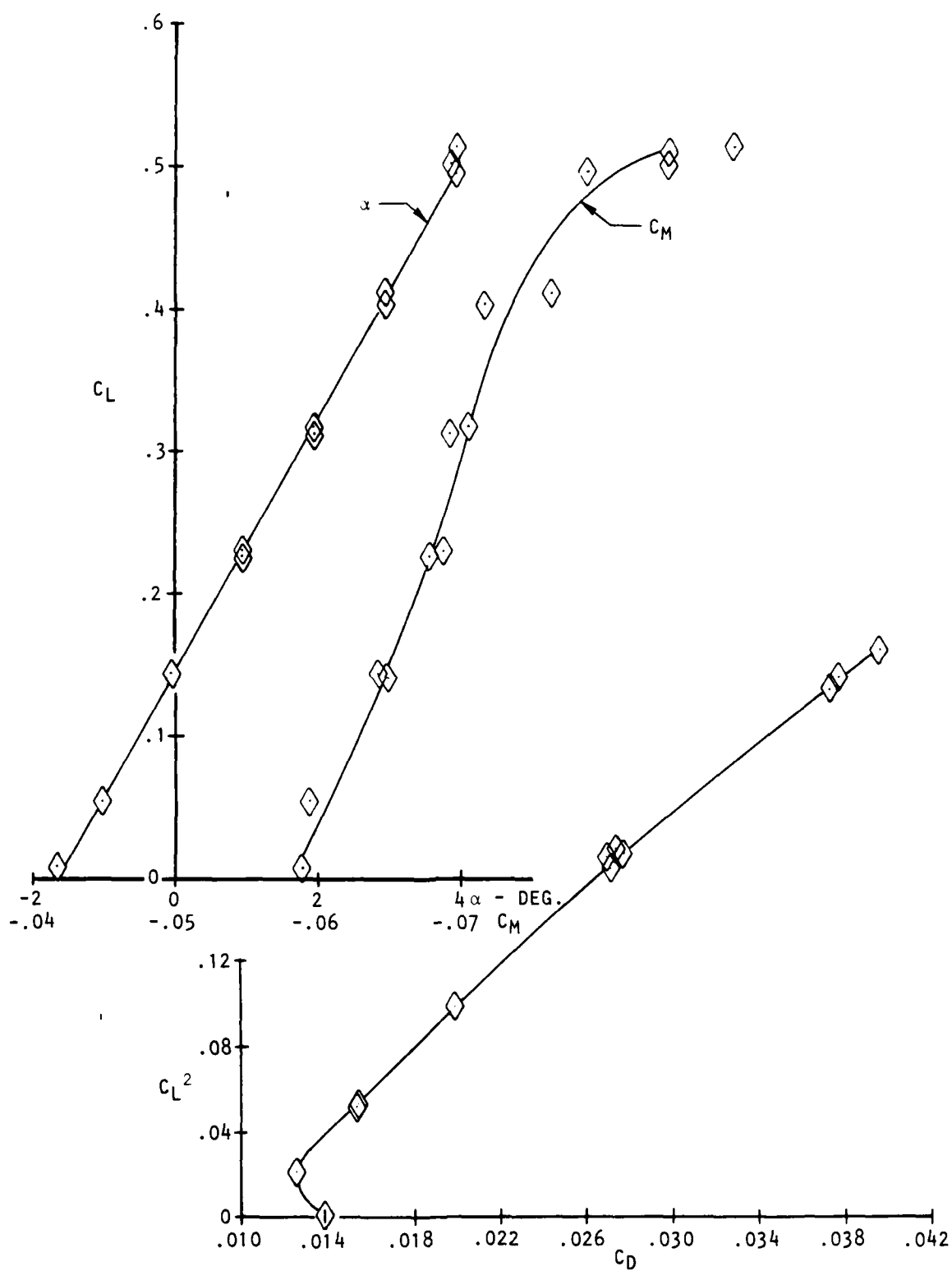


Figure 18 . - Evaluation of balance repeatability,  
Wing B,  $M = .9$ .

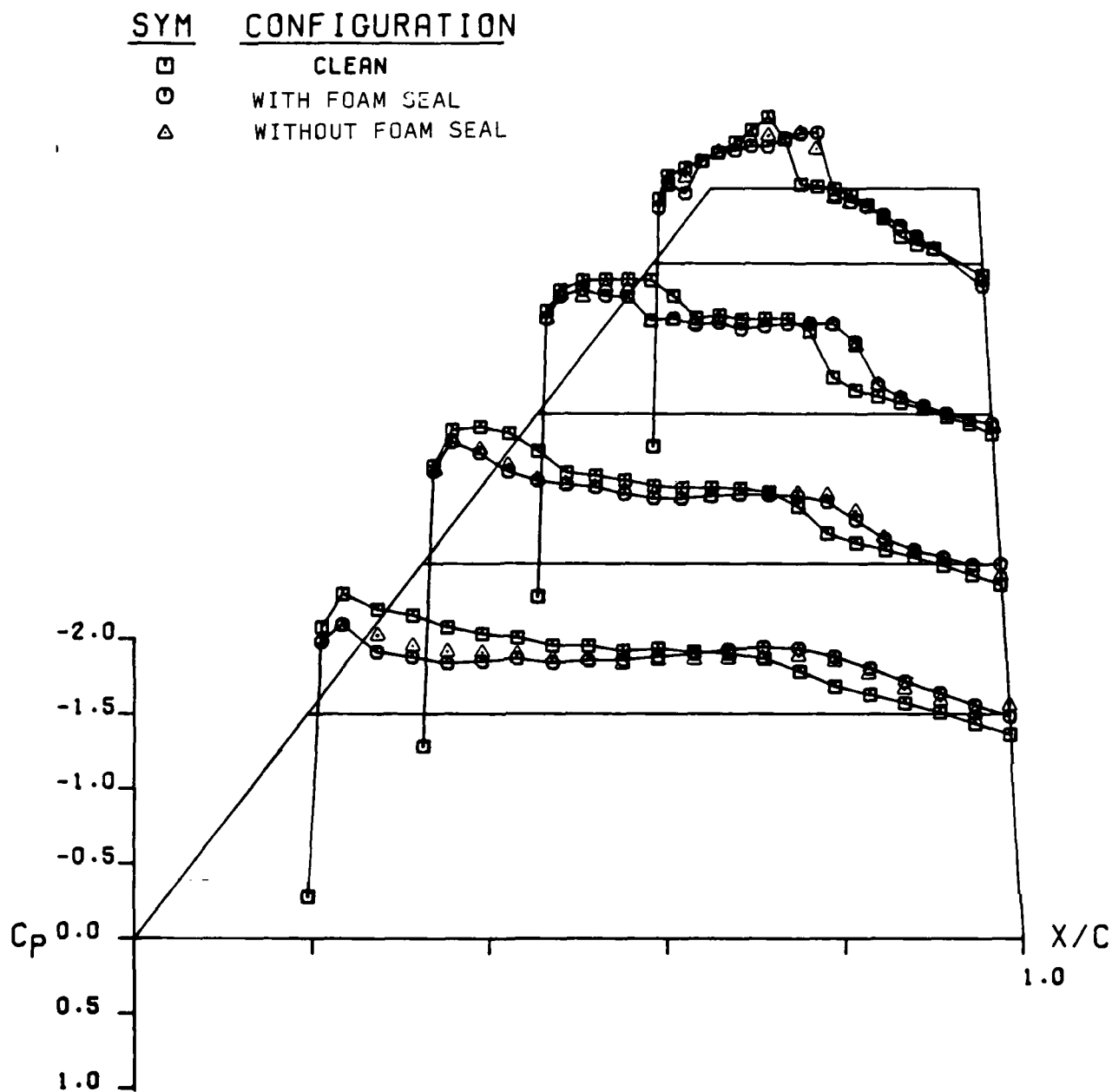


Figure 19 . Wing C upper surface distribution comparing wing-alone data with mid-wing/fuselage with and without foam seal at  $M = .90$ ,  $\alpha = 5^\circ$ .

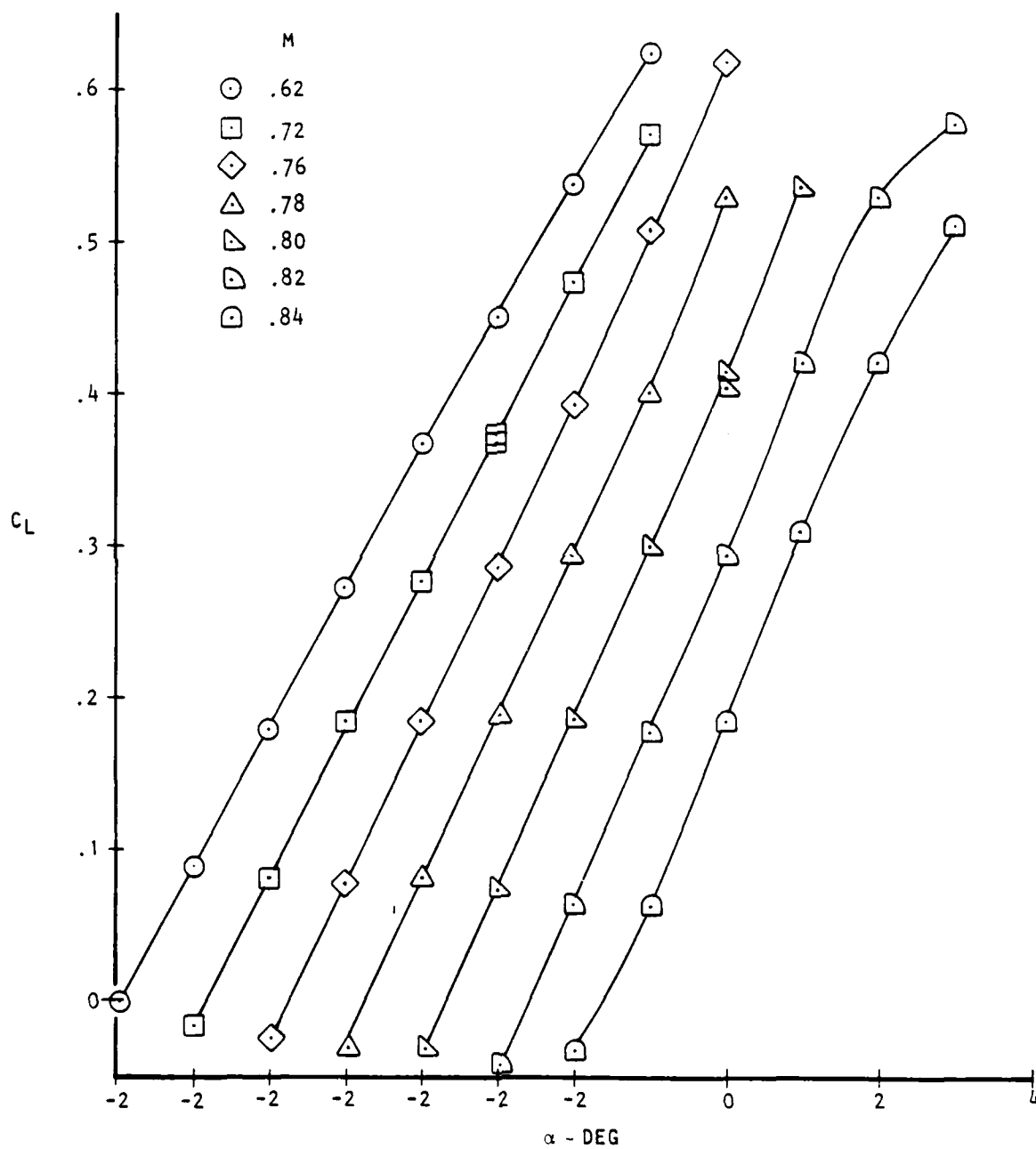


Figure 20 . - Summary of lift data for Wing A.

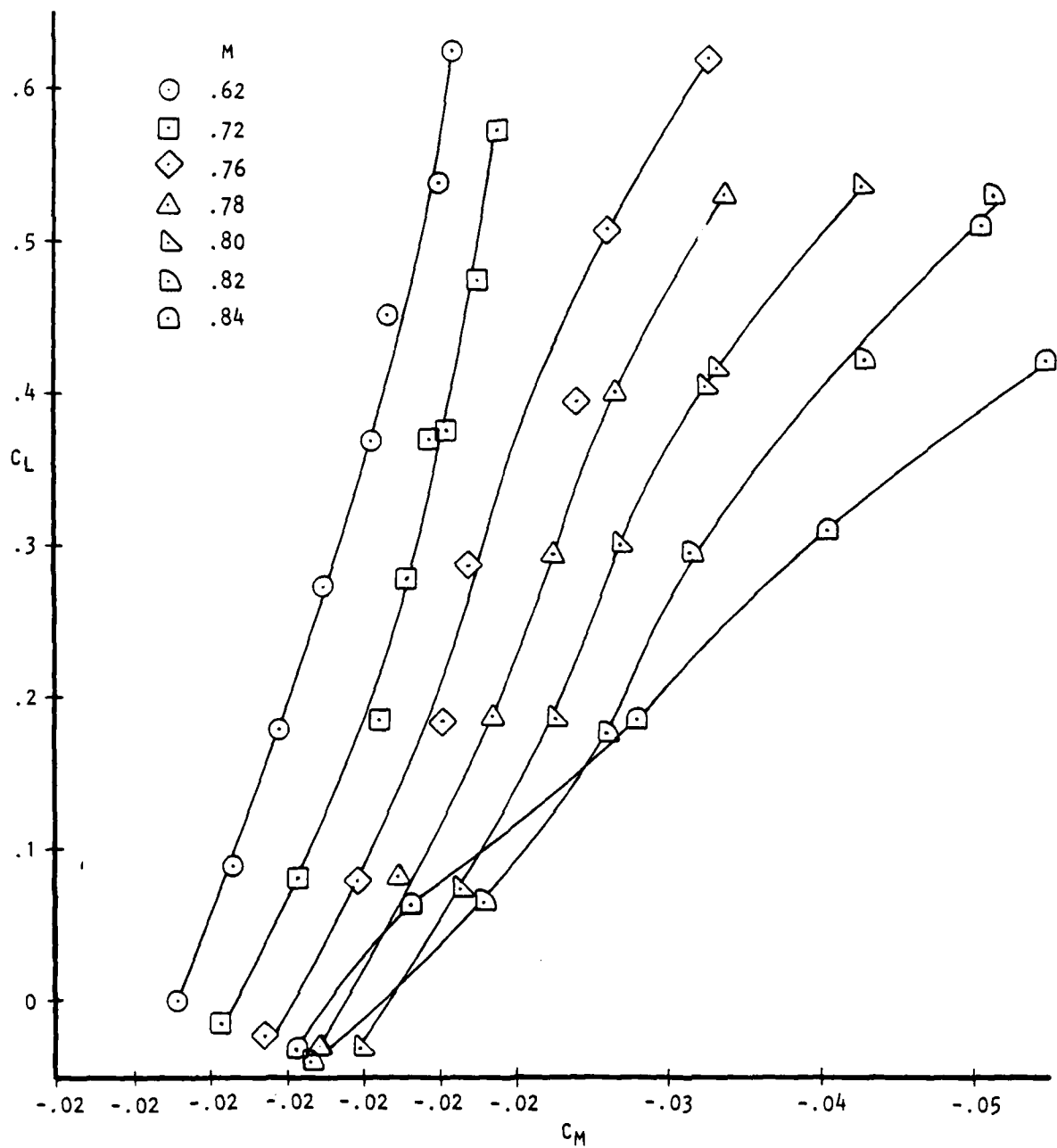


Figure 21. - Summary of pitching moment data for Wing A.

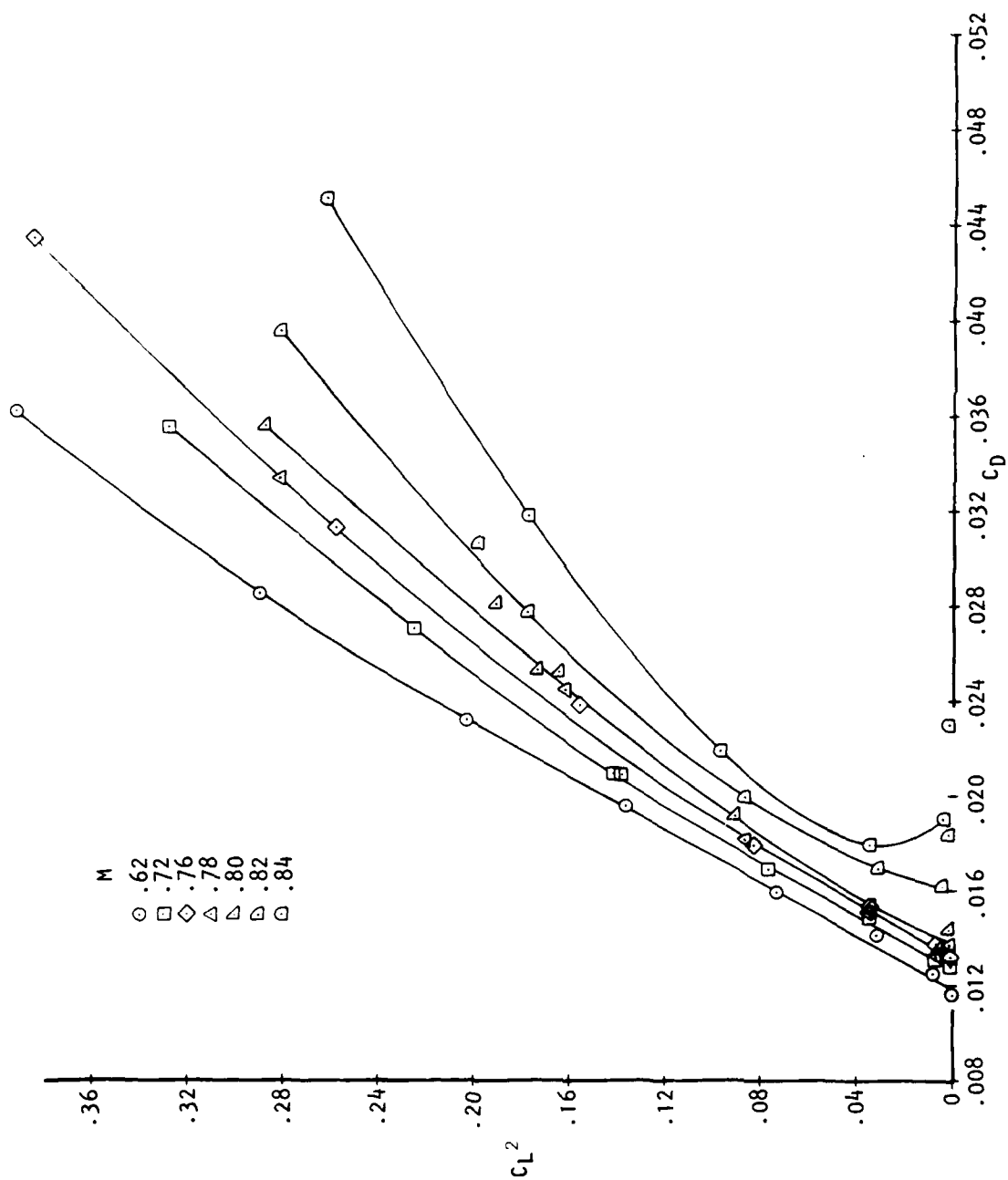


Figure 22. - Summary of drag data for Wing A.

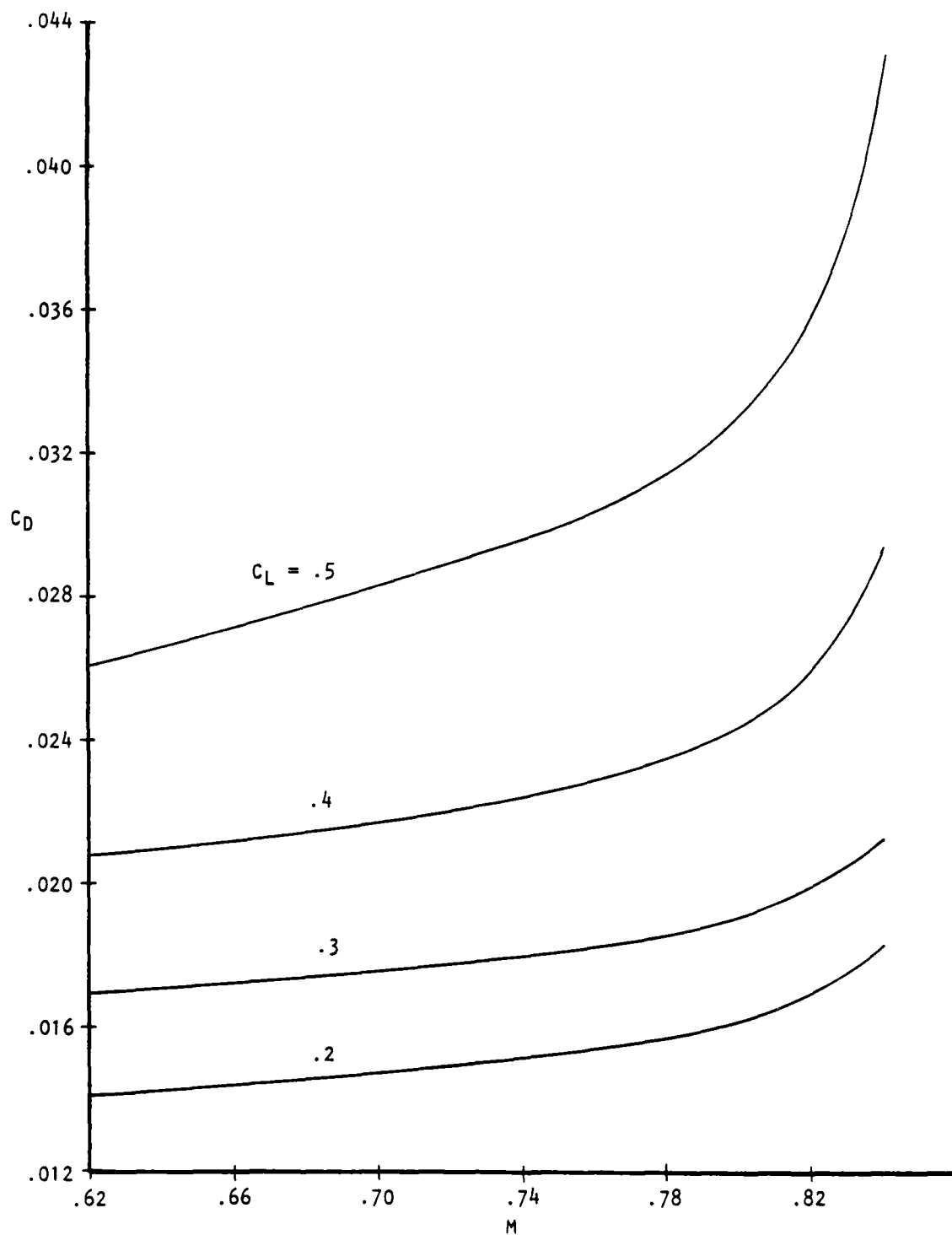


Figure 23. - Summary of drag versus Mach number for Wing A.

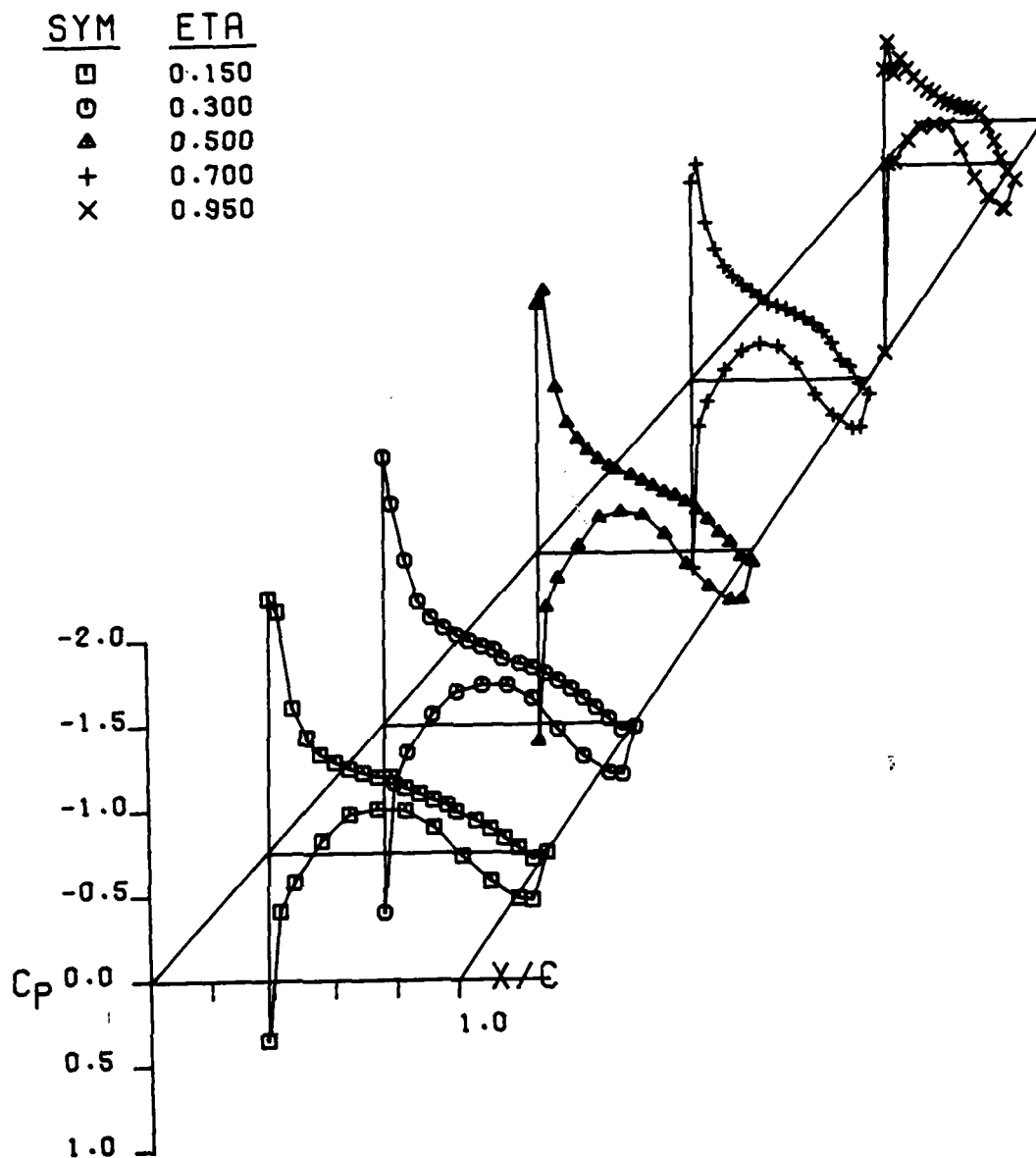


Figure 24. Wing A pressure distribution at  $M = 0.622$ ,  $\alpha = 2.98$ ,  
 $C_L = 0.451$ ,  $C_D = 0.0232$ ,  $C_M = -0.042$ .

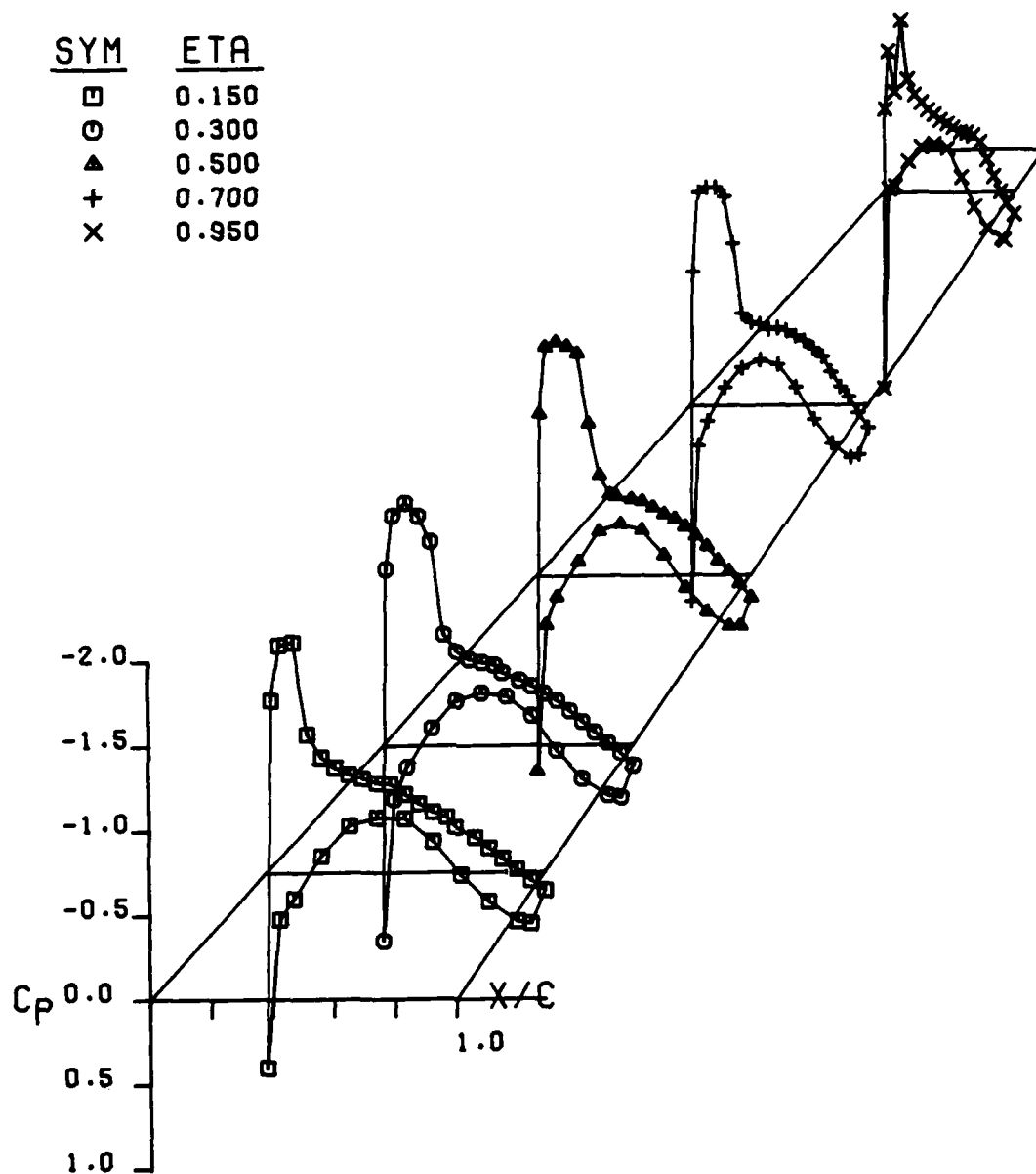


Figure 25. Wing A pressure distribution at  $M = 0.761$ ,  $\alpha = 2.955$ ,  
 $C_L = 0.508$ ,  $C_D = 0.0313$ ,  $C_M = -0.046$



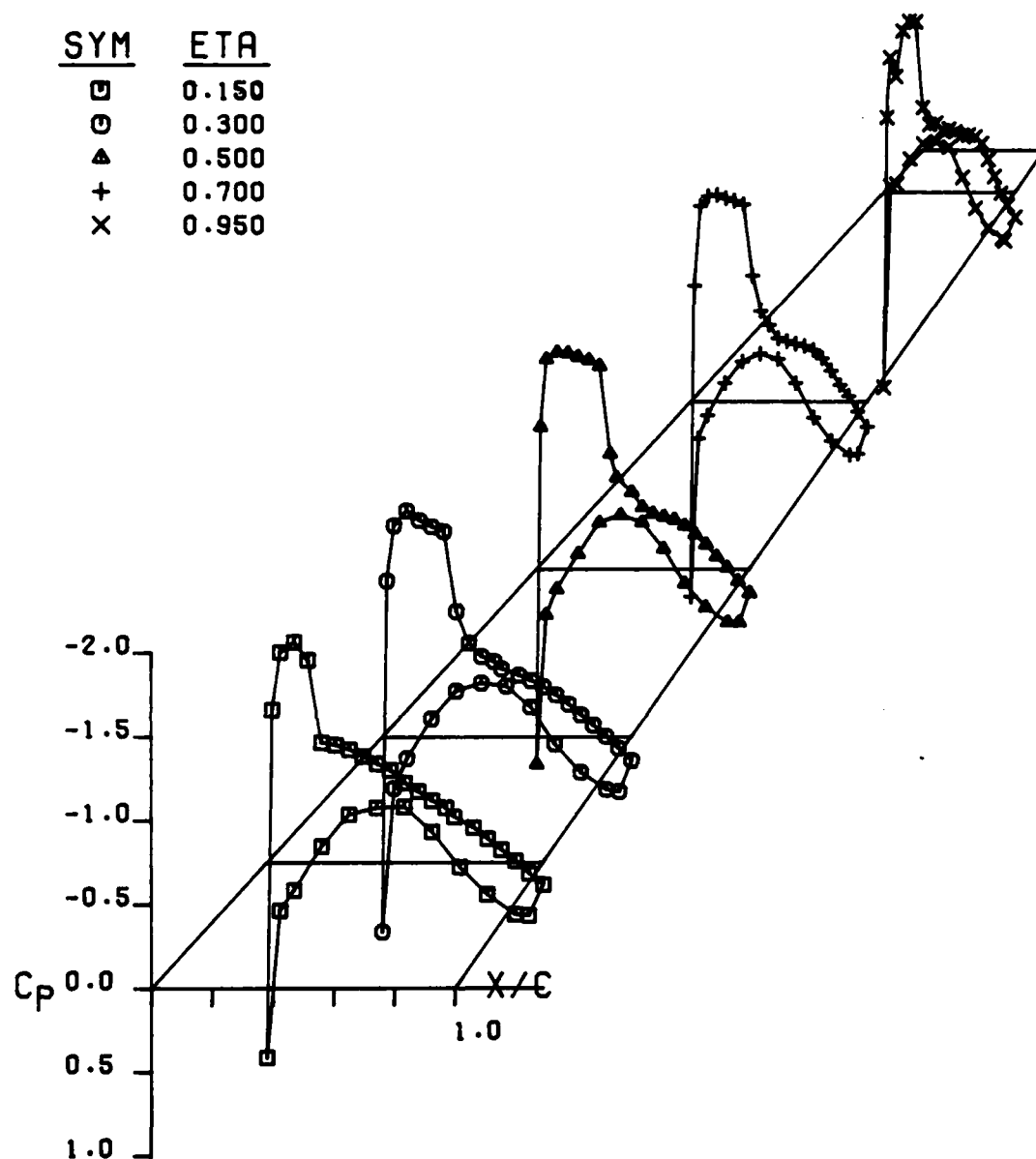


Figure 26. Wing A pressure distribution at  $M = 0.784$ ,  $\alpha = 2.952$ ,  
 $C_L = 0.530$ ,  $C_D = 0.0334$ ,  $C_M = -0.049$

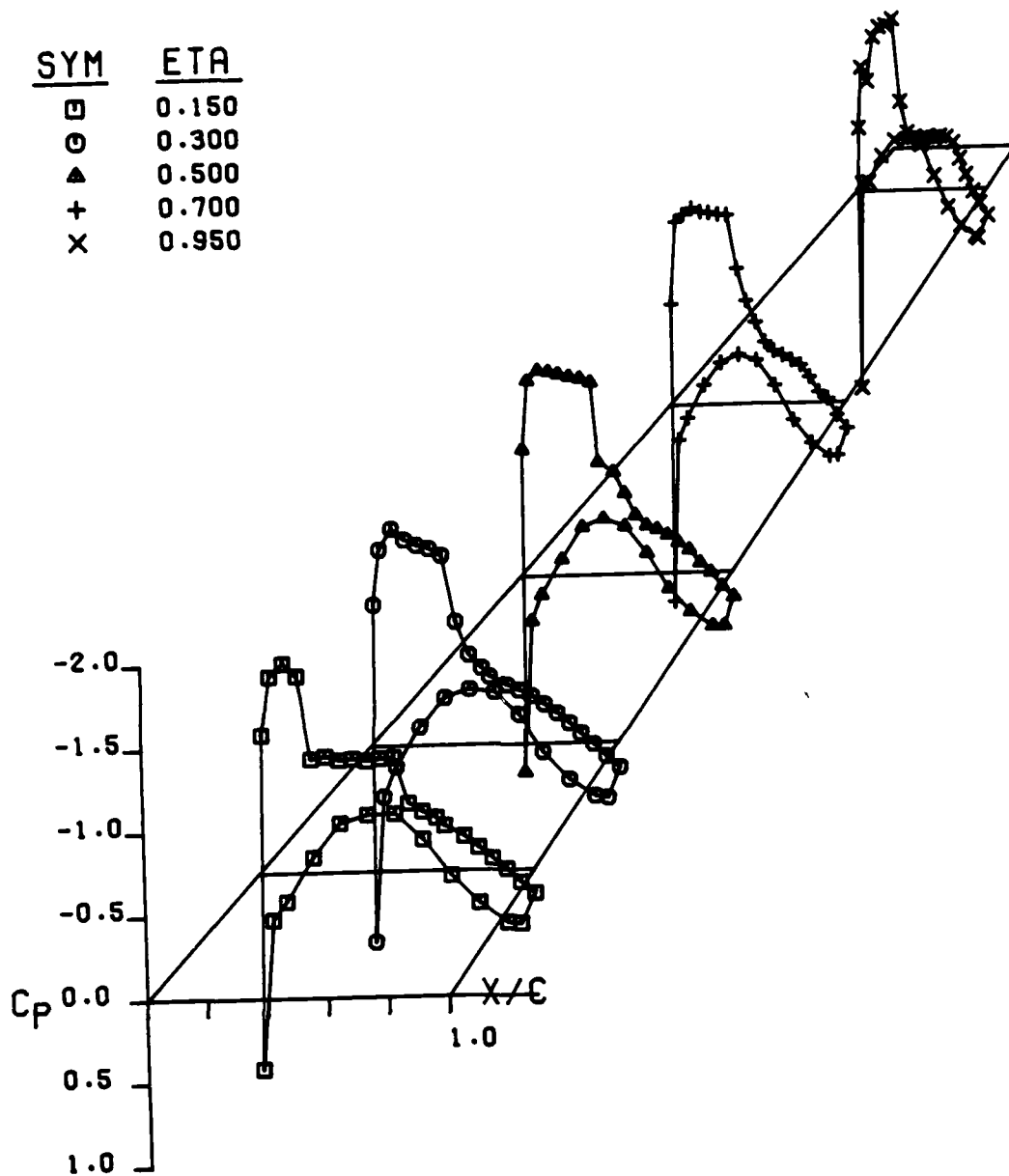


Figure 27. Wing A pressure distribution at  $M = 0.801$ ,  $\alpha = 2.941$ ,  
 $C_L = 0.536$ ,  $C_D = 0.0356$ ,  $C_M = -0.053$

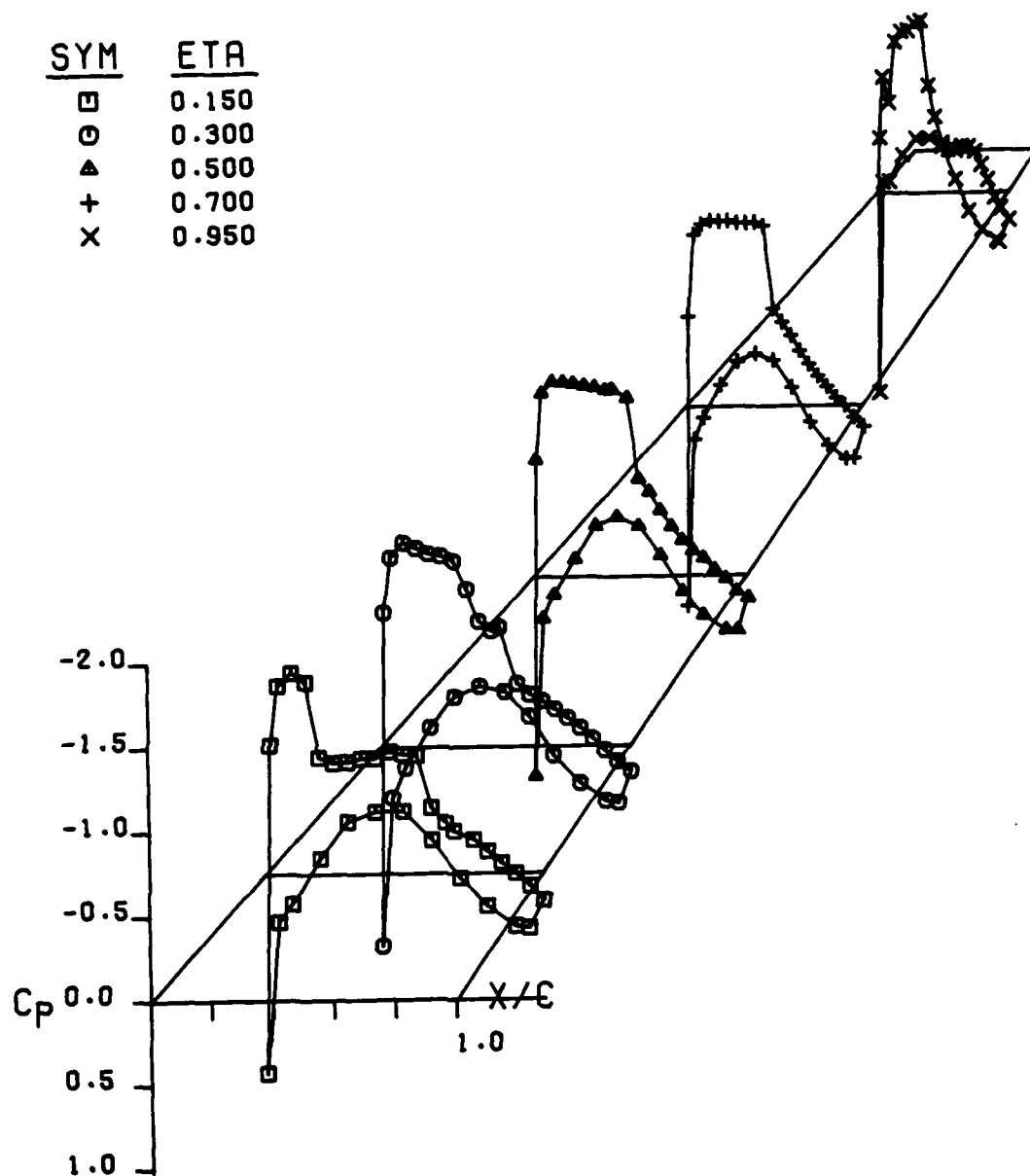


Figure 28.-Wing A pressure distribution at  $M = 0.818$ ,  $\alpha = 2.940$ ,  
 $C_L = 0.530$ ,  $C_D = 0.0395$ ,  $C_M = -0.056$

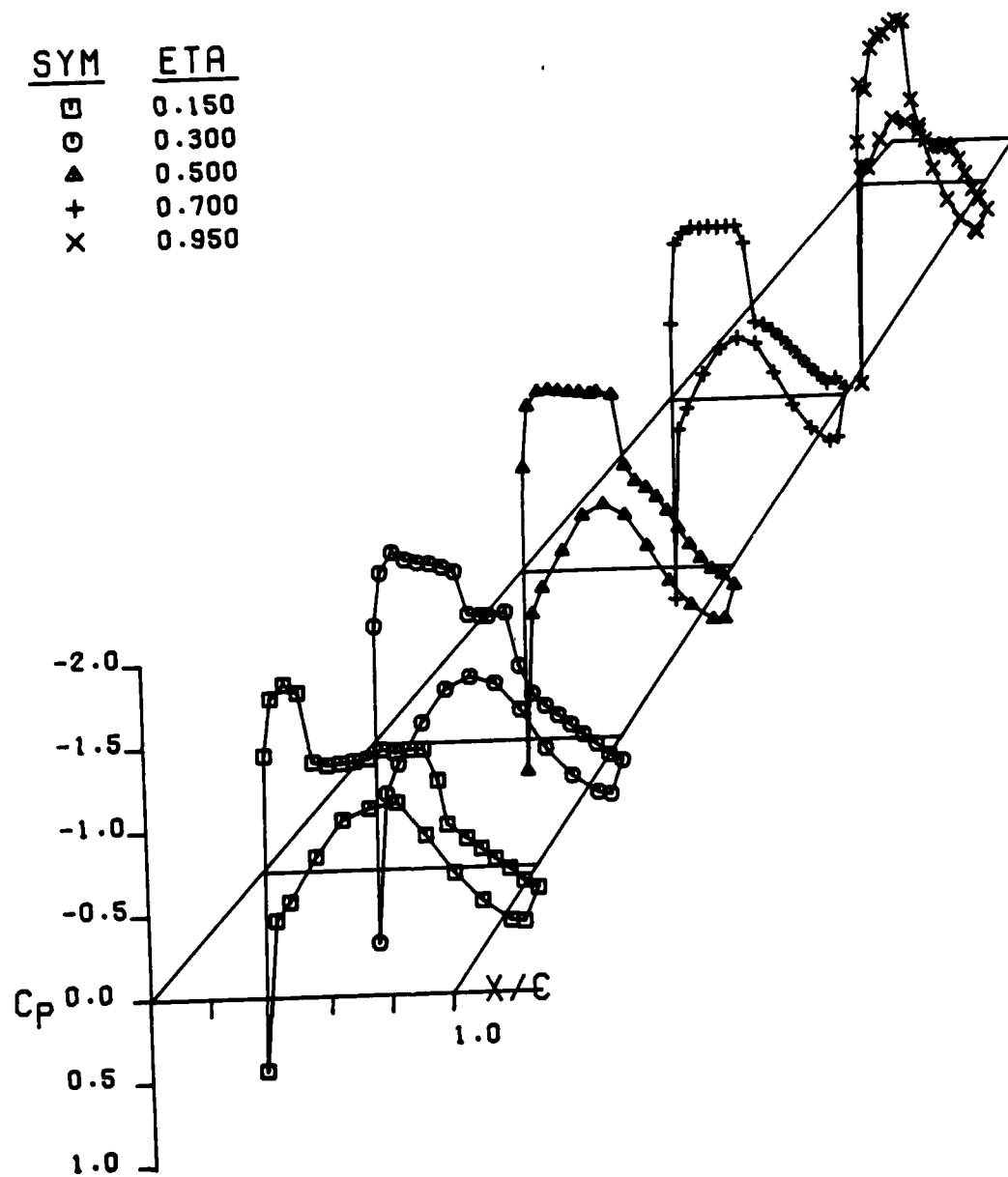


Figure 29. Wing A pressure distribution at  $M = 0.839$ ,  $\alpha = 2.931$ ,  
 $C_L = 0.512$ ,  $C_D = 0.0451$ ,  $C_M = -0.051$

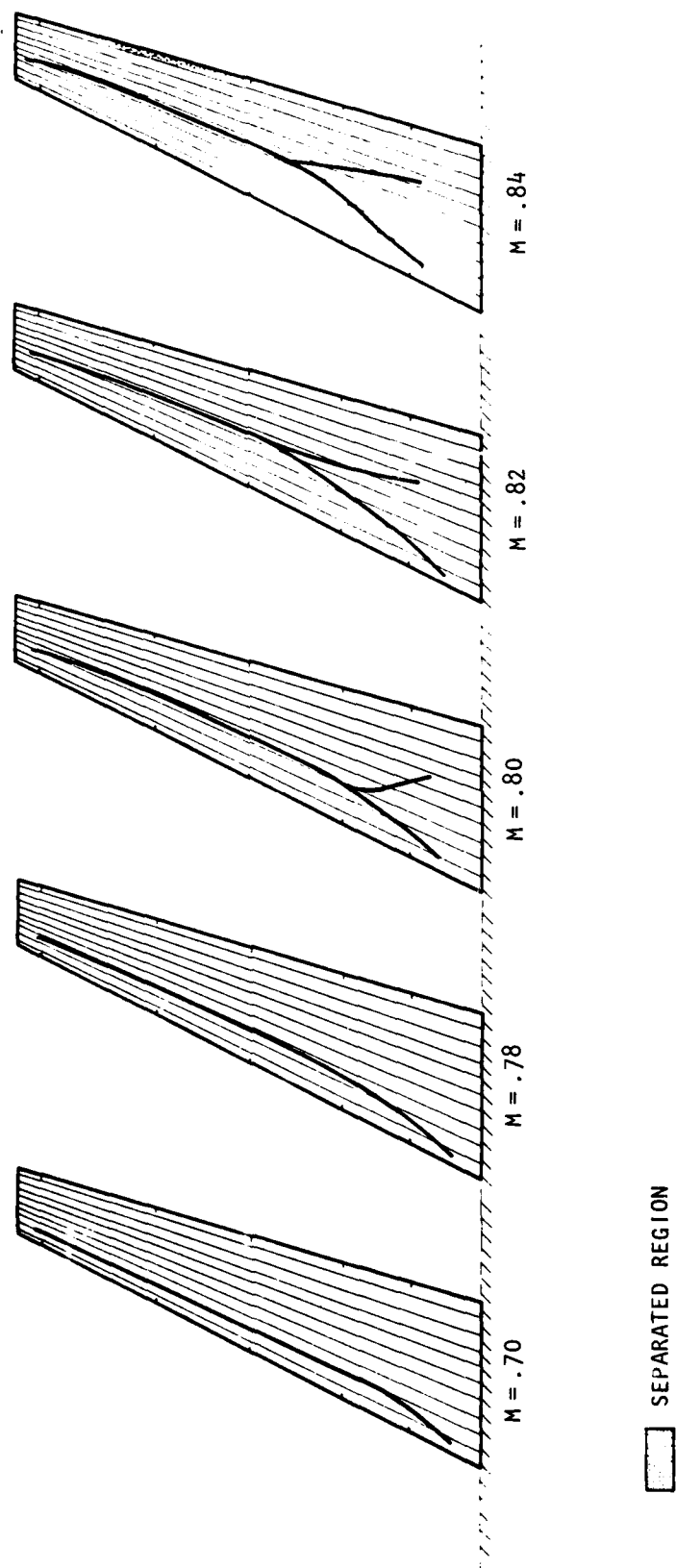


Figure 30. - Wing A shock pattern at various Mach numbers at an angle of attack of  $3^\circ$ .

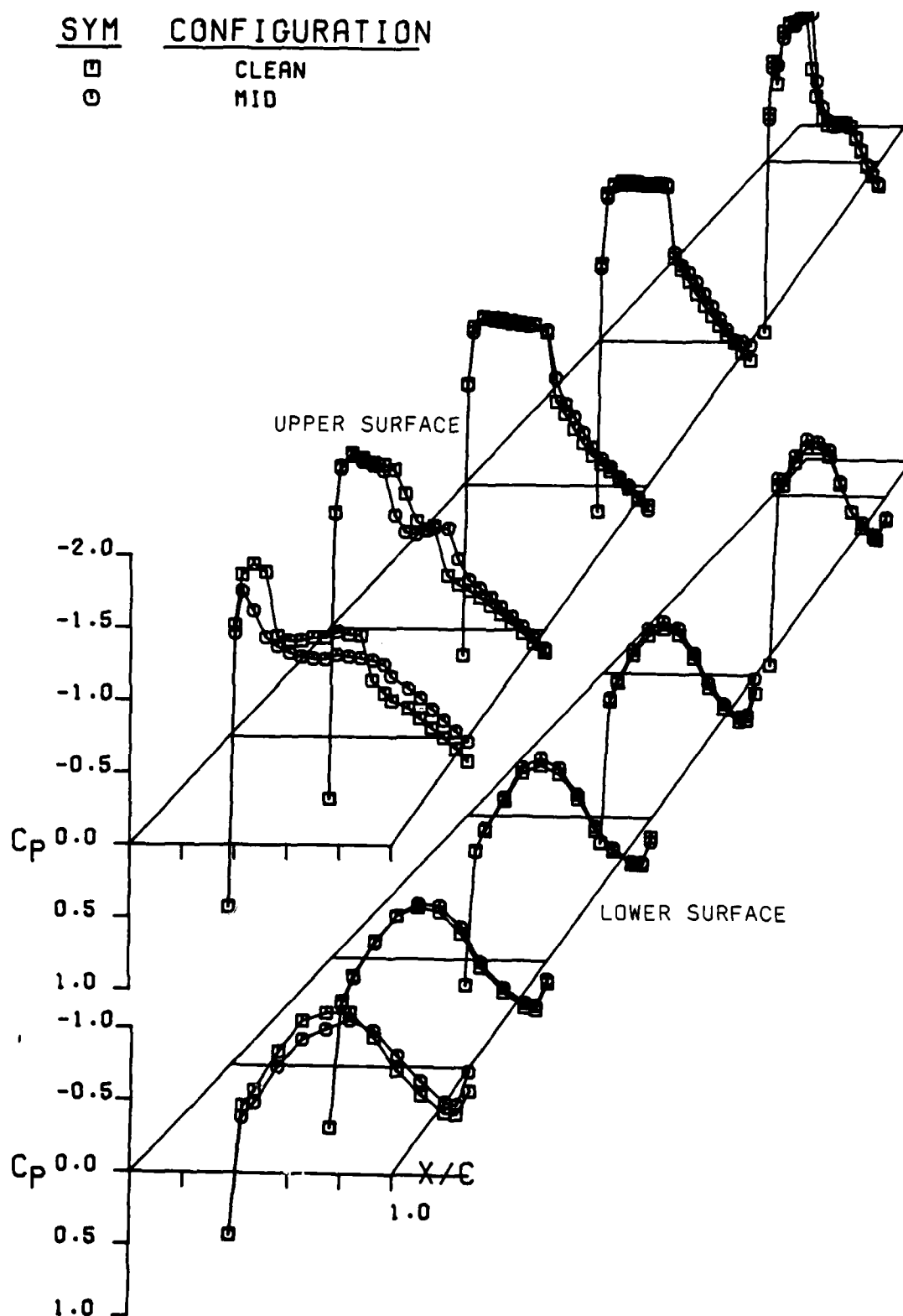


Figure 31 . - Comparison of Wing A pressures with and without a mid wing fuselage at  $M = .82$ ,  $\alpha = 3^\circ$ .

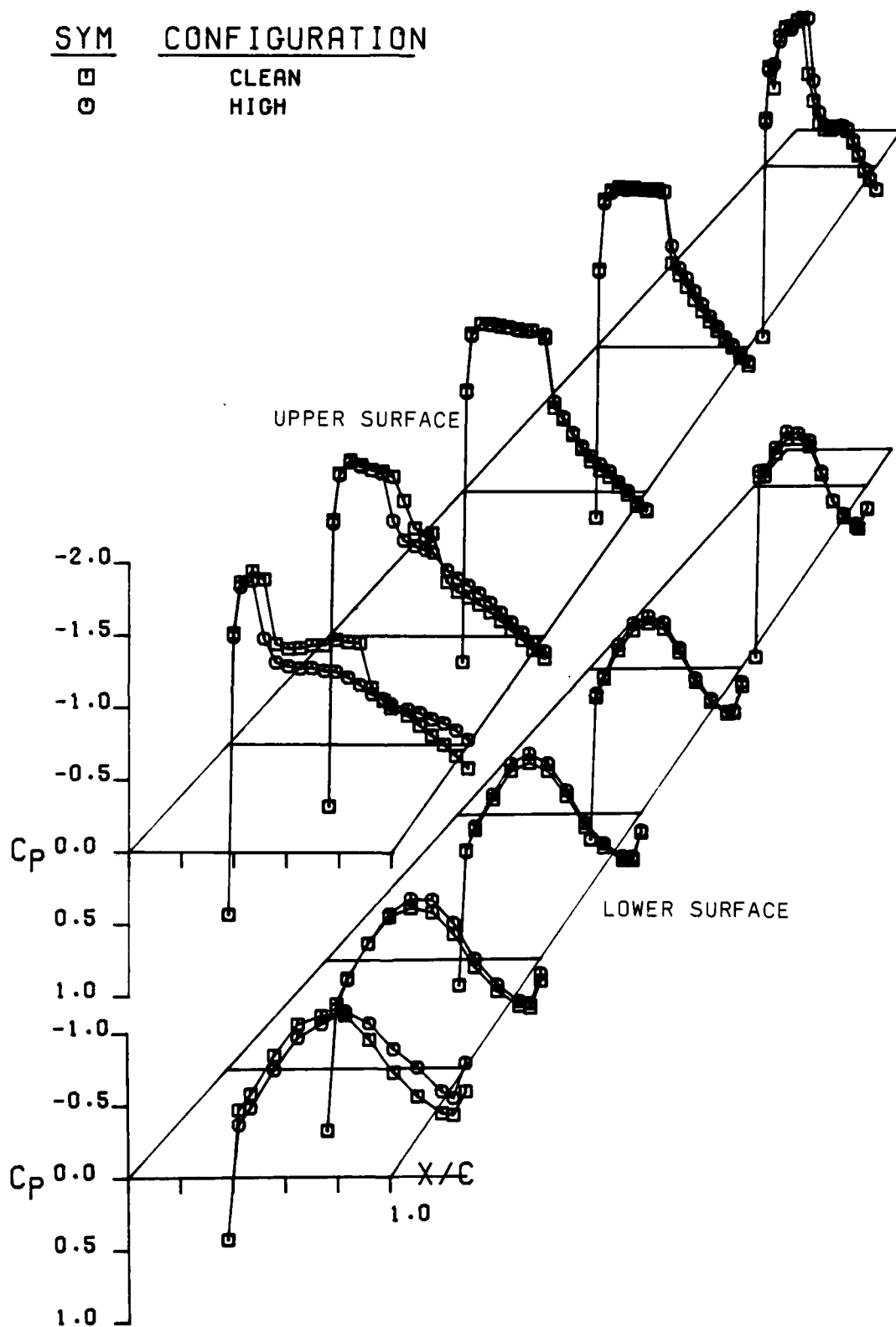


Figure 32 . - Comparison of Wing A pressures with and without a high wing fuselage at  $M = .82$ ,  $\alpha = 3^\circ$ .

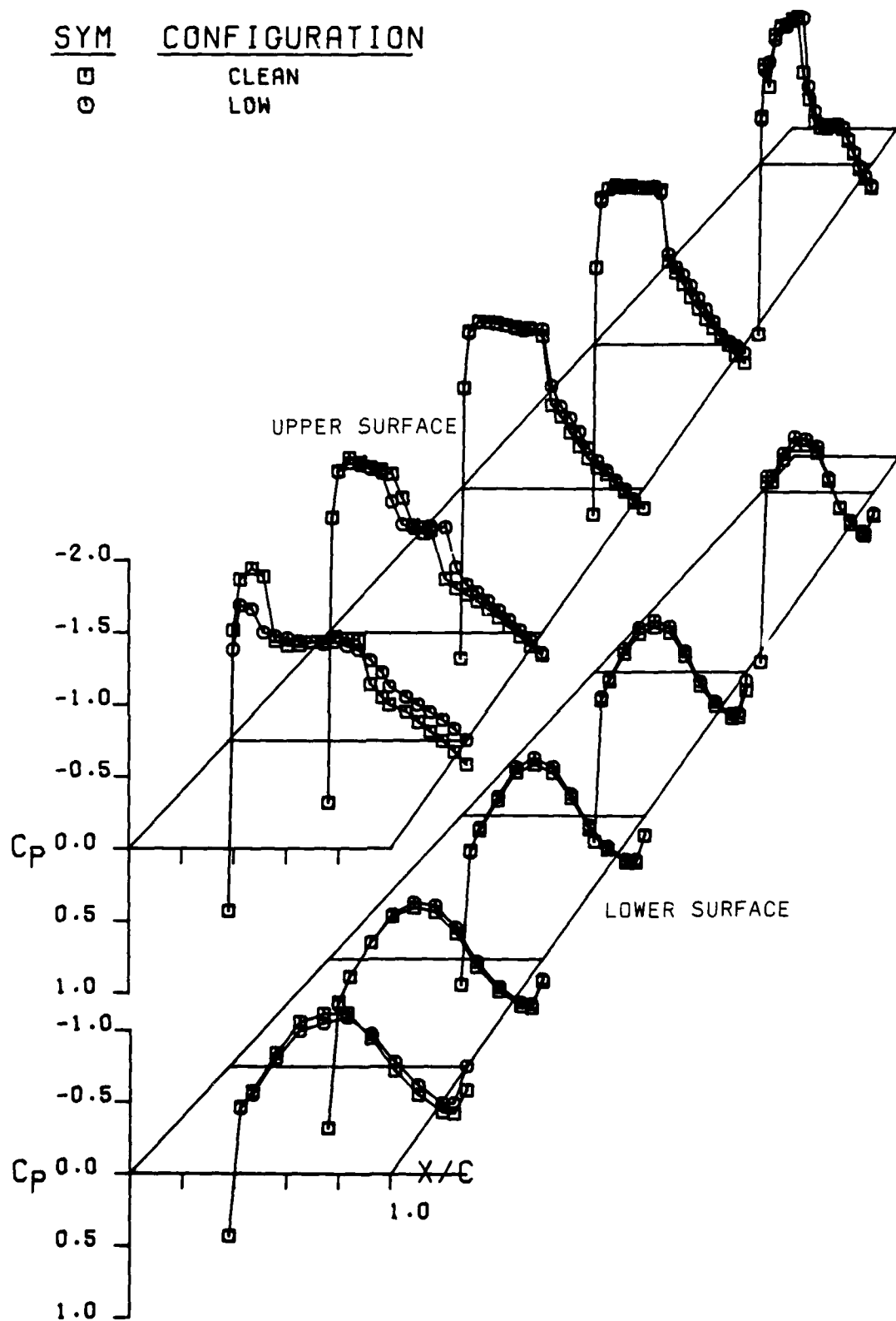


Figure 33 . - Comparison of Wing A pressures with and without a low wing fuselage at  $M = .82$ ,  $\alpha = 3^\circ$ .



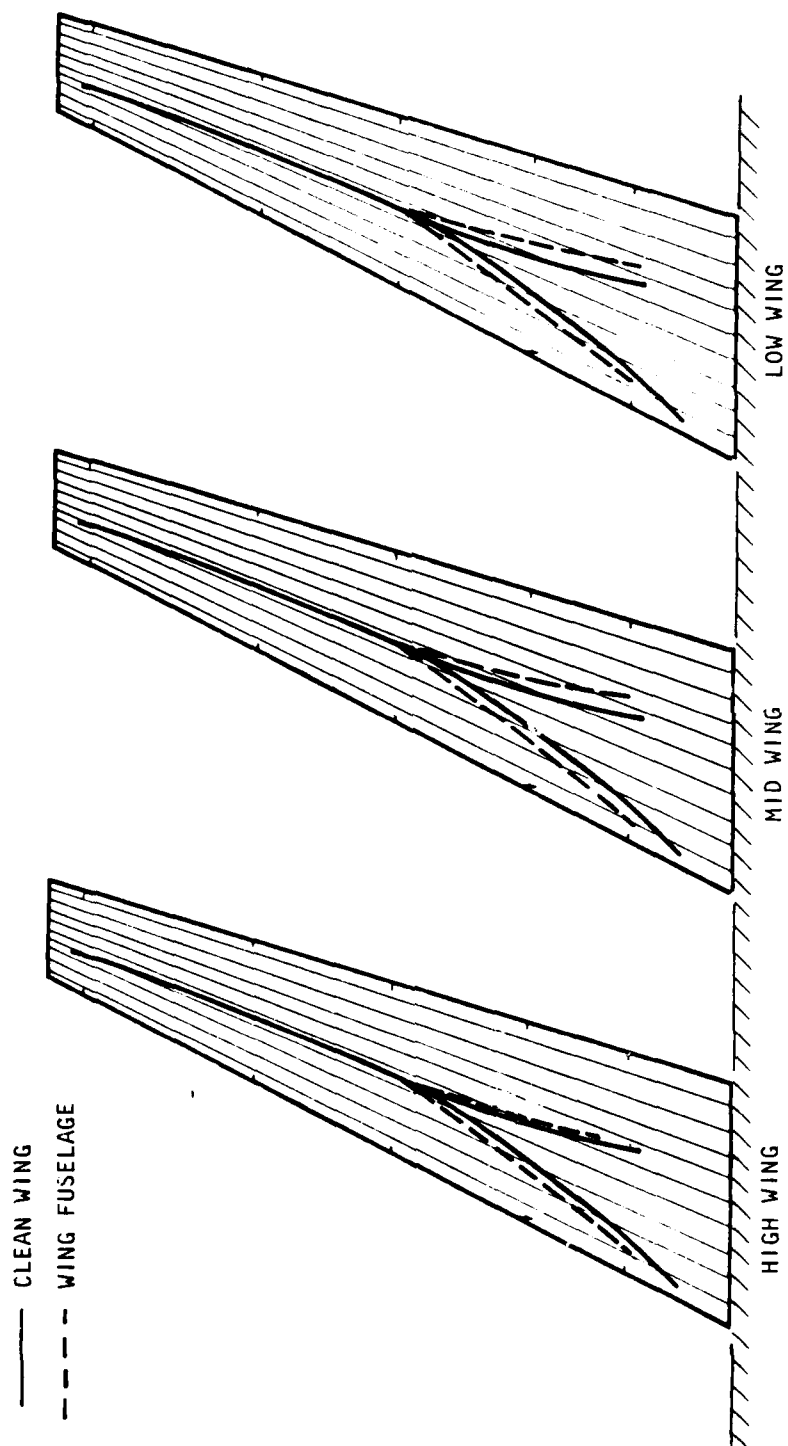


Figure 34 . - Comparison of Wing A alone shock pattern with various wing/fuselage configurations at  $M = .82$ ,  $\alpha = 3^\circ$ .

AD-A085 258

LOCKHEED-GEORGIA CO MARIETTA

F/G 20/4

ACQUISITION AND APPLICATION OF TRANSONIC WING AND FAR-FIELD TES--ETC(U)

MAR 80 B L HINSON, K P BURDGES

F4962n-78-C-0068

UNCLASSIFIED

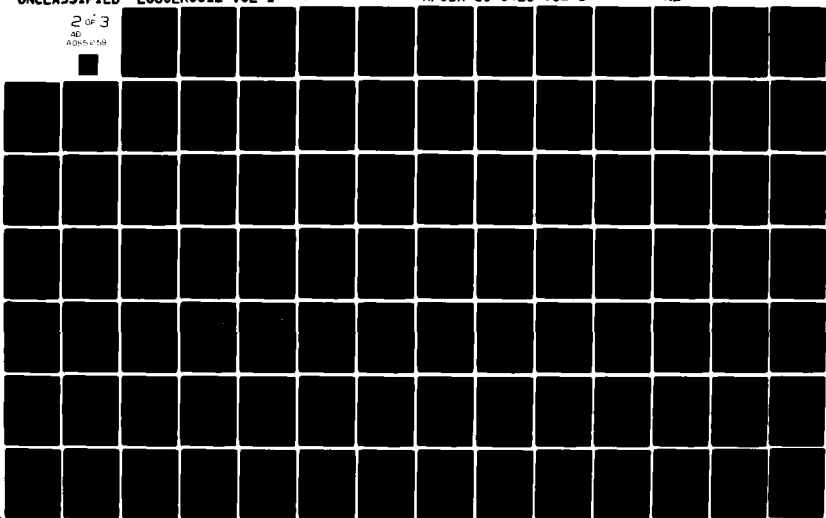
L680ER0012-VOL-1

AFOSR-80-0421-VOL-1

NL

2 of 3

AD  
A085 258



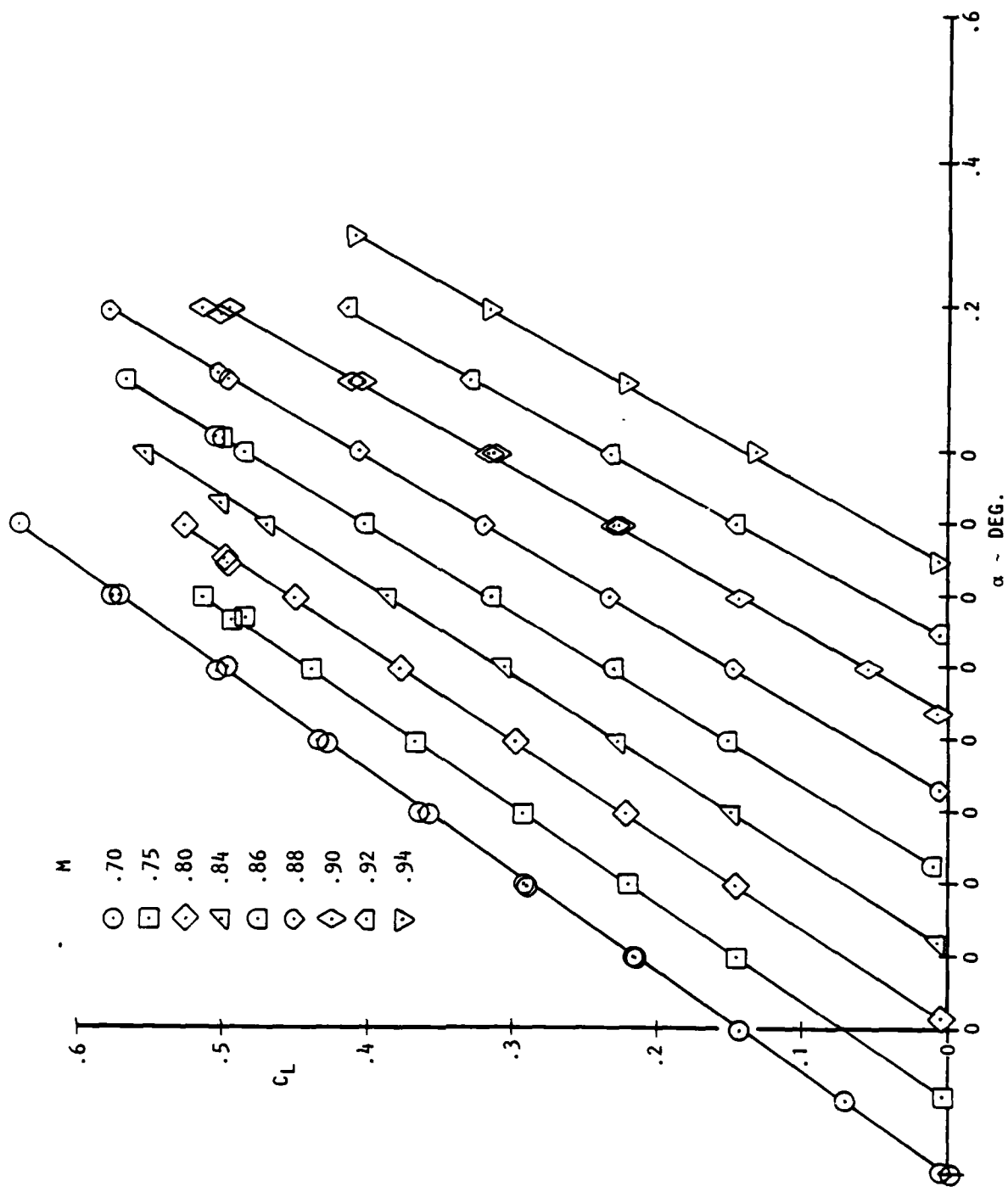


Figure 35 . - Summary of lift data for Wing B.

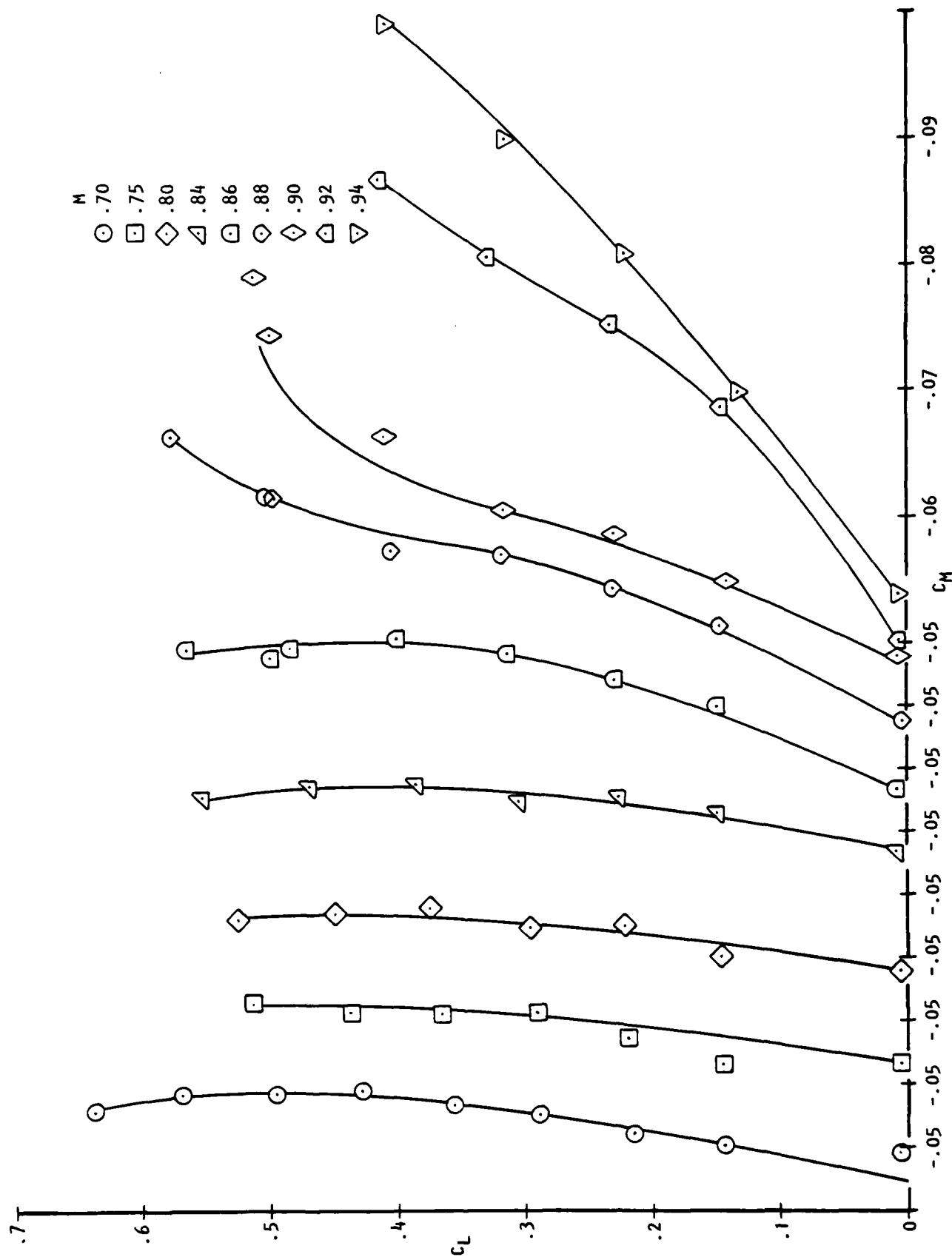


Figure 36 . - Summary of pitching moment data for Wing B.

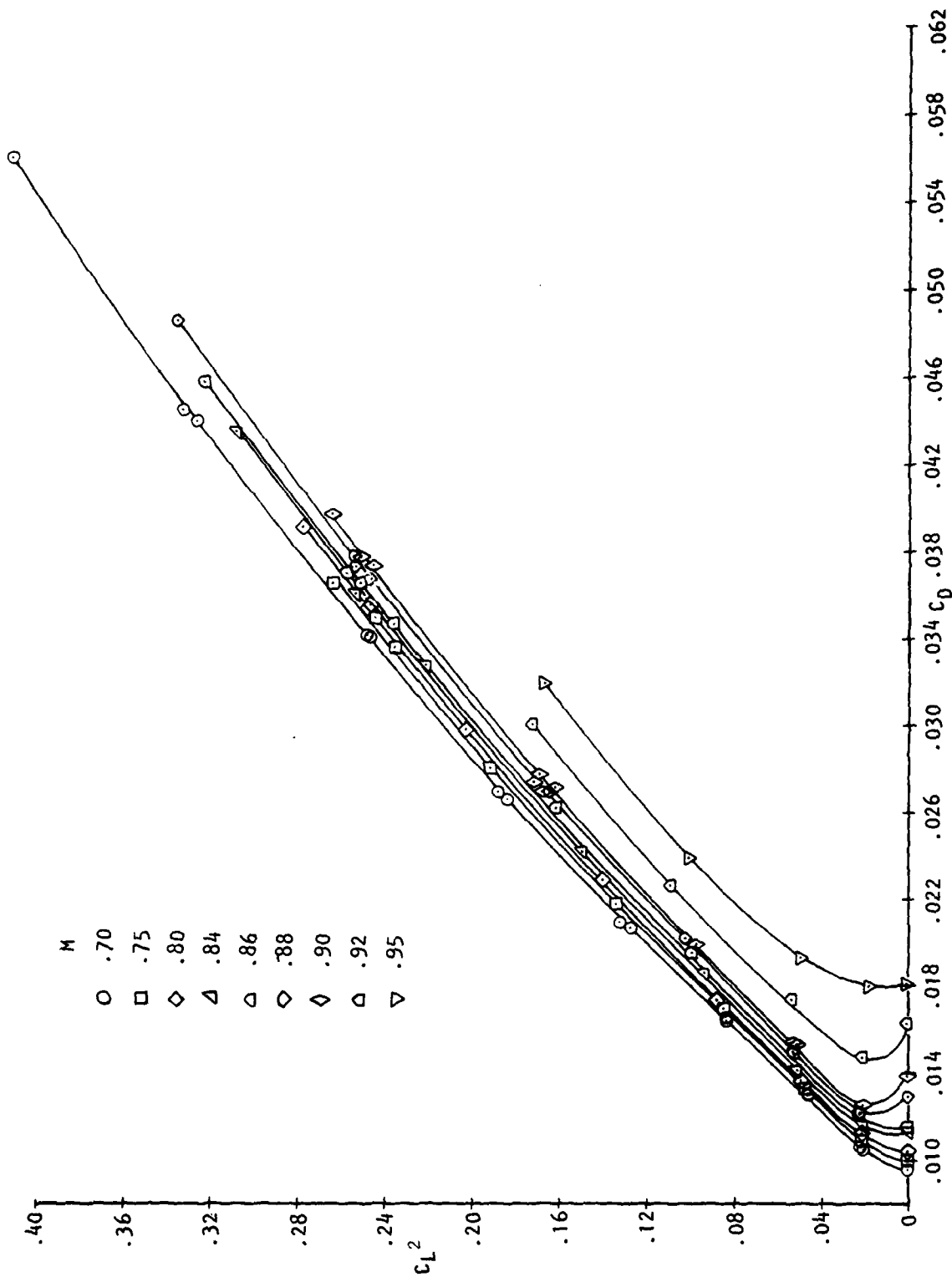


Figure 37 . - Summary of drag data for Wing B.

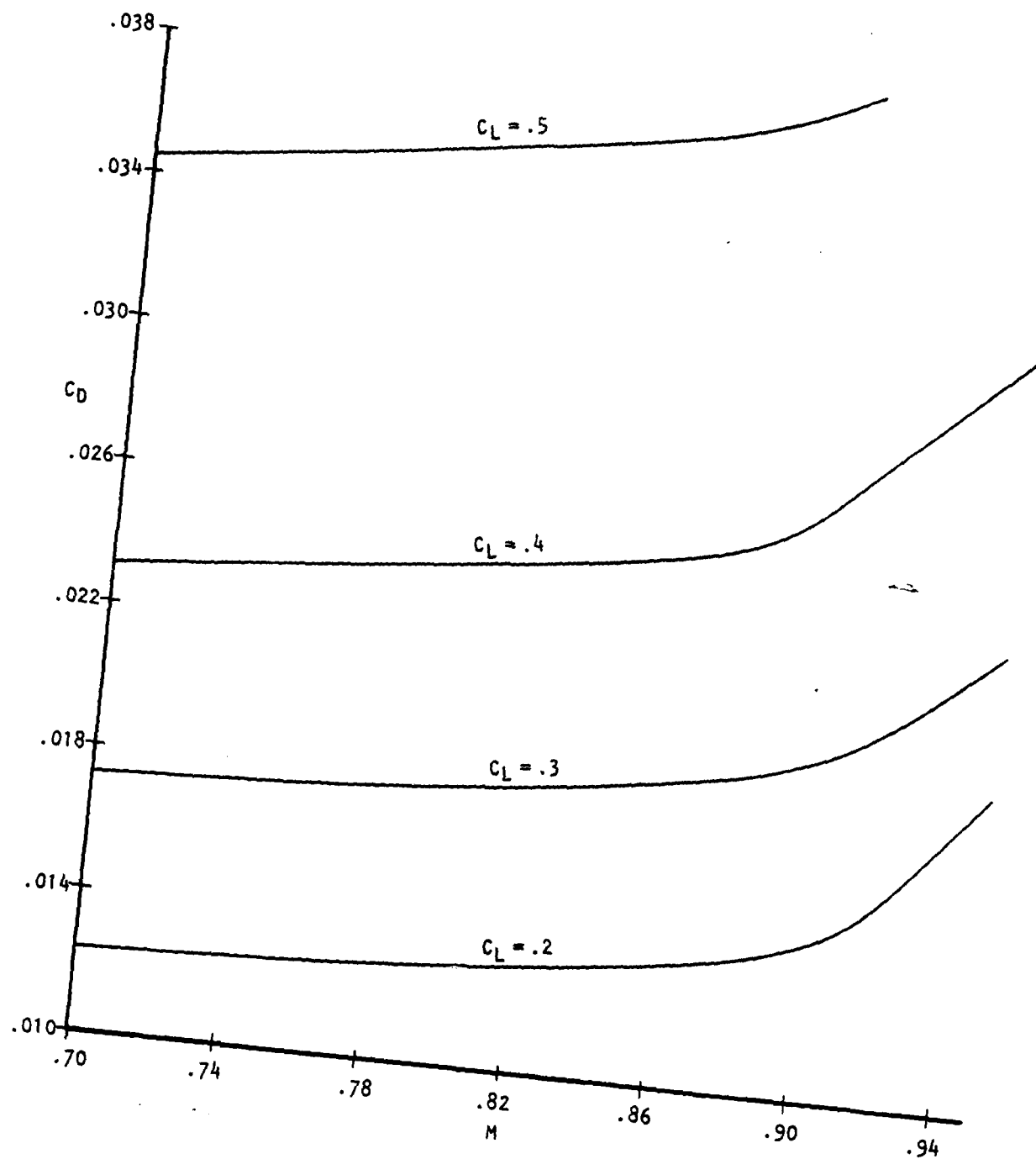


Figure 38 . - Summary of drag versus Mach number for Wing B.

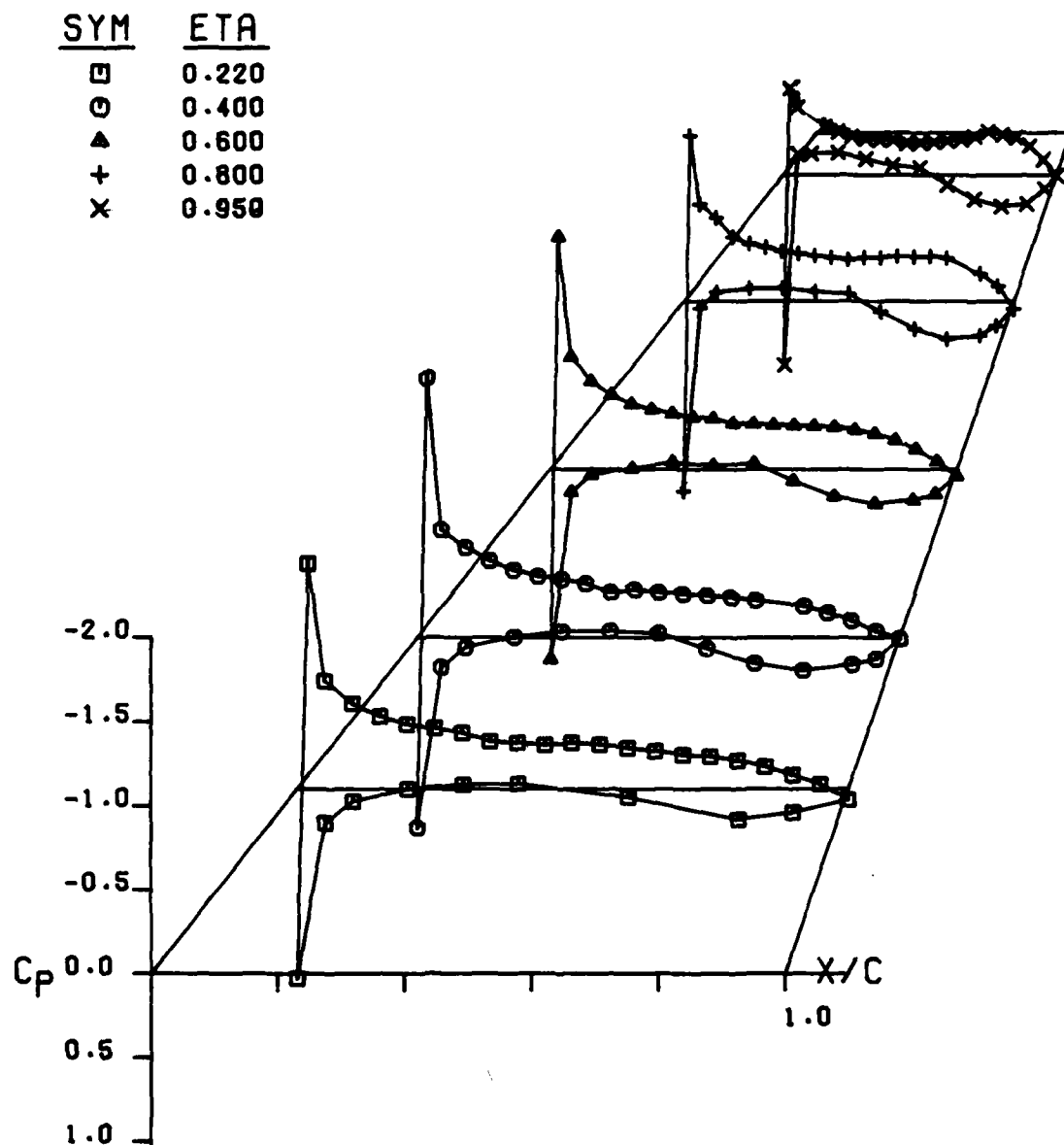


Figure 39 . - Wing B pressure distribution at  $M = .703$ ,  $\alpha = 2.979$ ,  
 $C_L = .363$ ,  $C_D = .021$ ,  $C_M = -.052$ .

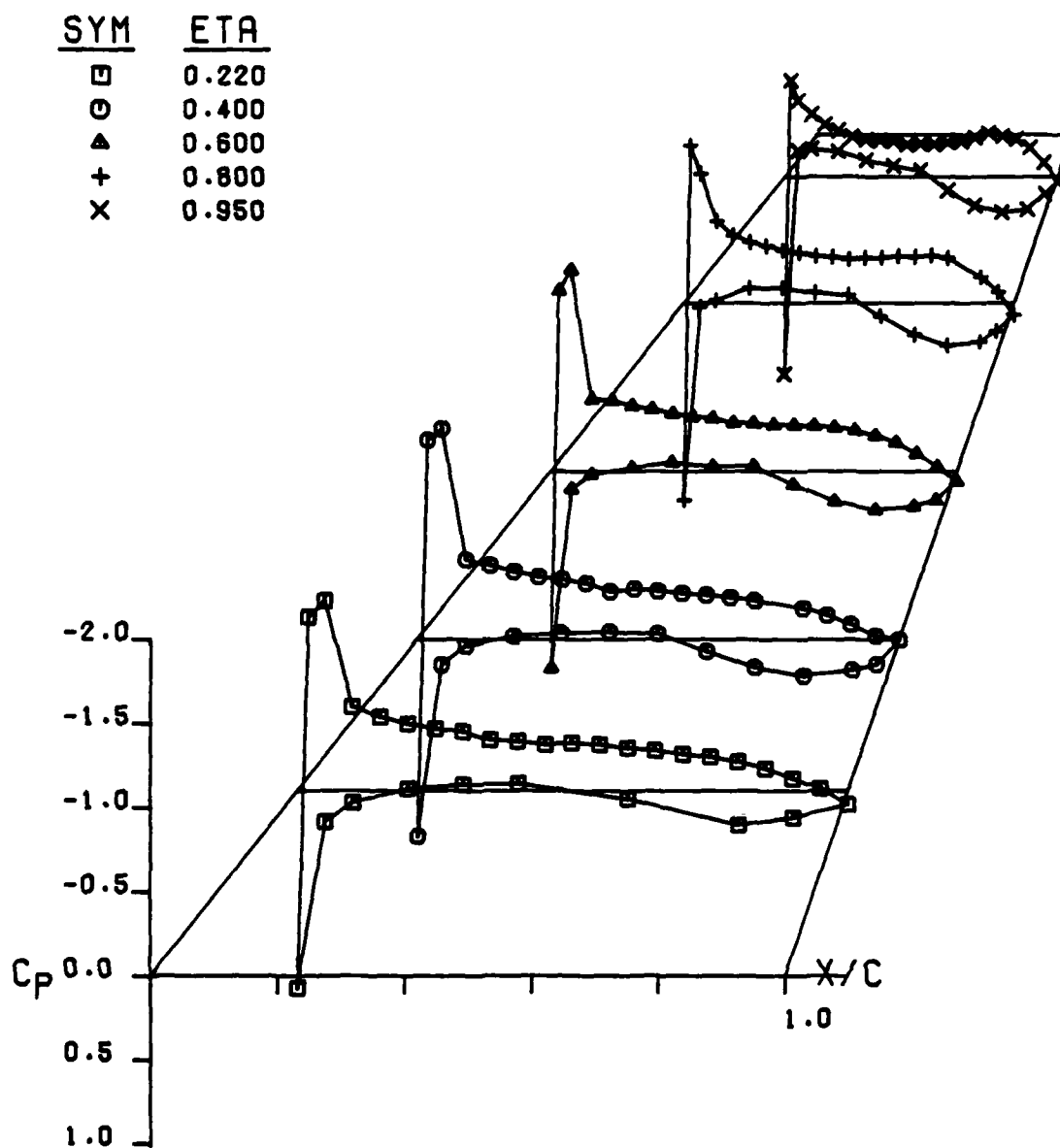


Figure 40 . - Wing B pressure distribution at  $M = .802$ ,  $\alpha = 2.974$ ,  
 $C_L = .376$ ,  $C_D = .023$ ,  $C_M = -.059$ .



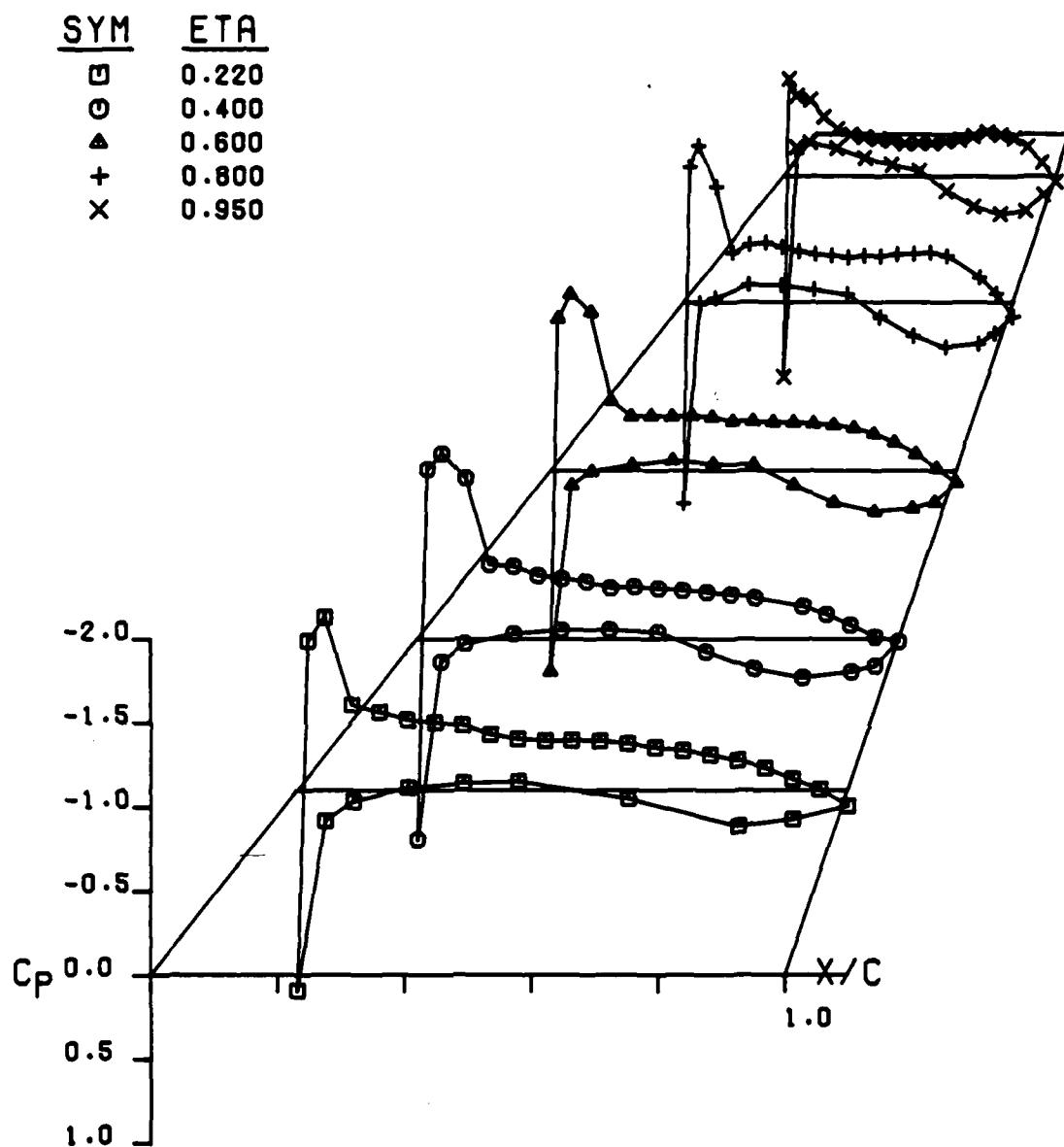


Figure 41 . - Wing B pressure distribution at  $M = .851$ ,  $\alpha = 2.950$ ,  
 $C_L = .388$ ,  $C_D = .024$ ,  $C_M = -.063$ .

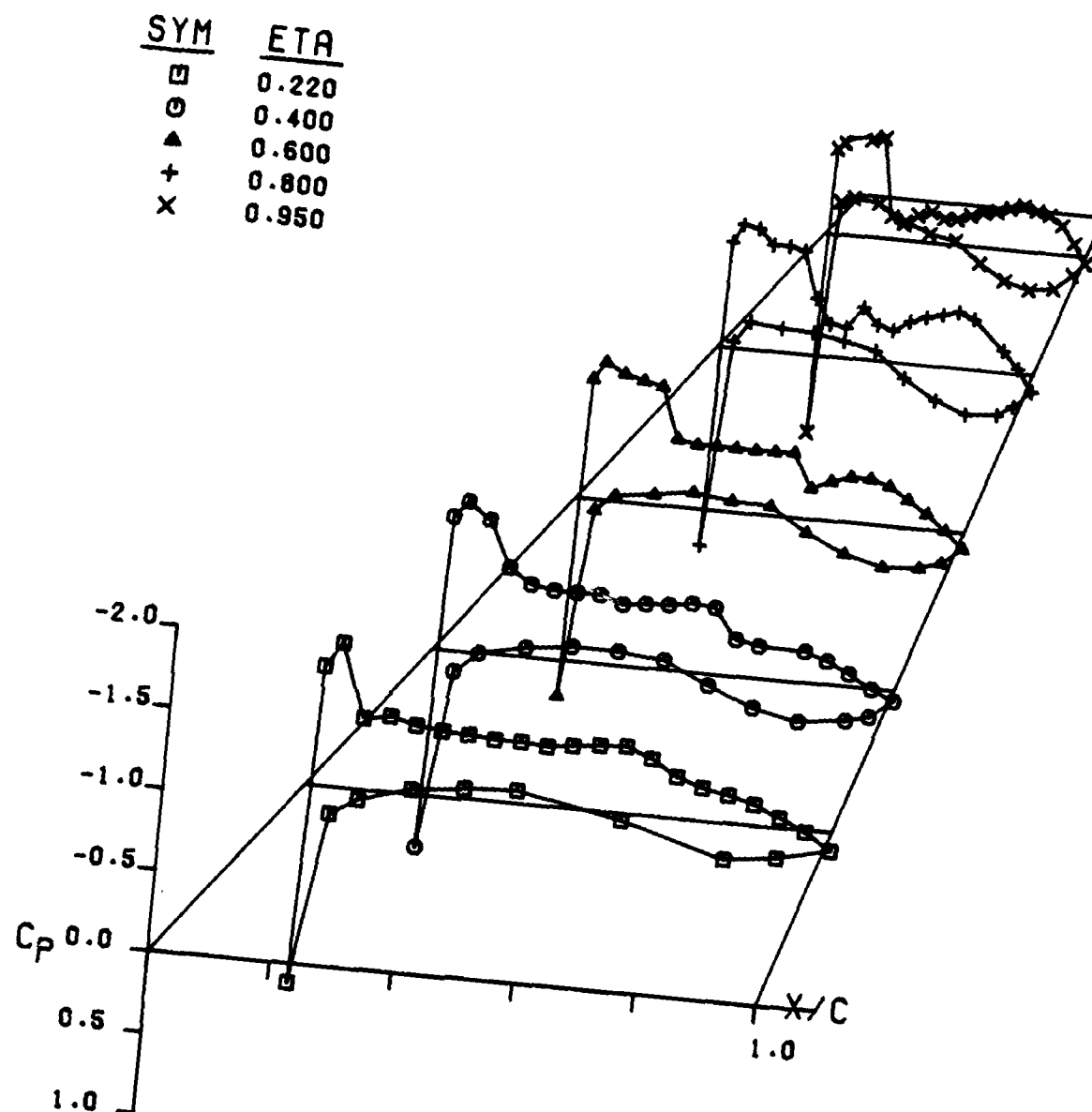


Figure 42 . - Wing B pressure distribution at  $M = .901$ ,  $\alpha = 2.946$ ,  
 $C_L = 0.402$ ,  $C_D = .027$ ,  $C_M = -.072$ .

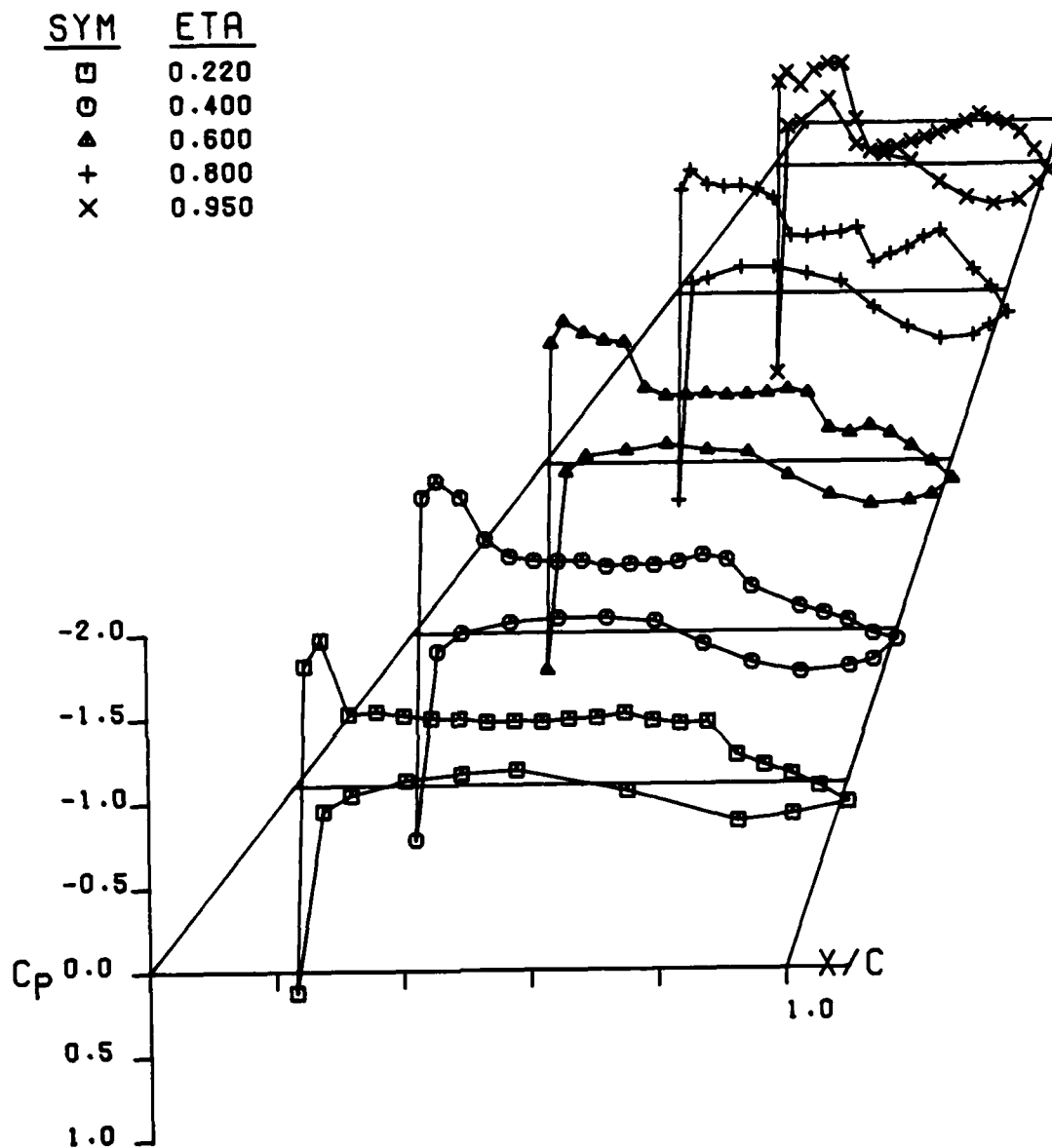


Figure 43 . - Wing B pressure distribution at  $M = .910$ ,  $\alpha = 2.942$ ,  
 $C_L = .417$ ,  $C_D = .029$ ,  $C_M = -.084$ .

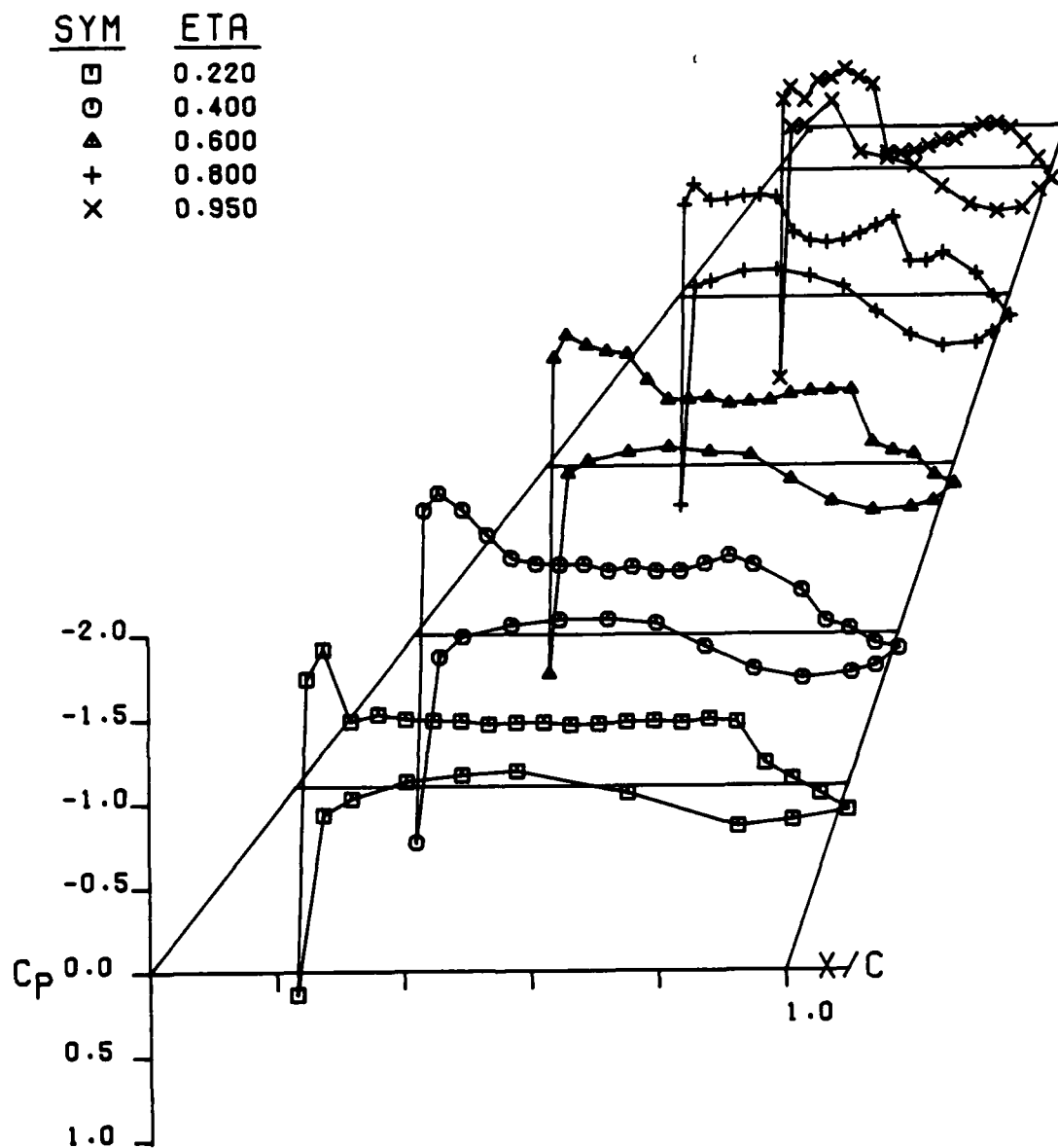


Figure 44 . - Wing B pressure distribution at  $M = .928$ ,  $\alpha = 2.957$ ,  
 $C_L = .414$ ,  $C_D = .030$ ,  $C_M = -.092$ .

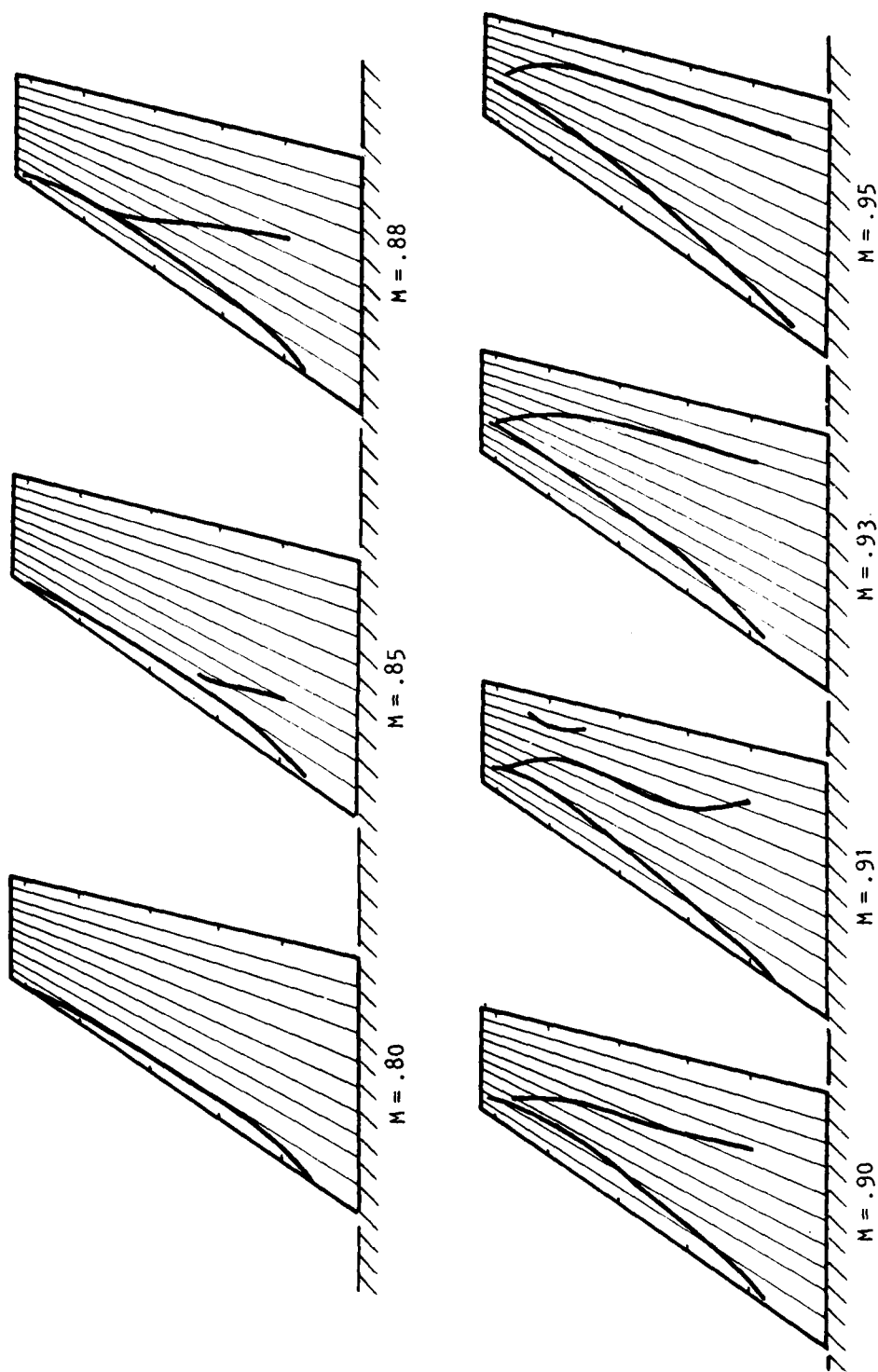


Figure 45 . - Wing B shock pattern at various Mach numbers at an angle of attack of  $3^\circ$ .

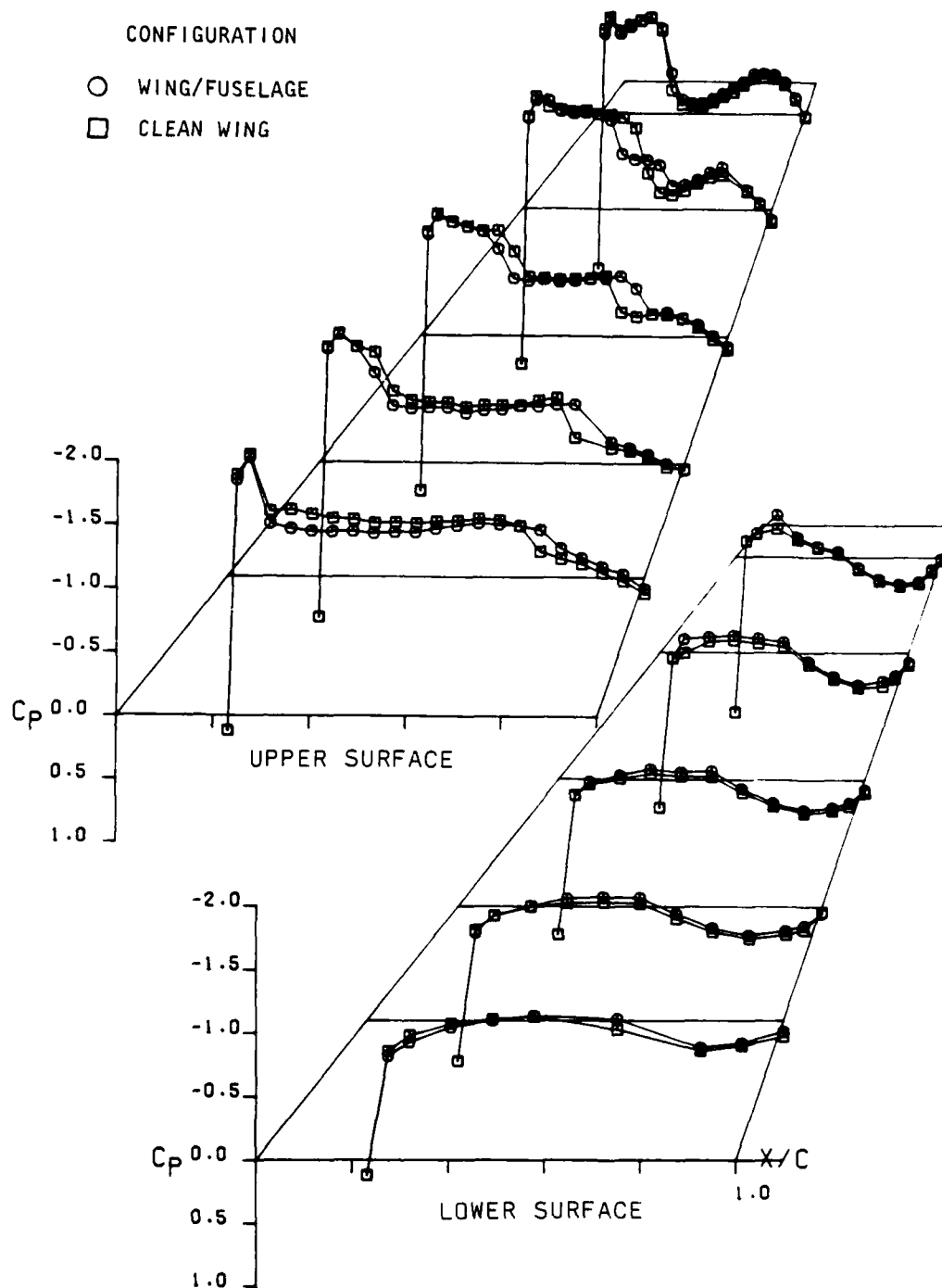


Figure 46 . - Comparison of Wing B alone pressure distribution with high-wing/fuselage data at  $M = .9$ ,  $\alpha = 4^\circ$ .

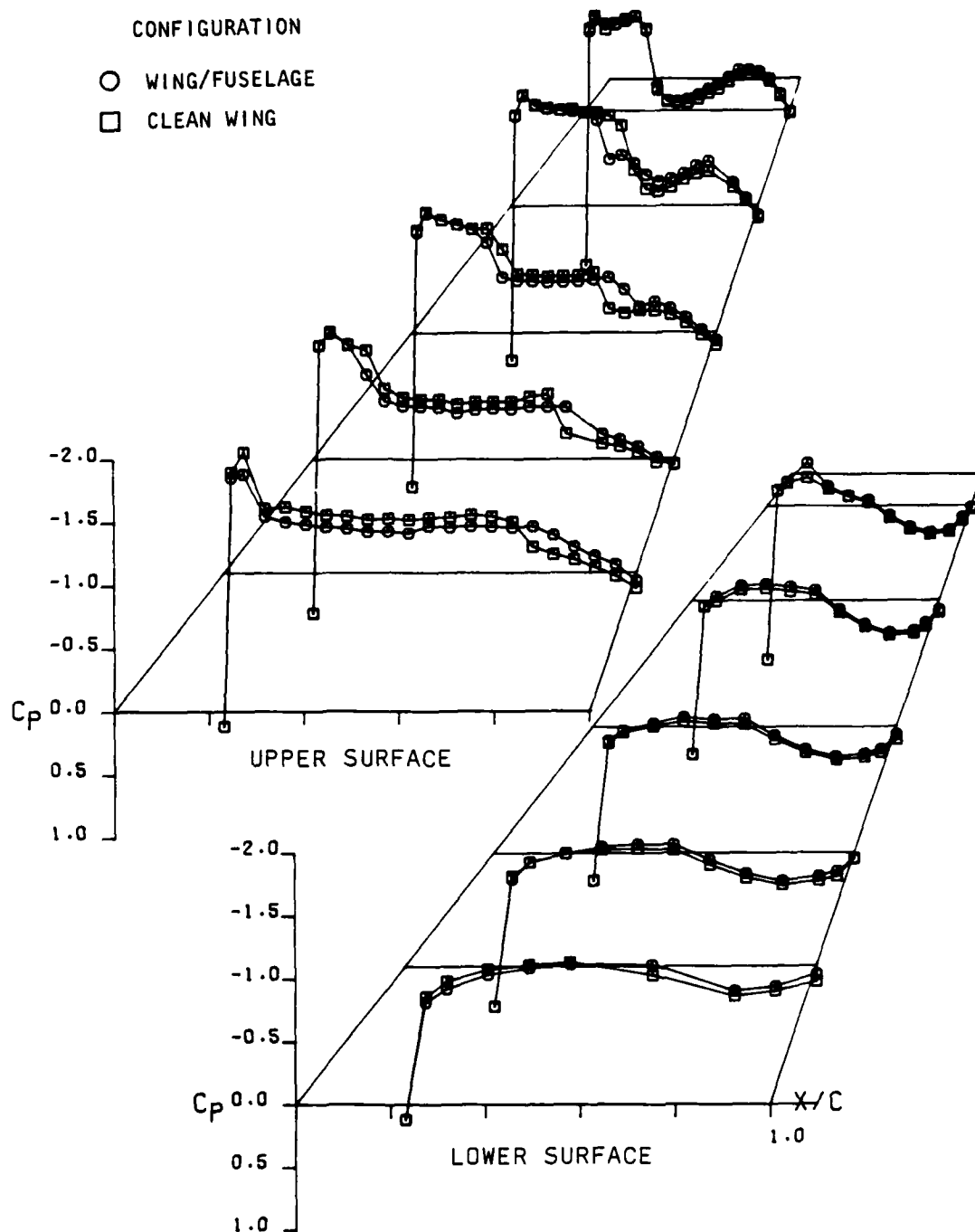


Figure 47 . - Comparison of Wing B alone pressure distribution with mid-wing/fuselage data at  $M = .90$ ,  $\alpha = 4^\circ$ .

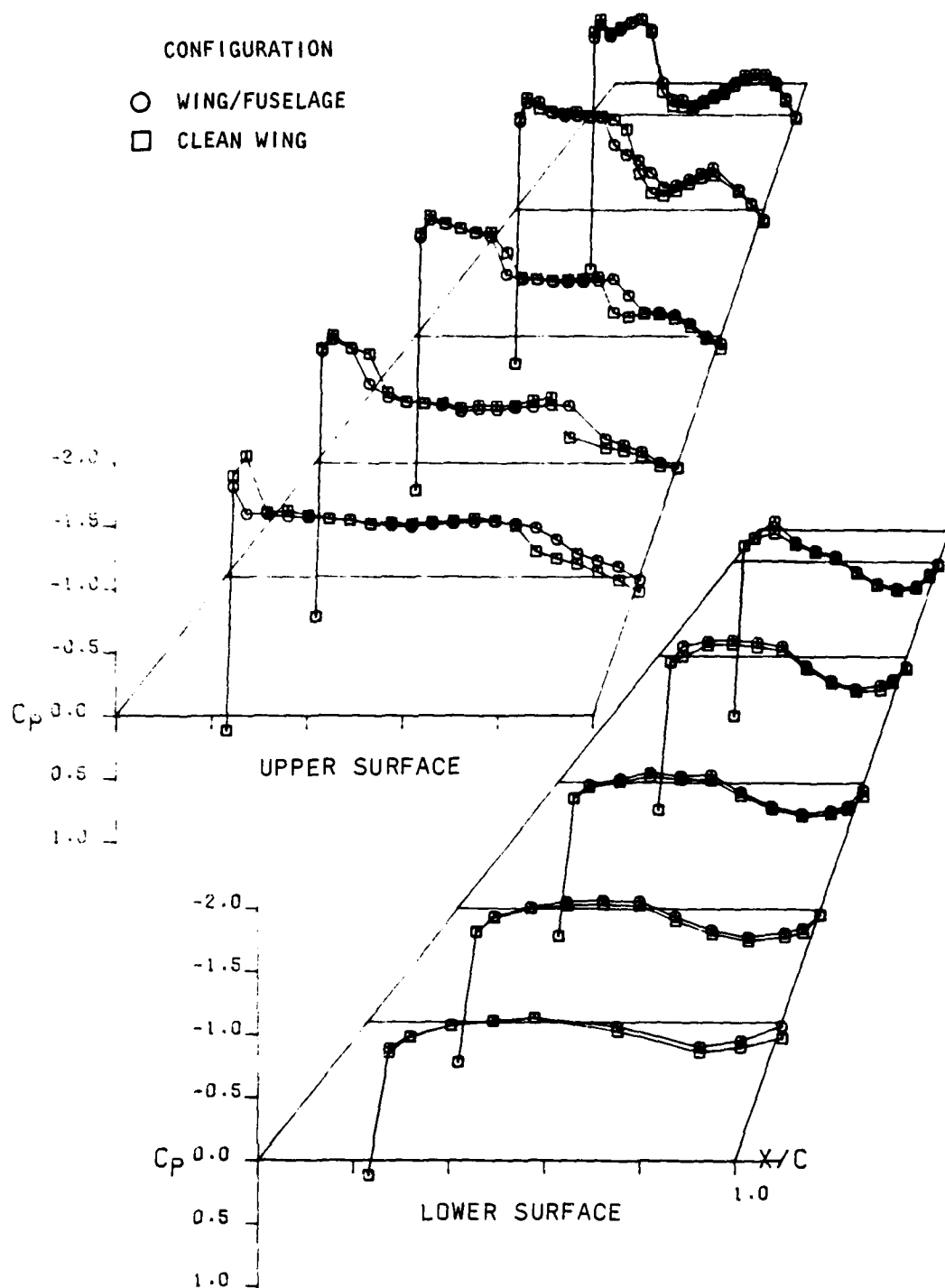


Figure 48 . - Comparison of Wing B alone pressure distribution with low-wing/fuselage data at  $M = .90$ ,  $\alpha = 4^\circ$ .



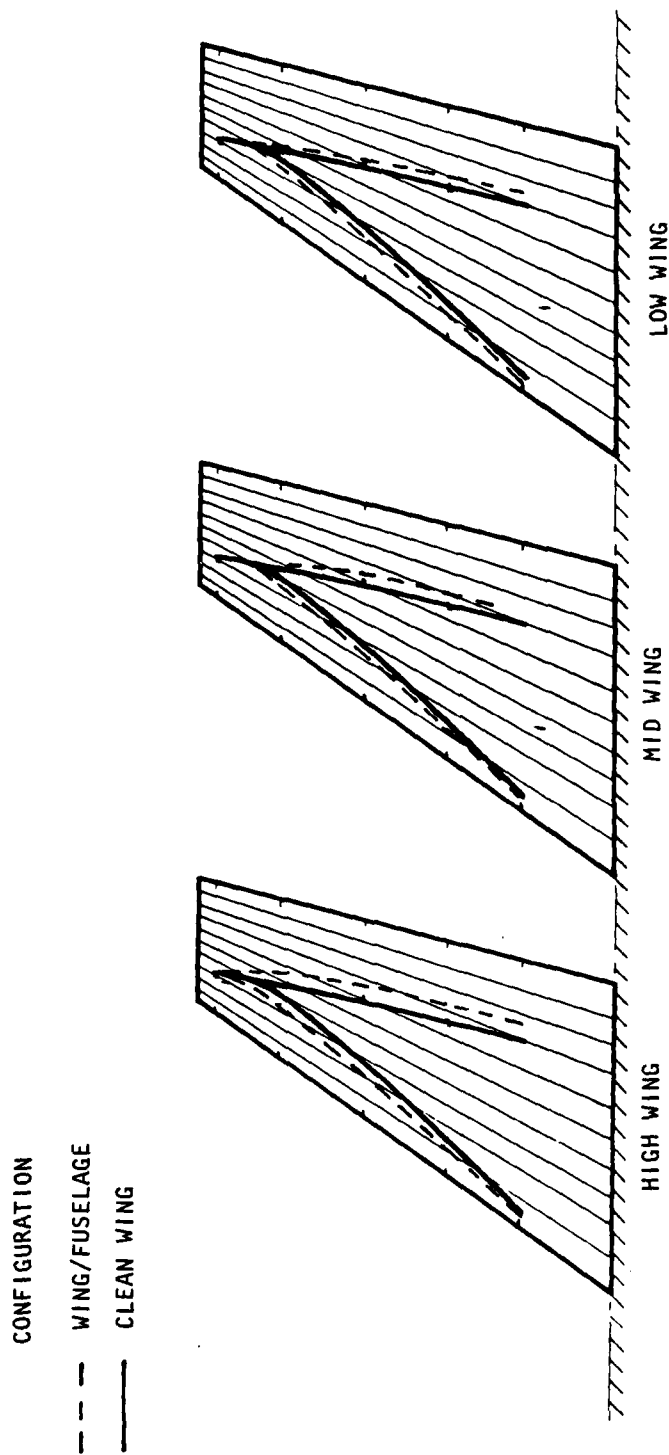


Figure 49 . - Comparison of the Wing B alone shock pattern with various wing/fuselage configurations at  $M = .90$ , and  $\alpha = 4^\circ$ .

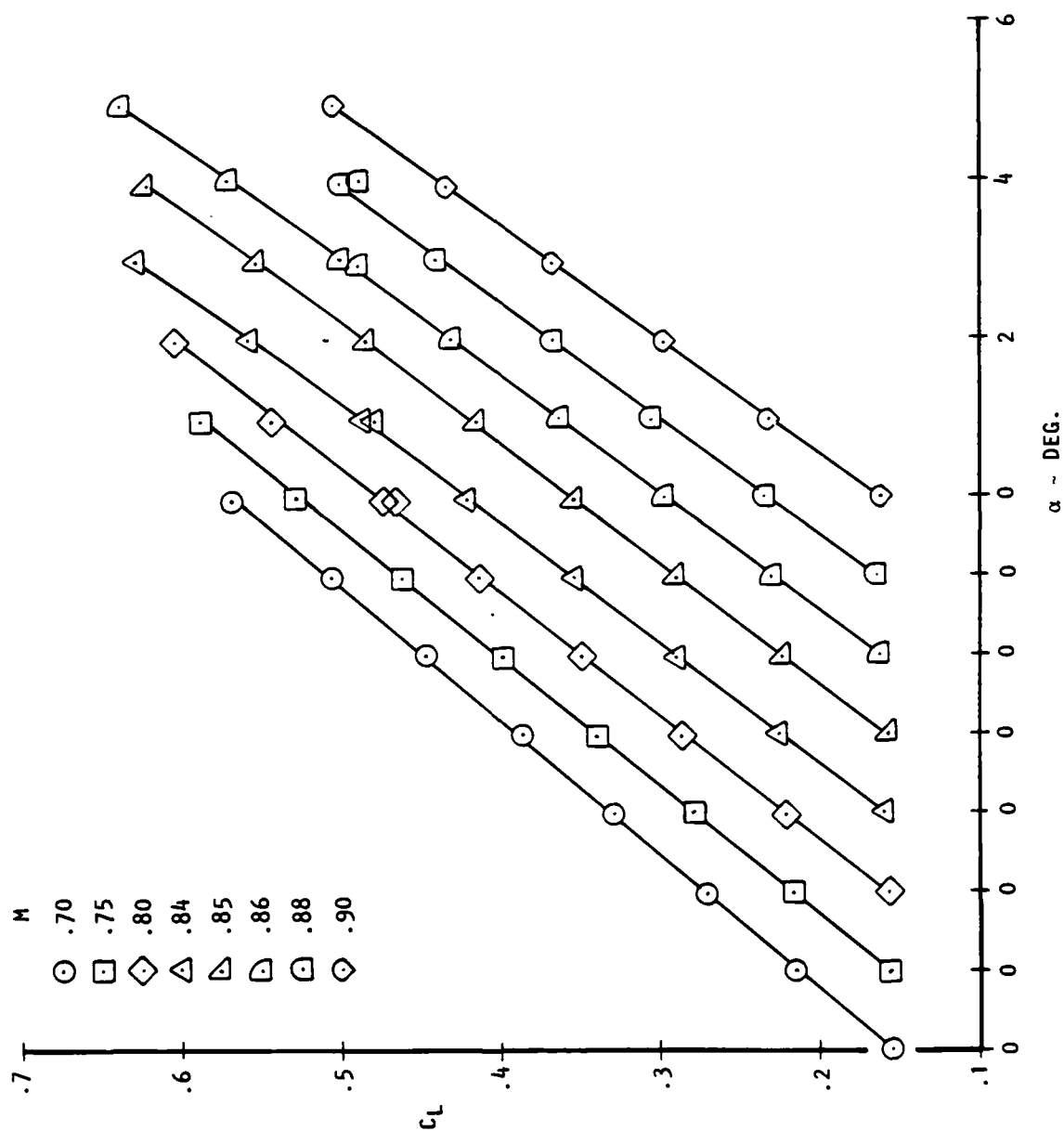


Figure 50 . - Summary of lift data for Wing C.

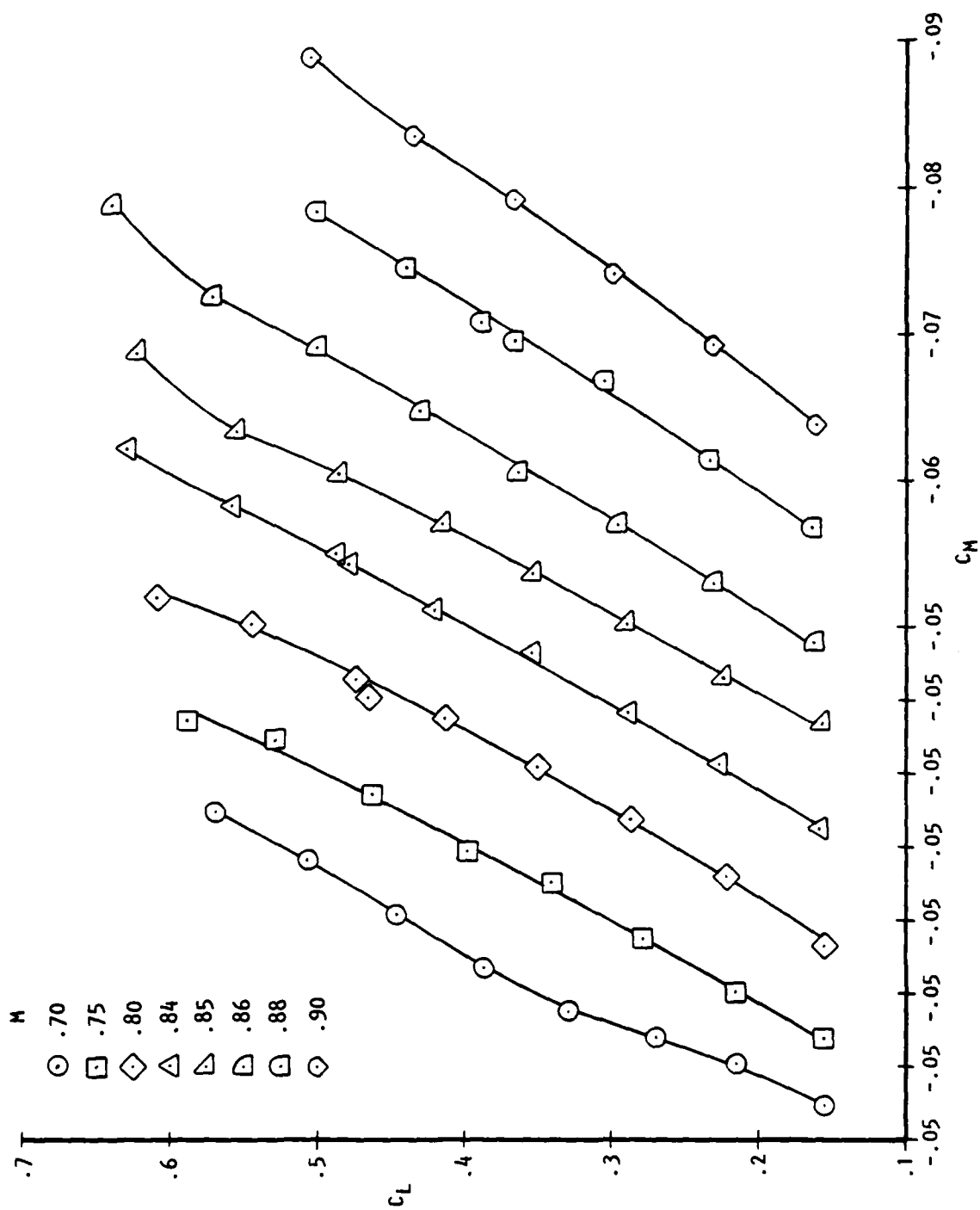


Figure 51. - Summary of pitching moment data for Wing C.

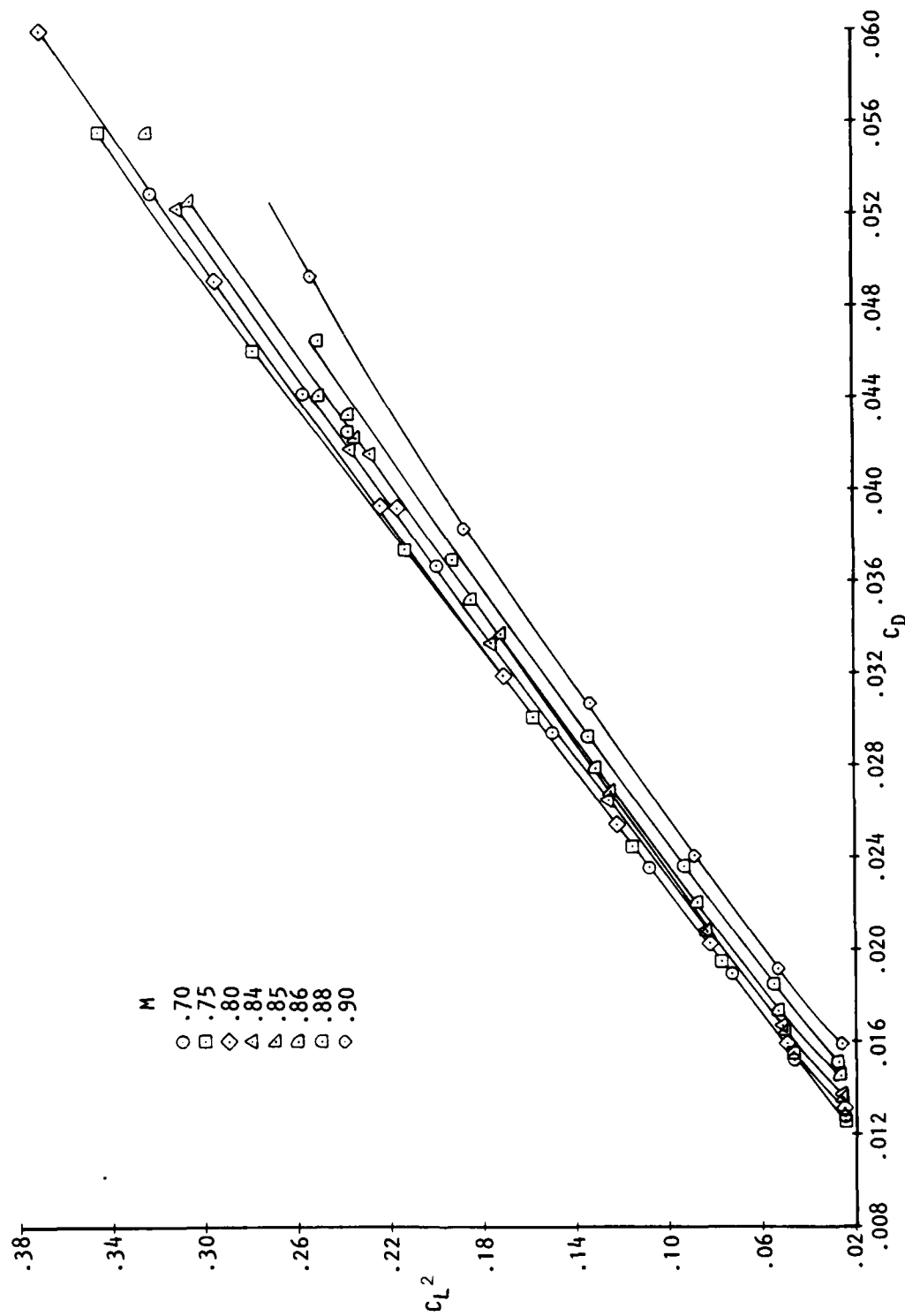


Figure 52. - Summary of drag data for Wing C.

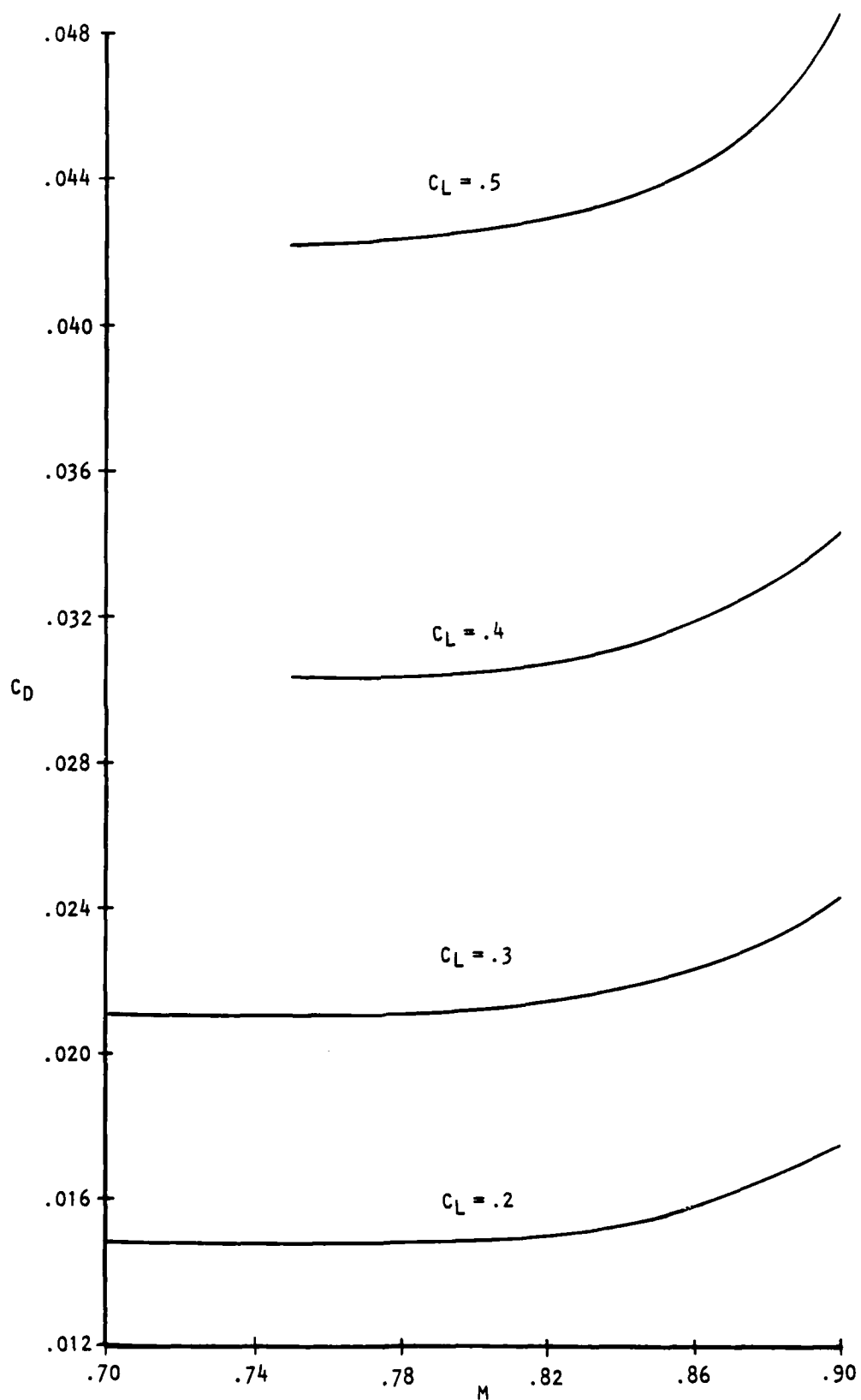


Figure 53 . - Summary of drag versus Mach number for Wing C.

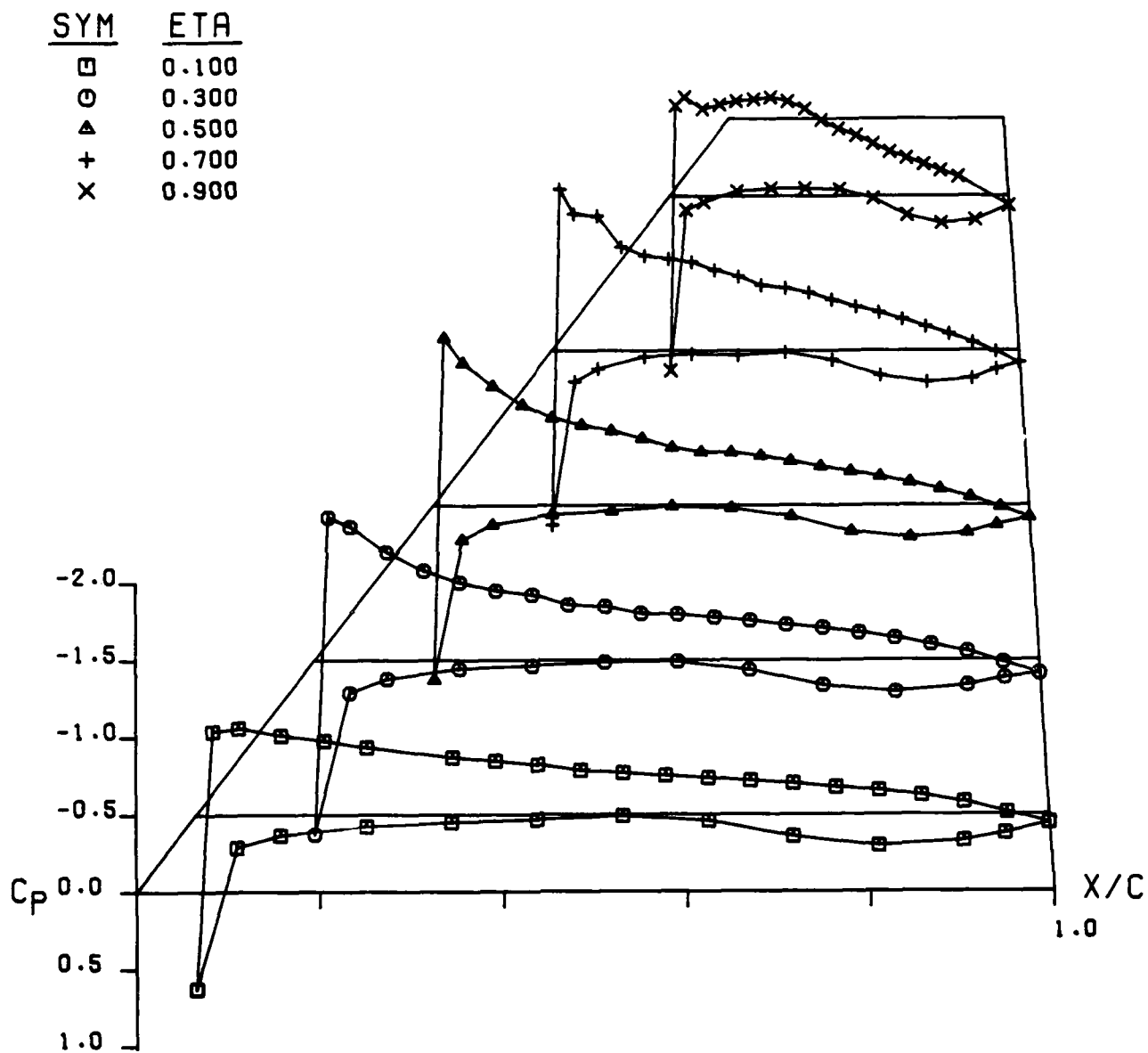


Figure 54 . - Wing C pressure distribution at  $M=0.701$ ,  $\alpha=4.949$ ,  
 $C_L=0.447$ ,  $C_D=0.037$ ,  $C_M=-0.065$ .

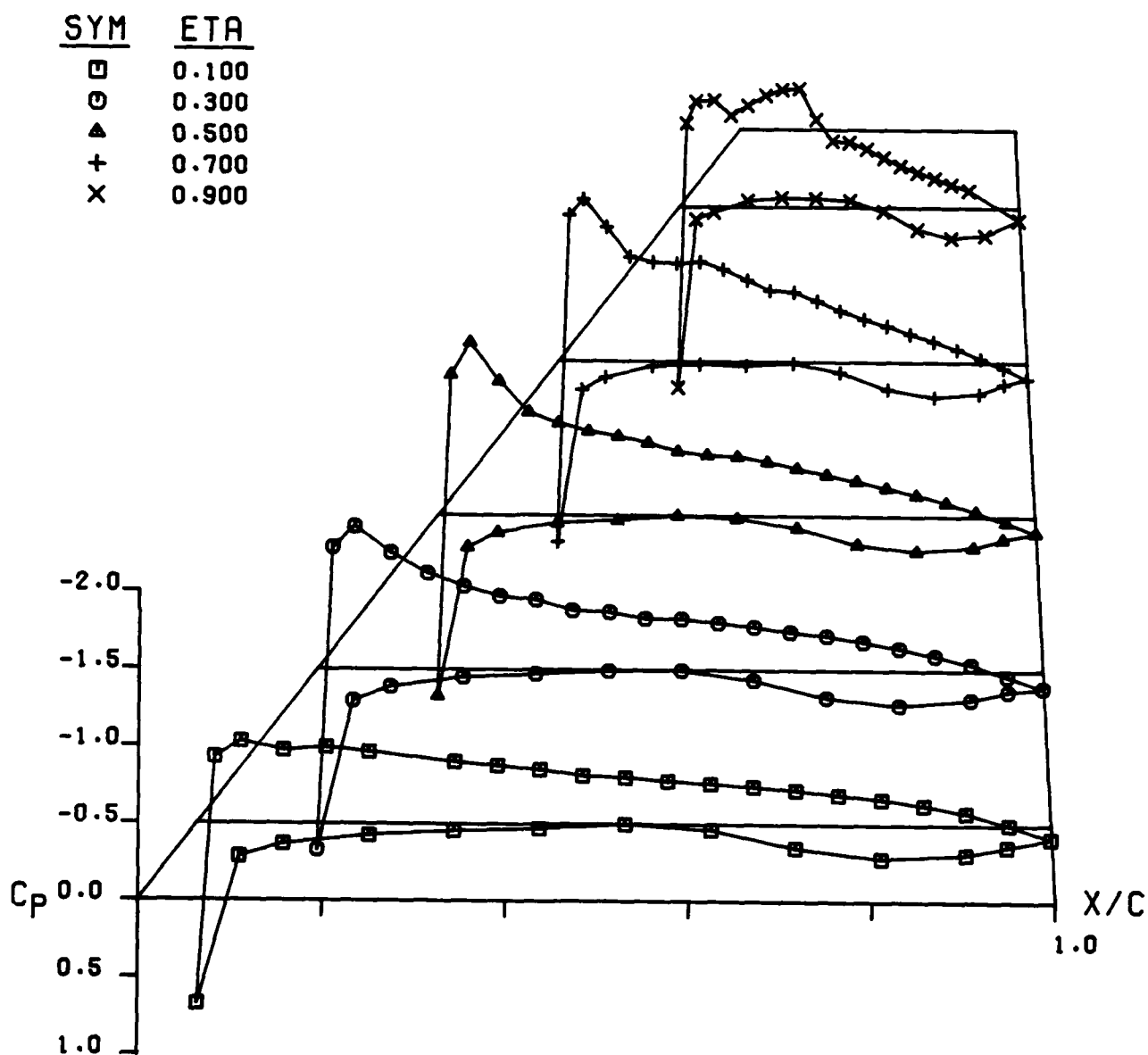


Figure 55 . - Wing C pressure distribution at  $M=0.802$ ,  $\alpha=4.924$ ,  
 $C_L=0.465$ ,  $C_D=0.039$ ,  $C_M=-0.070$ .

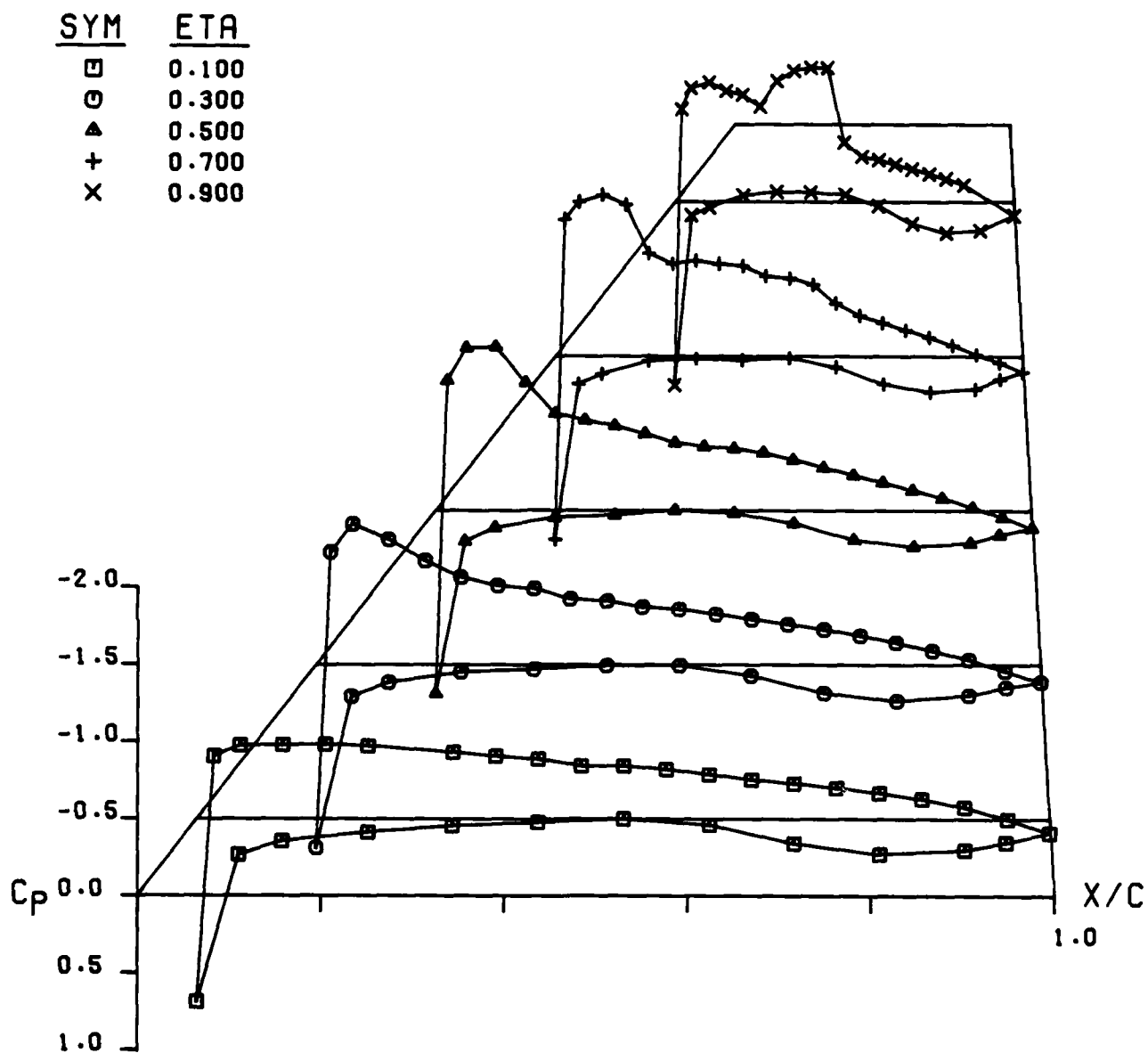


Figure 56 . - Wing C pressure distribution at  $M=0.837$ ,  $\alpha=4.960$ ,  
 $C_L=0.487$ ,  $C_D=0.042$ ,  $C_M=-0.075$ .



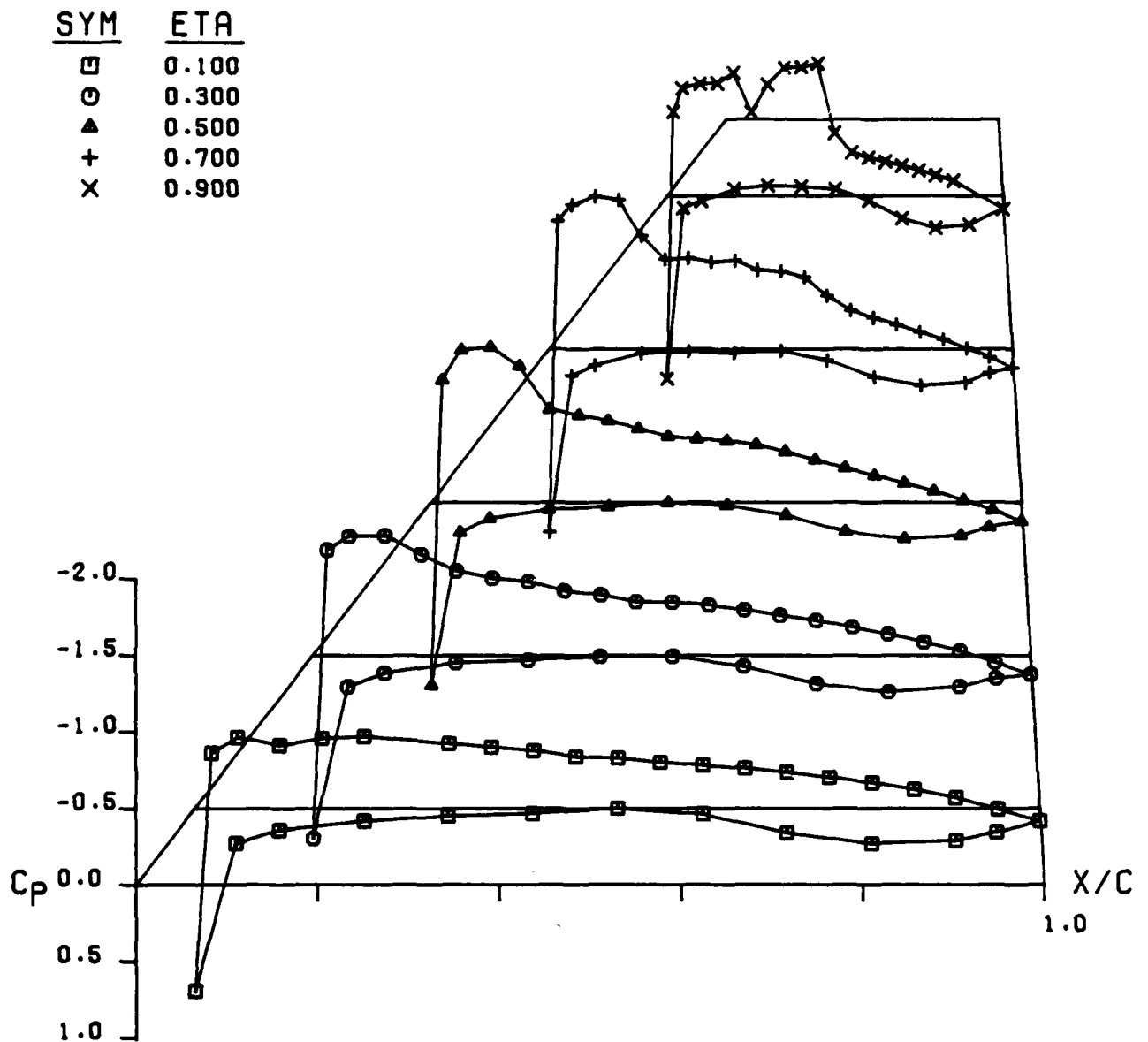


Figure 57 . - Wing C pressure distribution at  $M = 0.851$ ,  $\alpha = 4.900$ ,  
 $C_L = 0.484$ ,  $C_D = 0.042$ ,  $C_M = -0.075$ .

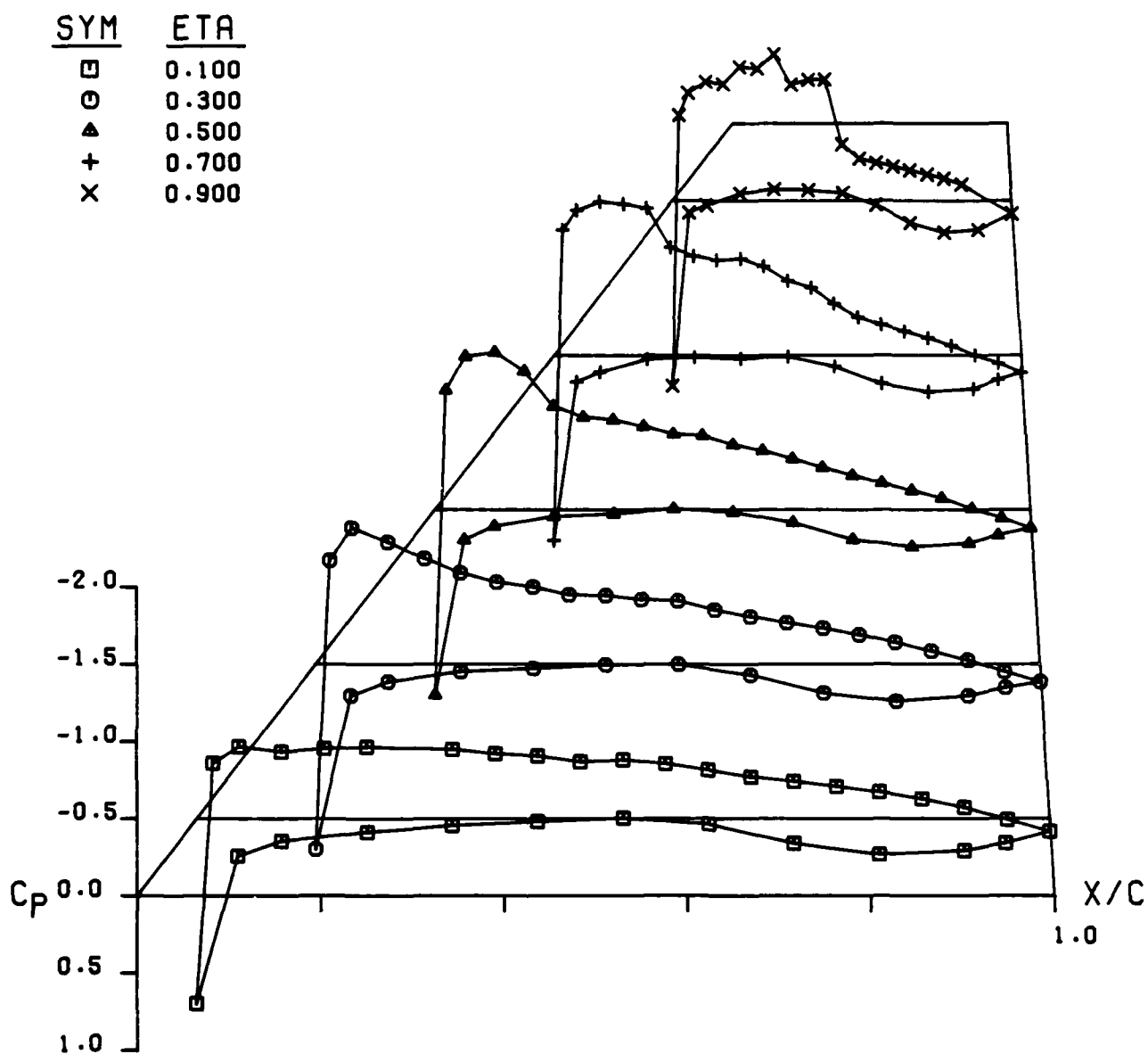


Figure 58 . - Wing C pressure distribution at  $M=0.860$ ,  $\alpha=4.968$ ,  
 $C_L=0.500$ ,  $C_D=0.044$ ,  $C_M=-0.079$ .

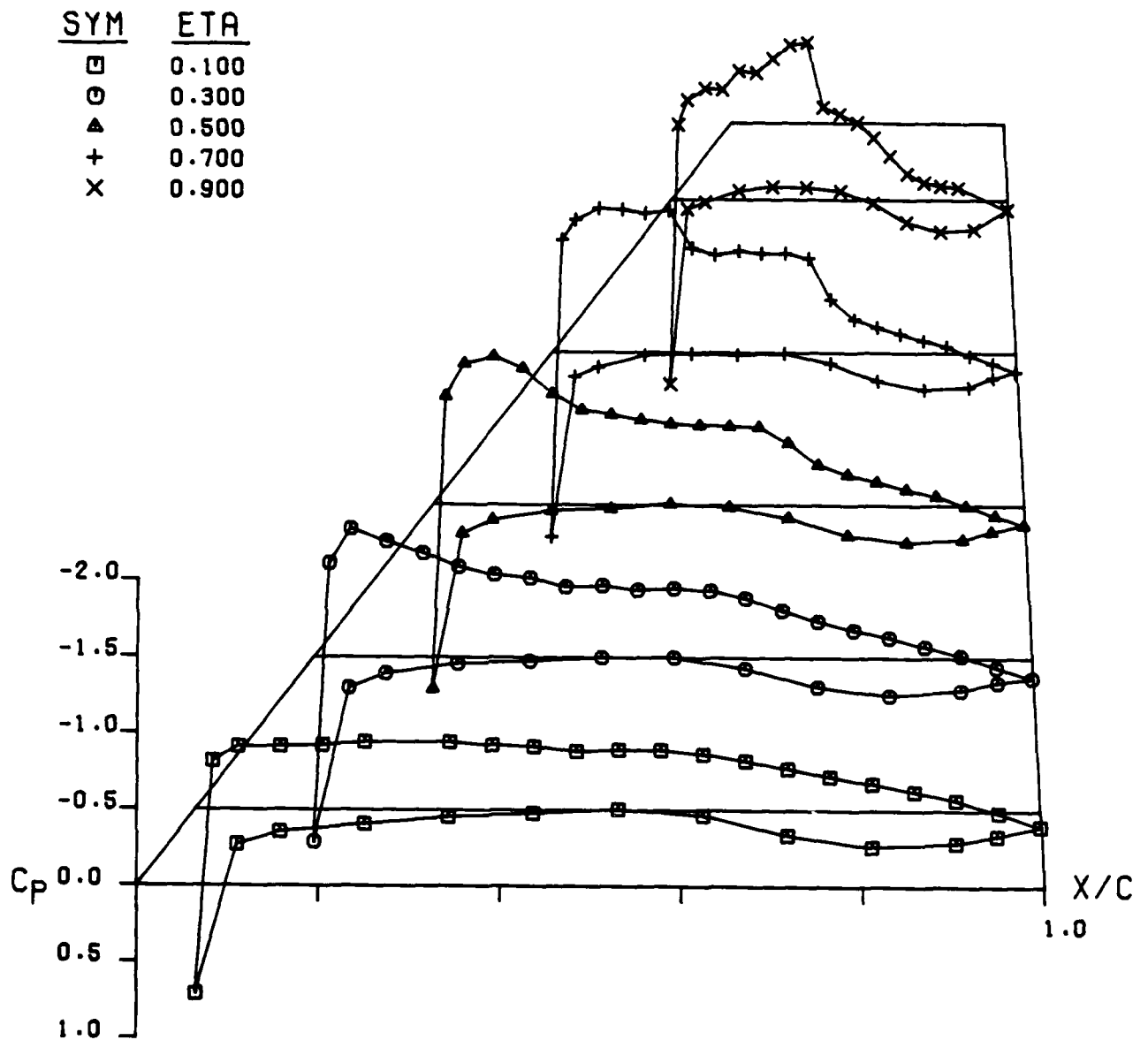


Figure 59 . - Wing C pressure distribution at  $M=0.882$ ,  $\text{Alpha}=4.935$ ,  
 $C_L=0.512$ ,  $C_D=0.048$ ,  $C_M=-0.086$ .

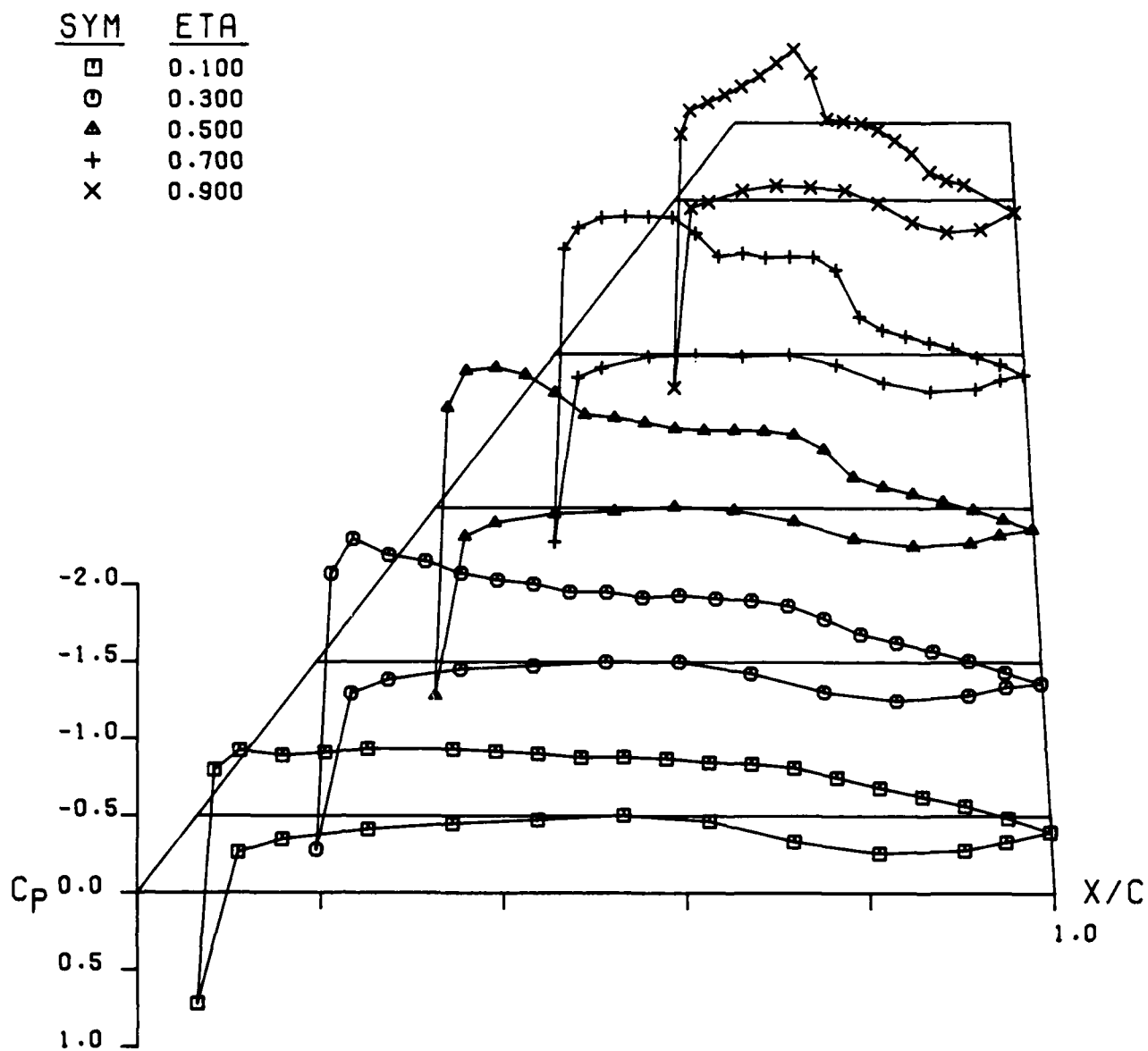


Figure 60 . - Wing C pressure distribution at  $M=0.900$ ,  $\alpha=4.914$ ,  
 $C_L=0.504$ ,  $C_D=0.049$ ,  $C_M=-0.089$ .

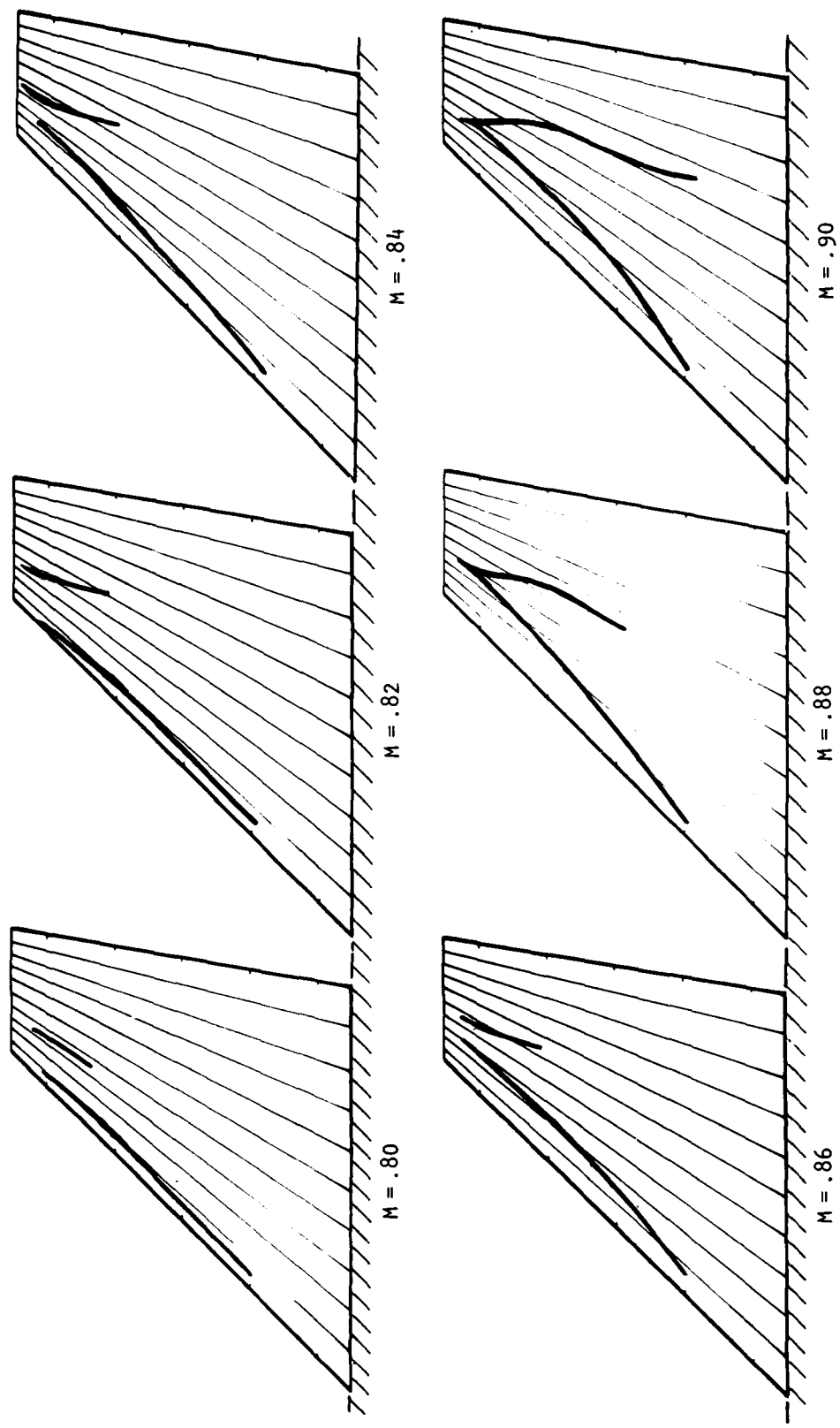


Figure 61. - Wing C shock pattern at various Mach numbers at an angle of attack of  $5^\circ$ .

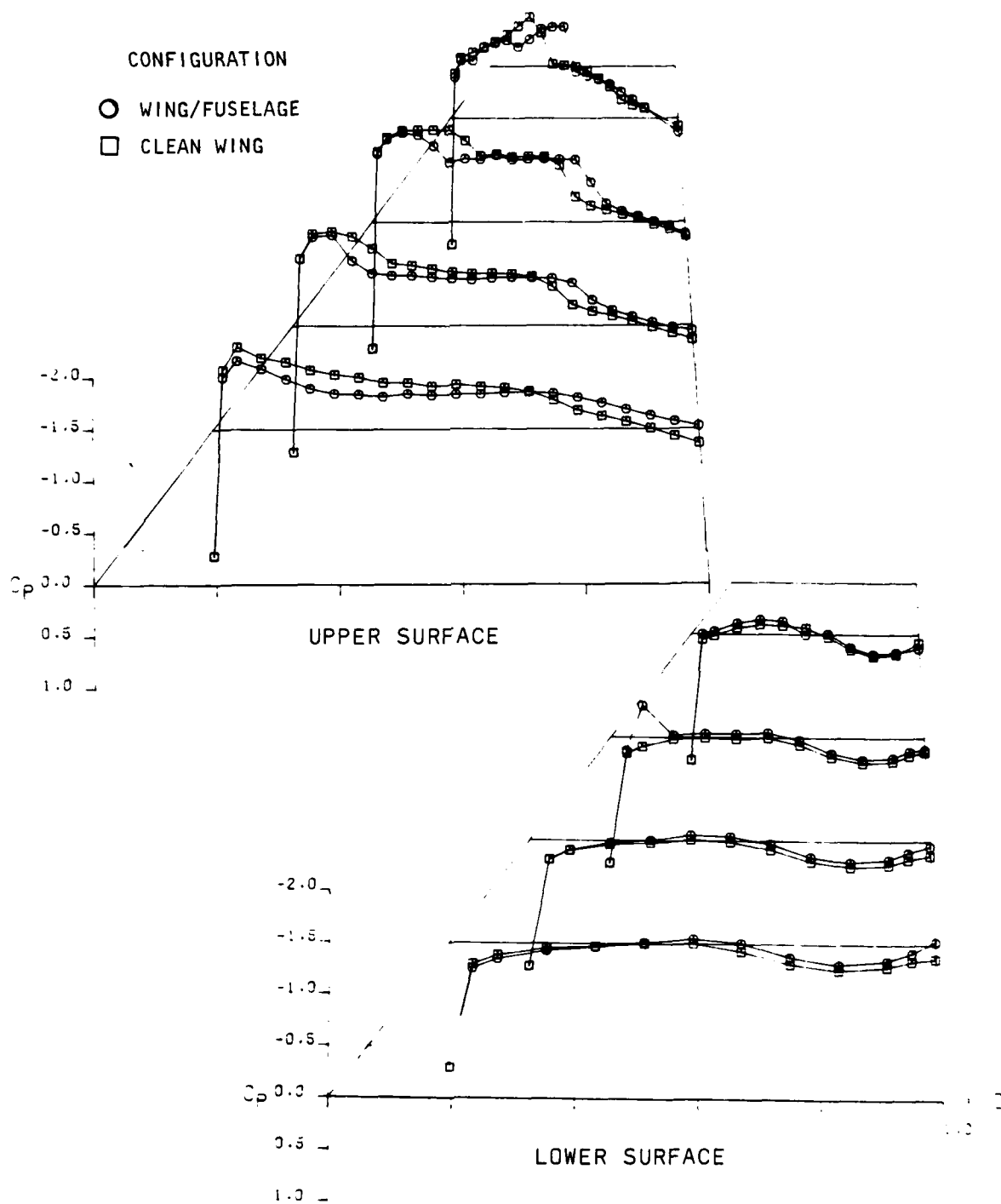


Figure 62. - Comparison of Wing C alone pressure distribution with high-wing/fuselage data at  $M = .90$ ,  $\alpha = 5^\circ$ .

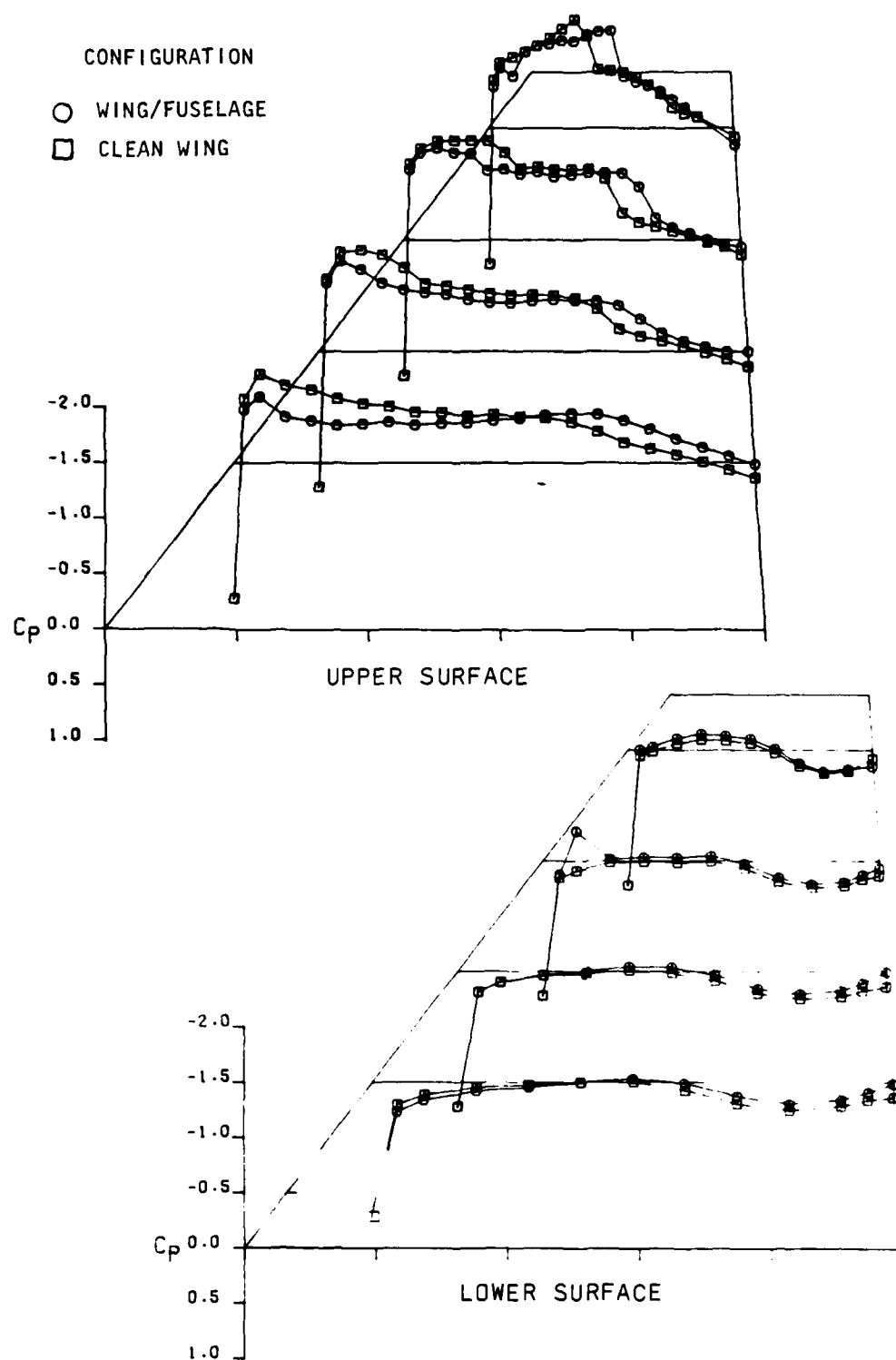


Figure 63. - Comparison of Wing C pressure distribution with mid-wing/fuselage data at  $M = .90$ ,  $\alpha = .5^\circ$ .

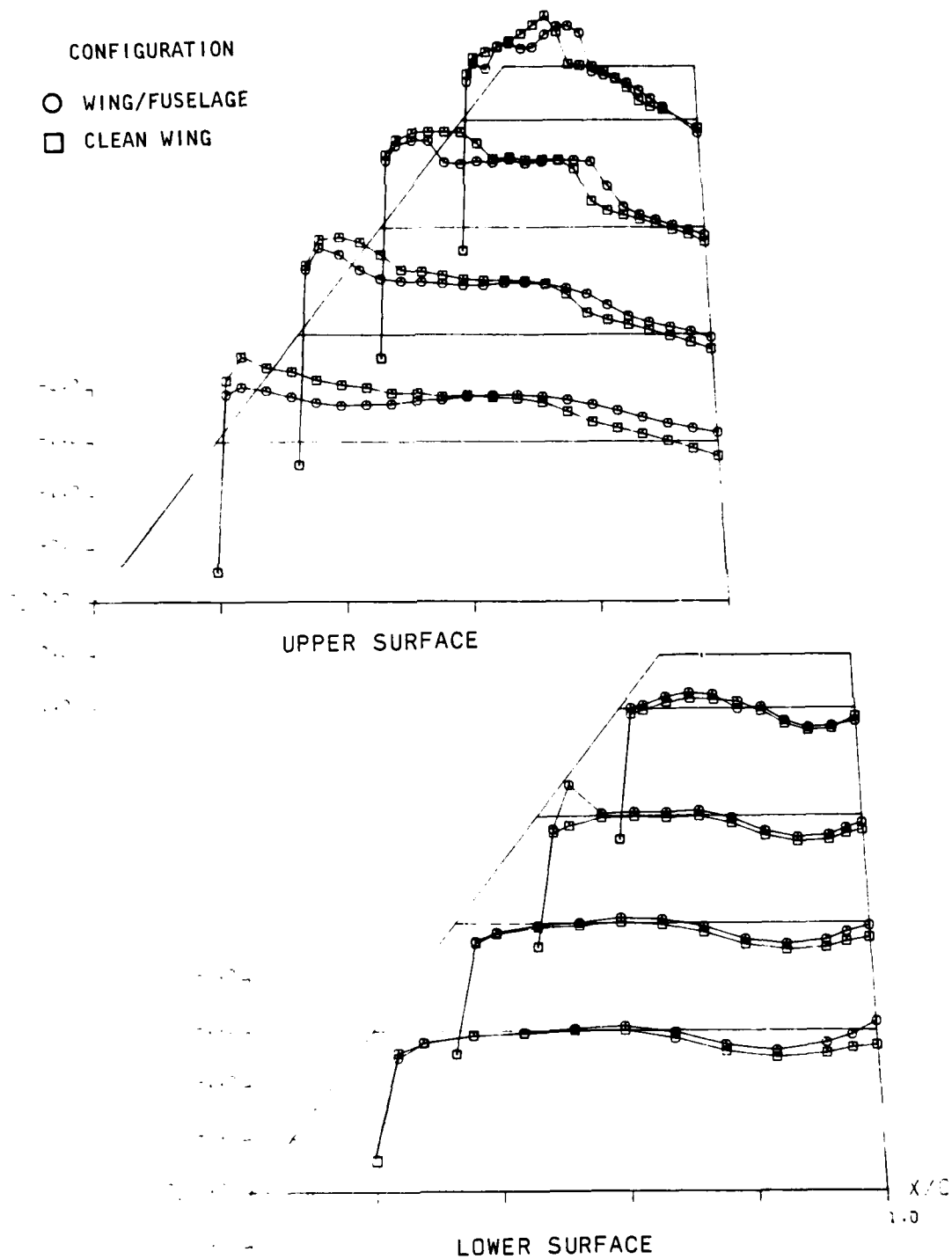


Figure 64 . - Comparison of Wing C alone pressure distribution with low-wing/fuselage data at  $M = .90$ ,  $\alpha = 5^\circ$ .



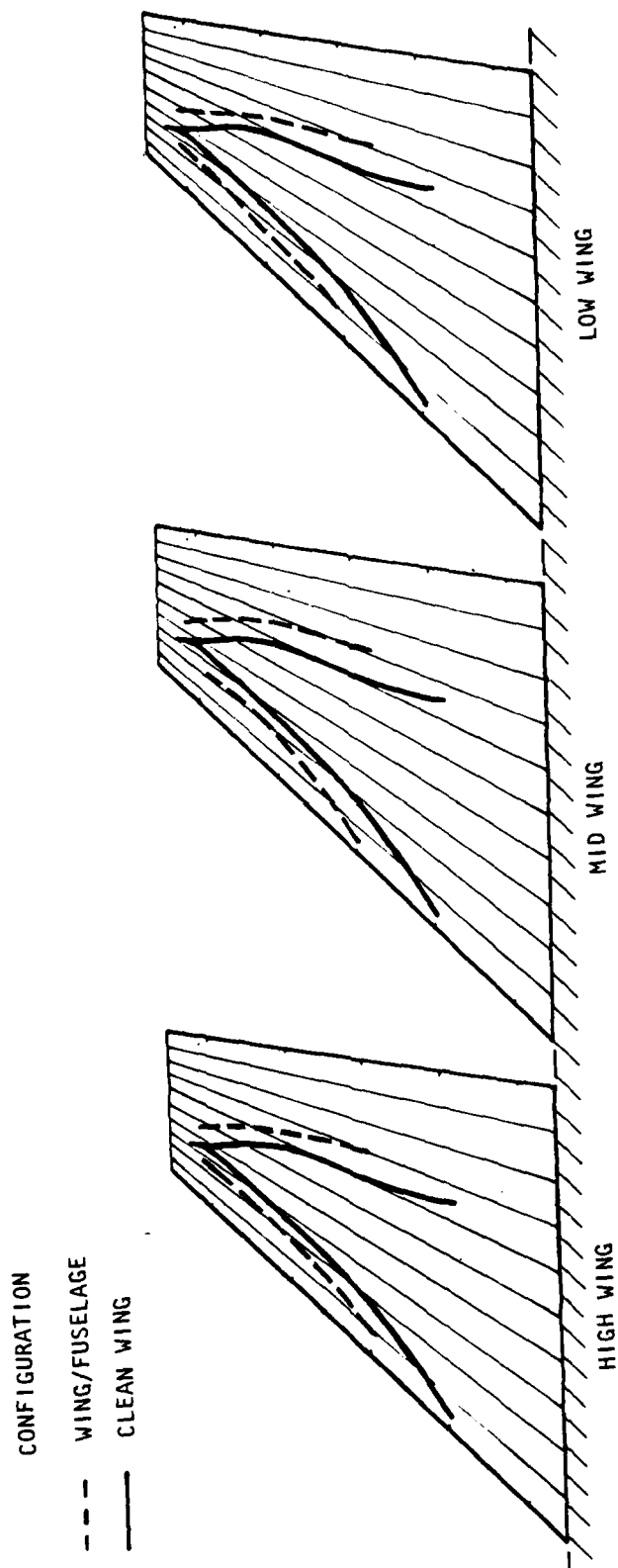
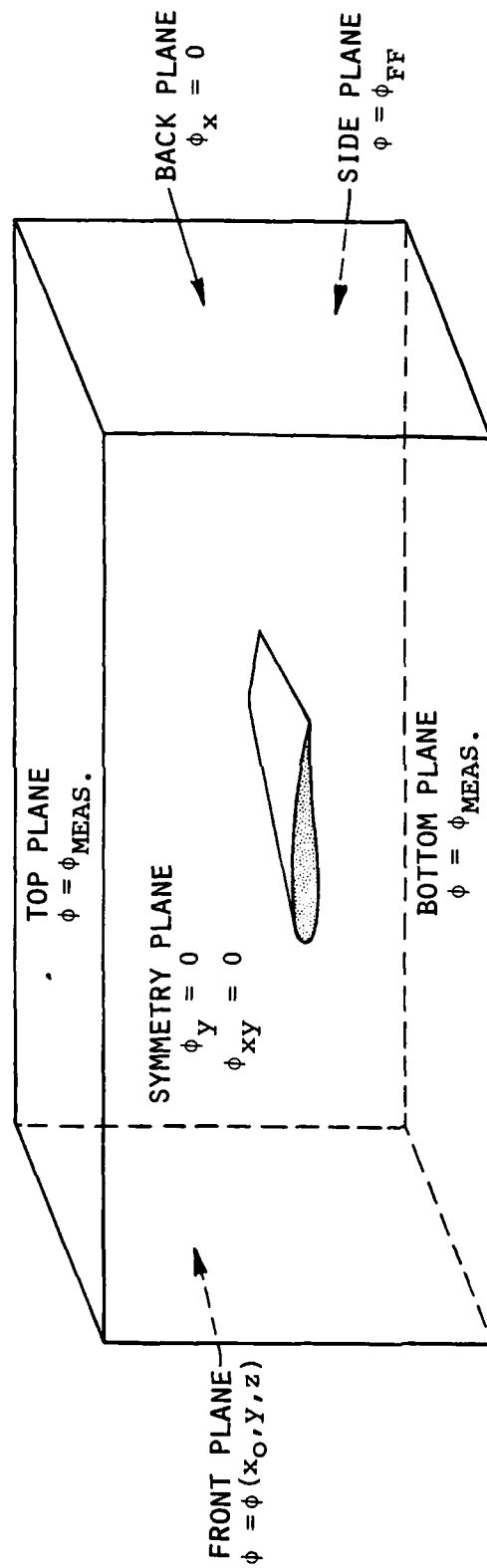


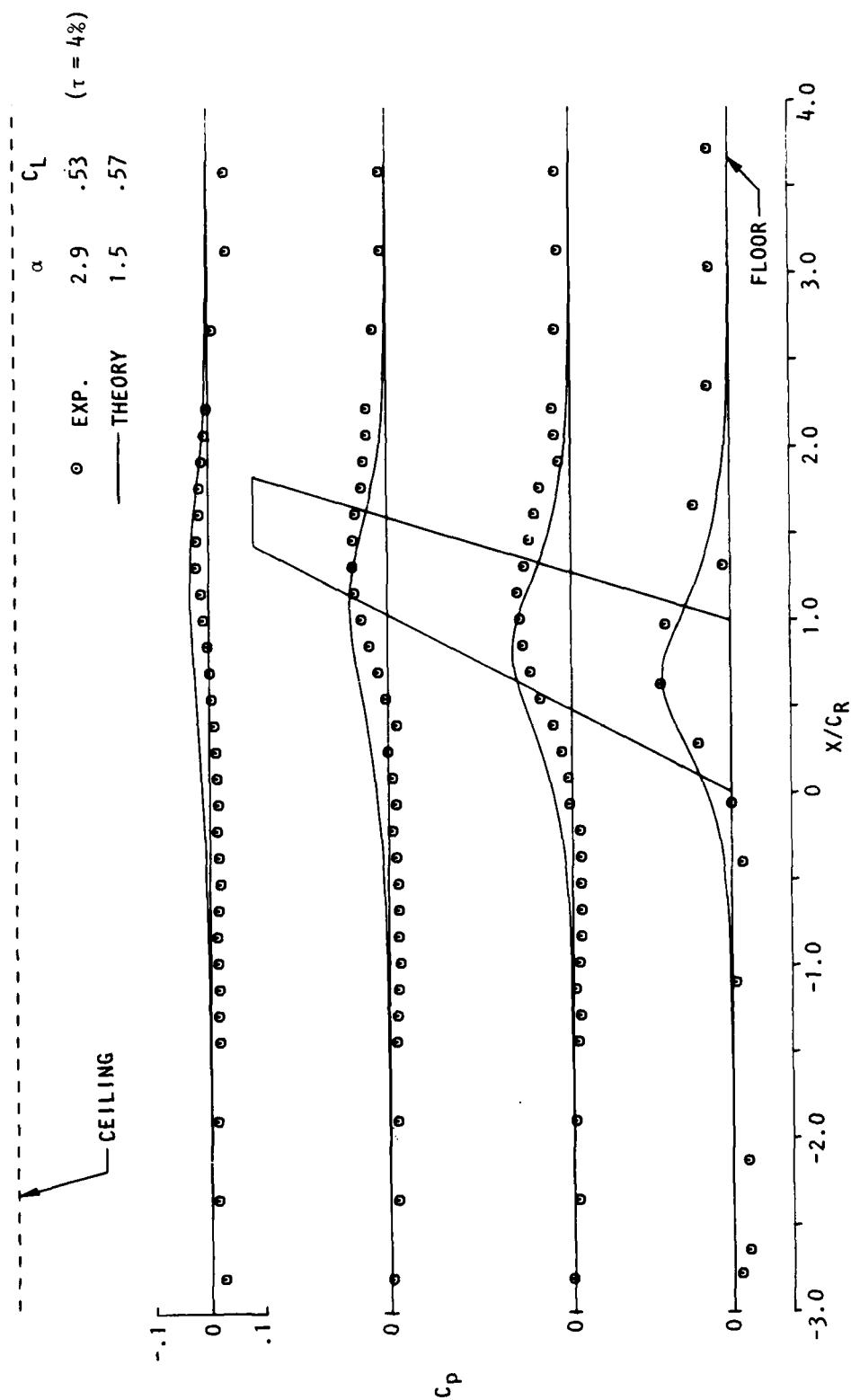
Figure 65. - Comparison of Wing C alone shock pattern with various wing/fuselage configurations at  $M = .90$ ,  $\alpha = 5^\circ$ .



$\phi_{FF} = \text{FREE-AIR FAR-FIELD POTENTIAL}$

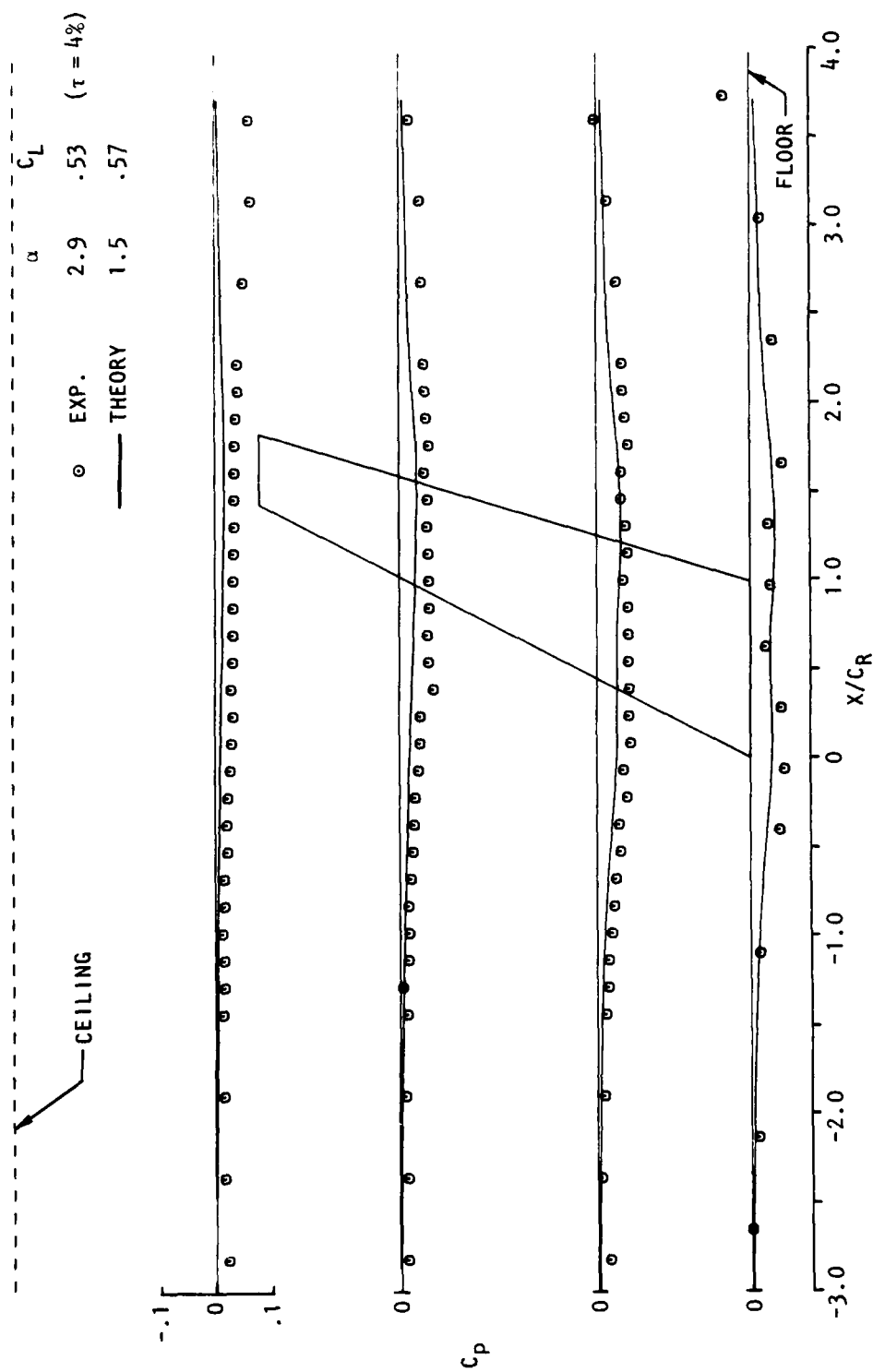
$$\phi_{MEAS} = -\frac{1}{2} \int_{x_O}^x C_{PM}(x, y, z) dx + \phi(x_O, y, z)$$

Figure 66. - Boundary conditions for wind-tunnel simulation.



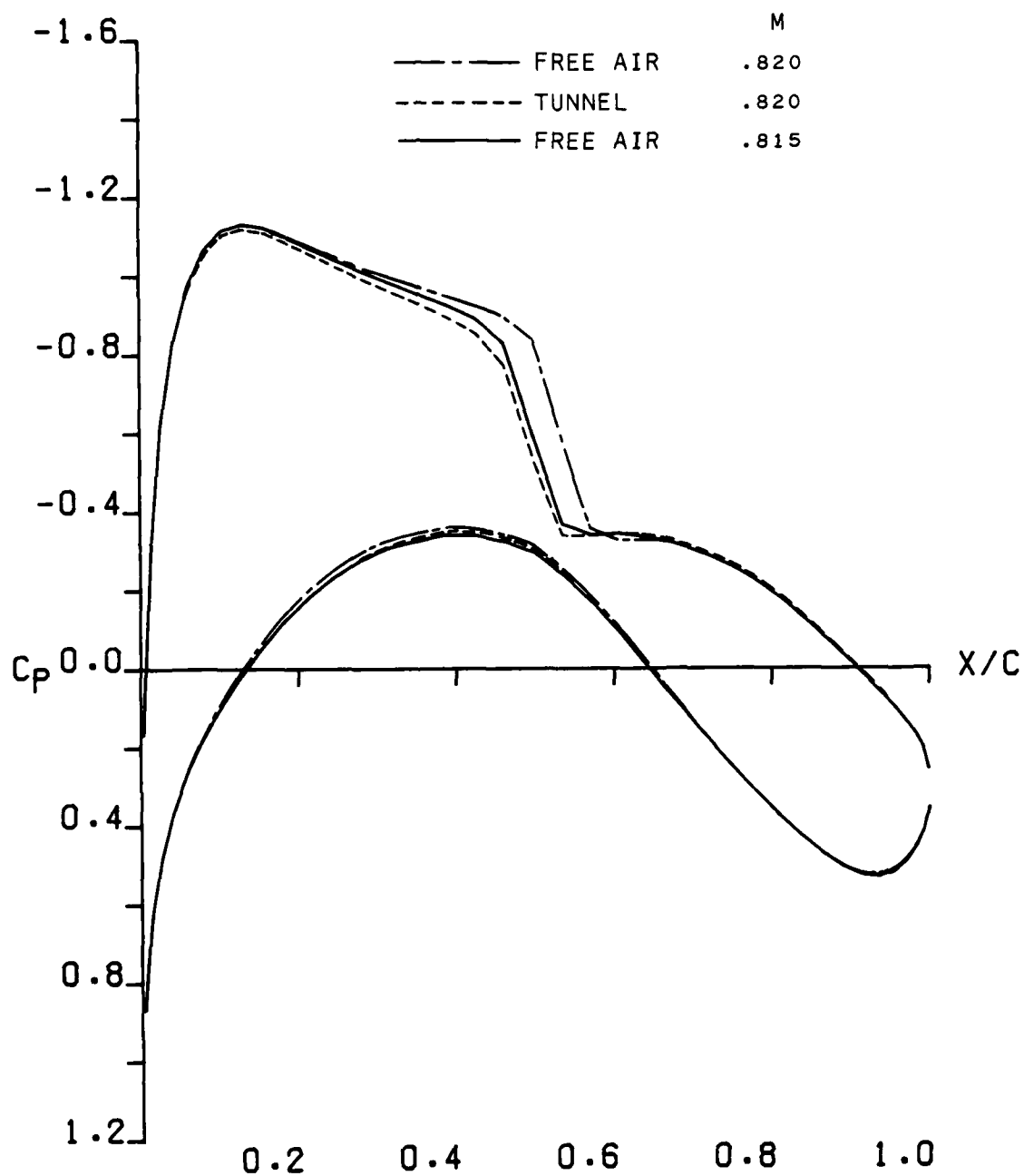
(a) Above wing

Figure 67. - Comparison of measured and theoretical free-air pressures near the tunnel wall for Wing A at  $M=0.82$ ,  $C_L=0.5$ .



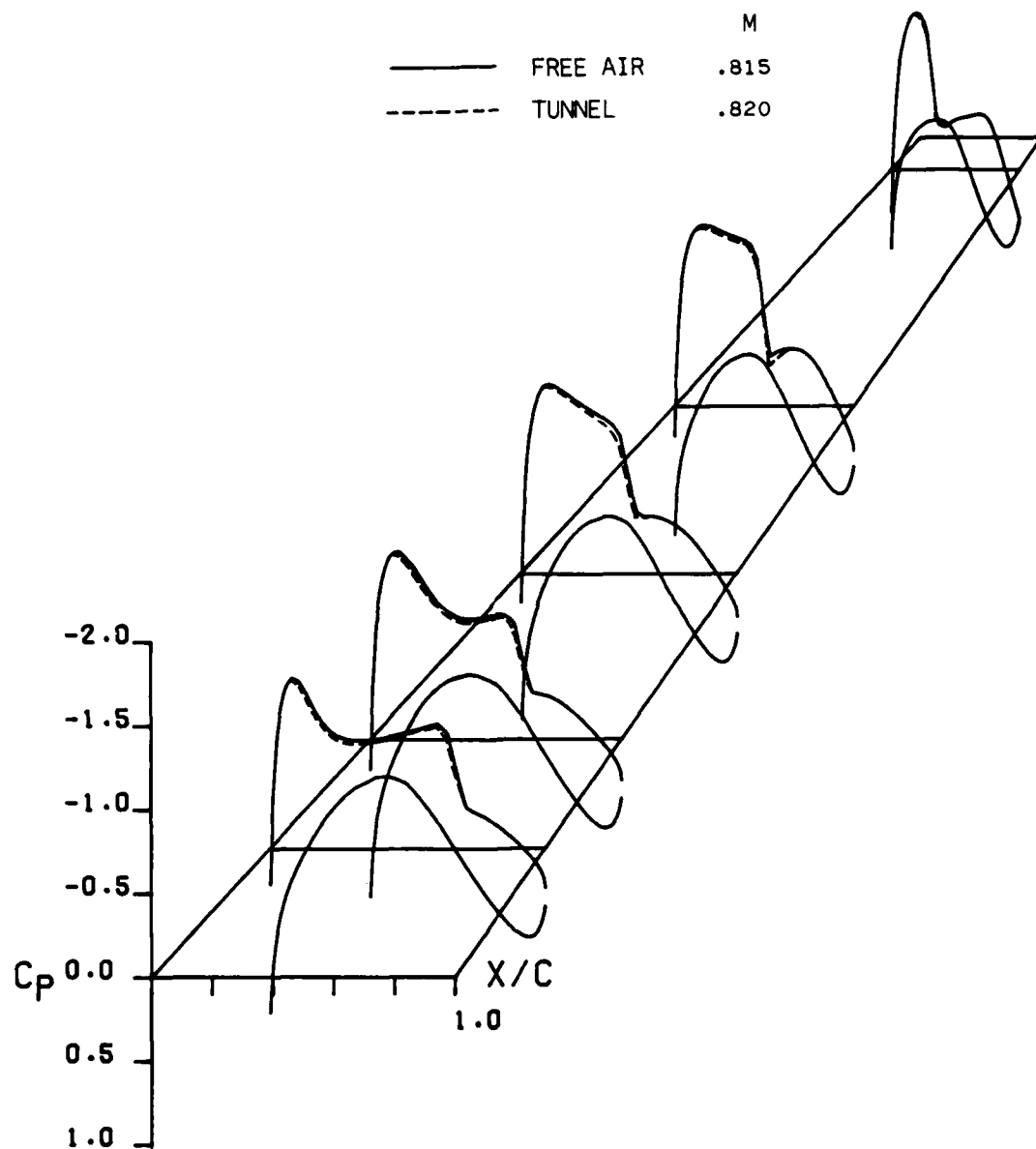
(b) Below wing

Figure 67 . - Concluded.



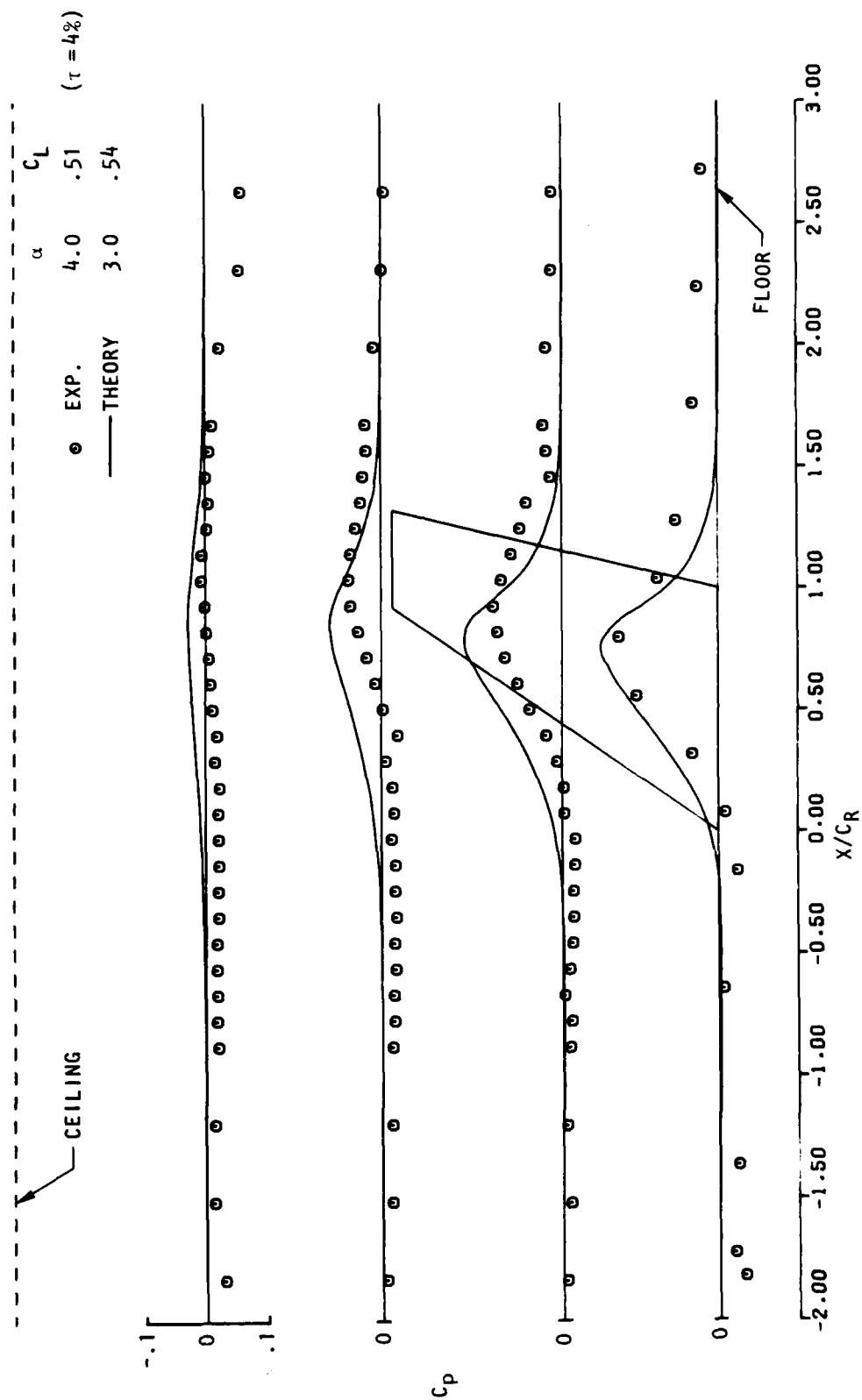
(a)  $\eta = .48$

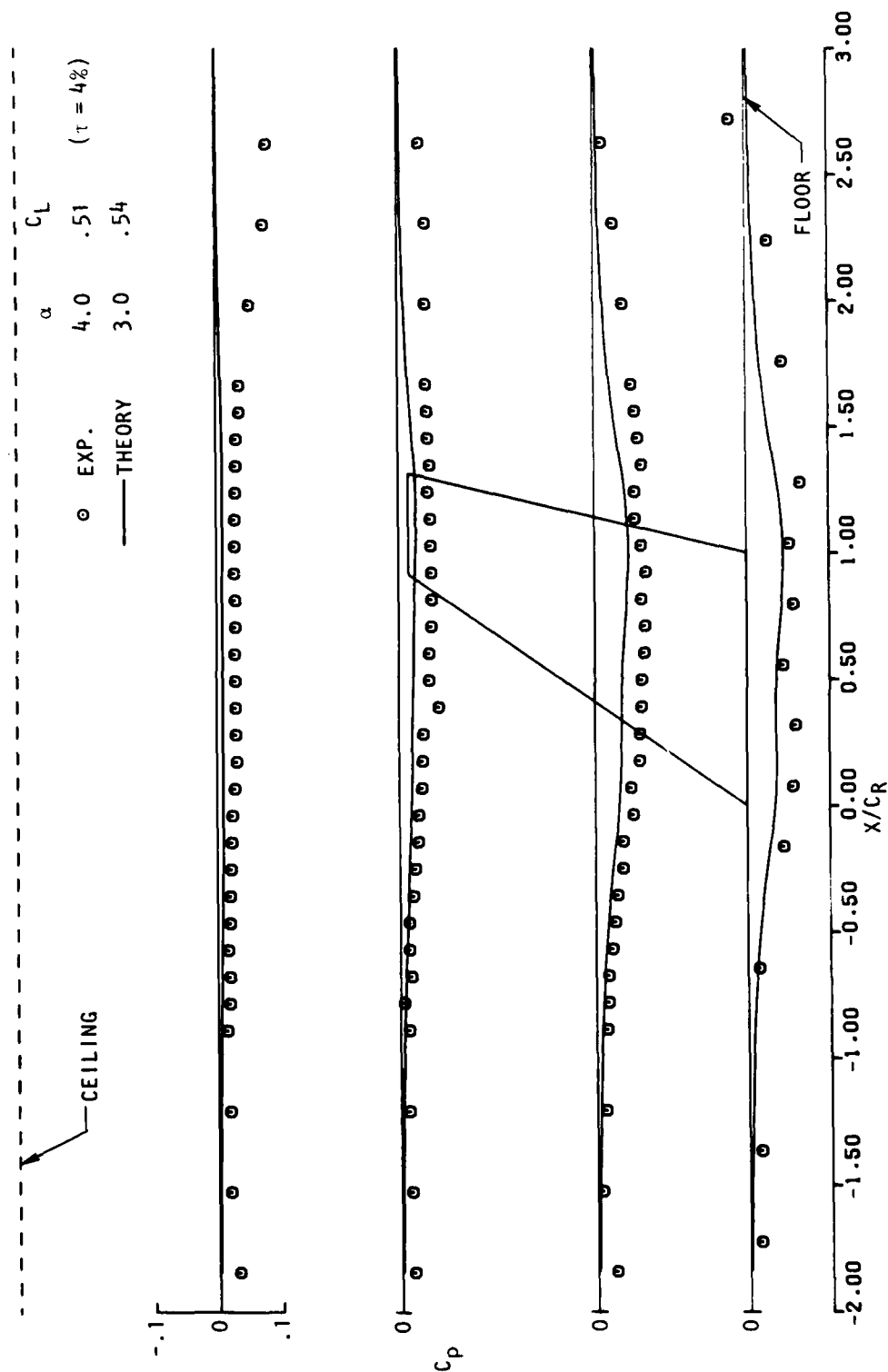
Figure 68. - Theoretical pressure distributions for Wing A using free-air and measured tunnel boundary conditions;  $\alpha = 1.5^\circ$ .



(b) Complete wing.

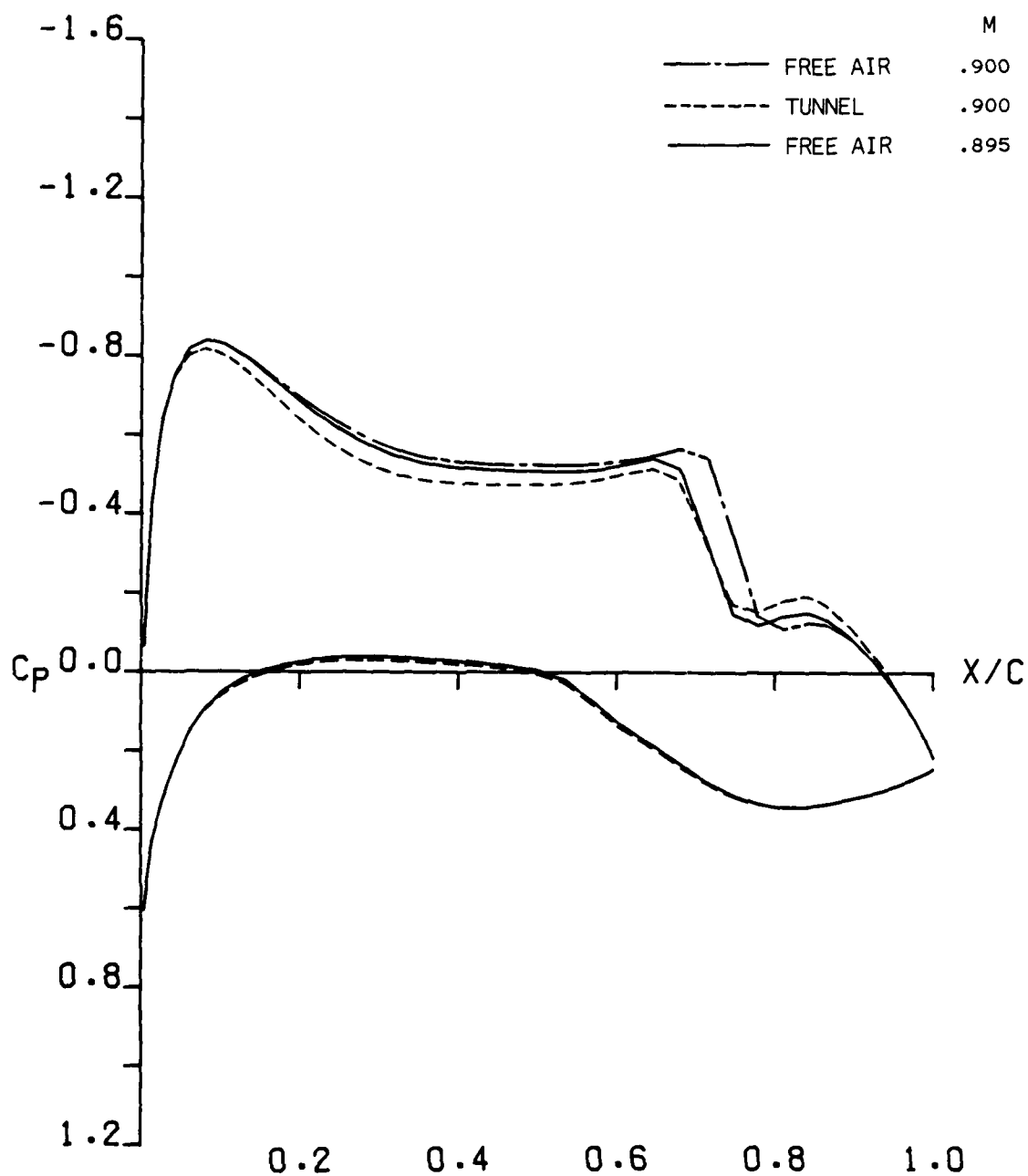
Figure 68 . - Concluded.





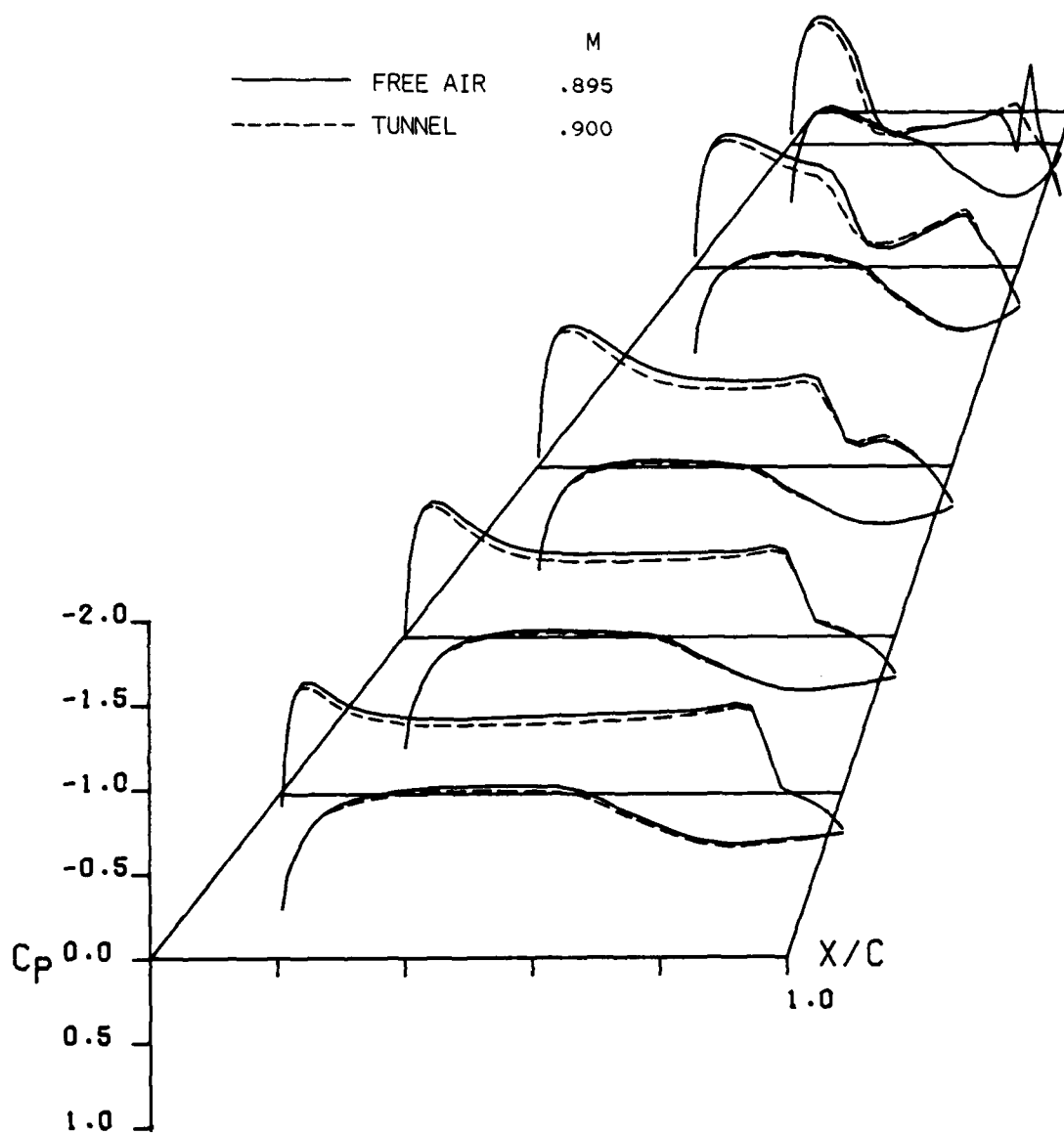
(b) Below wing  
Figure 69. - Concluded.





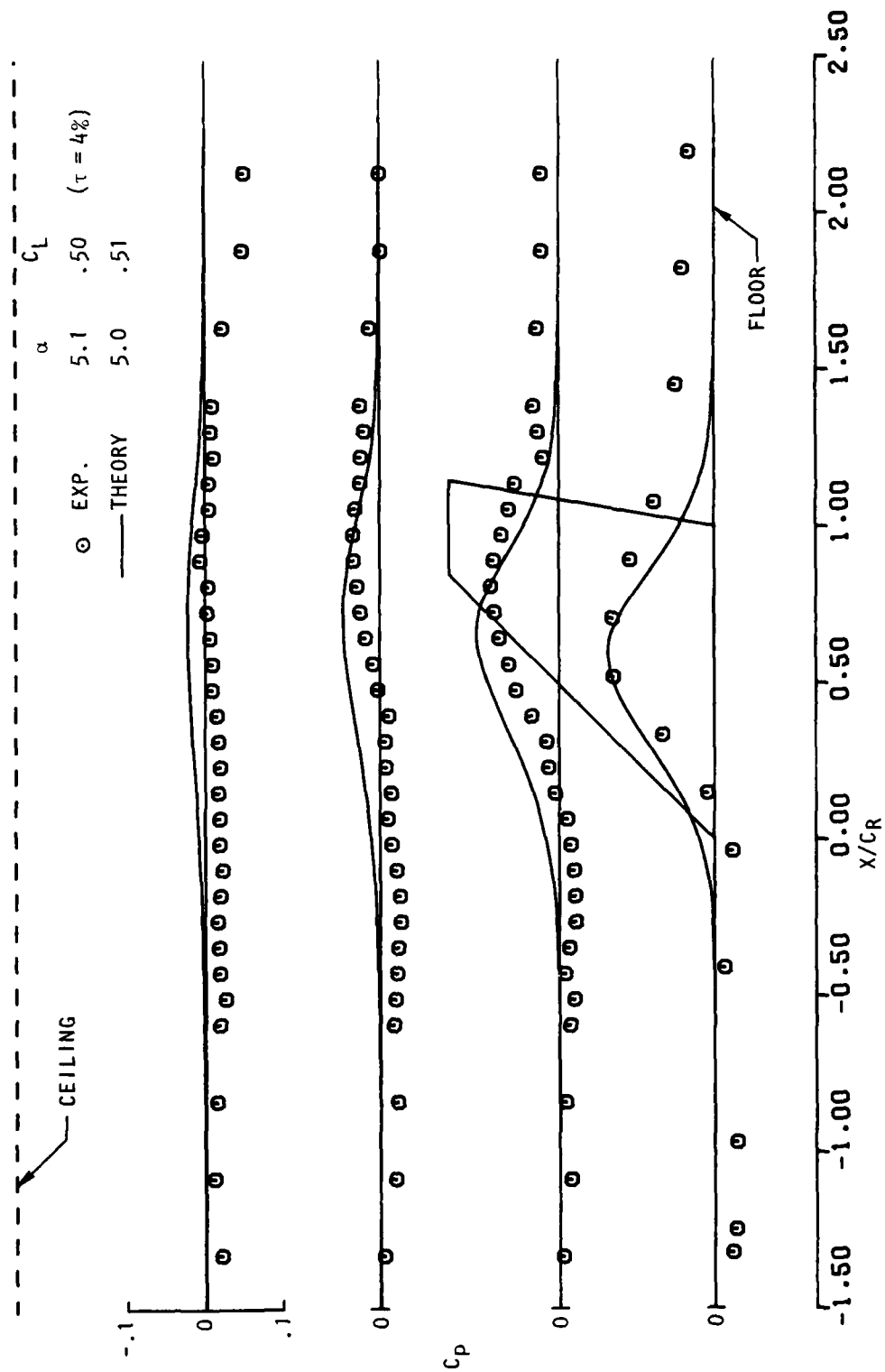
(a)  $\eta = .58$

Figure 70 . - Theoretical pressure distributions for Wing B using free-air and measured tunnel boundary conditions;  $\alpha = 3.0^\circ$ .



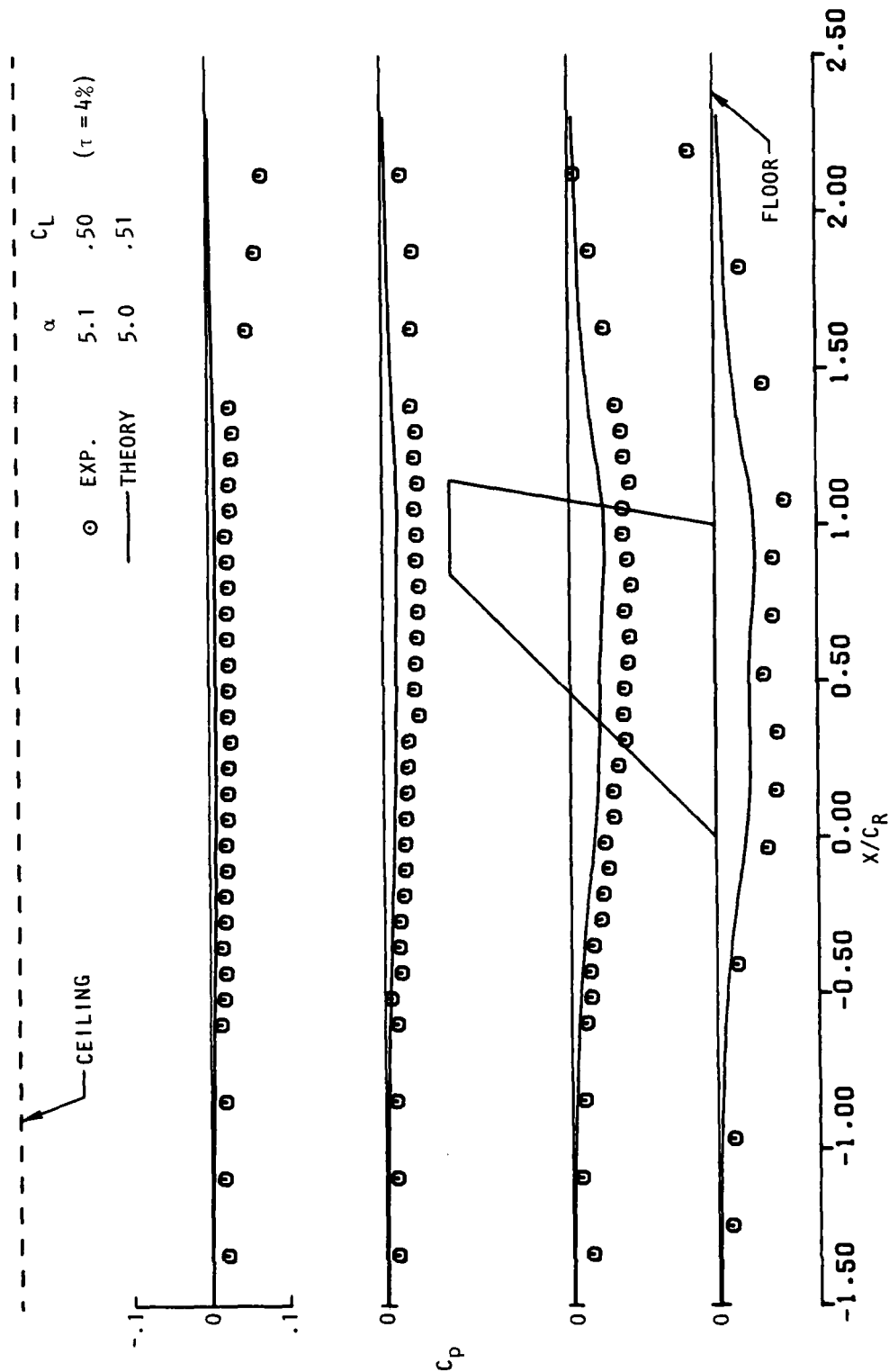
(b) Complete wing

Figure 70 . - Concluded.

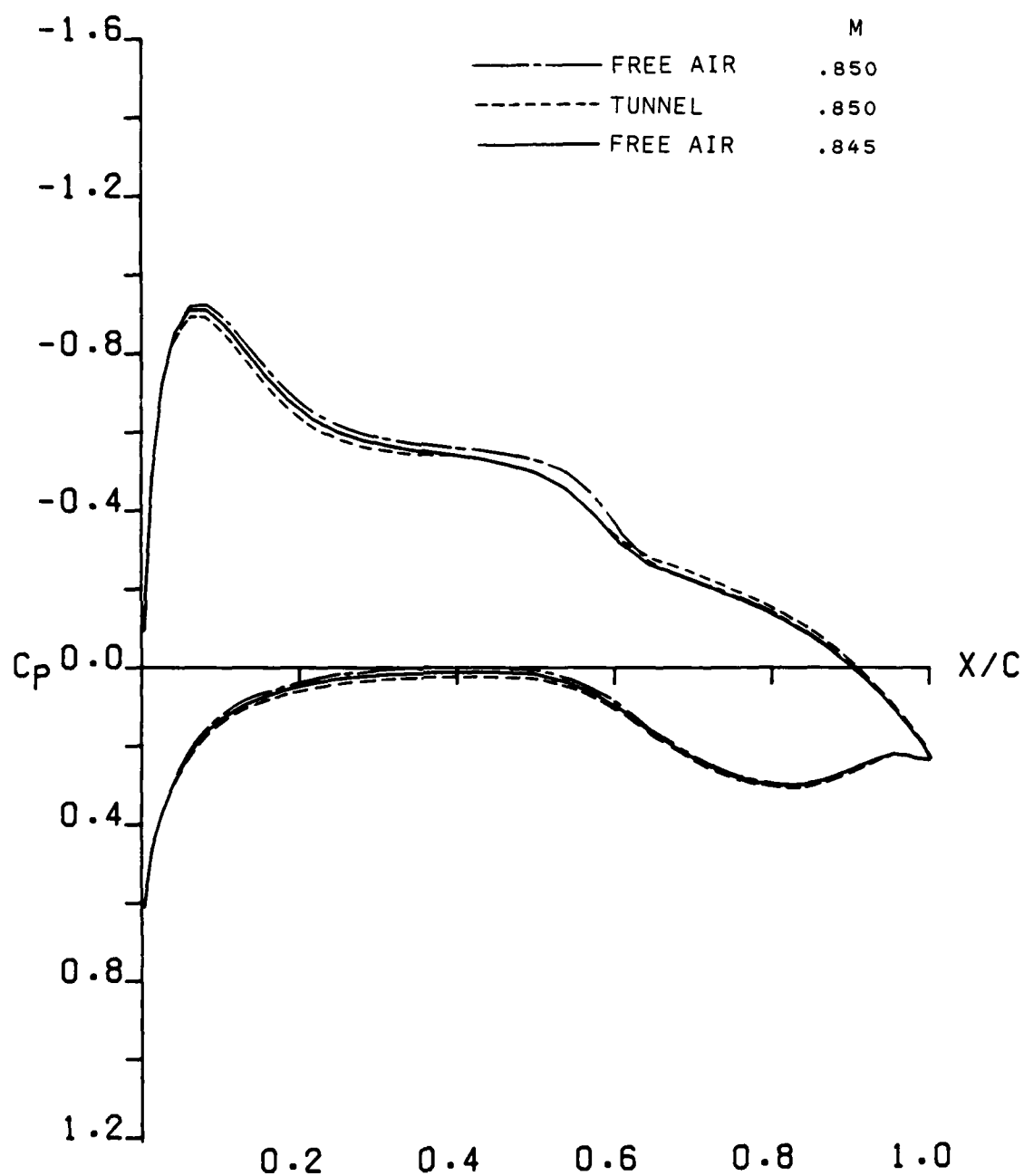


(a) Above wing

Figure 71 . - Comparison of measured and theoretical free-air pressures near the tunnel wall for Wing C at  $M=0.85$ ,  $C_L \approx 0.5$ .

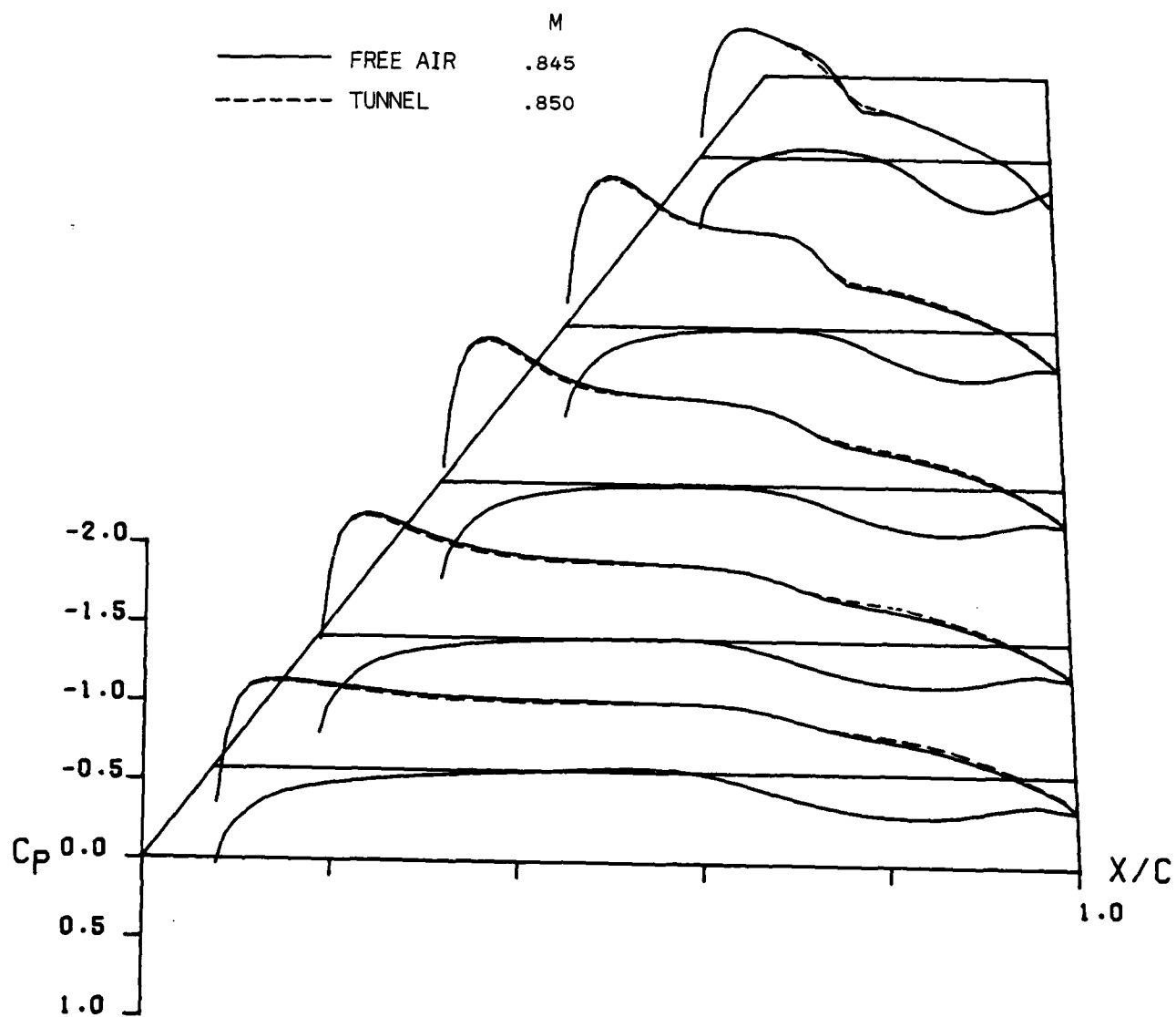


(b) Below wing  
Figure 71. - Concluded.



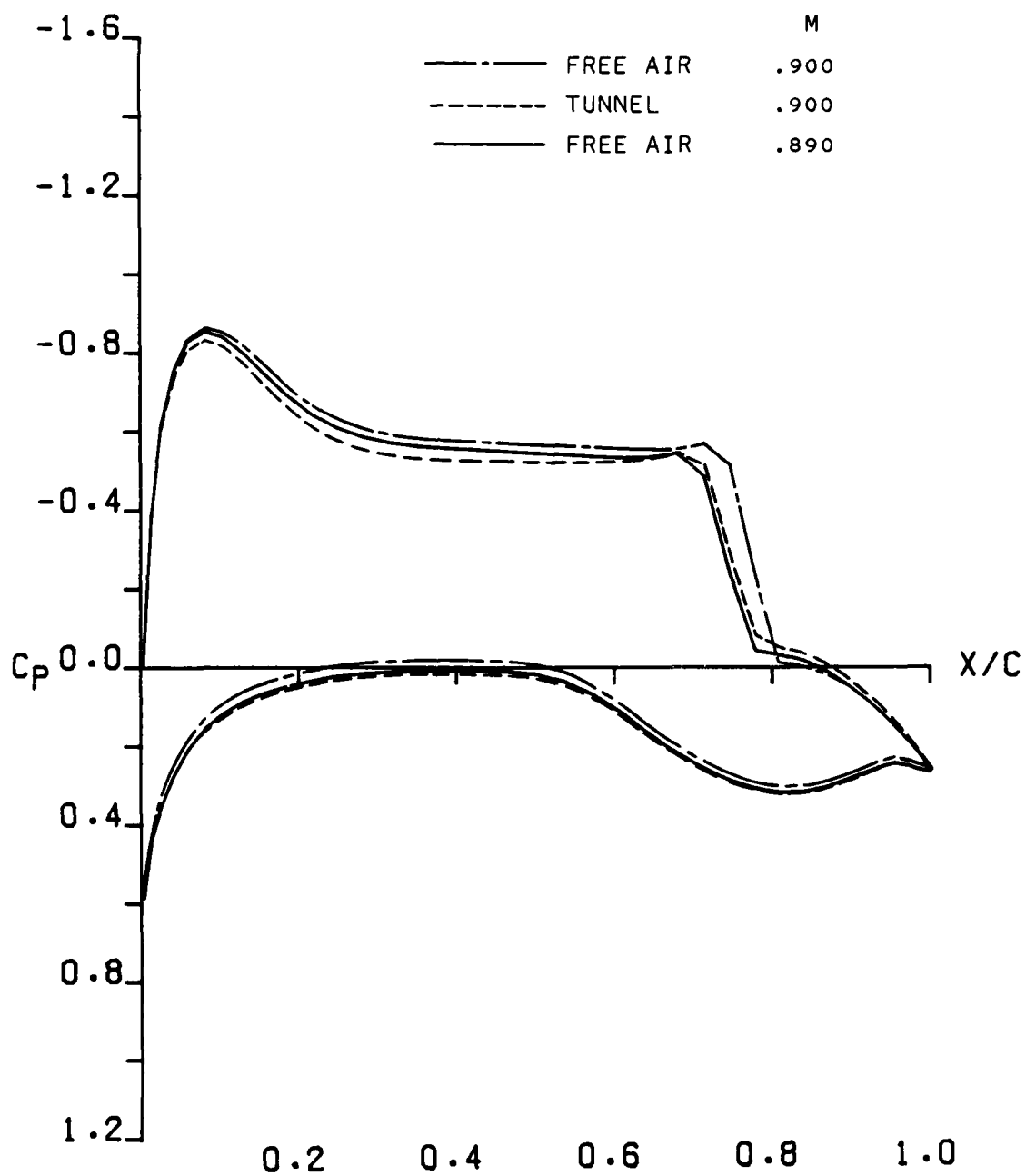
(a)  $\eta = .48$

Figure 72 . - Theoretical pressure distributions for Wing C using free-air and measured boundary conditions at  $M = .85^\circ$ ,  $\alpha = 5.0^\circ$ .



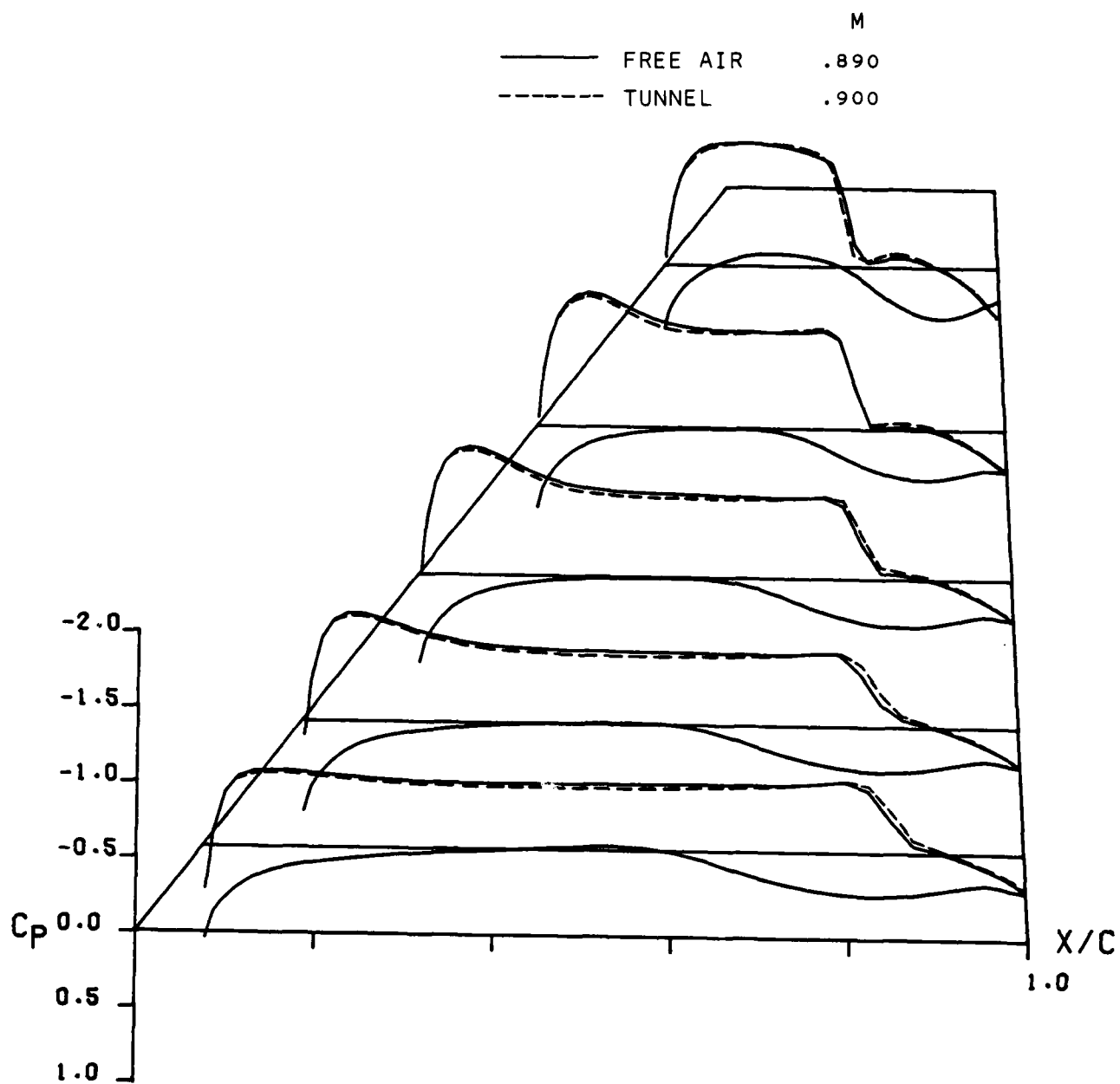
(b) Complete wing

Figure 72. - Concluded.



(a)  $\eta = .48$

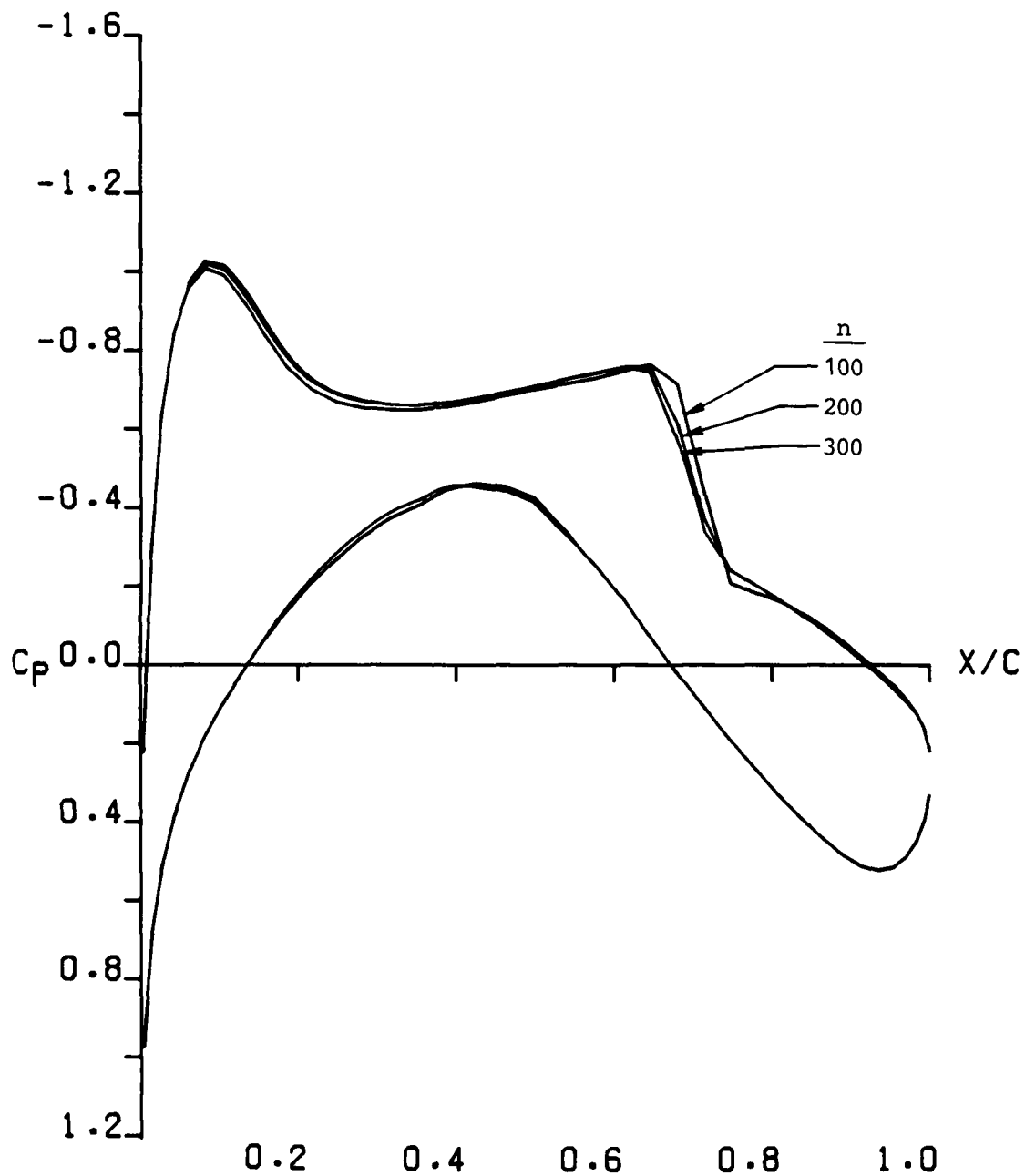
Figure 73 . - Theoretical distributions for Wing C using free-air and measured boundary conditions at  $M = .90$ ,  $\alpha = 5.0^\circ$ .



(b) Complete wing

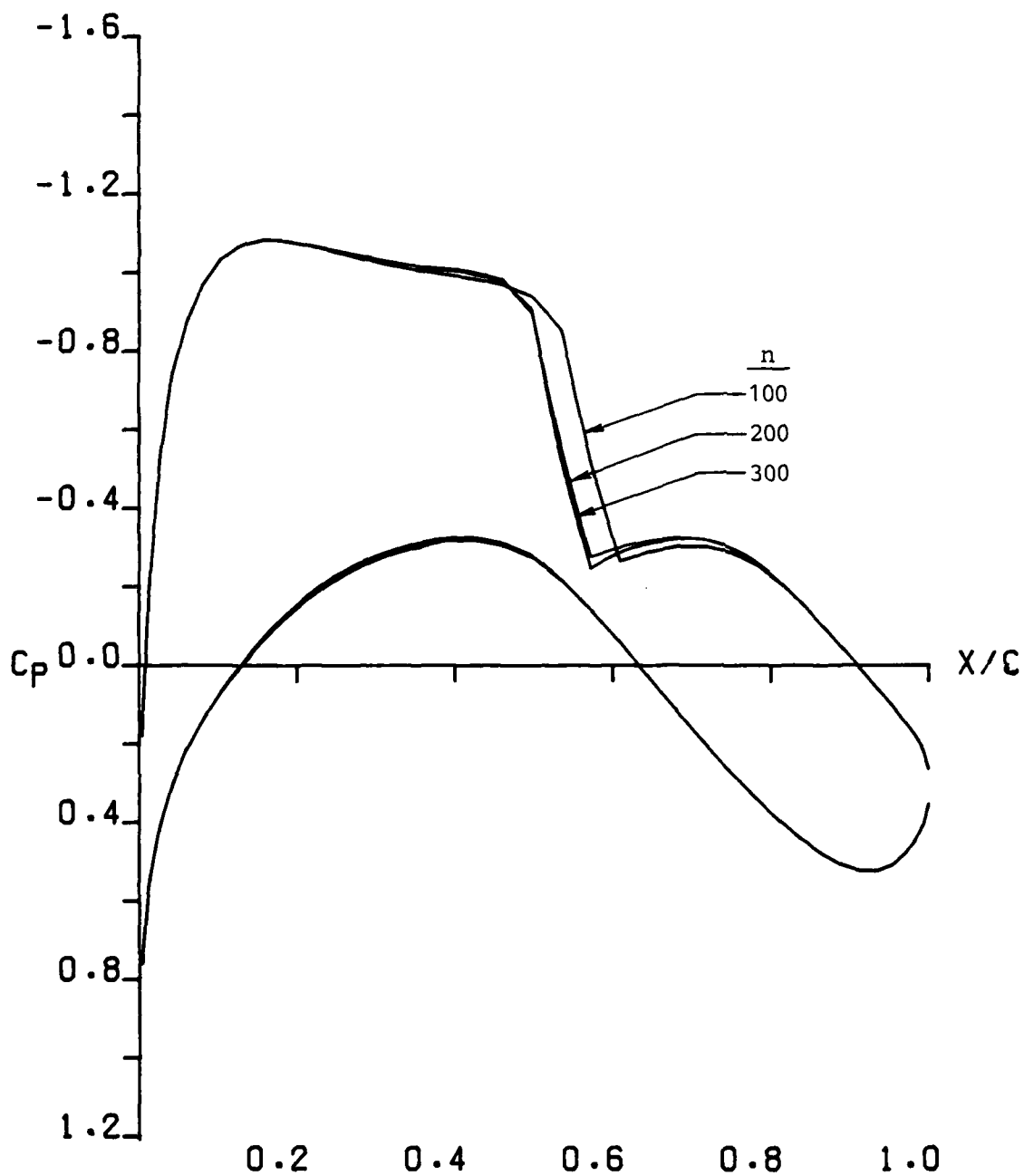
Figure 73 . - Concluded.





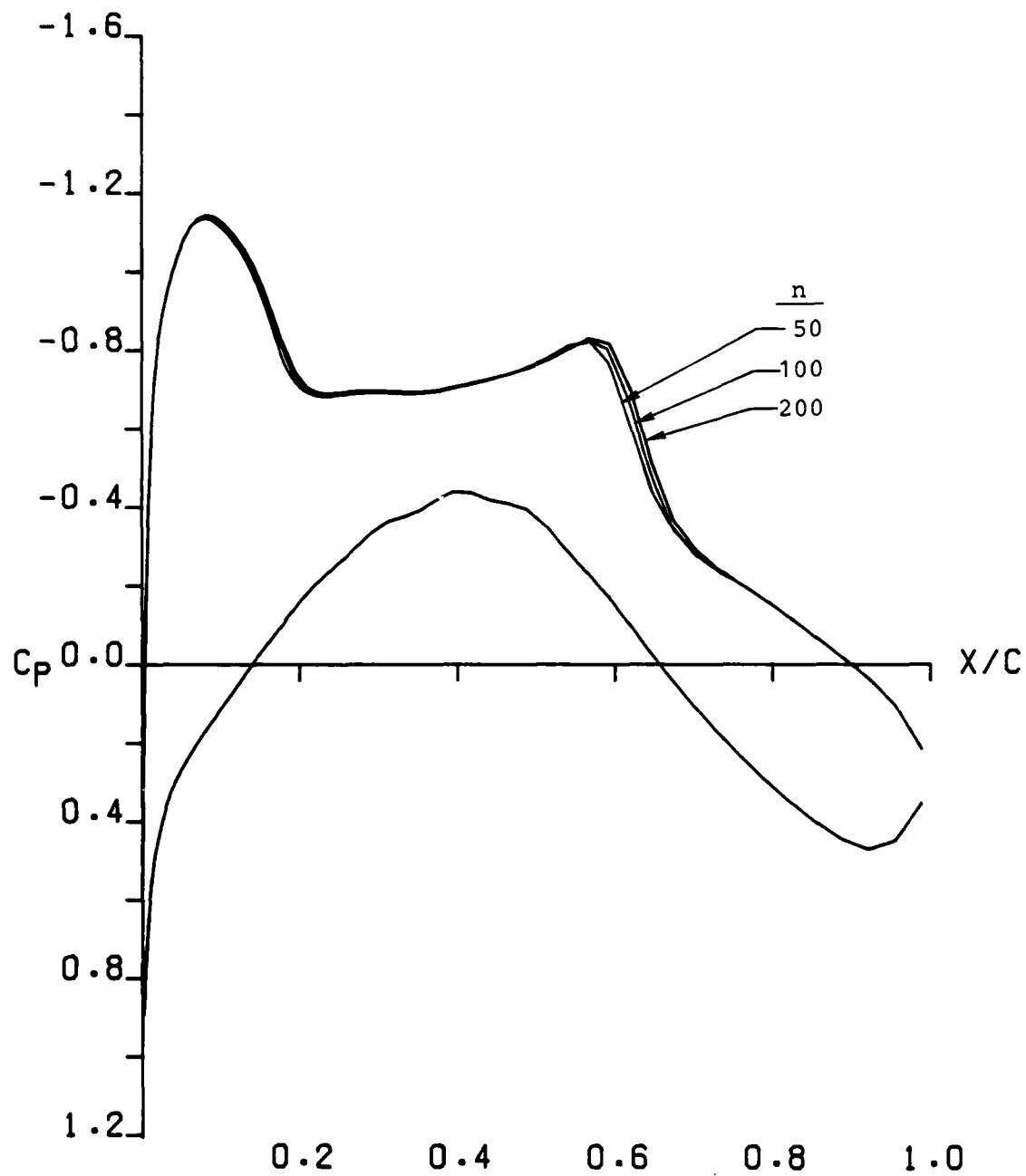
(a)  $\eta = .15$

Figure 74 . - Effect of iteration number on Bailey-Ballhaus code results; Wing A at  $M=0.82$  ,  $\alpha=1.5^\circ$ .



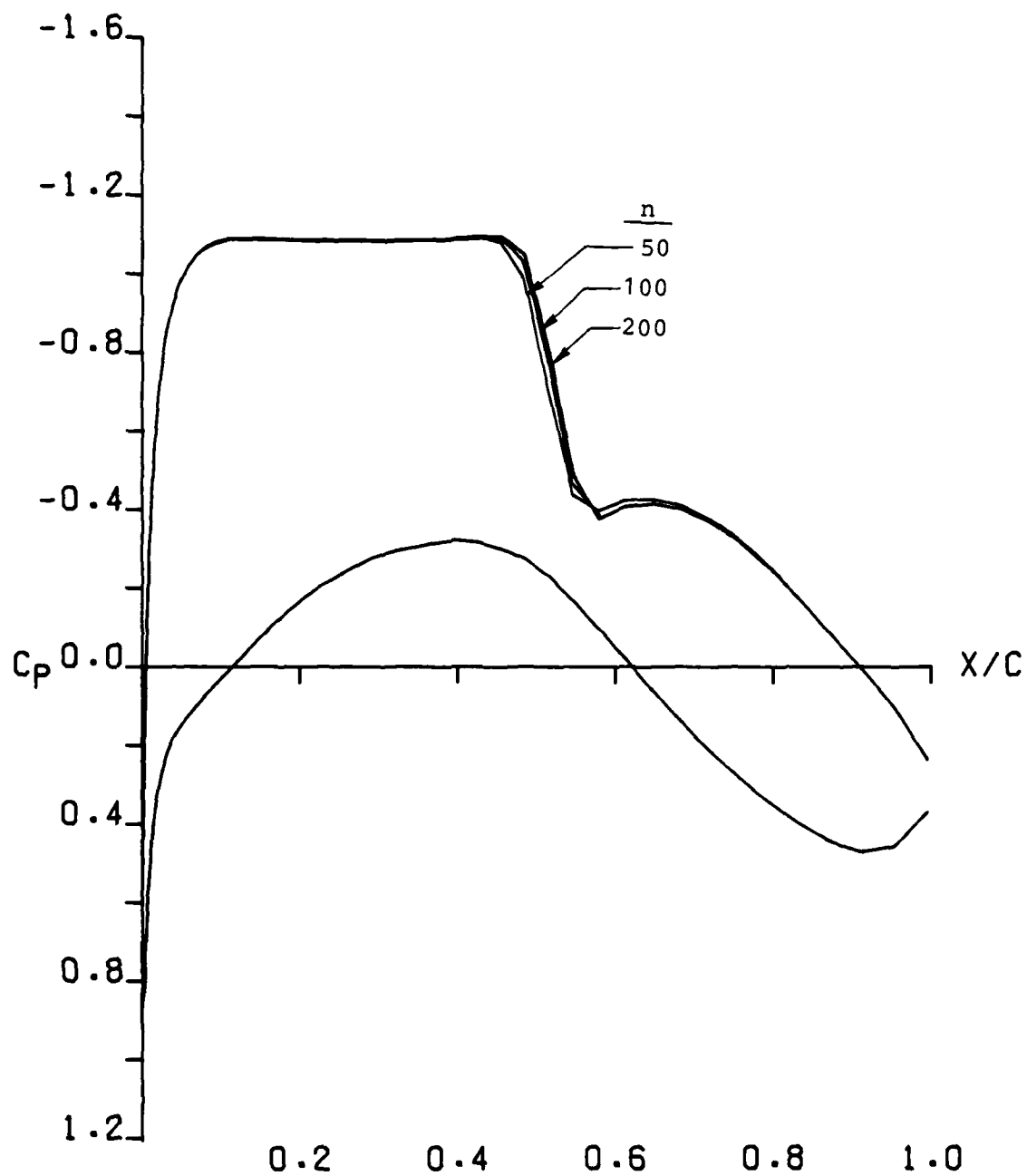
(b)  $\eta = .68$

Figure 74 . - Concluded.



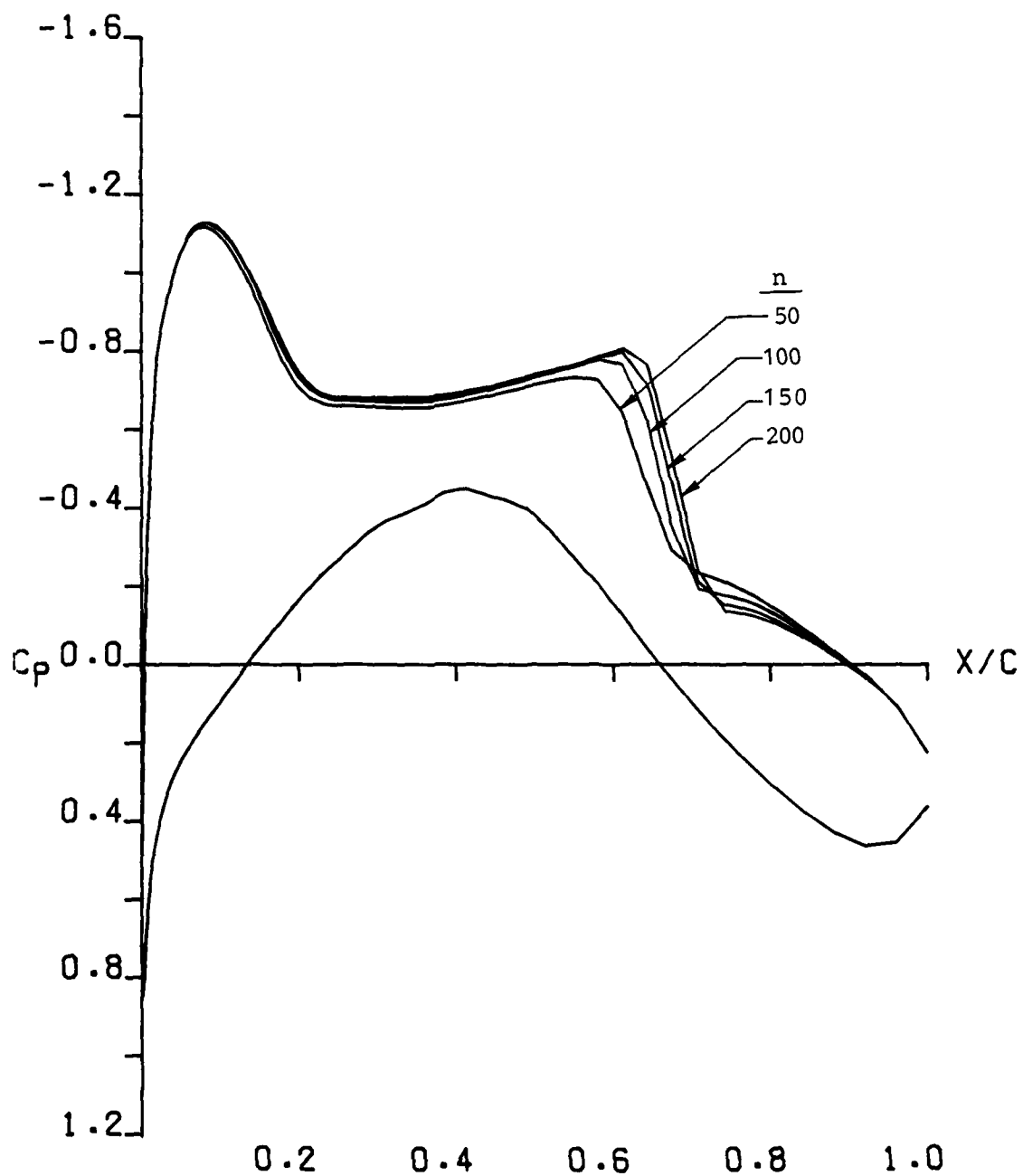
(a)  $\eta = .15$

Figure 75 . - Effect of iteration number on FLO-22 results;  
Wing A at  $M=0.82$  ,  $\alpha=1.5^\circ$ .



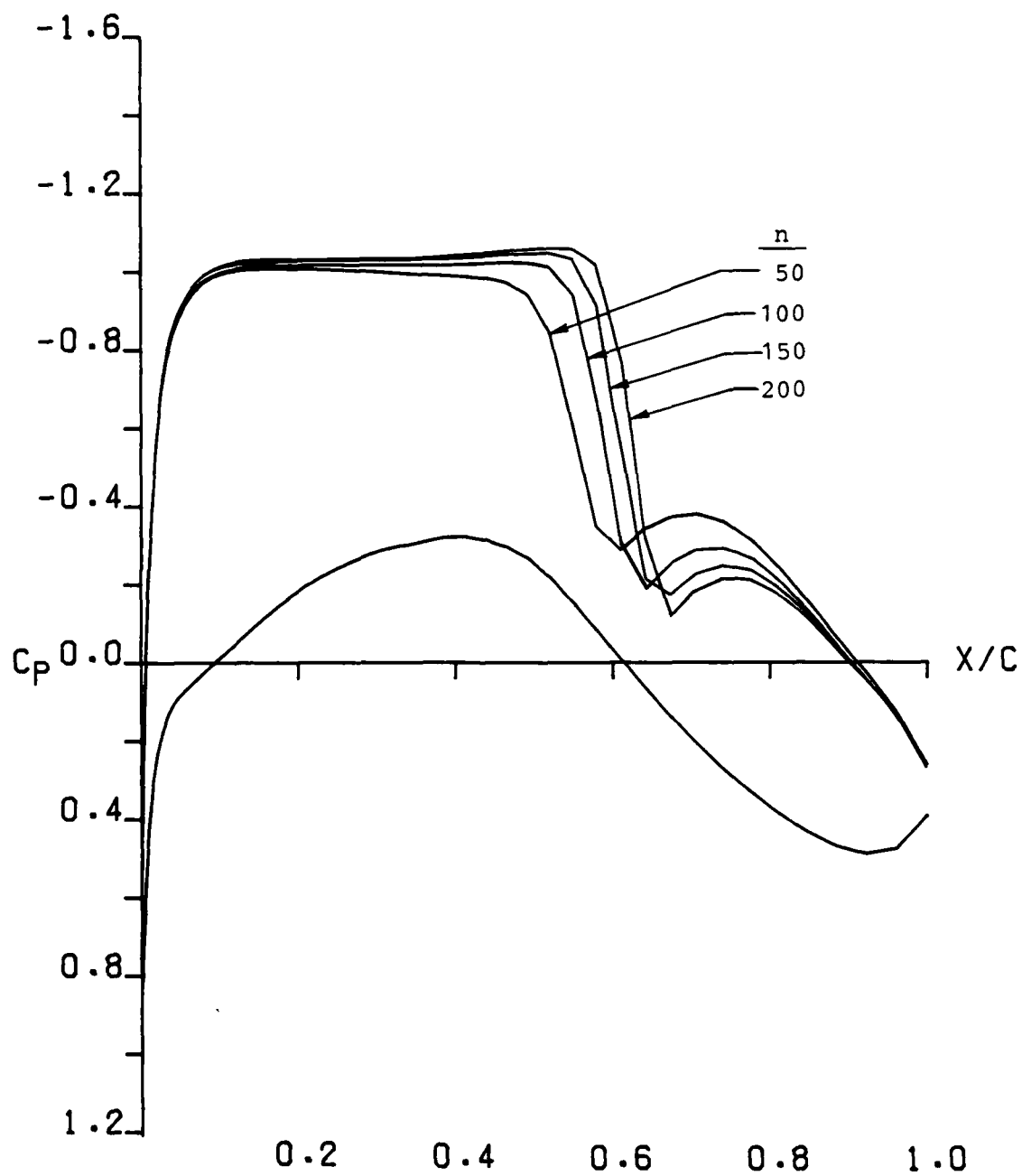
(b)  $\eta = .68$

Figure 75 . - Concluded.



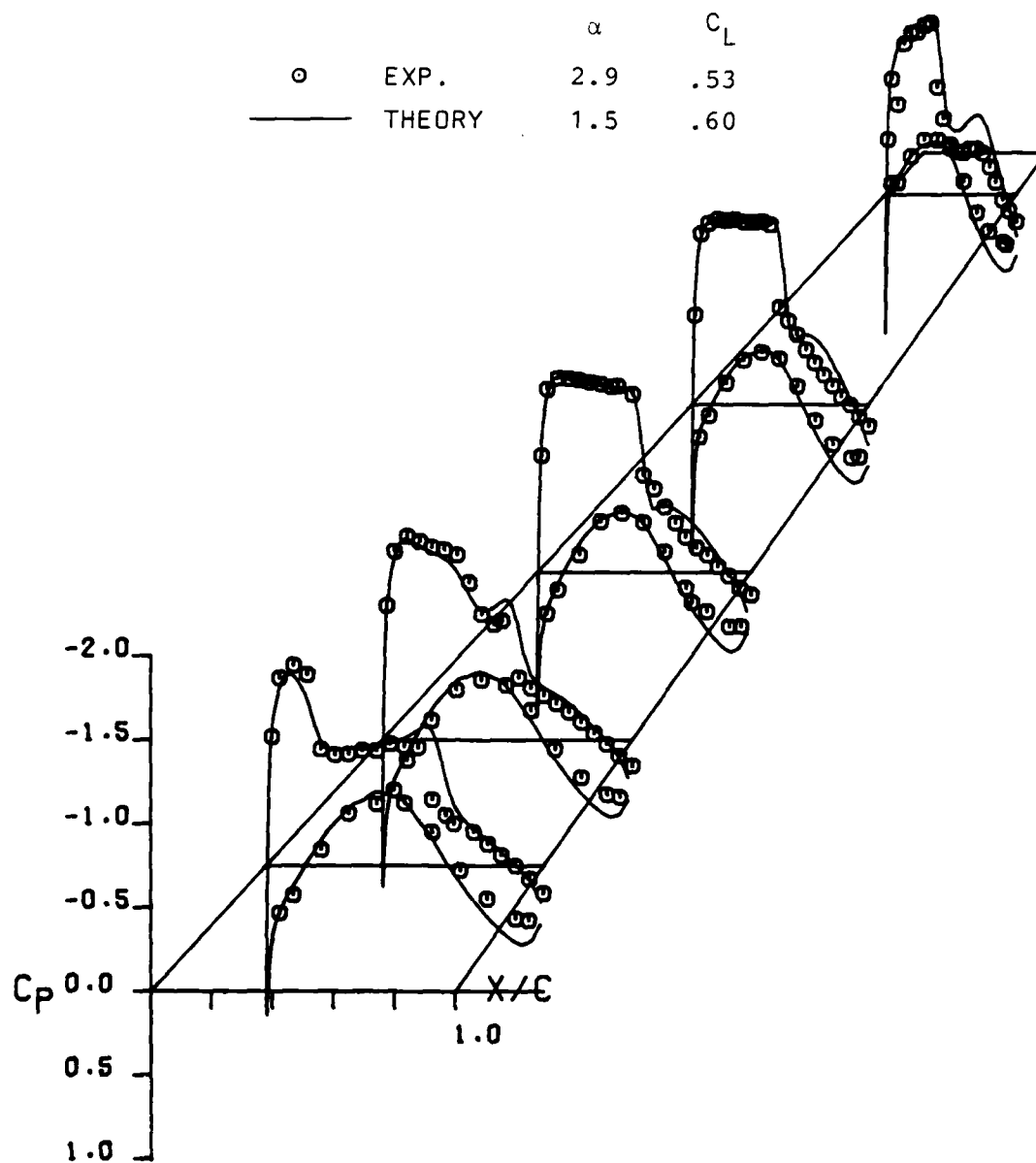
(a)  $\eta = .15$

Figure 76 . - Effect of iteration number on FL0-27 results;  
Wing A at  $M=0.82$  ,  $\alpha = 1.5^\circ$ .



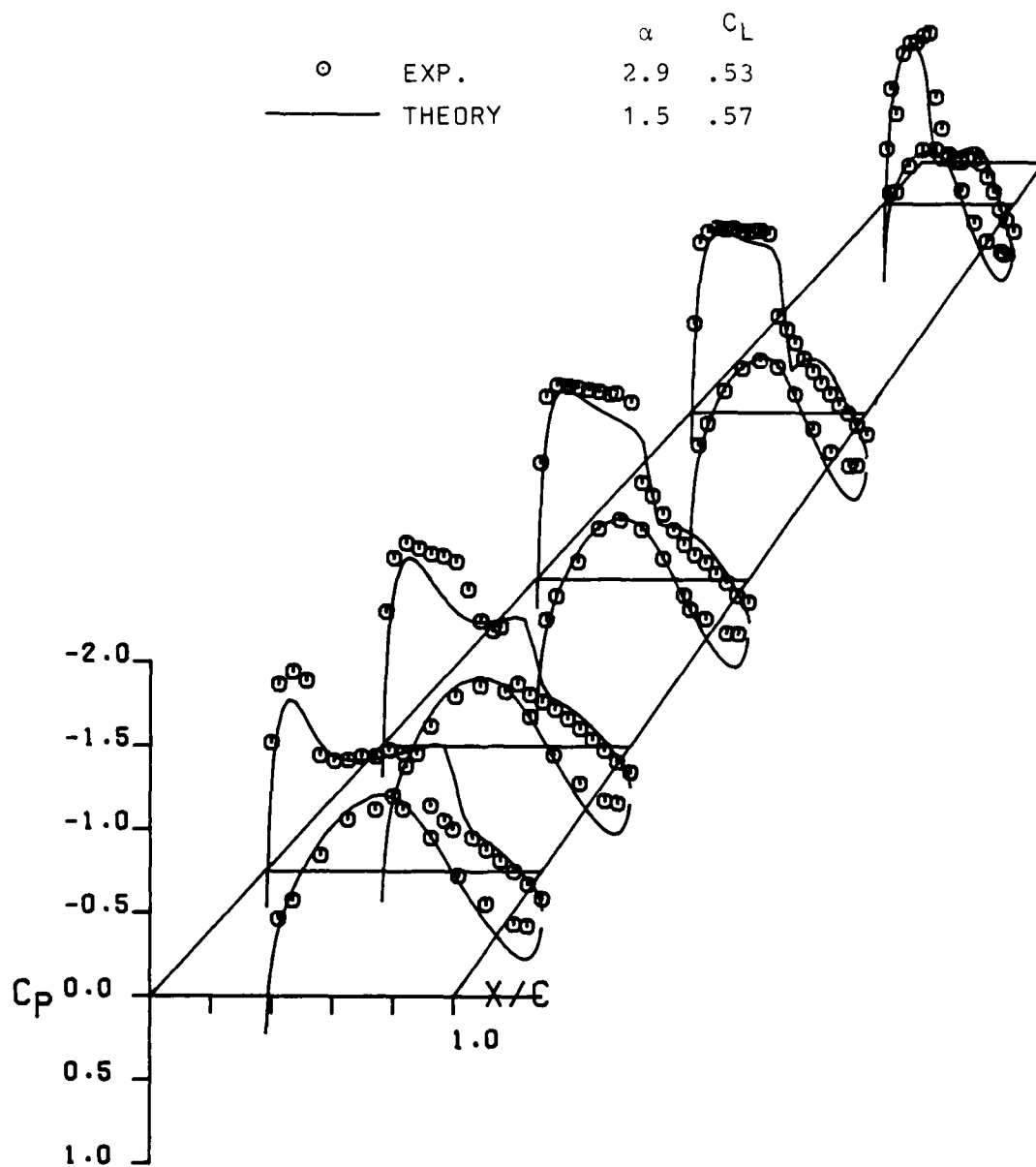
(b)  $n = .70$

Figure 76 . - Concluded.



(a) FL0-22 Code

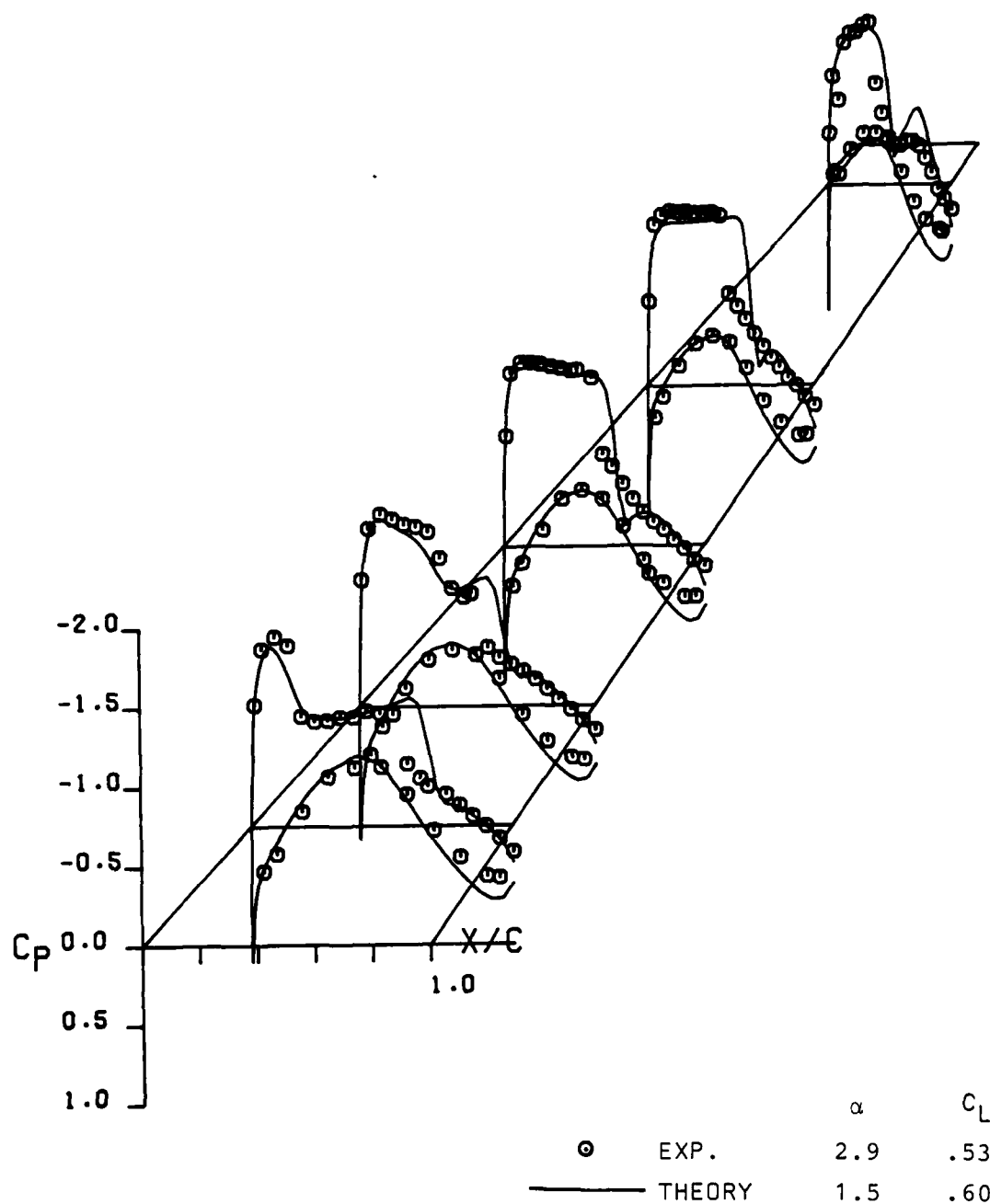
Figure 77. - Comparison of non-conservative solutions with experiment for Wing A at  $M = .82$ .



(b) Bailey-Ballhaus (NCR) code.

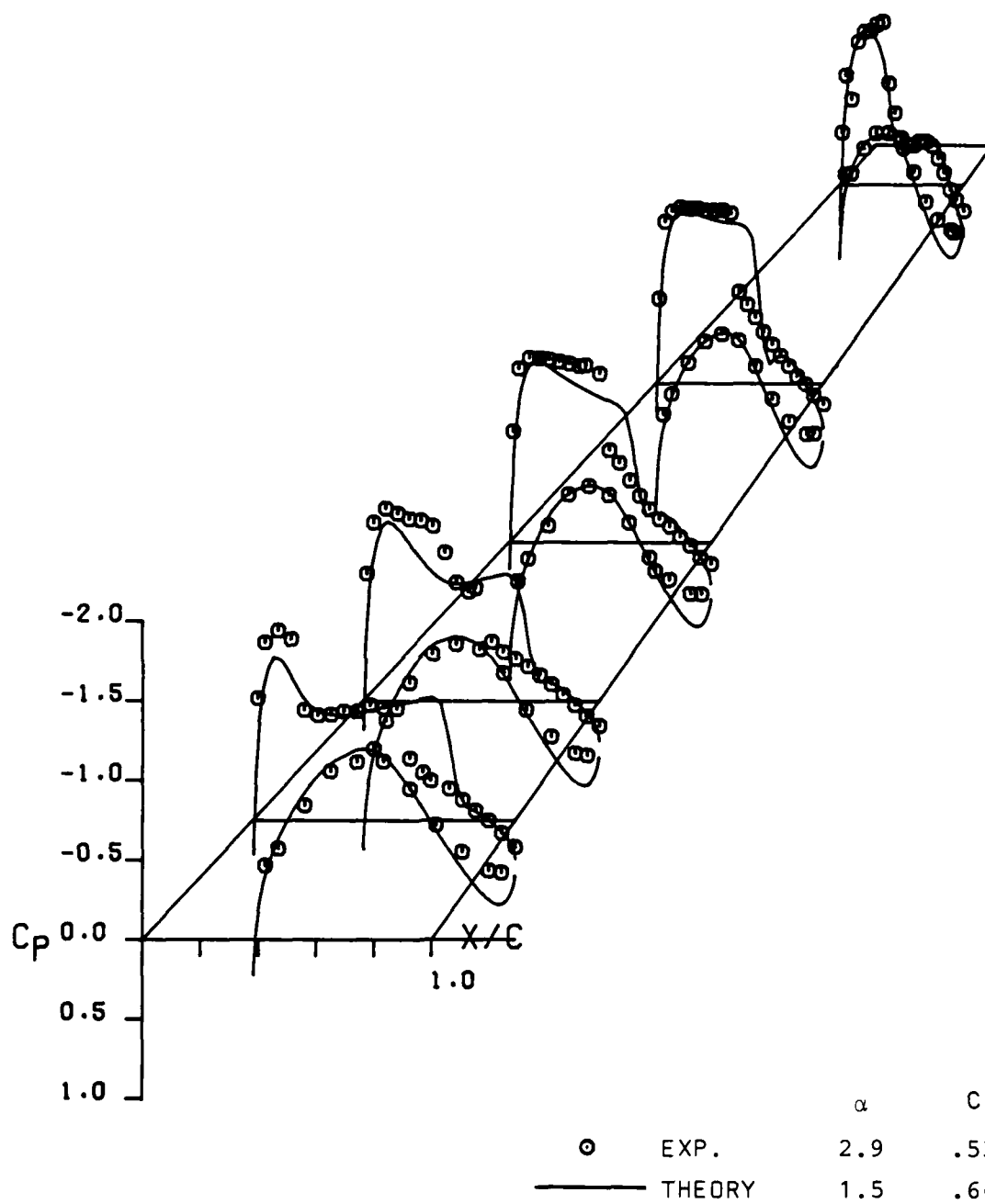
Figure 77. - Concluded.





(a) FL0-27 code.

Figure 78. - Comparison of conservative solutions with experiment for Wing A at  $M = .82$ .



(b) Bailey-Ballhaus FCR

Figure 78. - Concluded.

THEORY: FLQ-22 WITH ITERATED  
2-D BOUNDARY LAYER.

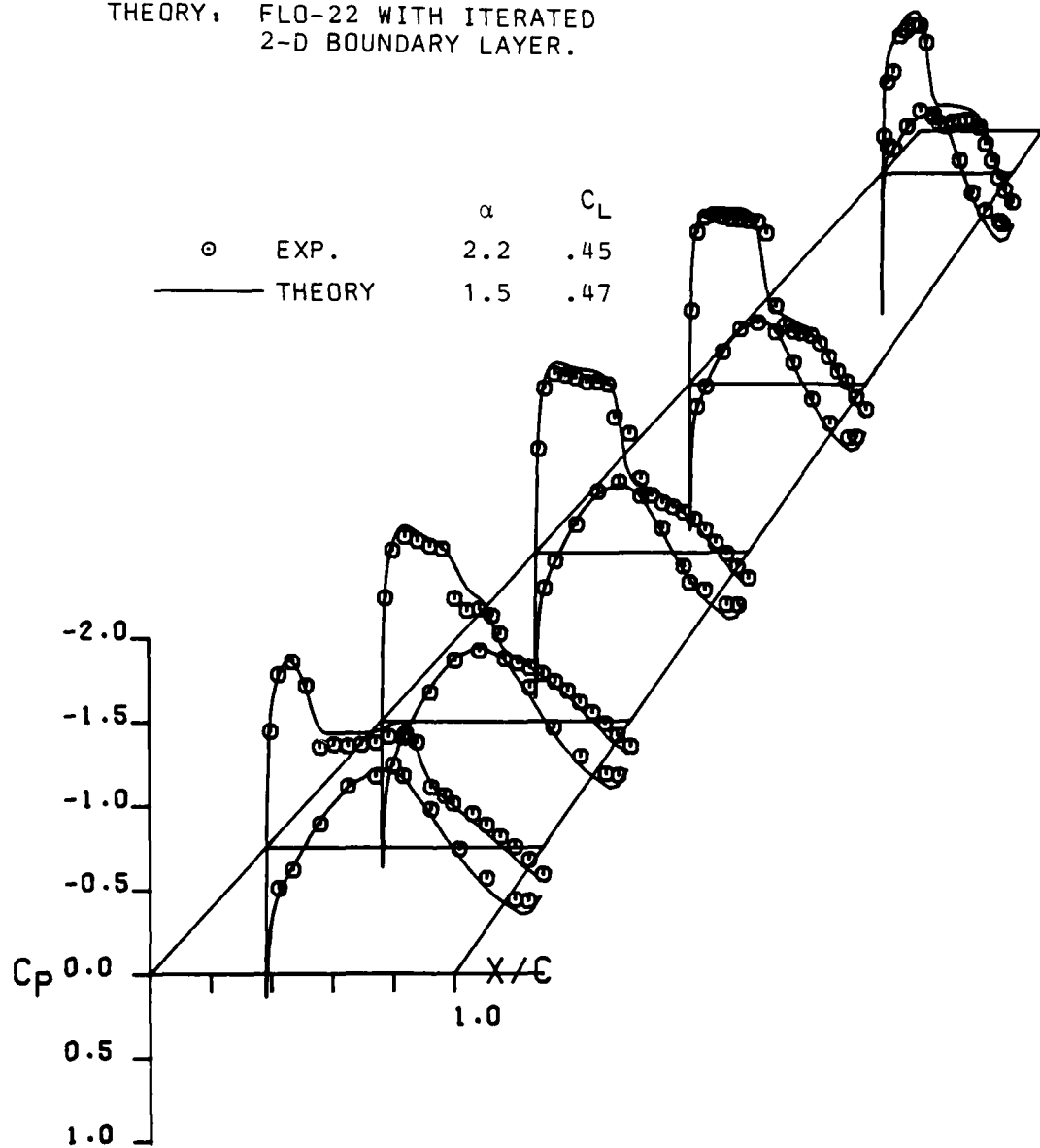


Figure 79 . - Comparison of FLQ-22 results with experiment when viscous corrections are included; Wing A,  $M = 0.82$ .

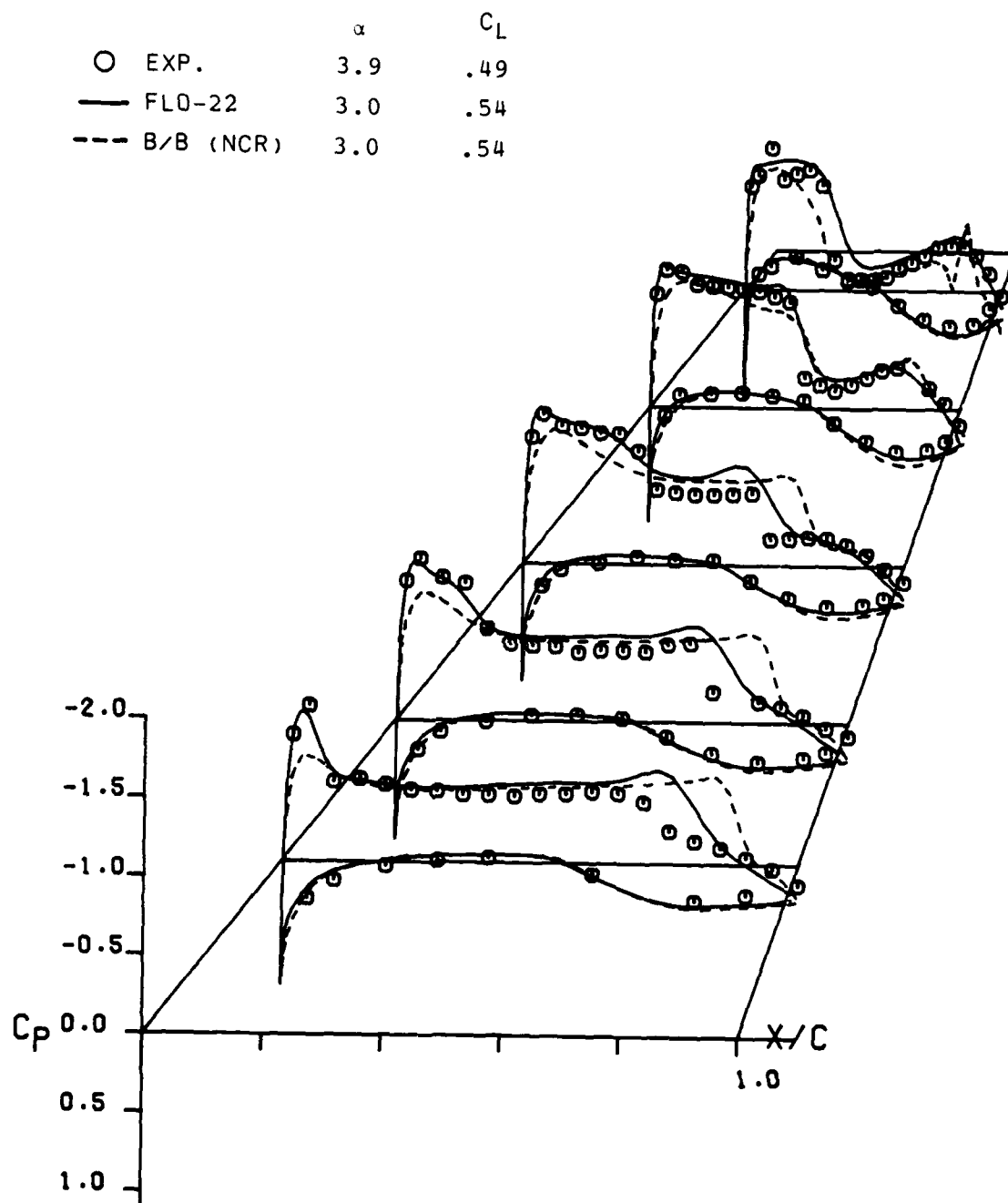


Figure 80. - Comparison of non-conservative solutions with experiment for Wing B at  $M = 0.90$ .

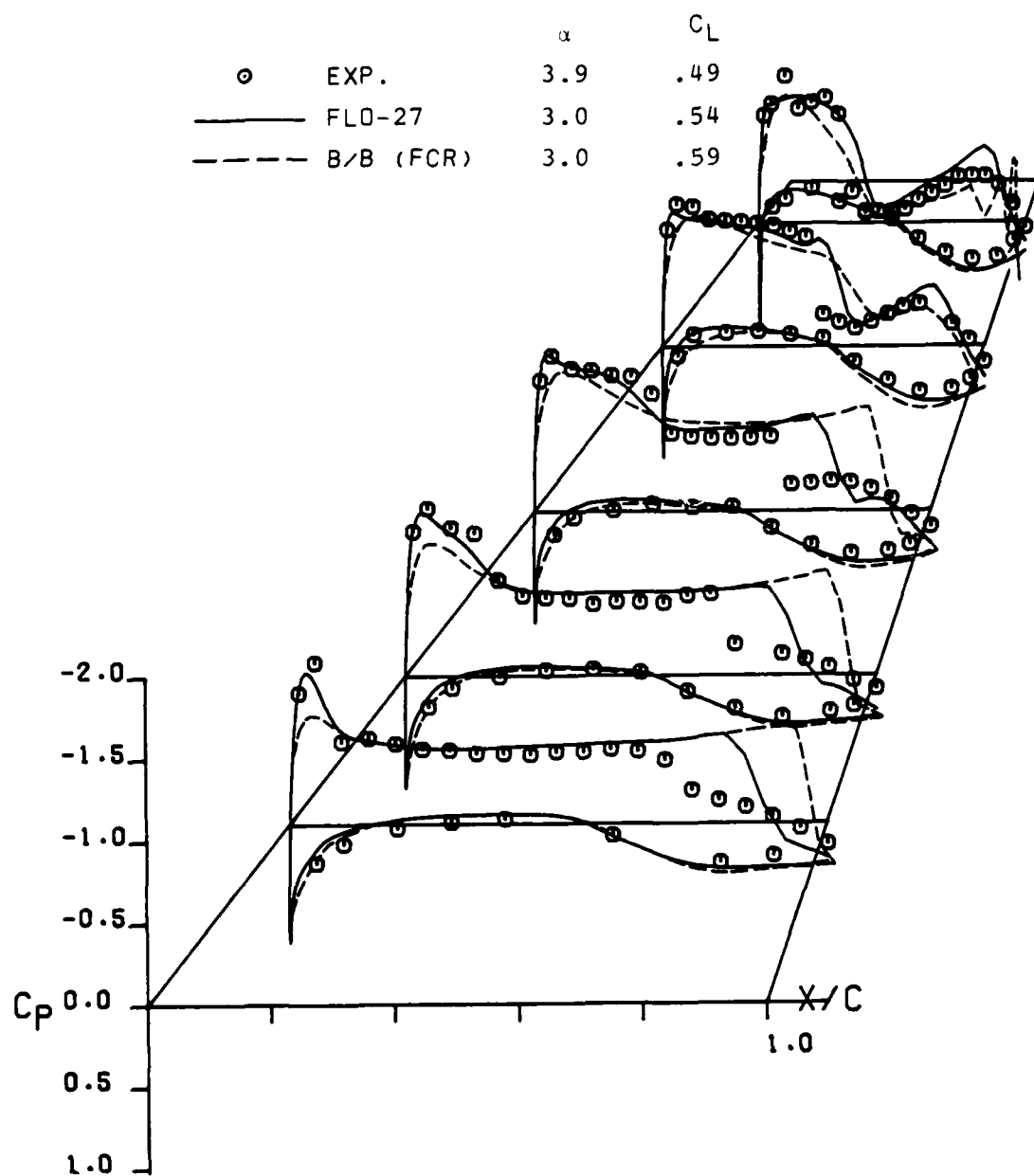


Figure 81. - Comparison of conservative solutions with experiment for Wing B at  $M = 0.90$ .

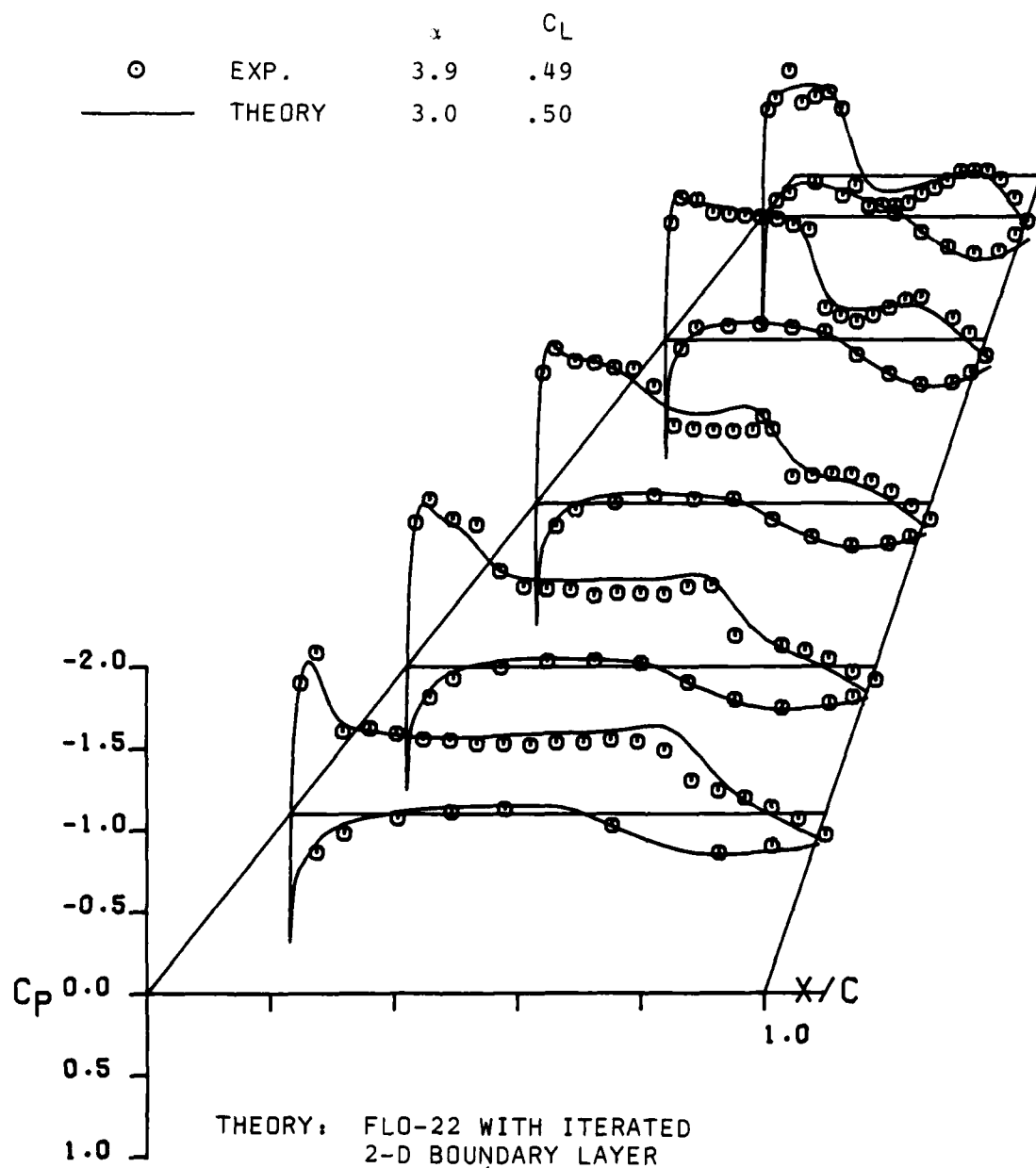


Figure 82 . - Comparison of FLO-22 results with experiment when viscous corrections are included; Wing B,  $M = 0.90$ .

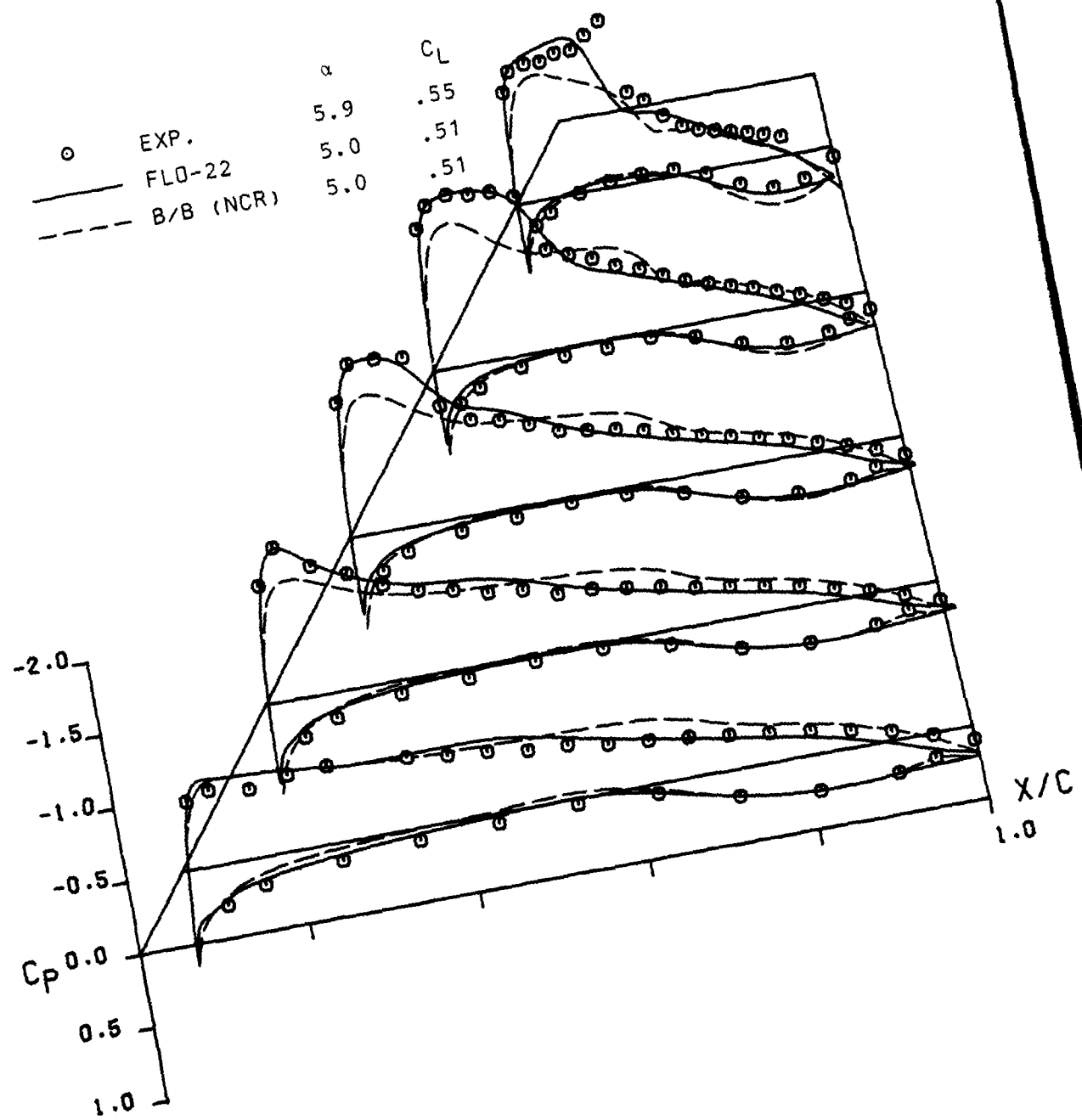


Figure 83. - Comparison of non-conservative solutions with experiment for Wing C at  $M = .85$ .

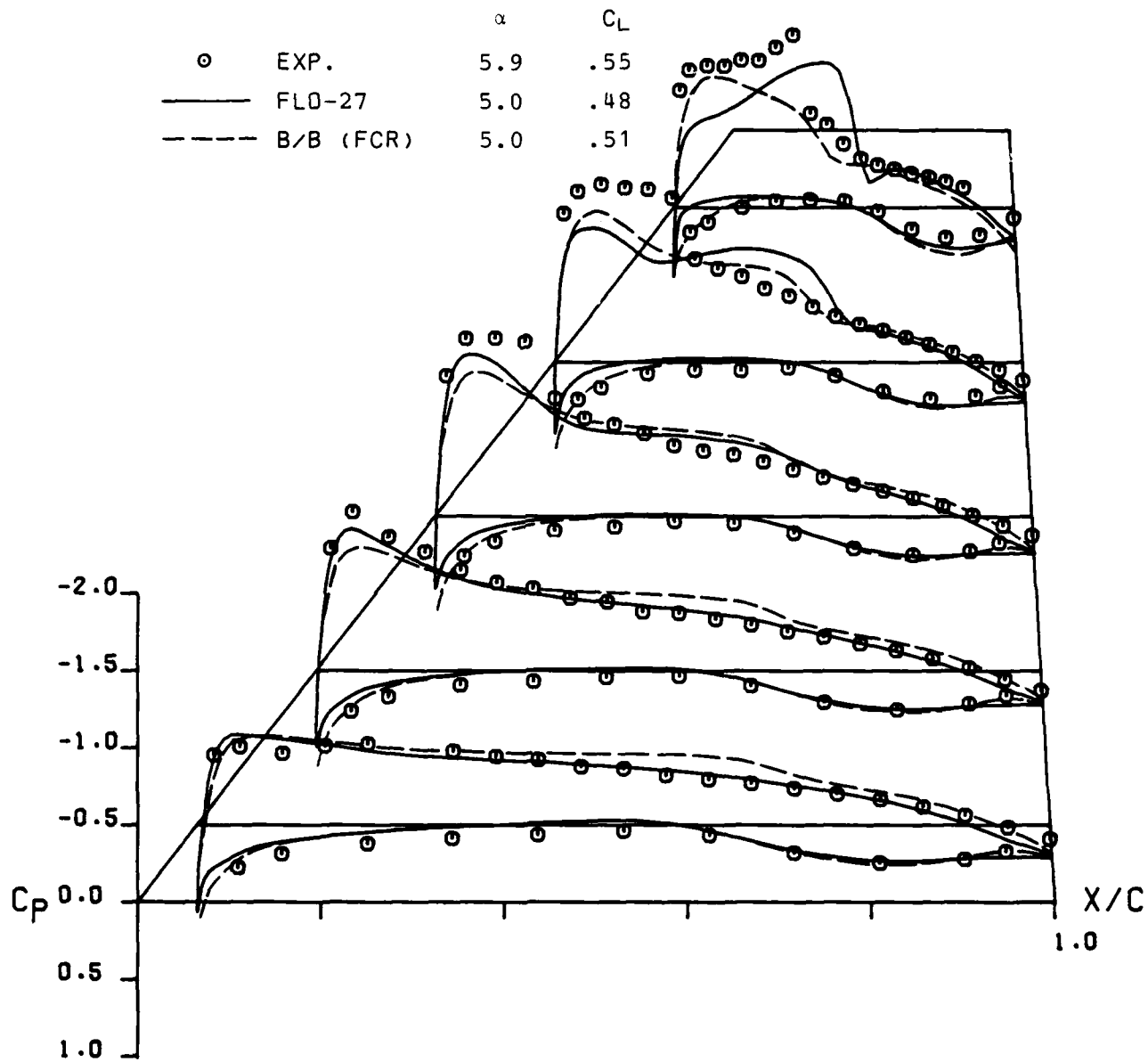


Figure 84. - Comparison of conservative solutions with experiment for Wing C at  $M = .85$ .



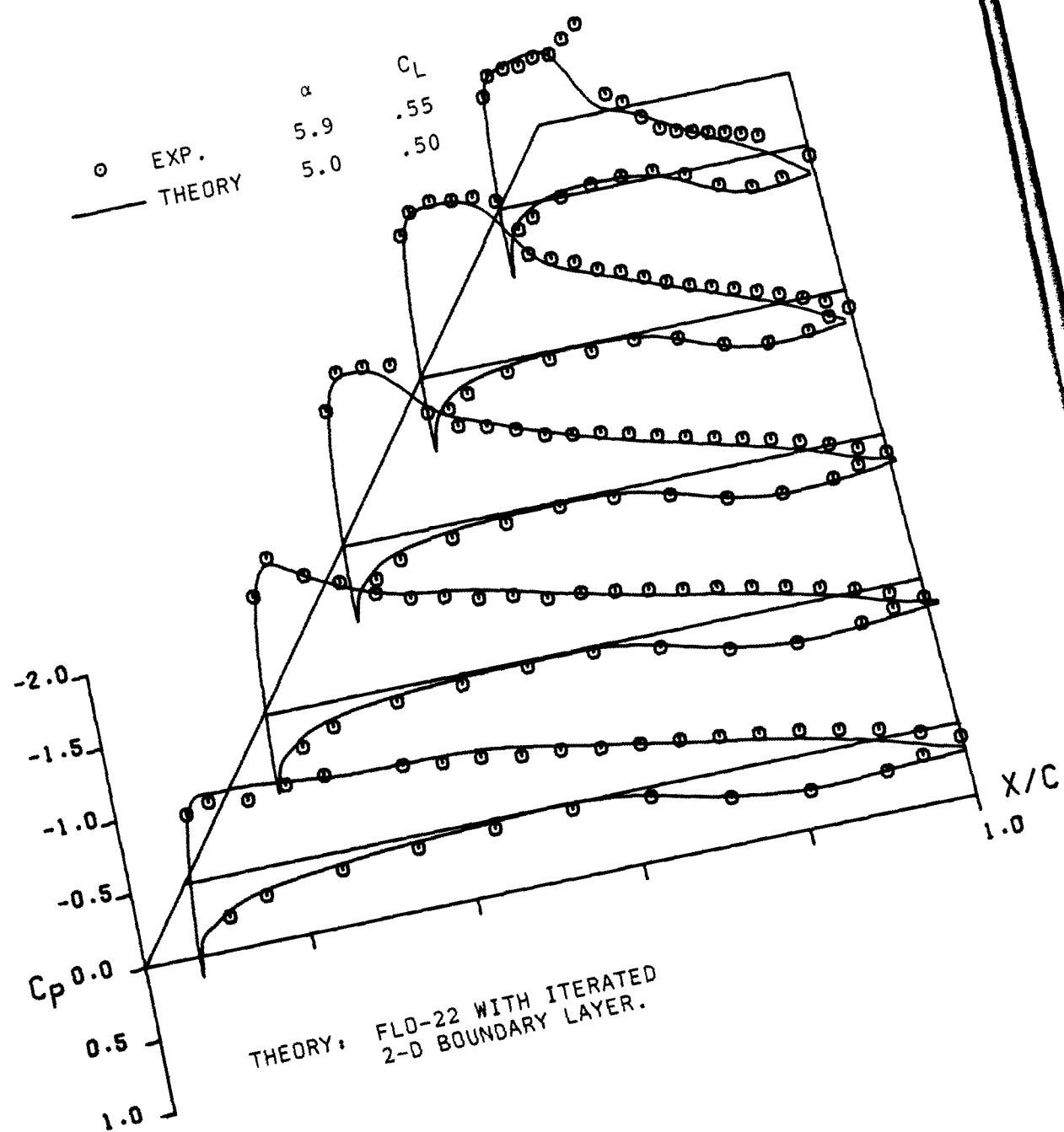


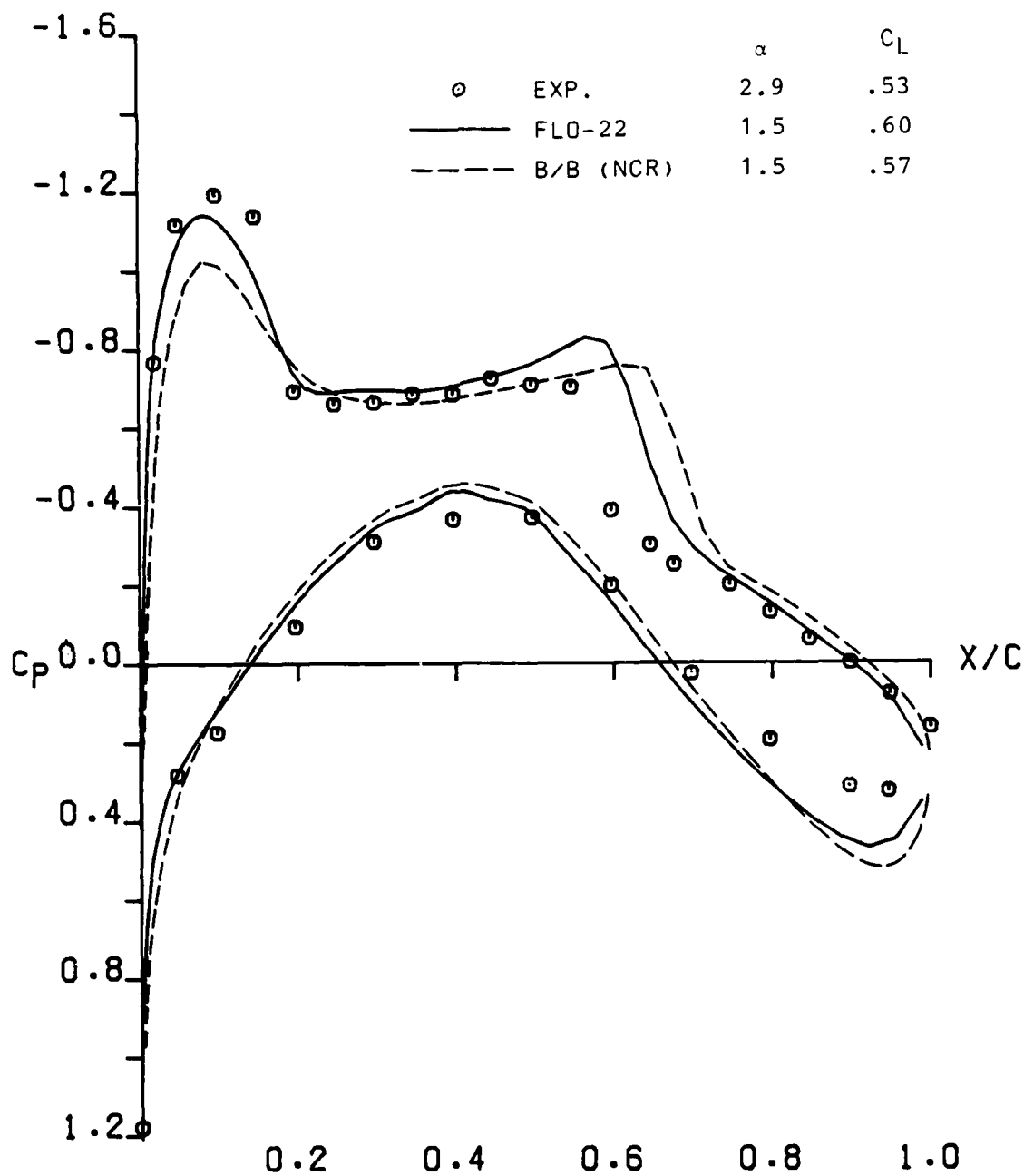
Figure 85 . - Comparison of FLO-22 results with experiment when viscous corrections are included; Wing C,  $M=0.85$ .

## APPENDIX A

### THREE-DIMENSIONAL TRANSONIC CODE CORRELATIONS

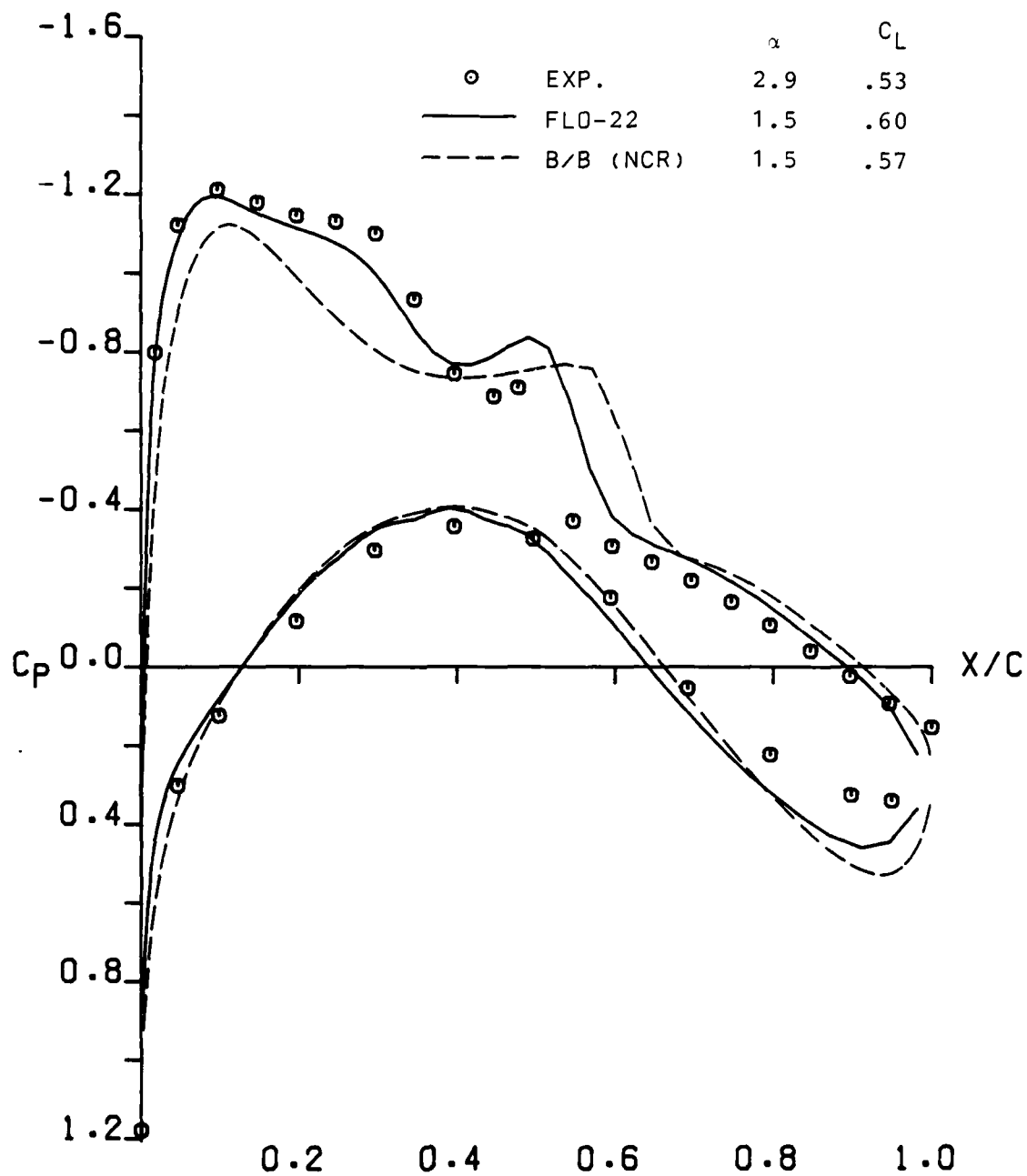
APPENDIX A  
THREE-DIMENSIONAL TRANSONIC CODE CORRELATIONS

This appendix contains the detailed results of comparisons of theoretical solutions with experimental data for Wings A, B, and C. These comparisons correspond to the summary results presented and discussed in Section 7.3 of this report. The data include pressure distribution comparisons at each span location and spanwise distributions of local section lift.



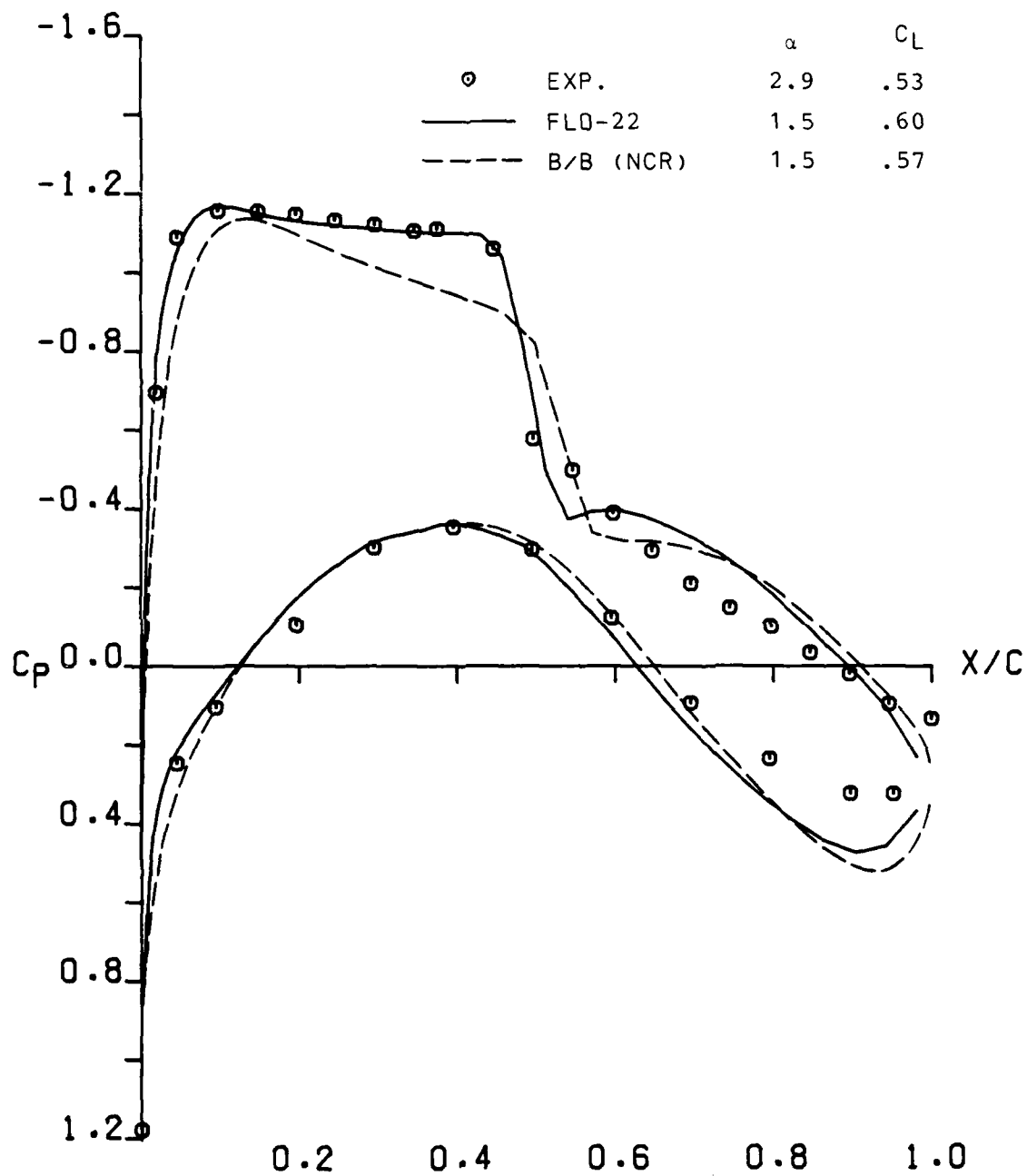
(a)  $\eta = .15$

Figure A-1. - Comparison of non-conservative code results with experiment for Wing A;  $M = .82$ ,  $C_L \approx .5$ .



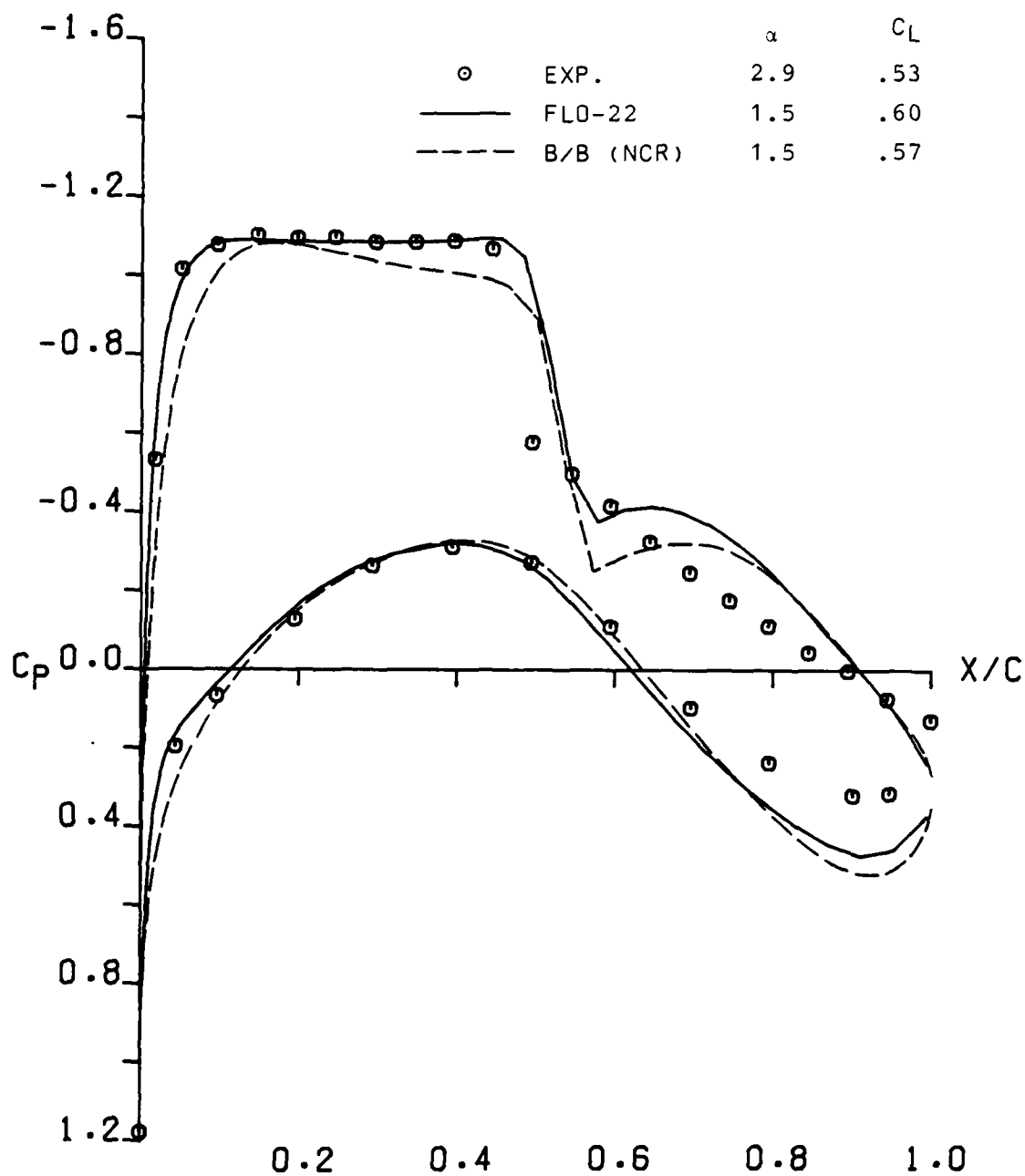
(b)  $\eta = .30$

Figure A-1. - Continued



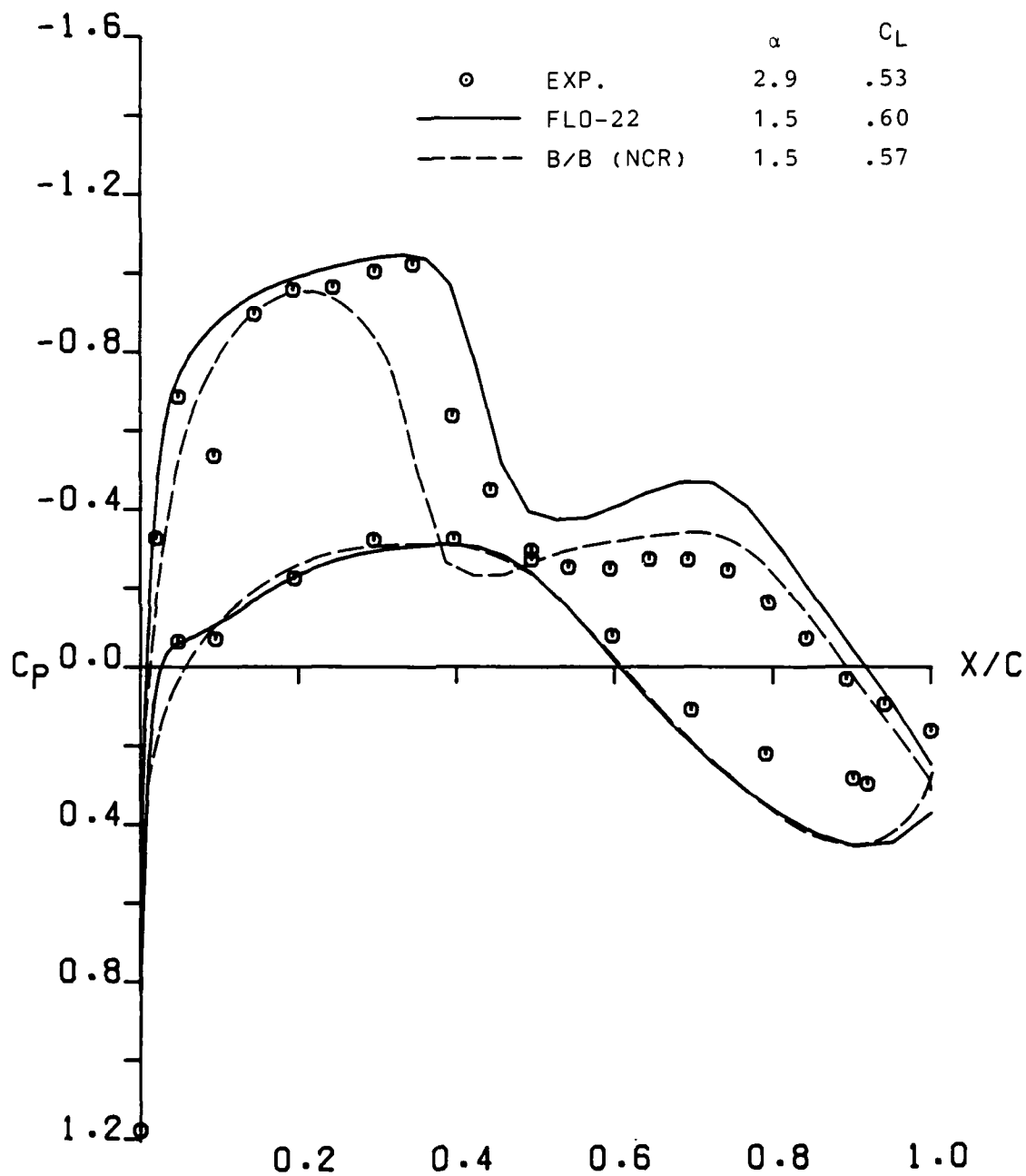
(c)  $n = .50$

Figure A-1. - Continued



(d)  $\eta = .70$

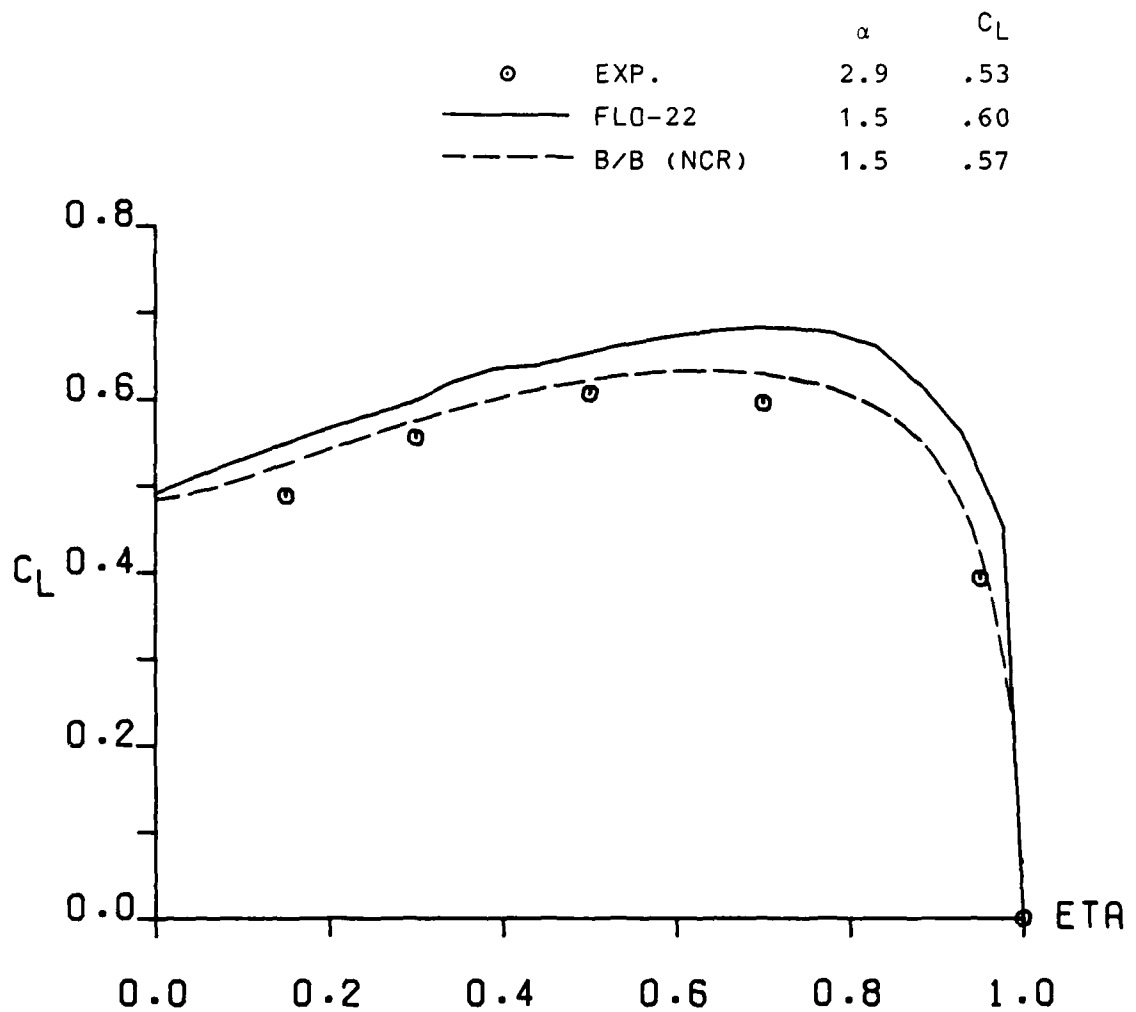
Figure A-1. - Continued



(e)  $\eta = .95$

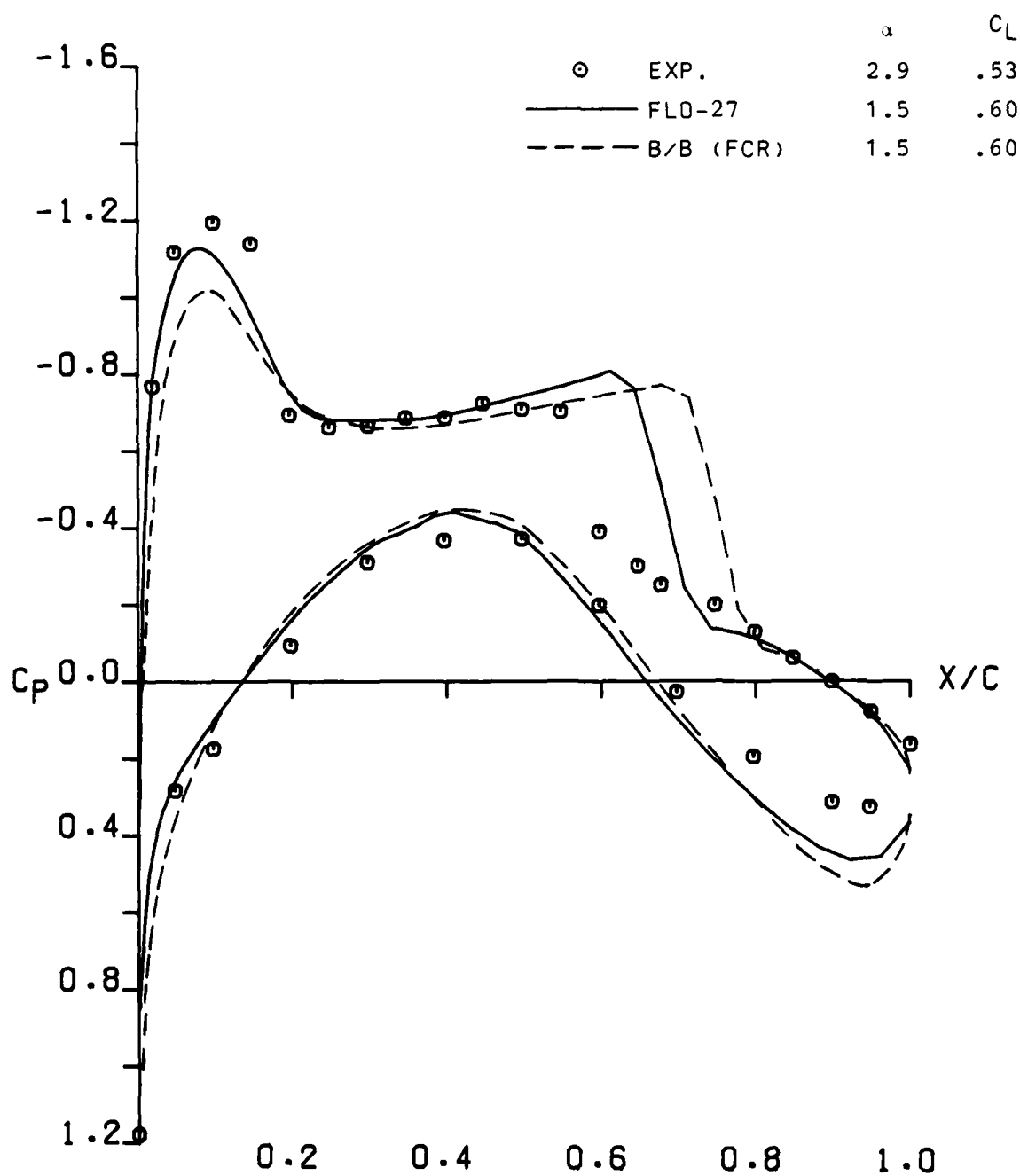
Figure A-1. - Continued





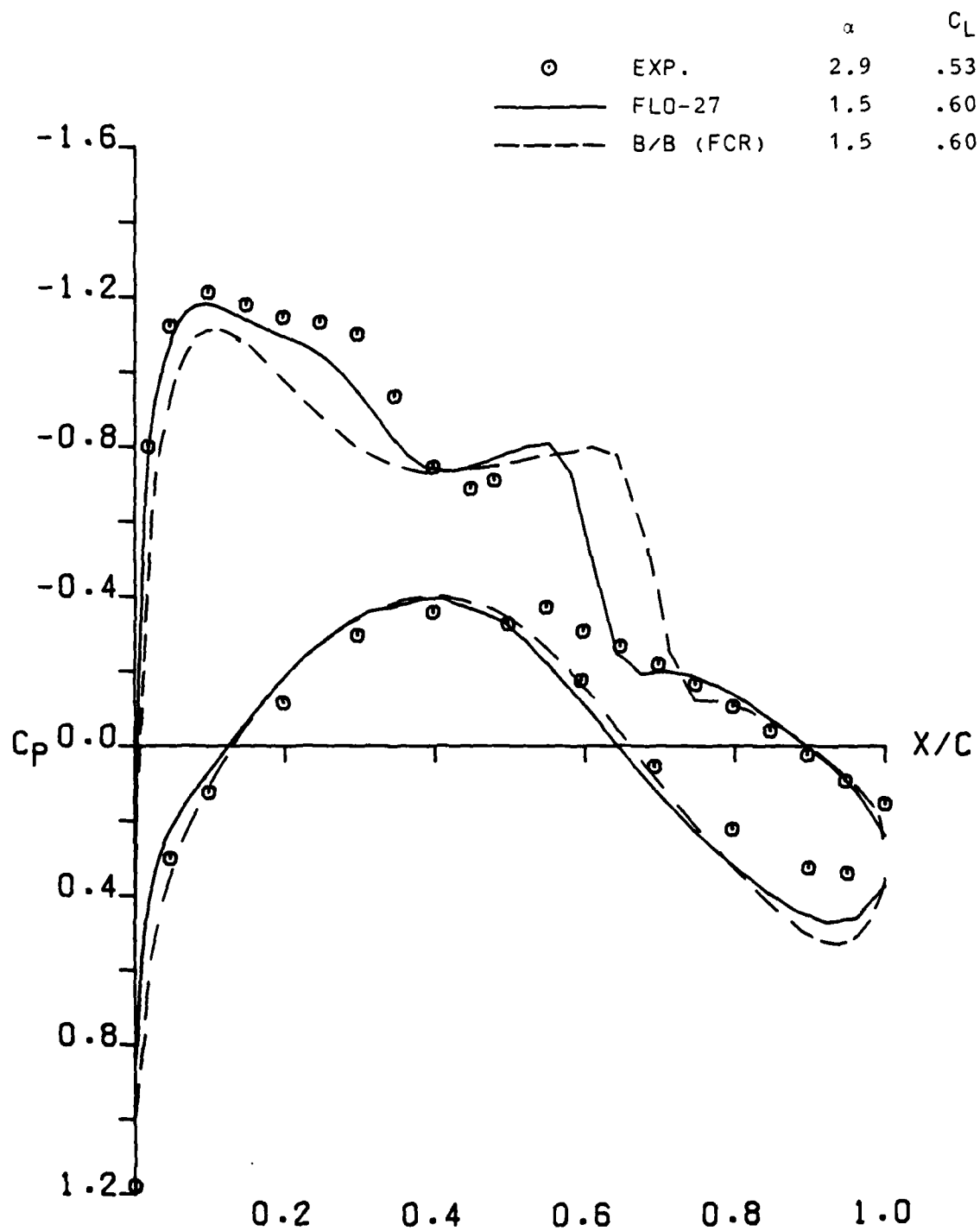
(f) Span load distribution

Figure A-1. - Concluded



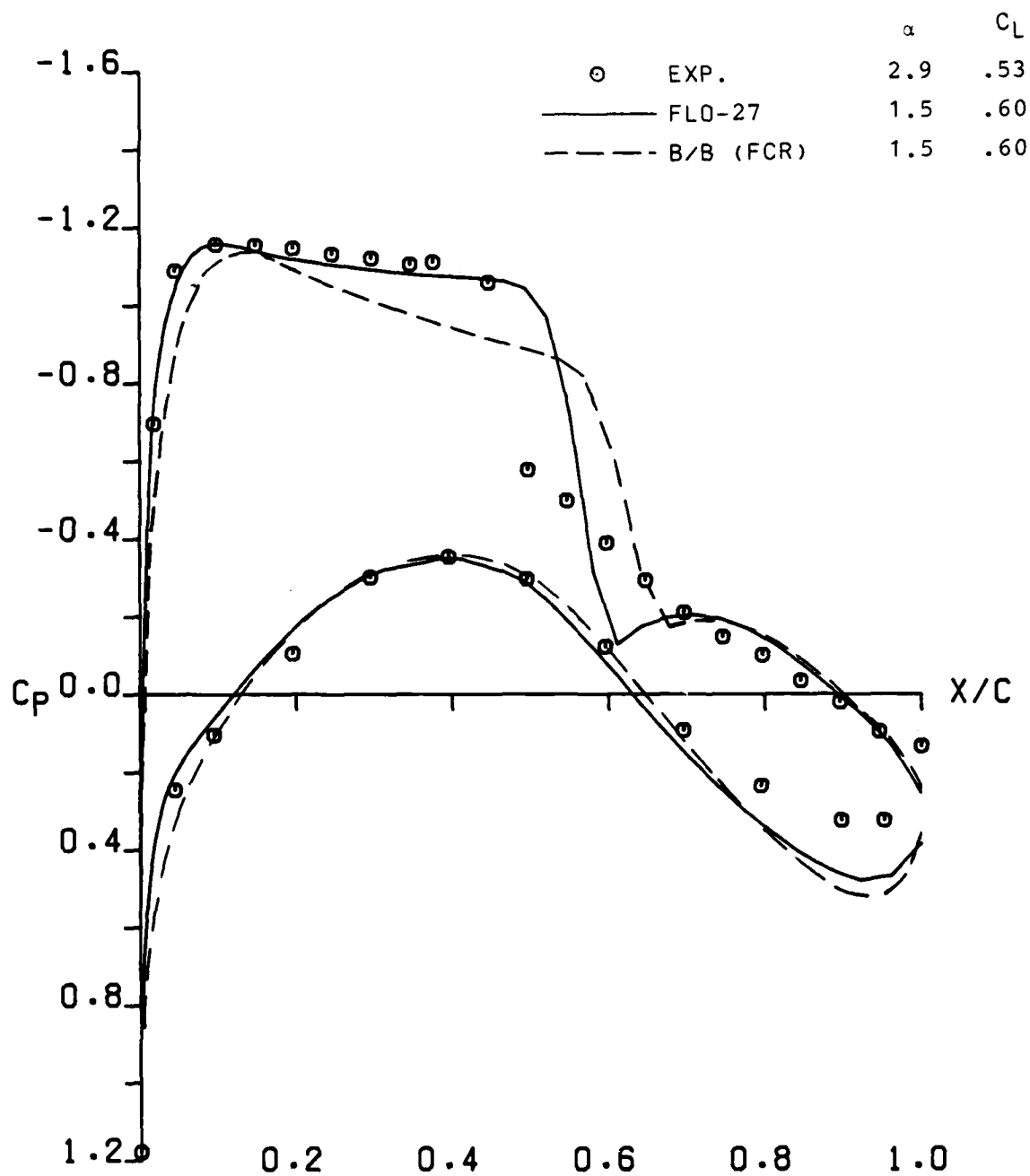
(a)  $\eta = .15$

Figure A-2. - Comparison of fully-conservative code results for Wing A;  $M = .82$ ,  $C_L \approx .5$ .



(b)  $\eta = .30$

Figure A-2. - Continued



(c)  $\eta = .50$

Figure A-2. - Continued

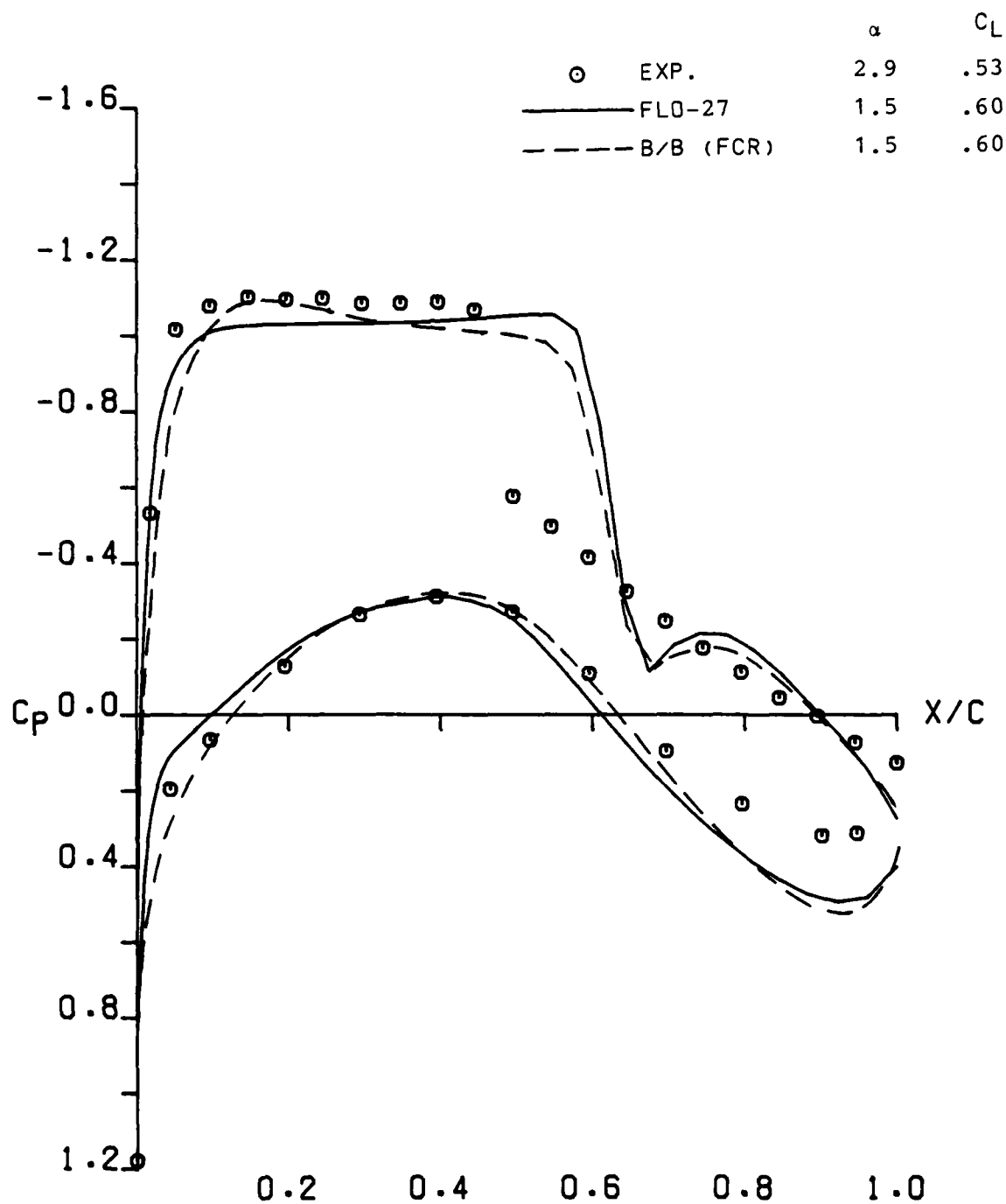
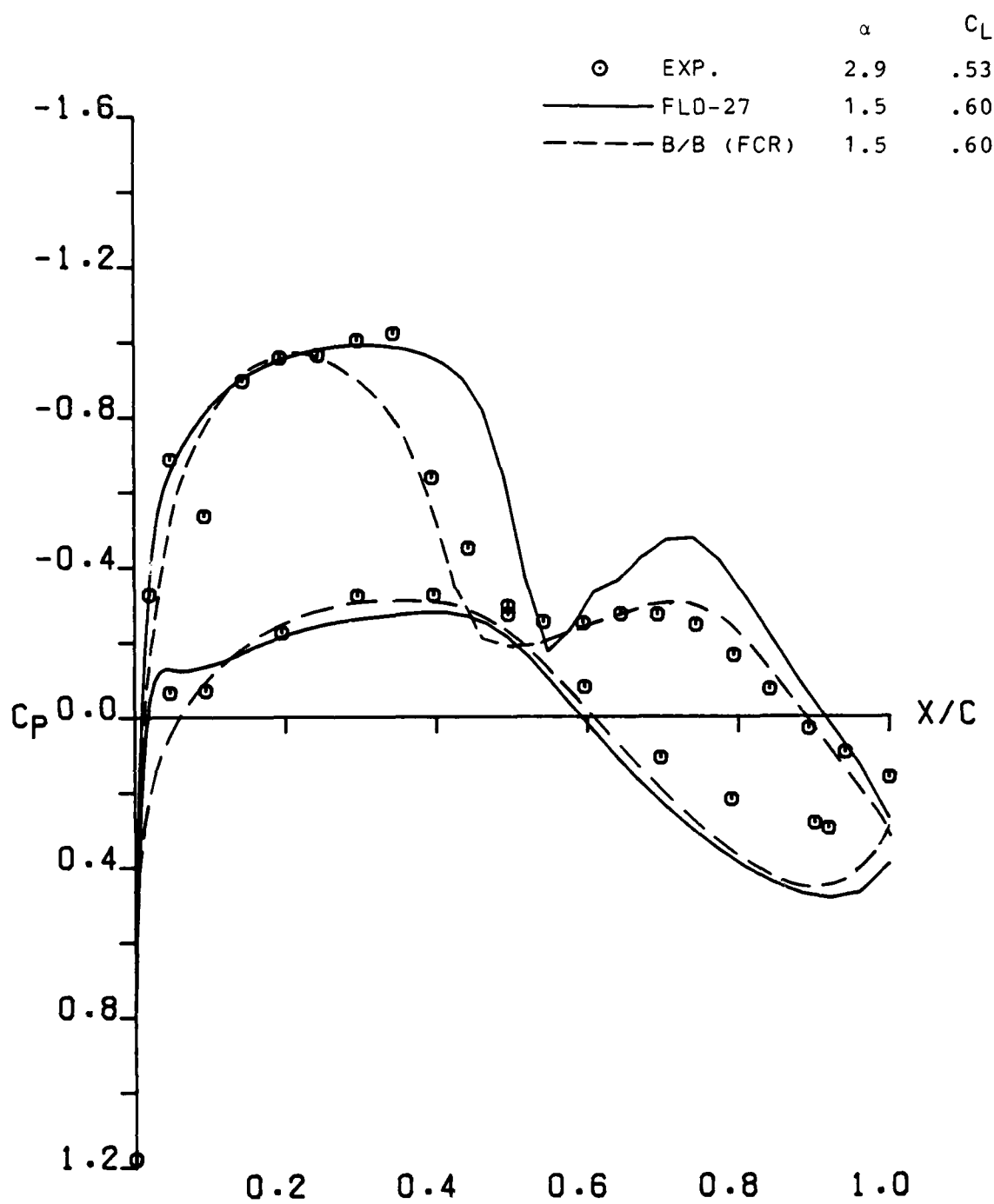


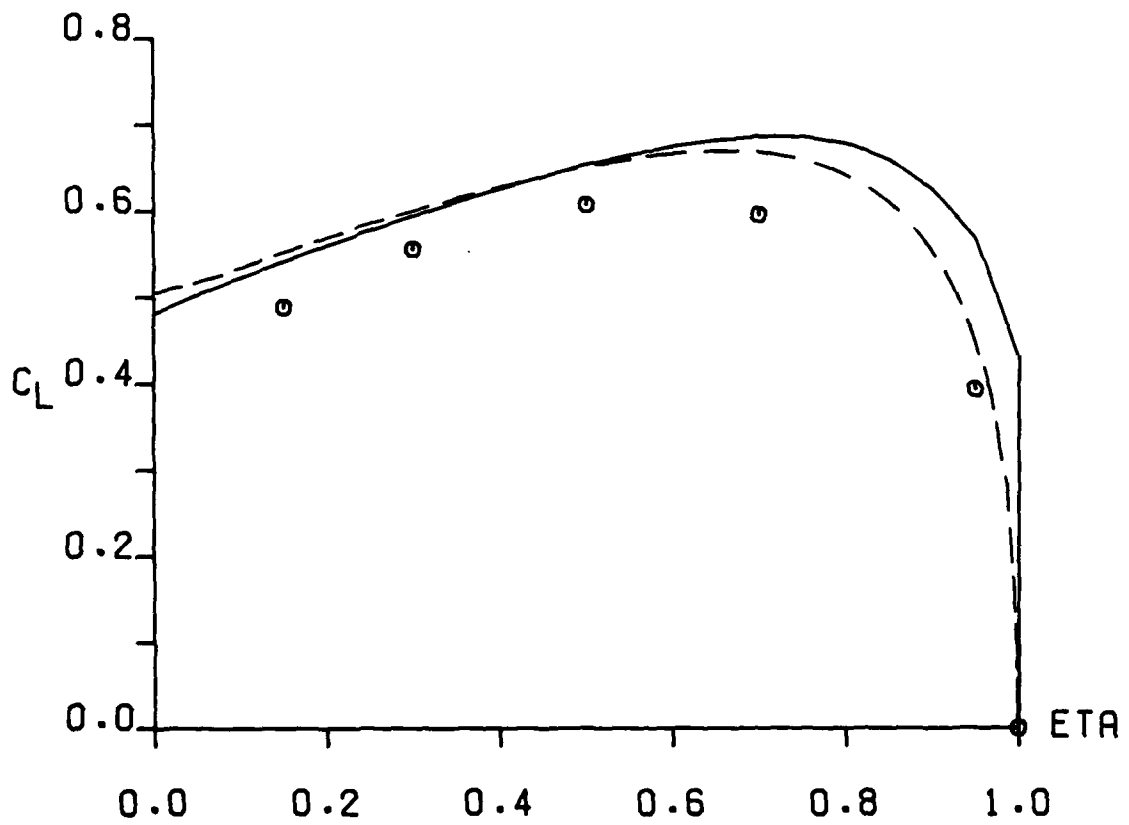
Figure A-2. - Continued



(e)  $\eta = .95$

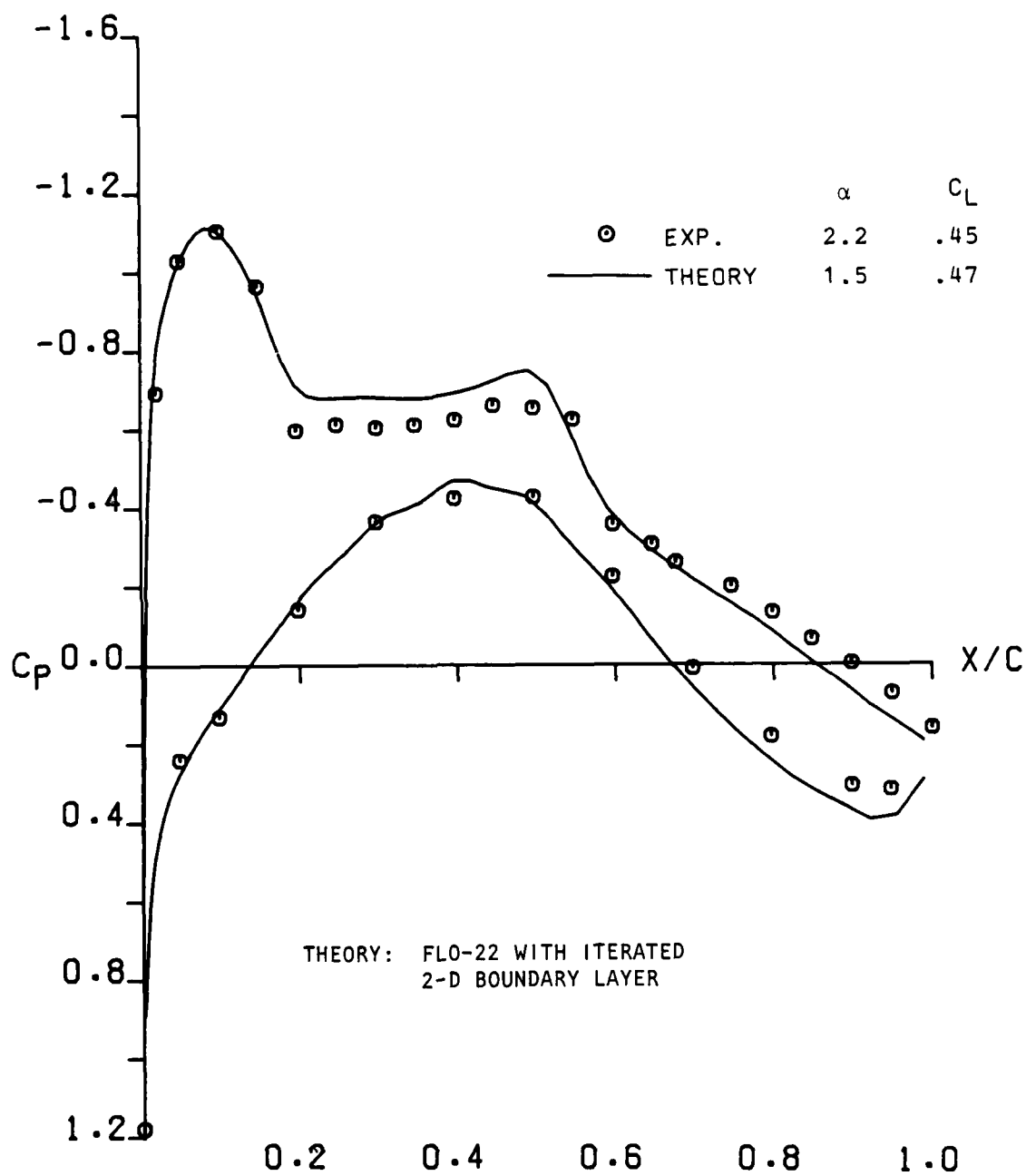
Figure A-2. - Continued

		$\alpha$	$C_L$
⊙	EXP.	2.9	.53
—	FLO-27	1.5	.60
- - -	B/B (FCR)	1.5	.60



(f) Span load distribution

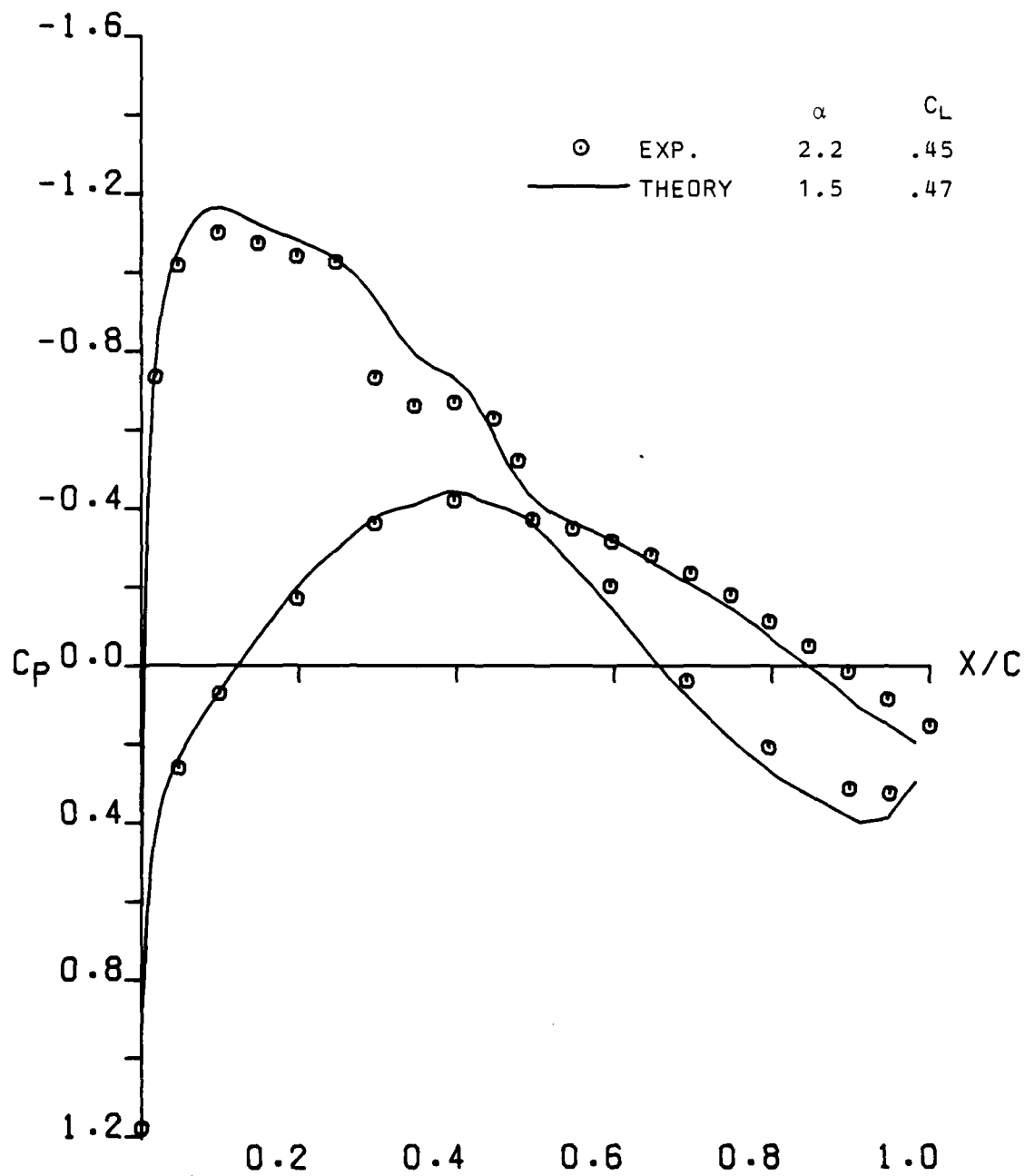
Figure A-2. - Concluded



(a)  $\eta = .15$

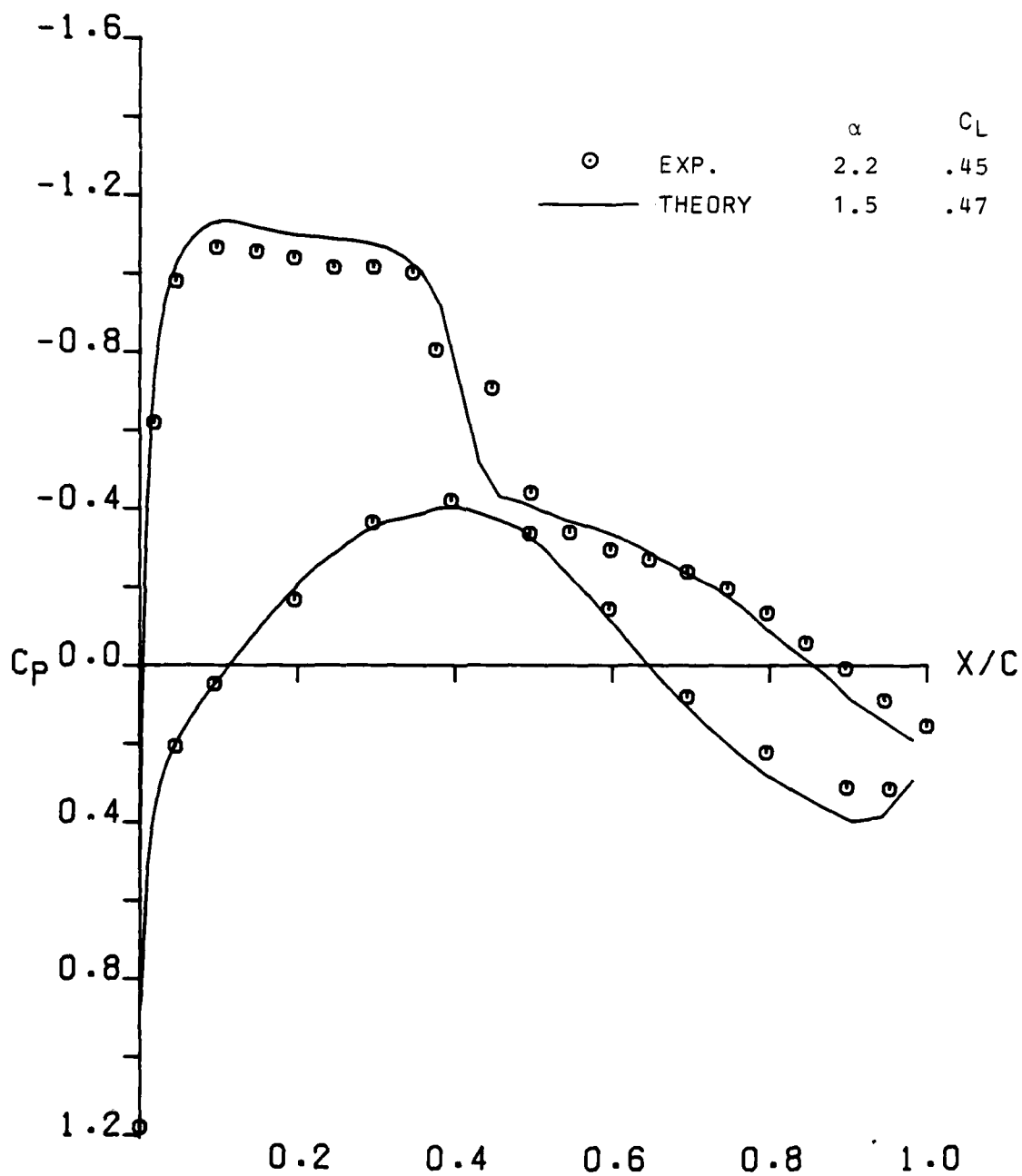
Figure A-3. - Comparison of FLO-22 results with experiment when viscous corrections are included; Wing A,  $M = .82$ .





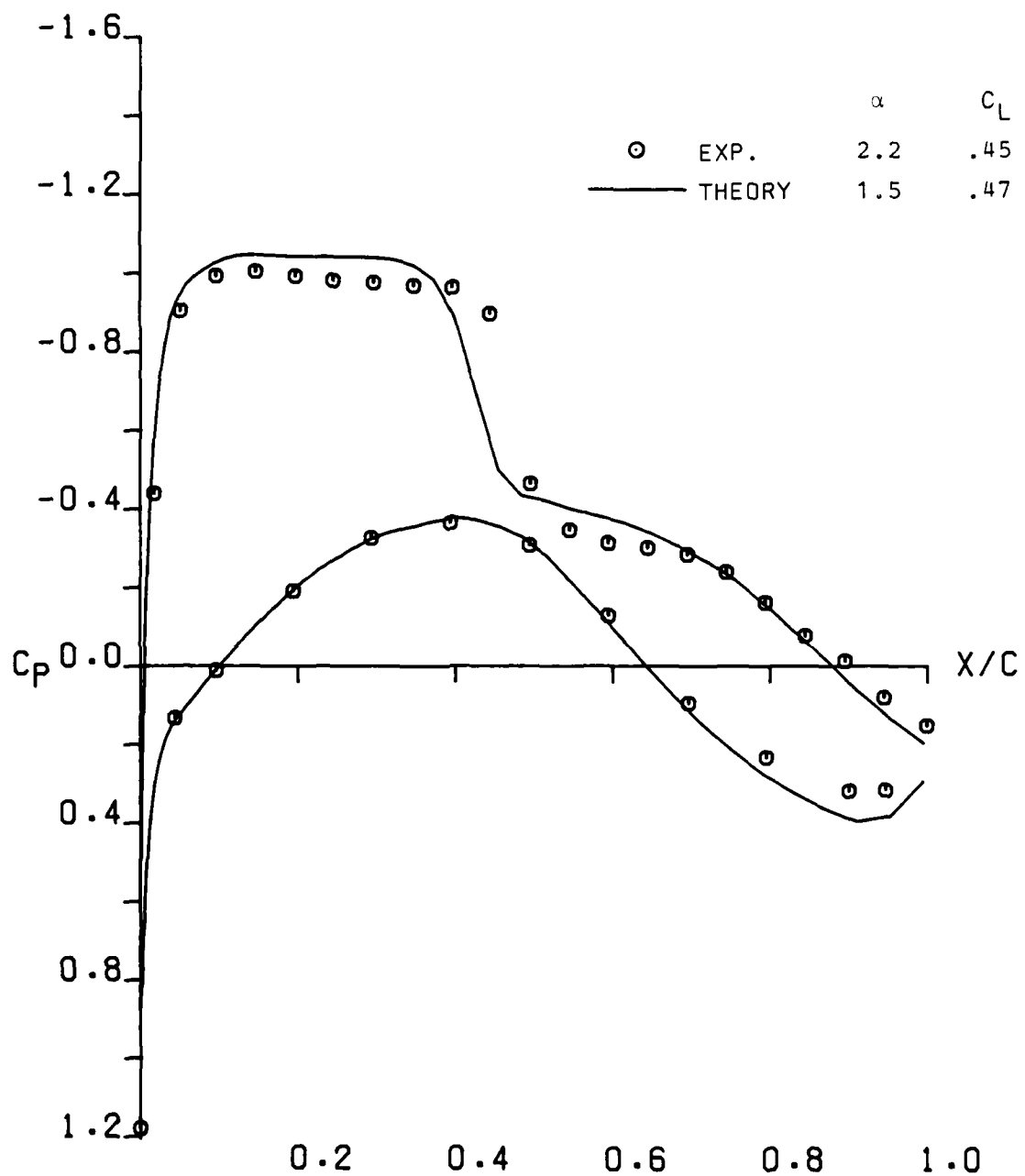
(b)  $\eta = .30$

Figure A-3. - Continued.



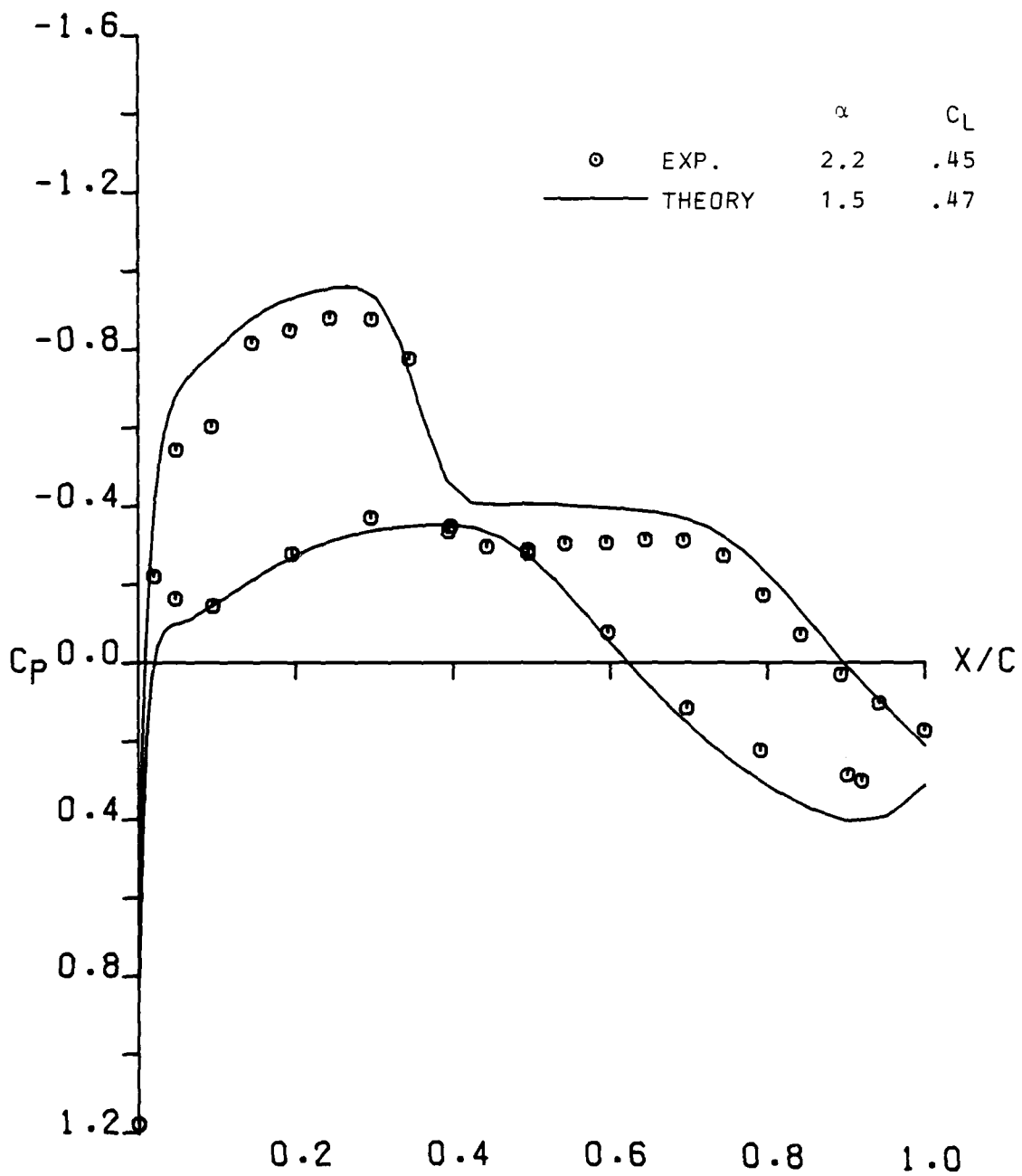
(c)  $\eta = .50$

Figure A-3. - Continued



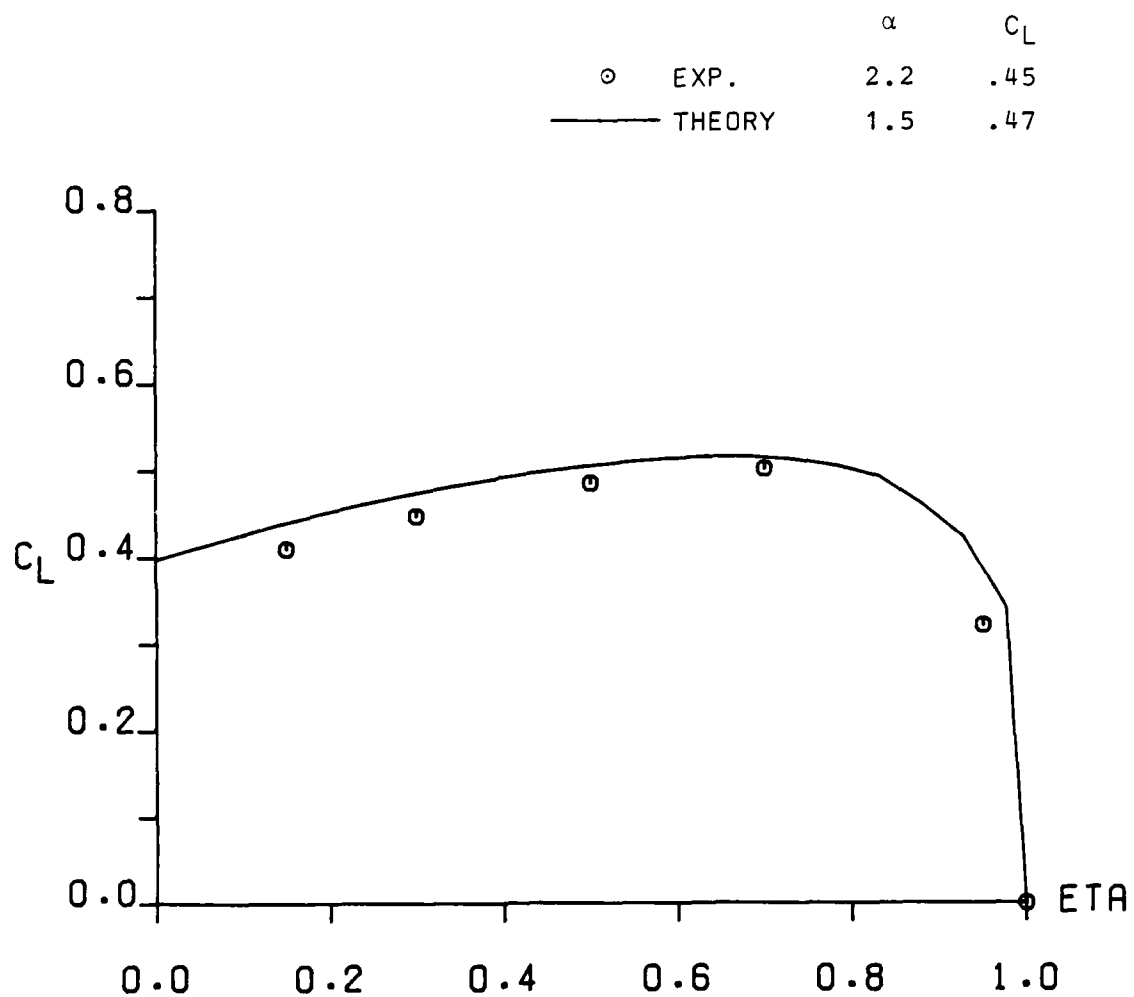
(d)  $\eta = .70$

Figure A-3. - Continued



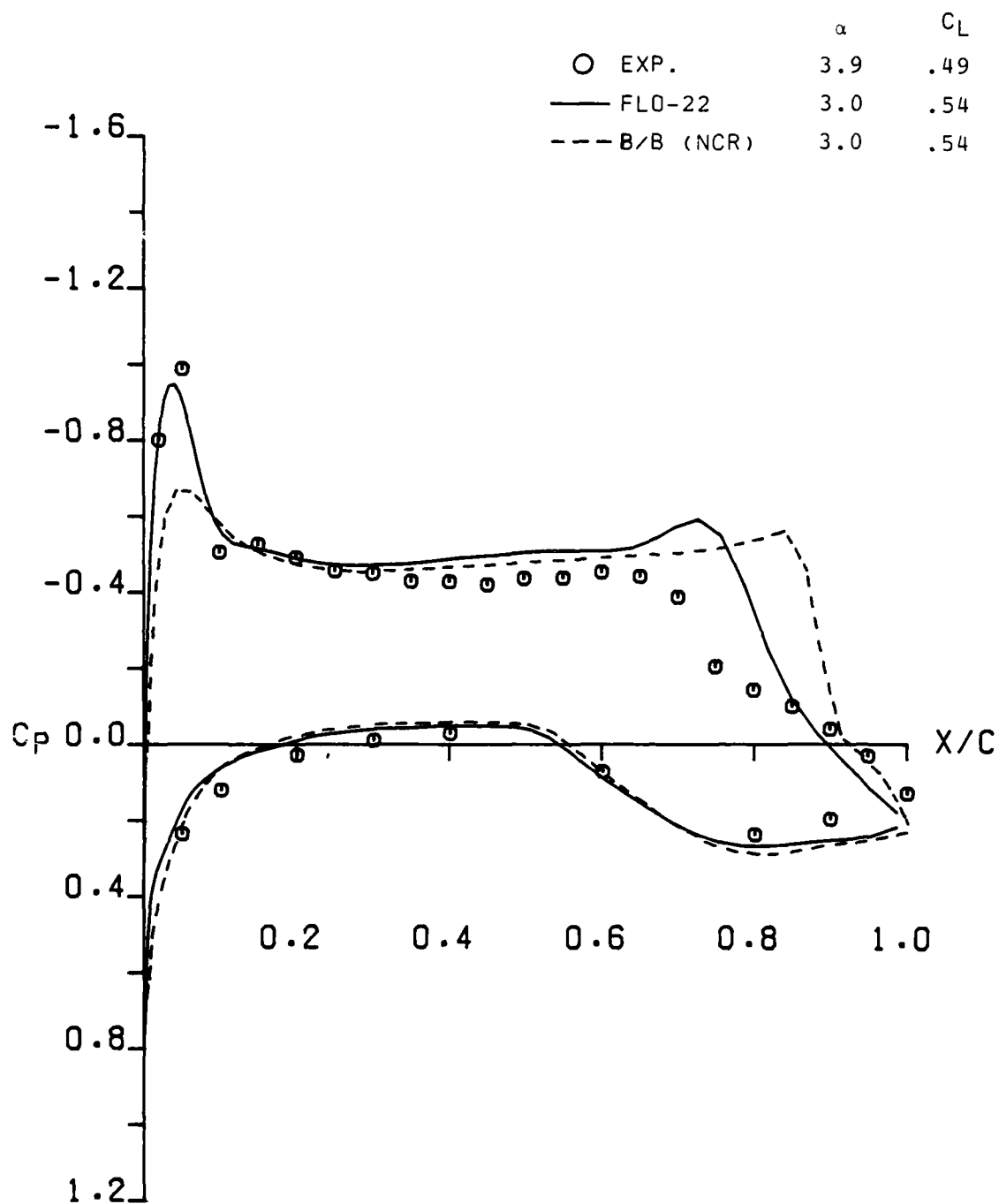
(e)  $\eta = .95$

Figure A-3. - Continued.



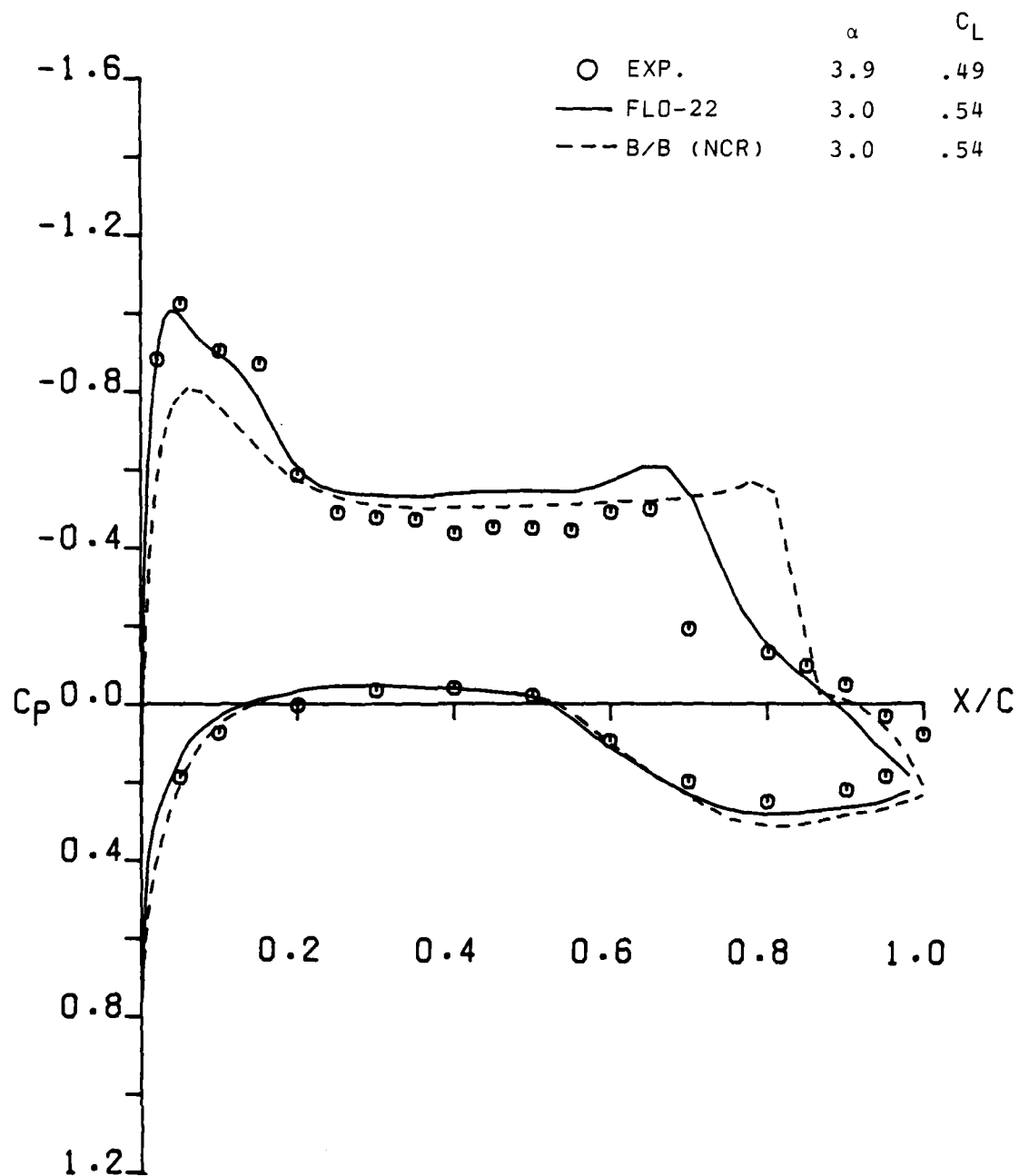
(f) Span load distribution

Figure A-3. - Concluded.



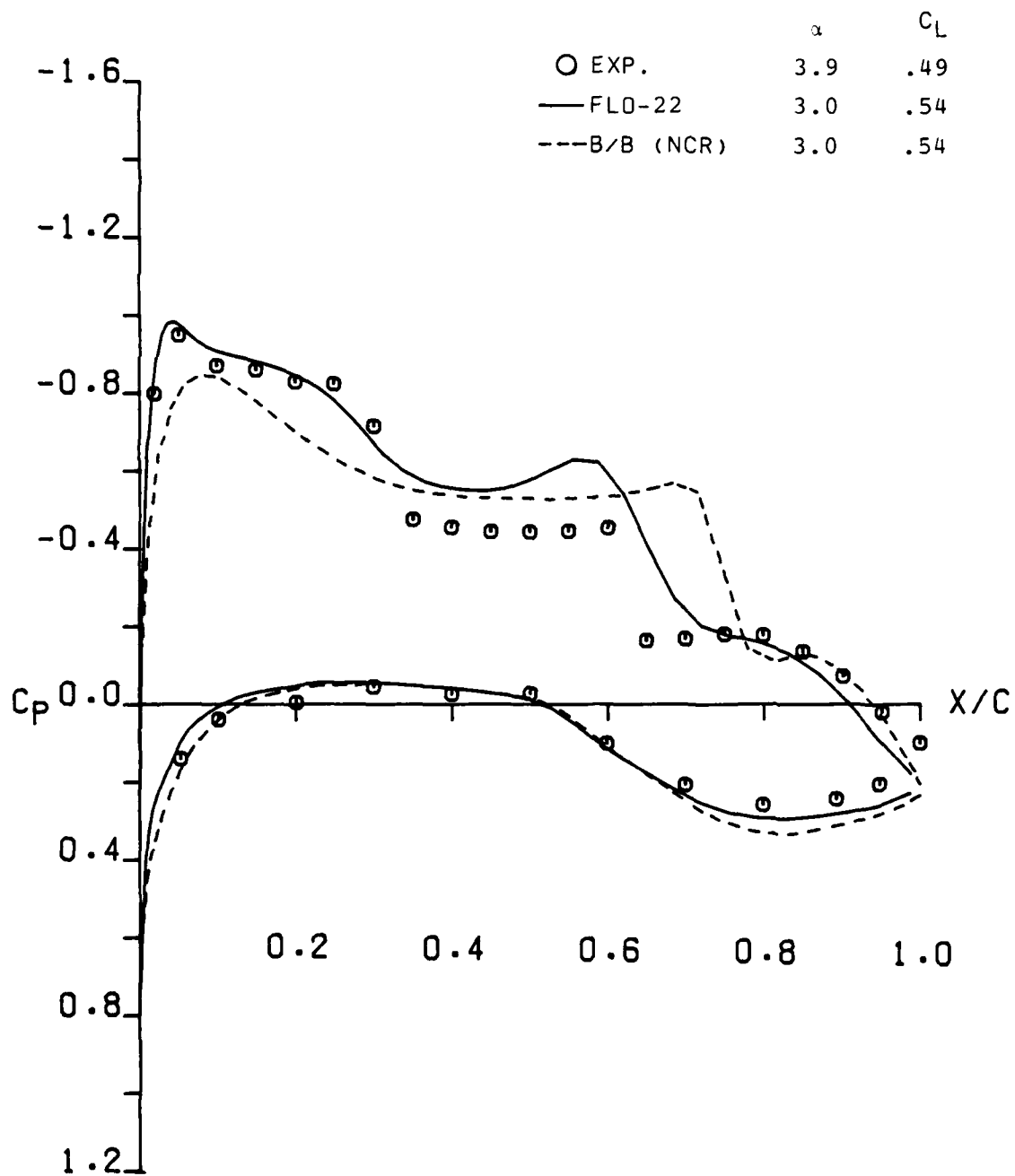
(a)  $\eta = .22$

Figure A-4. - Correlation of non-conservative codes using Wing B experimental data at  $M = 0.90$ ,  $C_L \approx .5$ .



(b)  $\eta = .40$

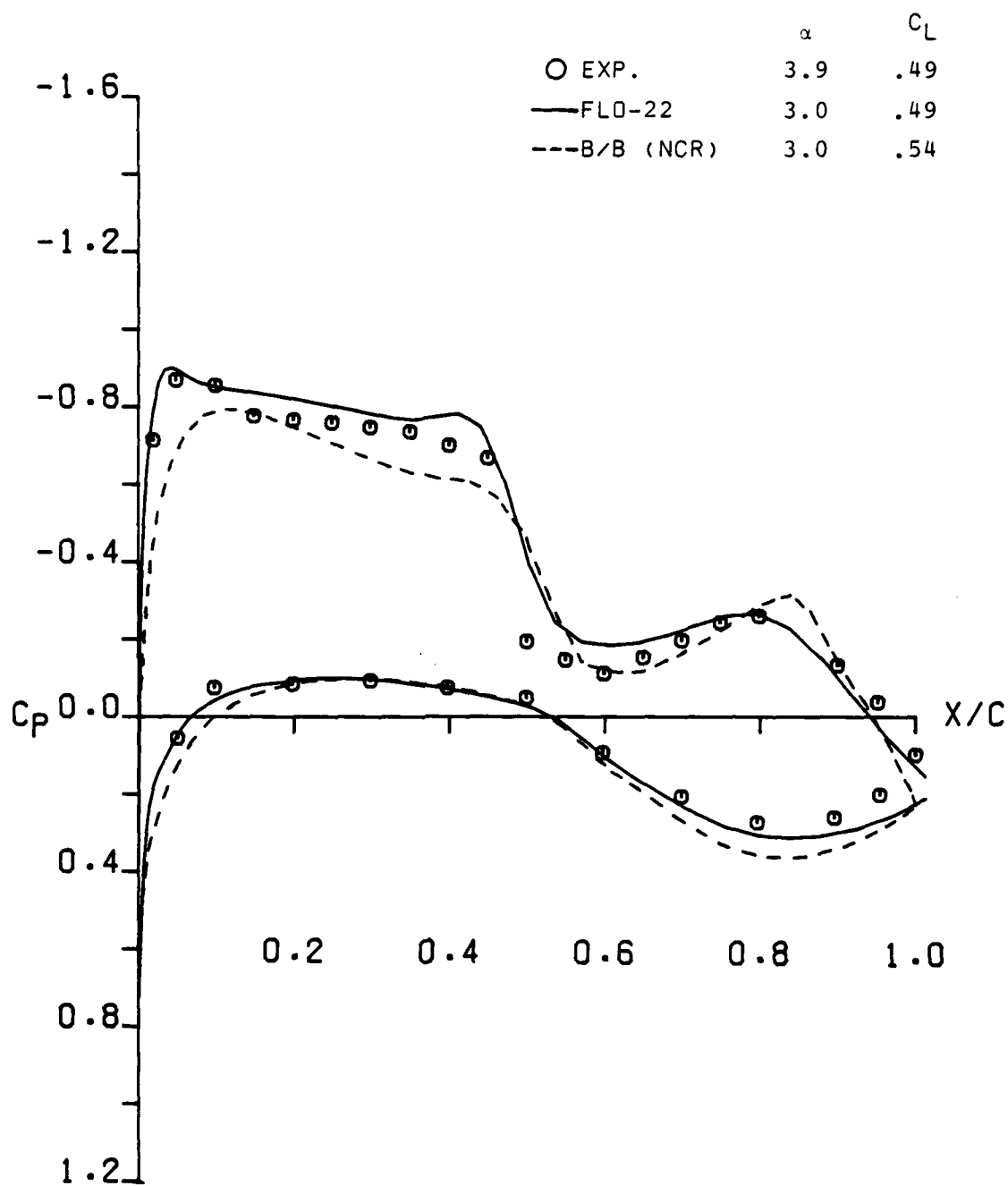
Figure A-4. - Continued.



(c)  $\eta = .60$

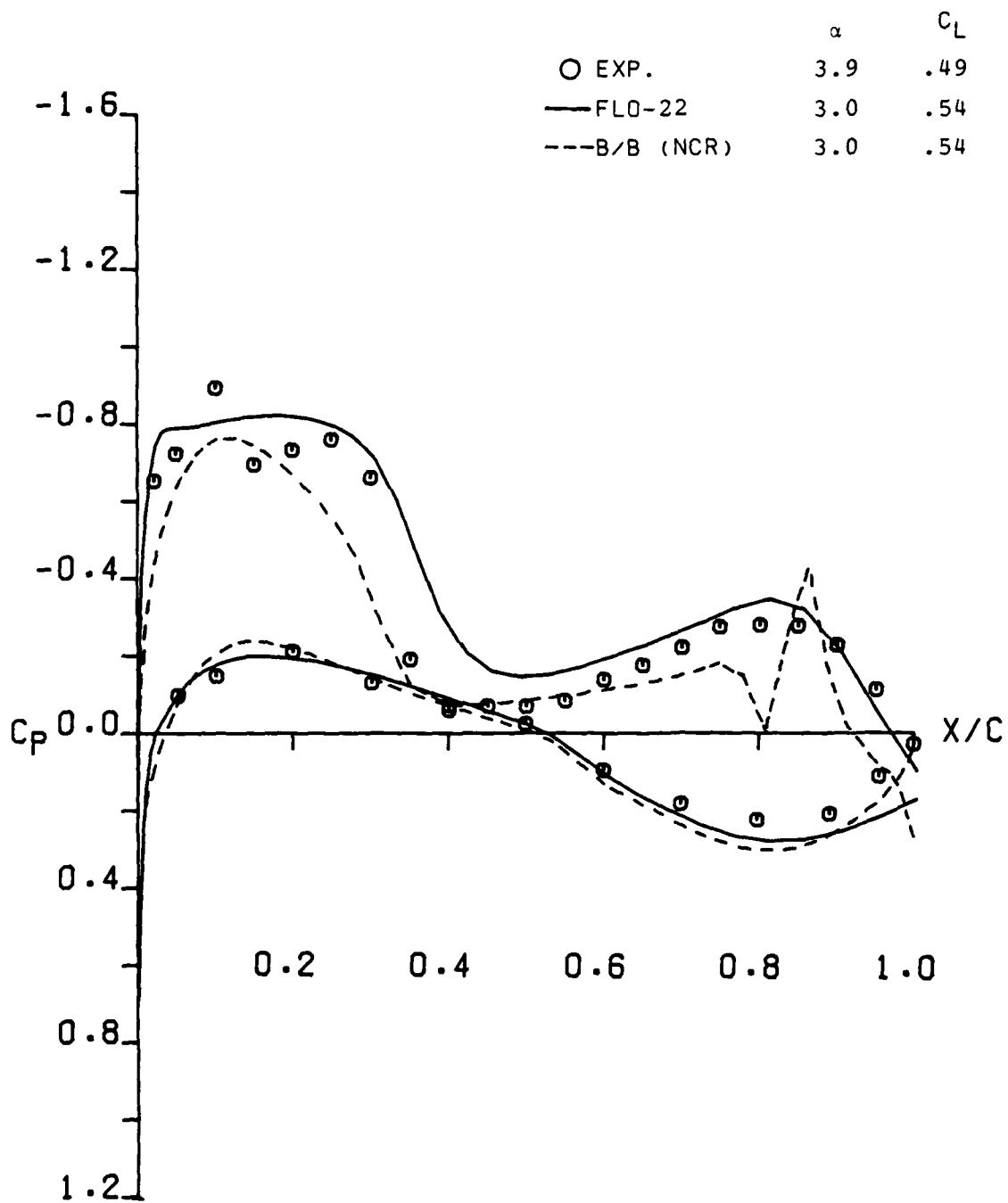
Figure A-4. - Continued.





(d)  $\eta = .80$

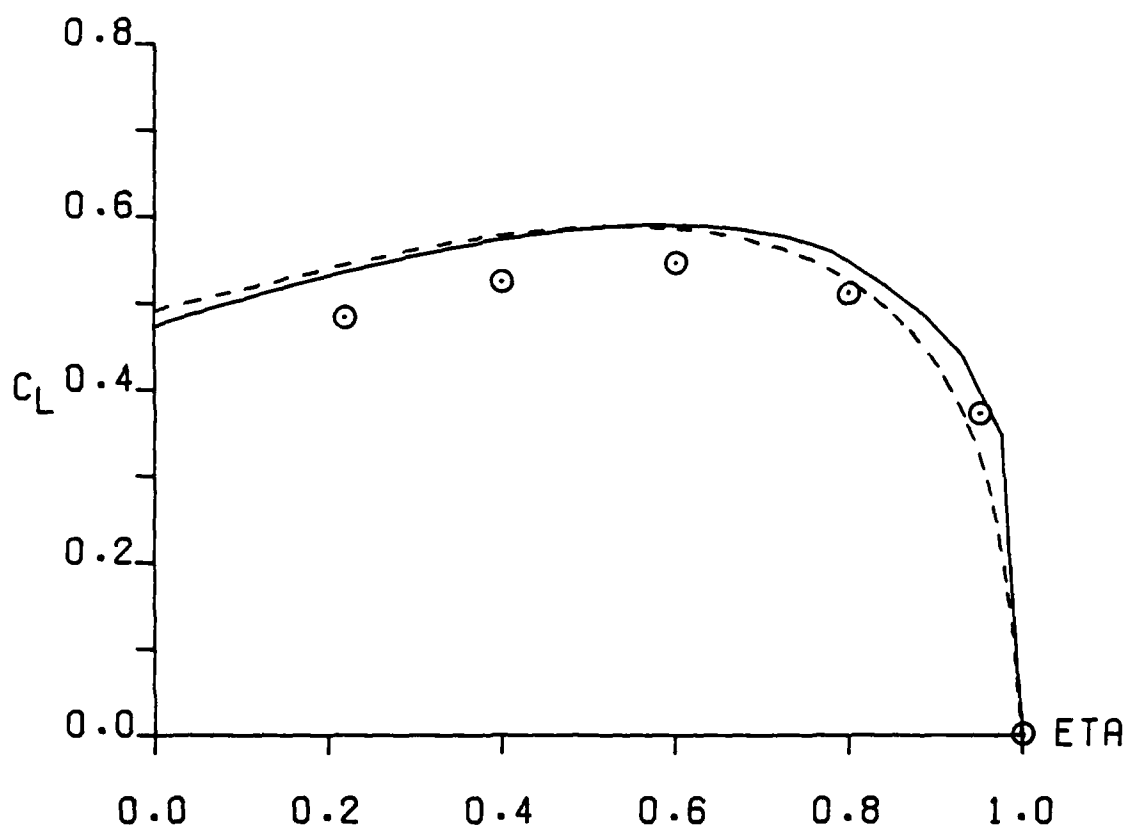
Figure A-4 . - Continued.



(e)  $\eta = .95$

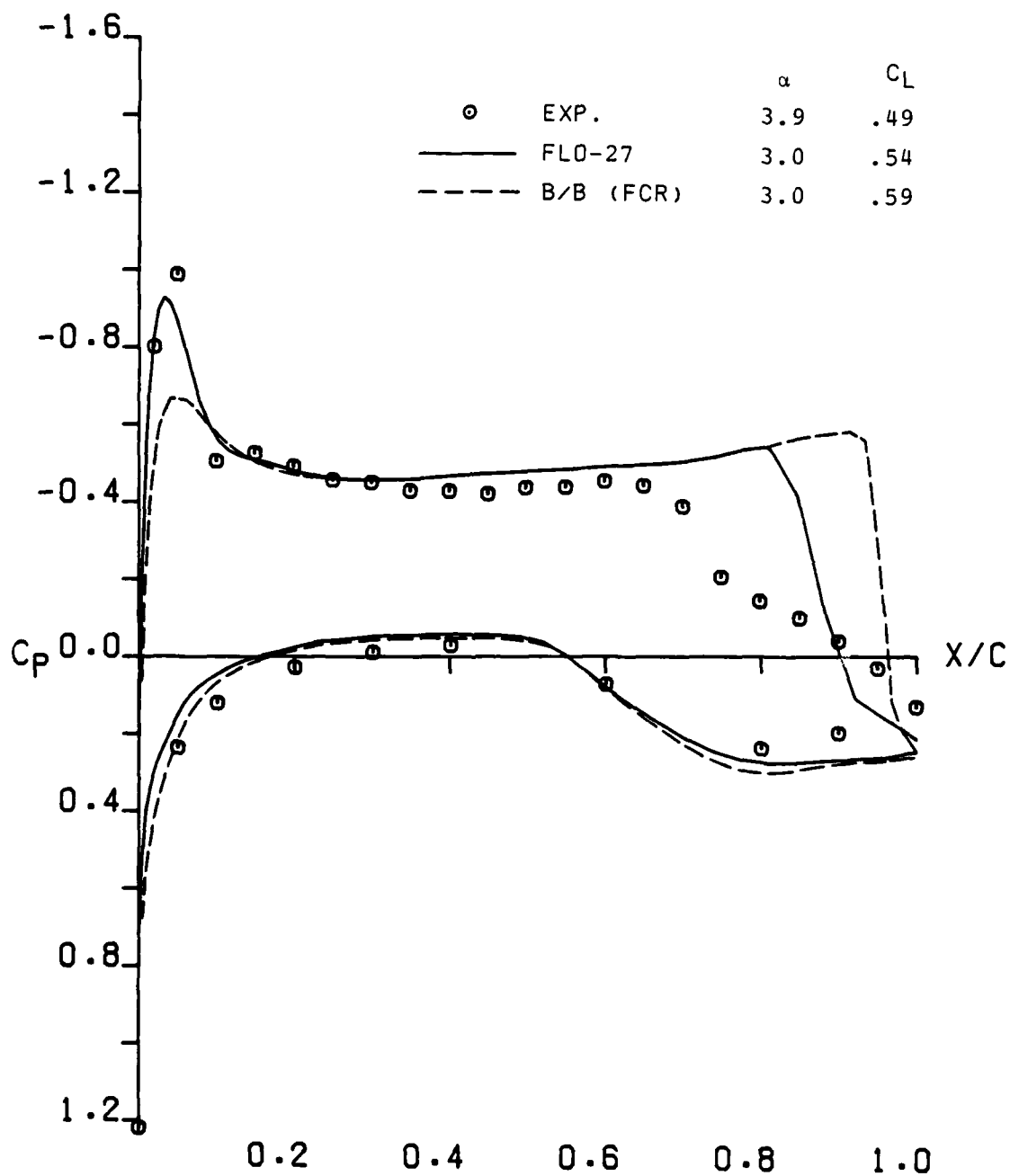
Figure A-4. - Continued.

	$\alpha$	$C_L$
○ EXP.	3.9	.49
— FLO-22	3.0	.54
--- B/B (NCR)	3.0	.54



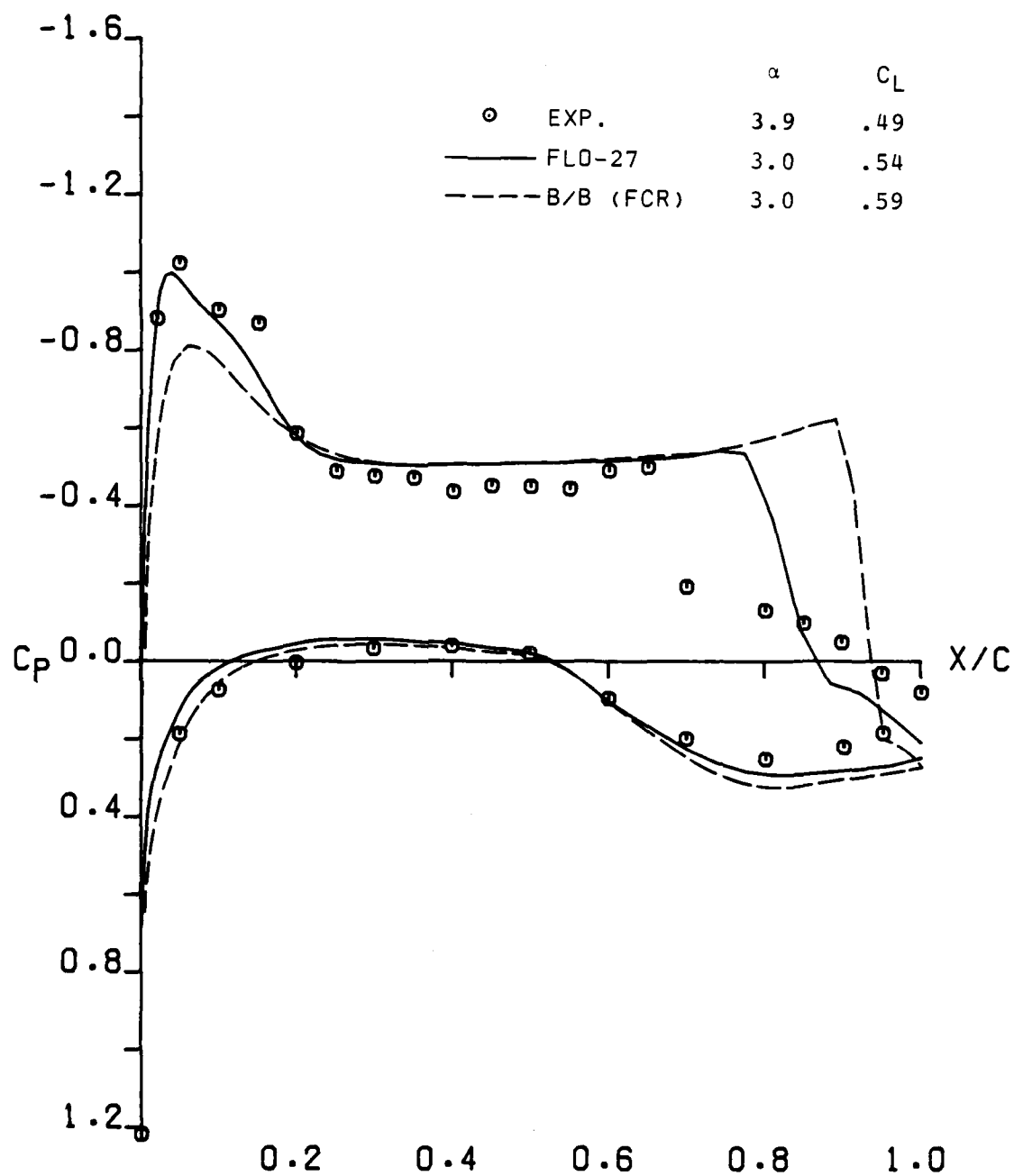
(f) Span load distribution

Figure A-4. - Concluded.



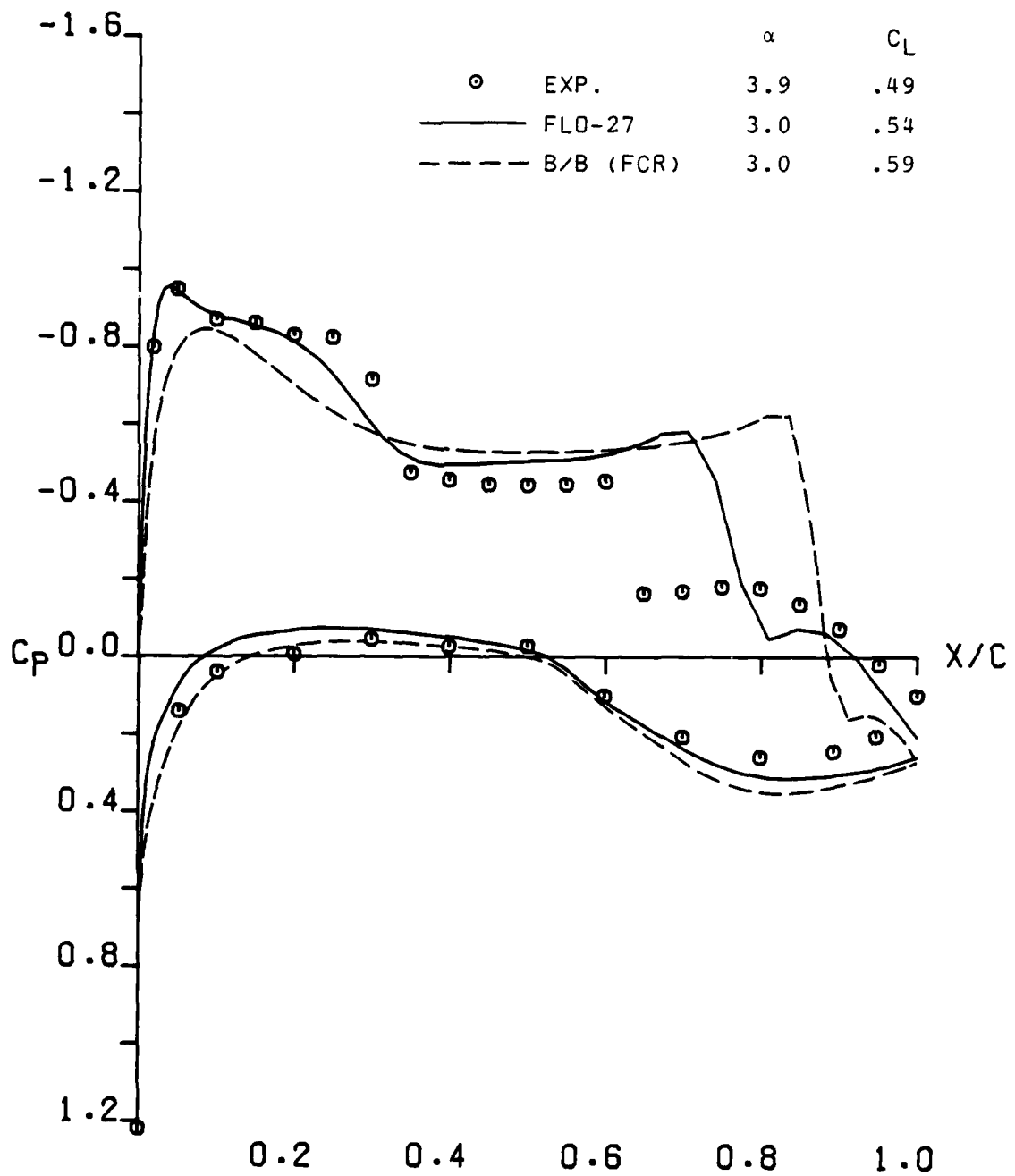
(a)  $\eta = .22$

Figure A-5. - Correlation of conservative codes using Wing B experimental data at  $M=0.90$ ,  $C_L \approx .5$ .



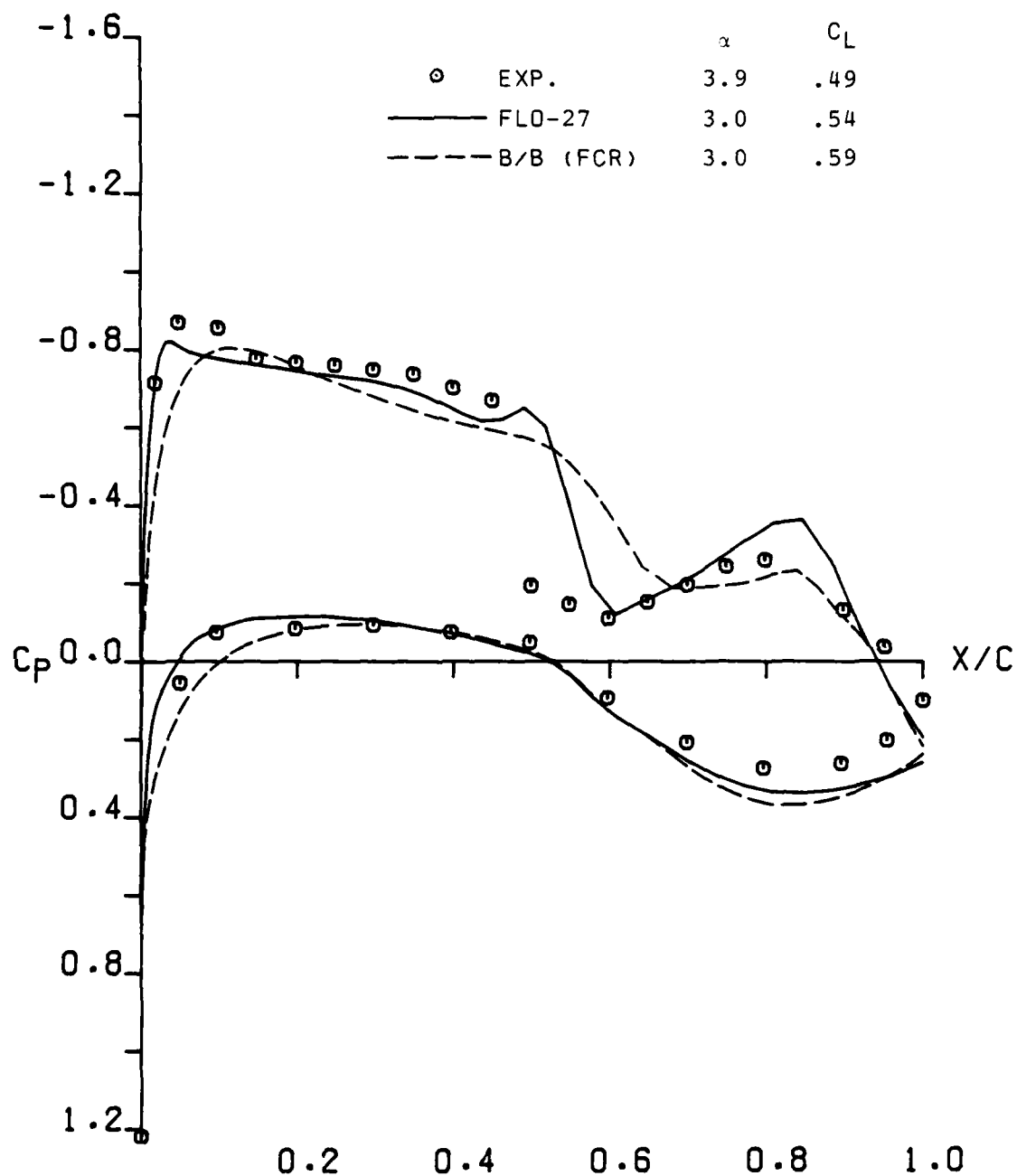
(b)  $\eta = .40$

Figure A-5. - Continued.



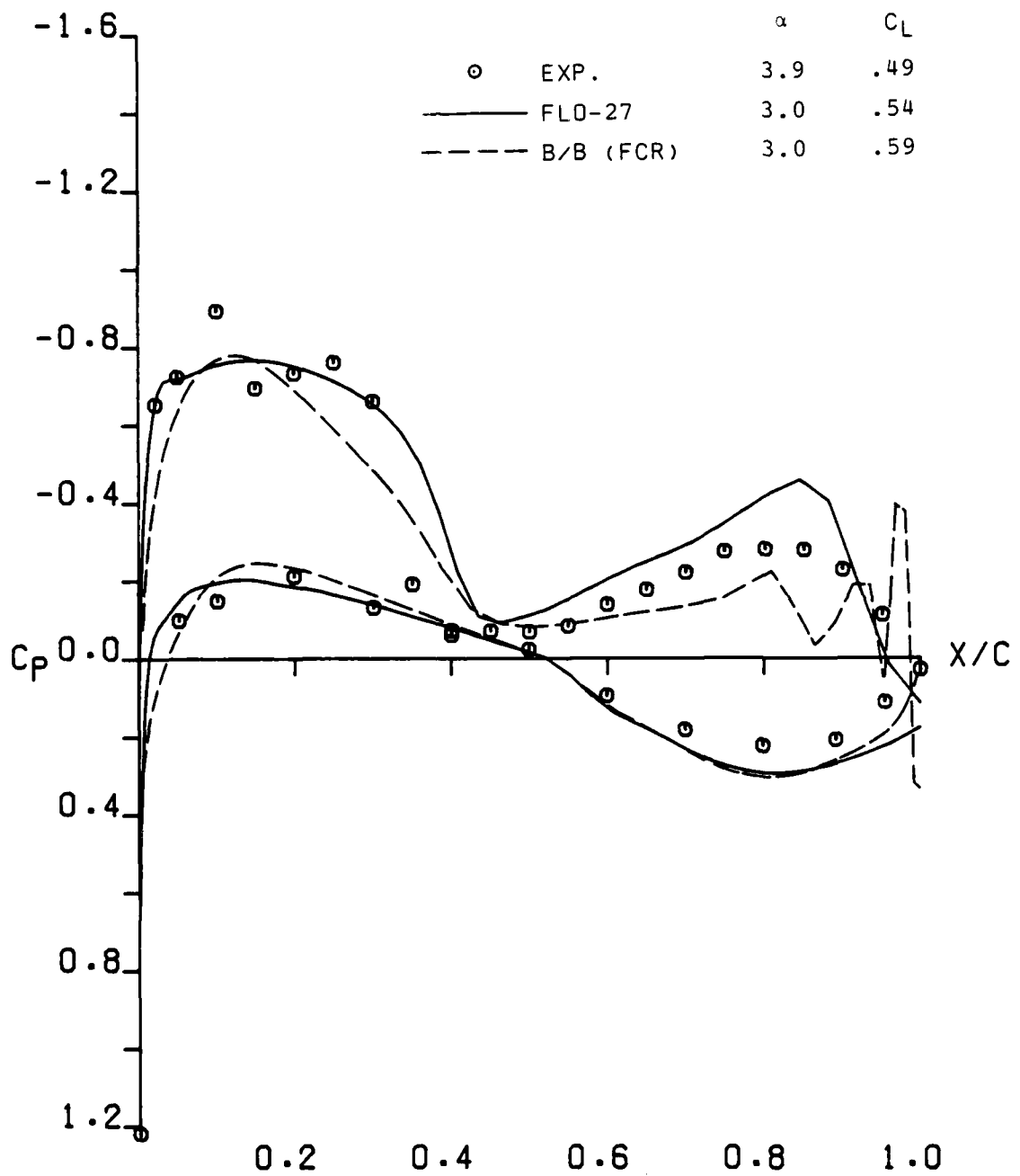
(c)  $\eta = .60$

Figure A-5. - Continued.



(d)  $\eta = .80$

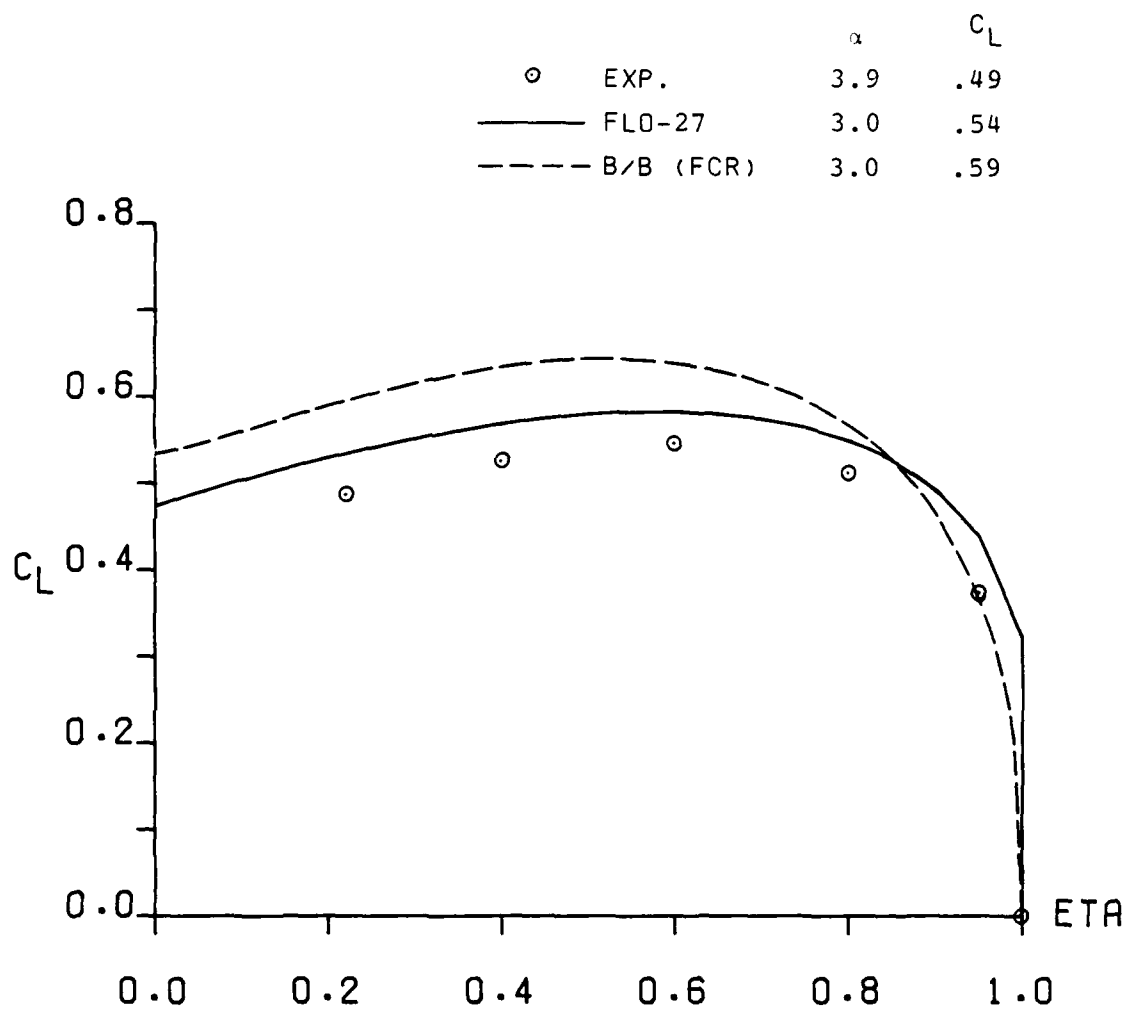
Figure A-5. - Continued.



(e)  $\eta = .95$

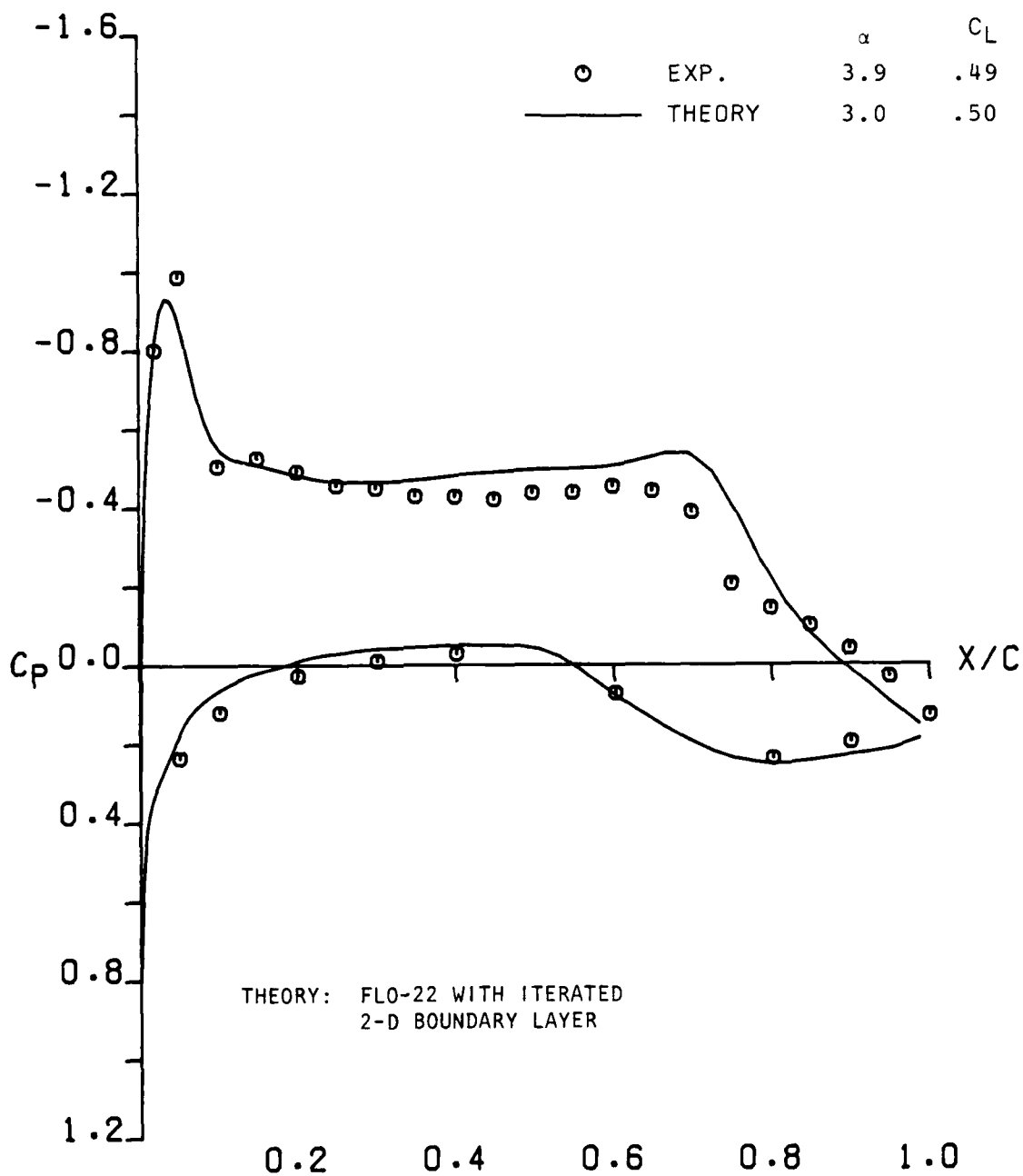
Figure A-5. - Continued.





(f) Span Load Distribution

Figure A-5 . - Concluded.



(a)  $\eta = .22$

Figure A-6. - Comparison of FLO-22 results with experiment when viscous corrections are included; Wing B,  $M = 0.90$ .

AD-A085 258

LOCKHEED-GEORGIA CO MARIETTA

F/G 20/4

ACQUISITION AND APPLICATION OF TRANSONIC WING AND FAR-FIELD TEST--ETC(U)

MAR 80 B L HINSON, K P BURDGES

F49620-78-C-0068

UNCLASSIFIED

L680ER0012-VOL-1

AFOSR-80-0421-VOL-1

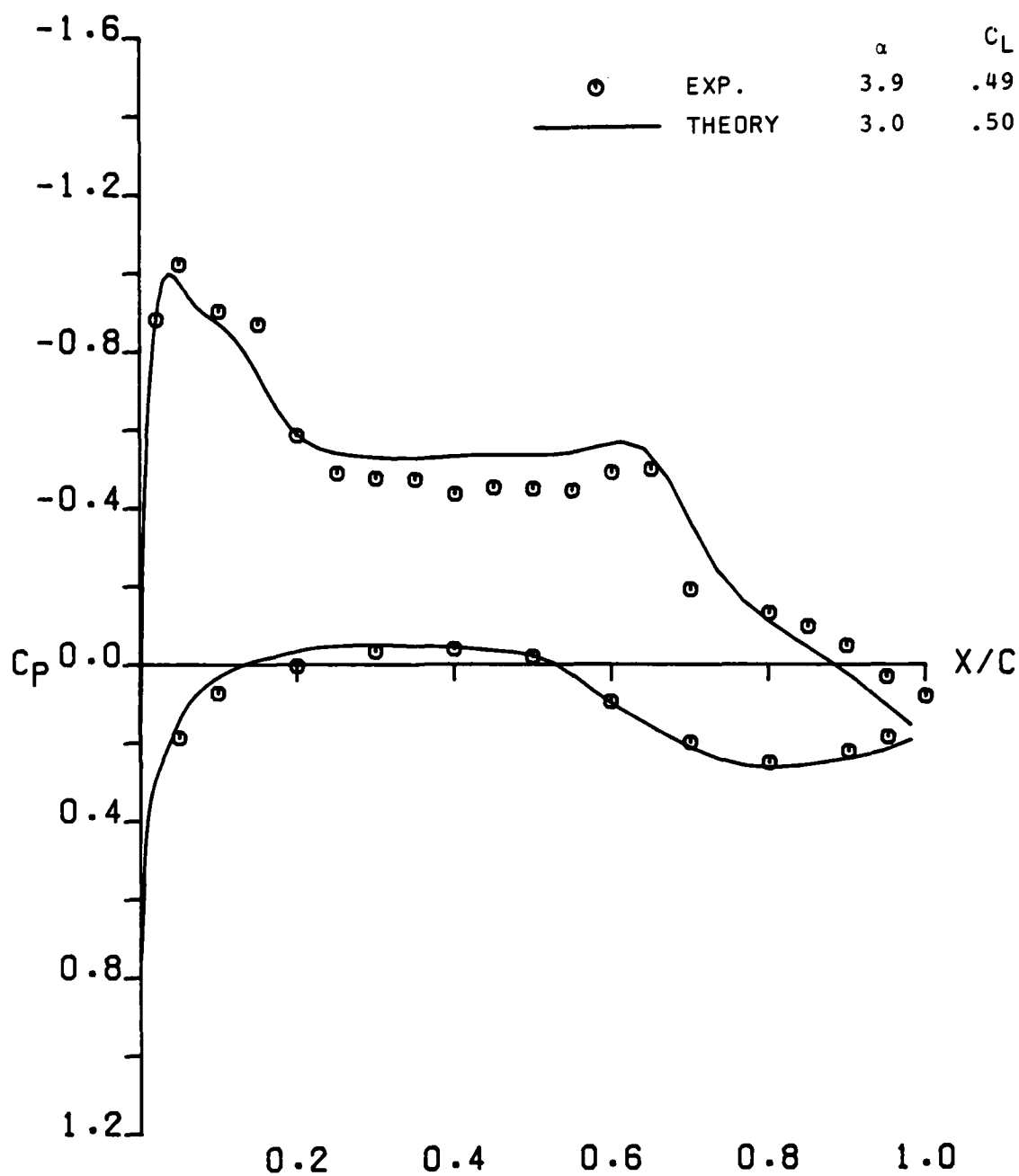
NL

3 OF 3

AD  
A085-258

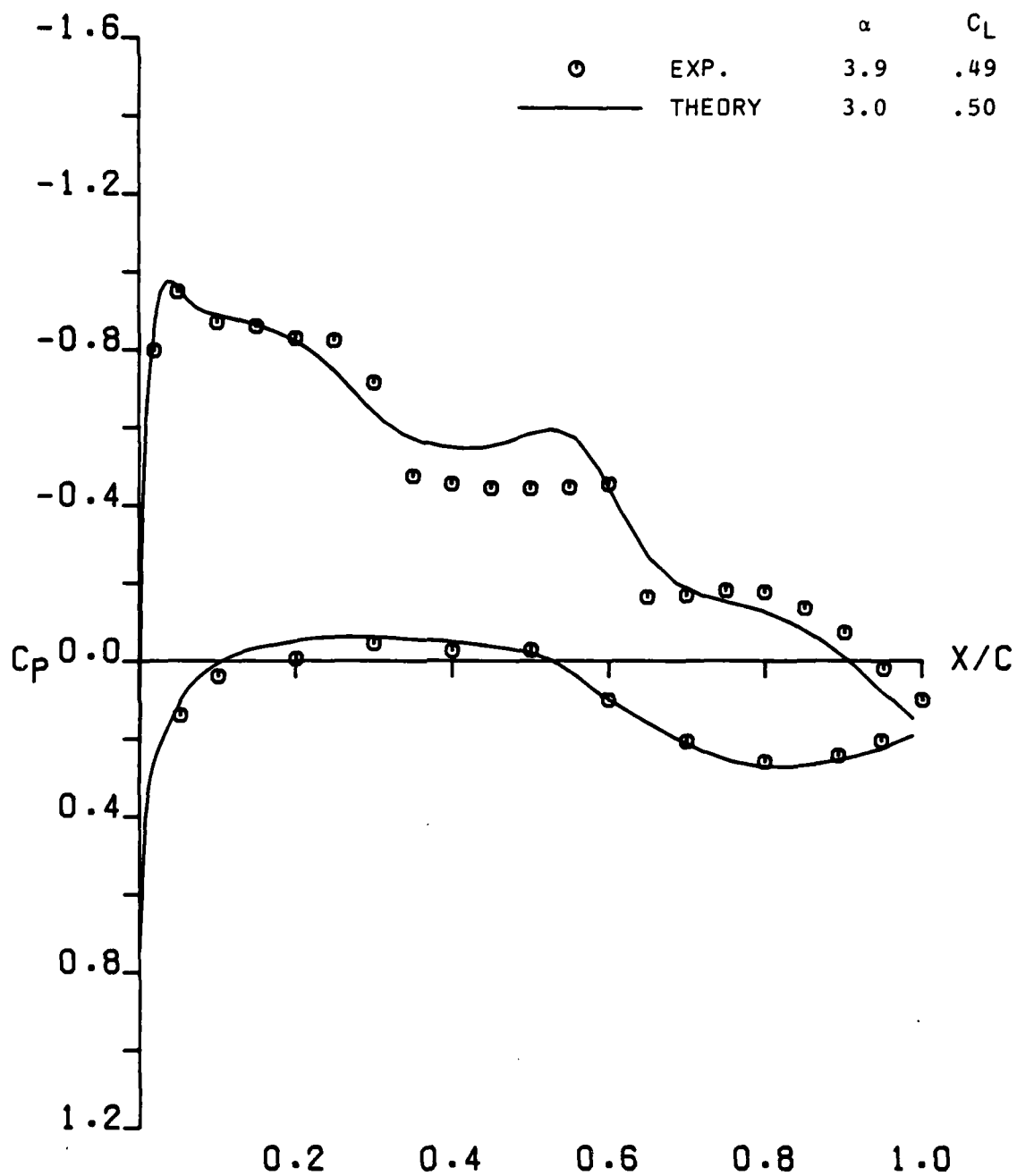


END  
DATE  
FILMED  
7-80  
DTIC



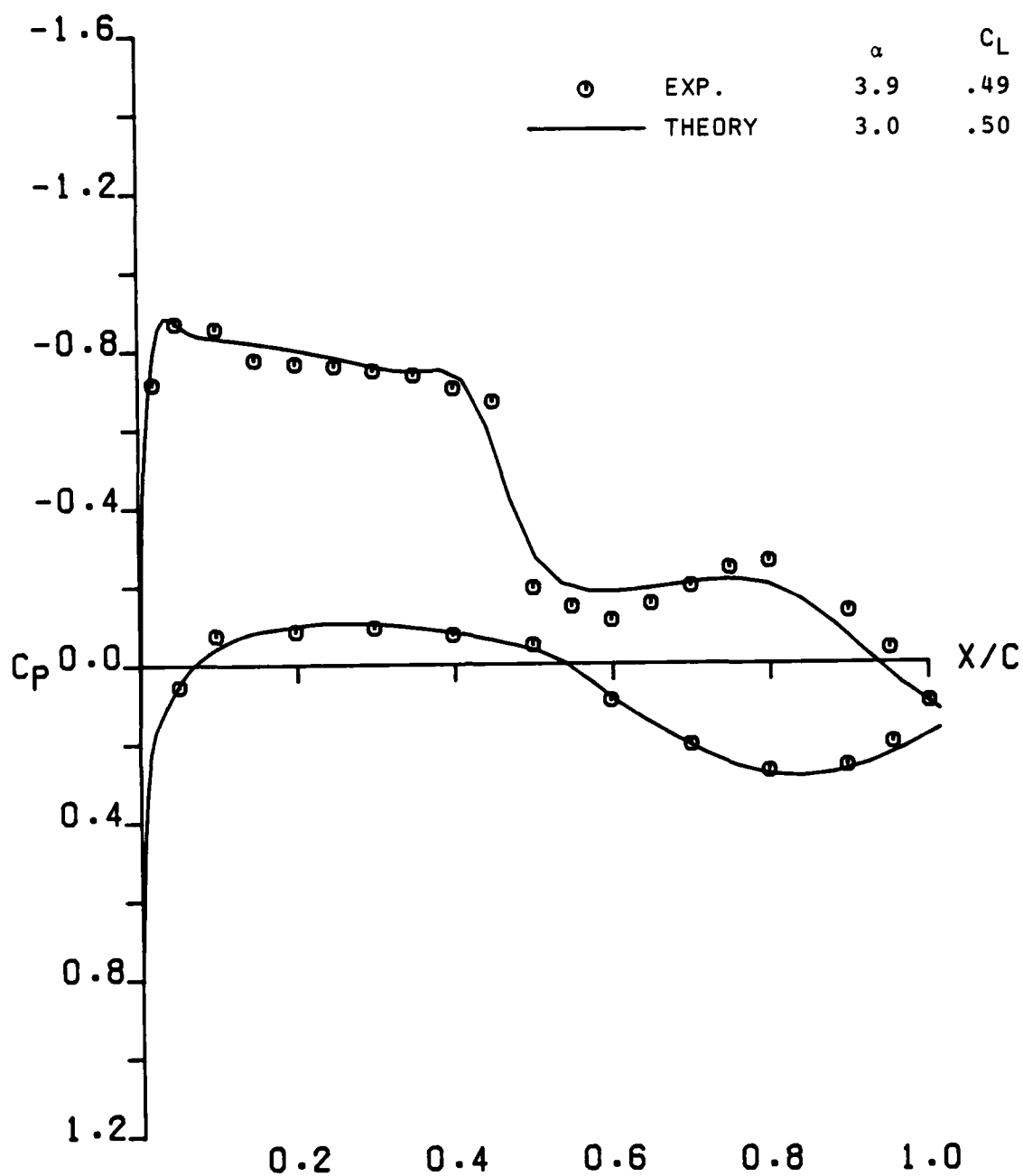
(b)  $\eta = .40$

Figure A-6. - Continued.



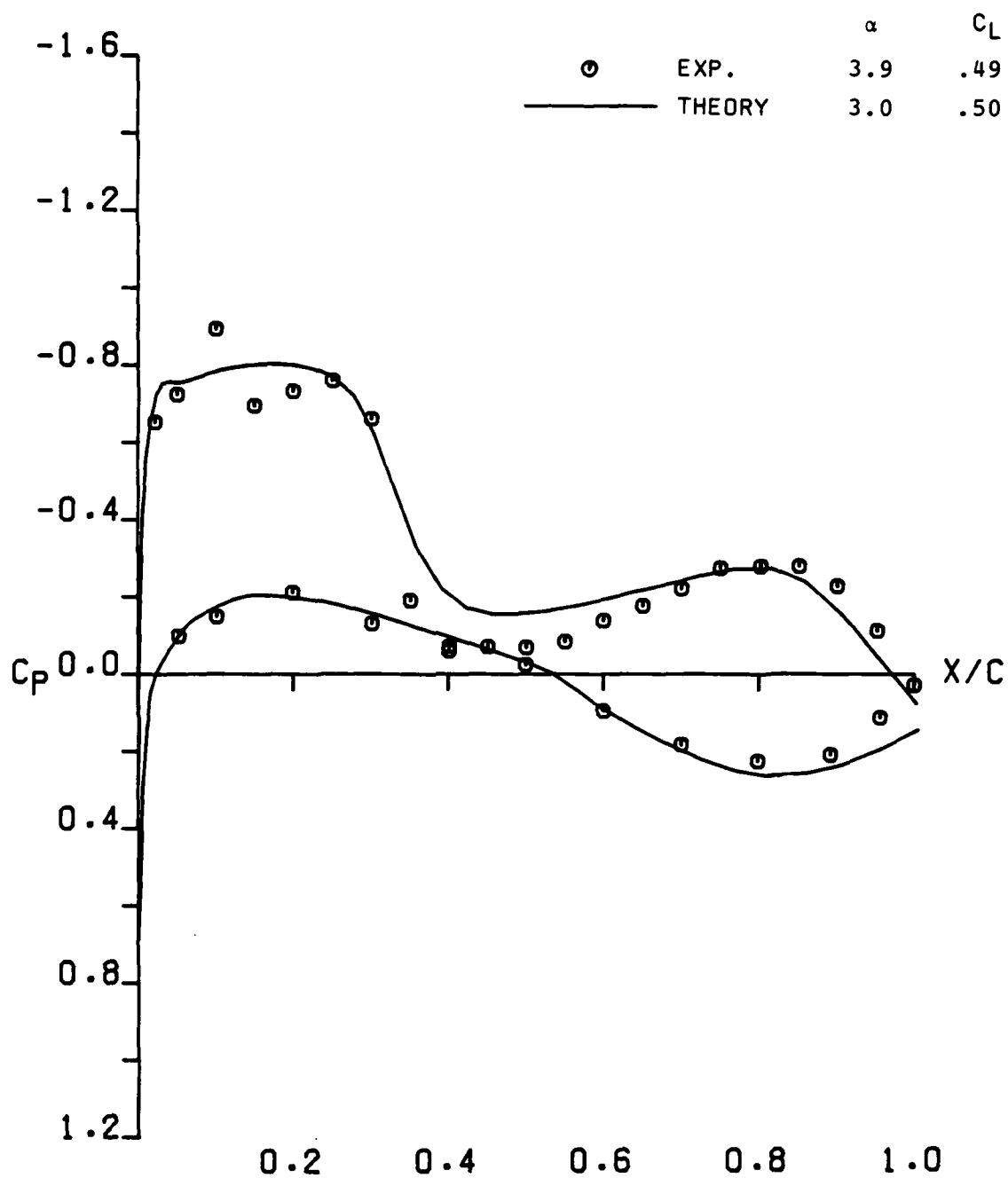
(c)  $\eta = .60$

Figure A-6. - Continued.



(d)  $\eta = .80$

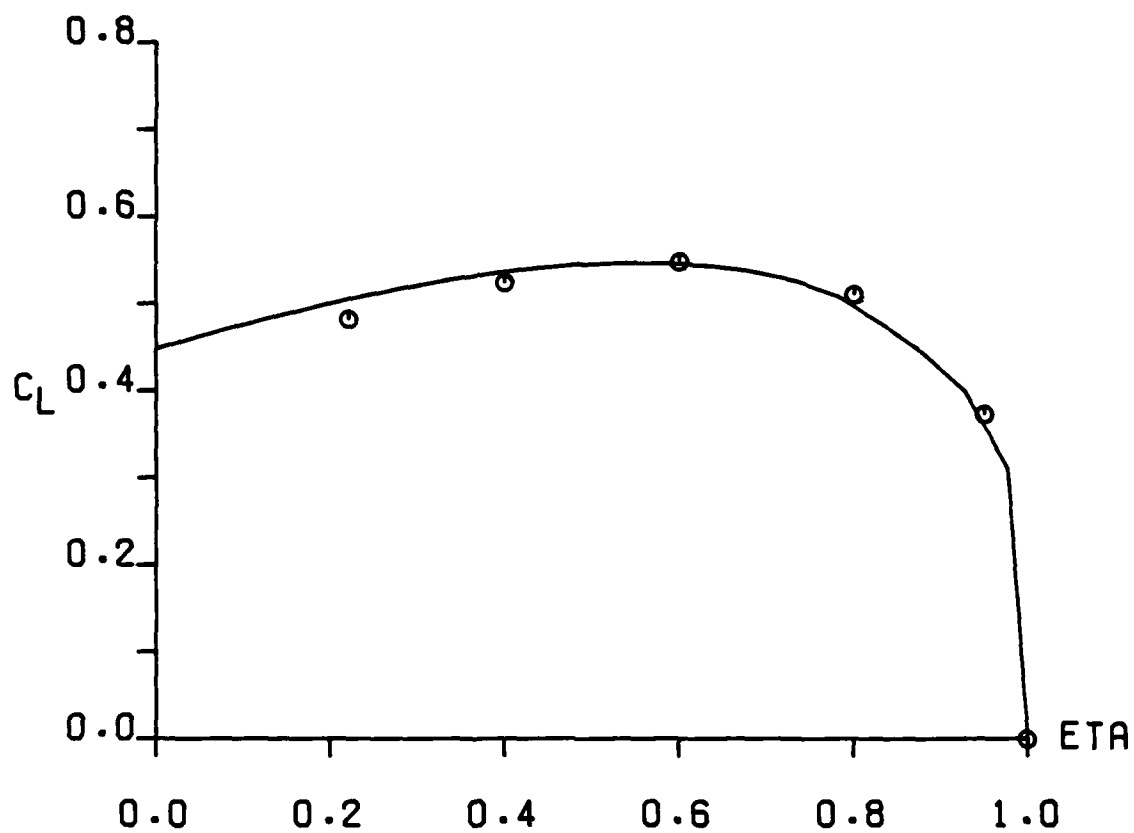
Figure A-6. - Continued.



(e)  $\eta = .95$

Figure A-6 - Continued.

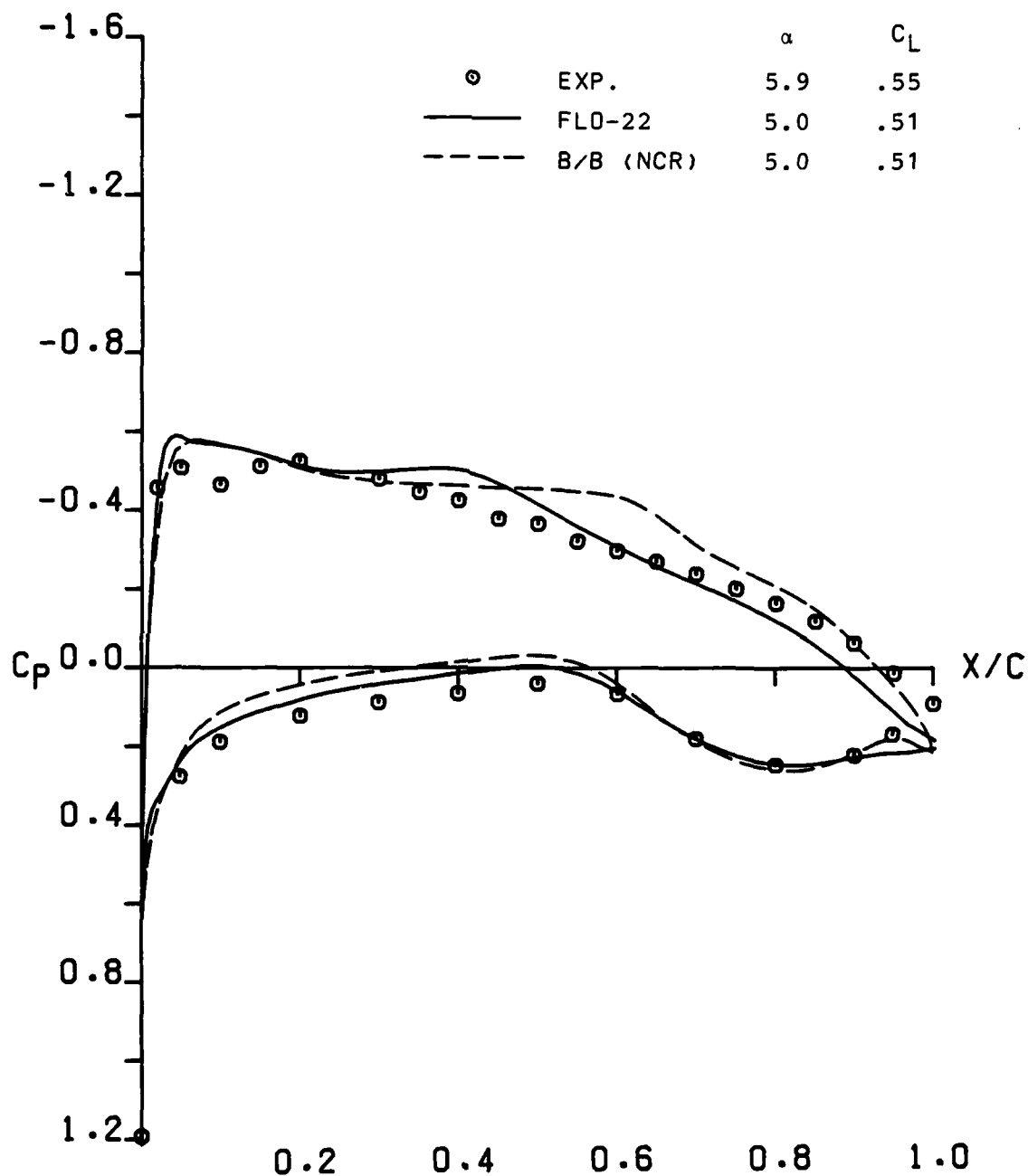
		$\alpha$	$C_L$
○	EXP.	3.9	.49
—	THEORY	3.0	.50



(f) Span load distribution

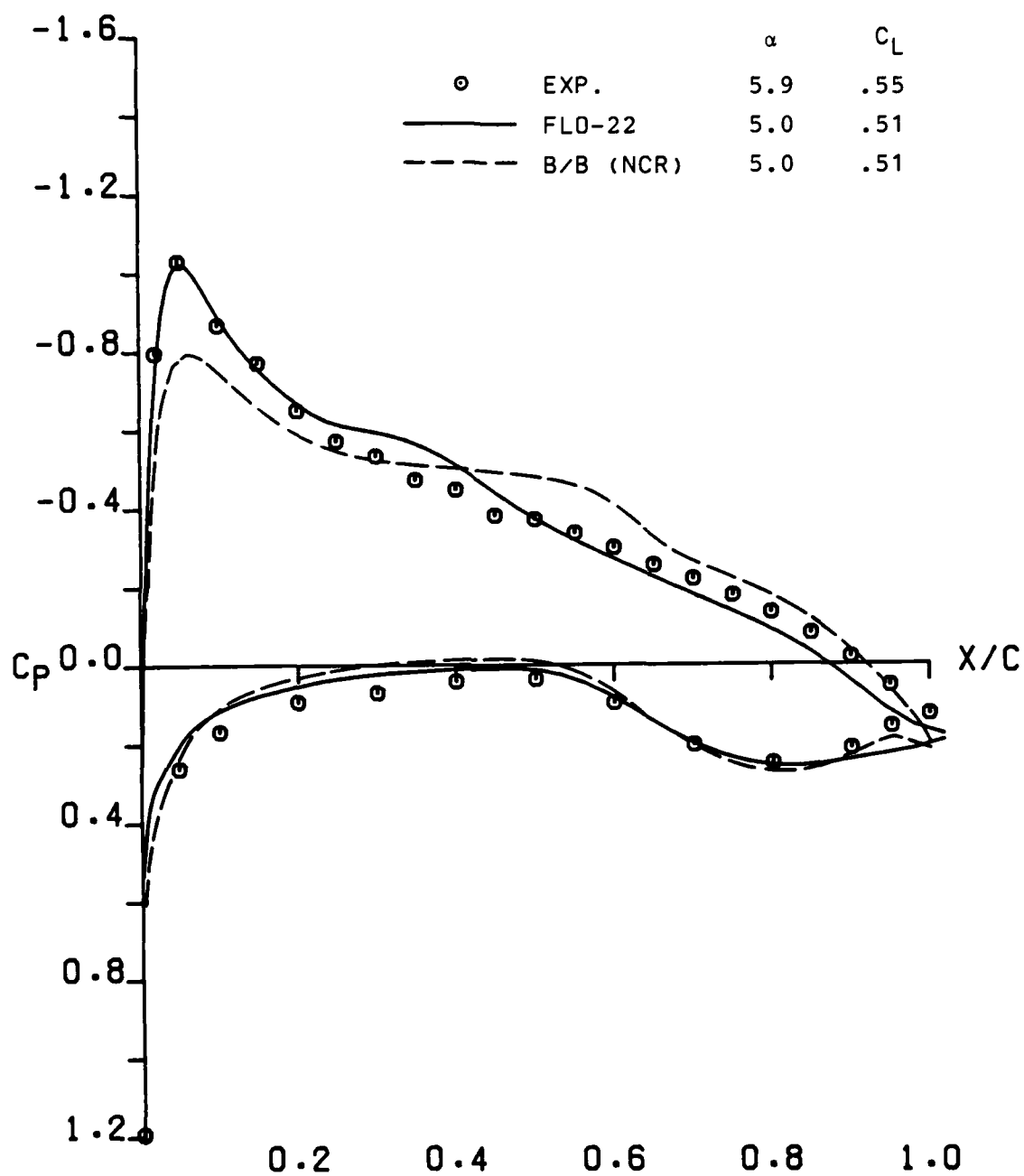
Figure A-6. - Concluded





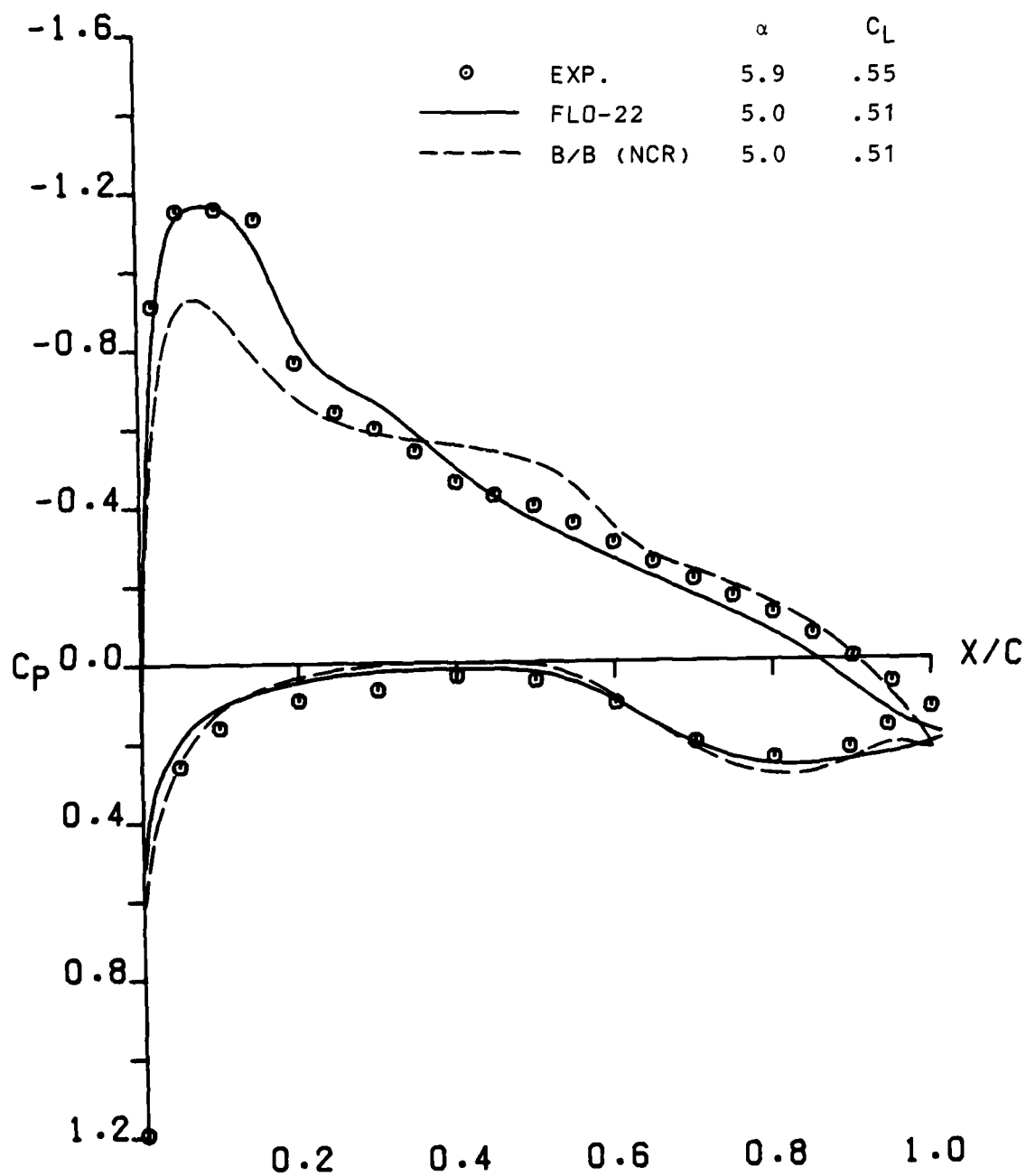
(a)  $\eta = 1.0$

Figure A-7. - Correlation of non-conservative codes using Wing C experimental data at  $M = .85$ ,  $C_L \approx .5$ .



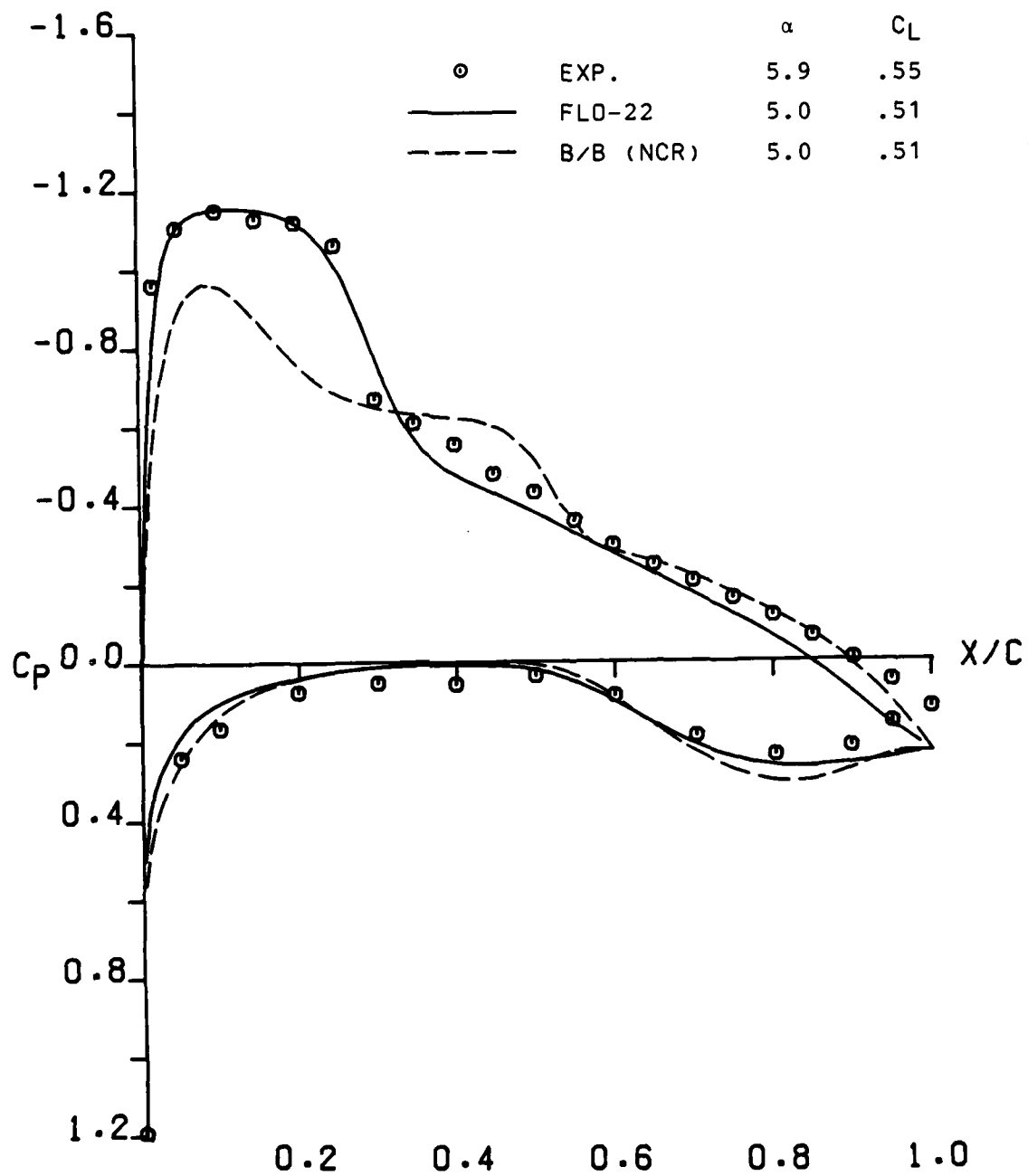
(b)  $\eta = .30$

Figure A-7. - Continued



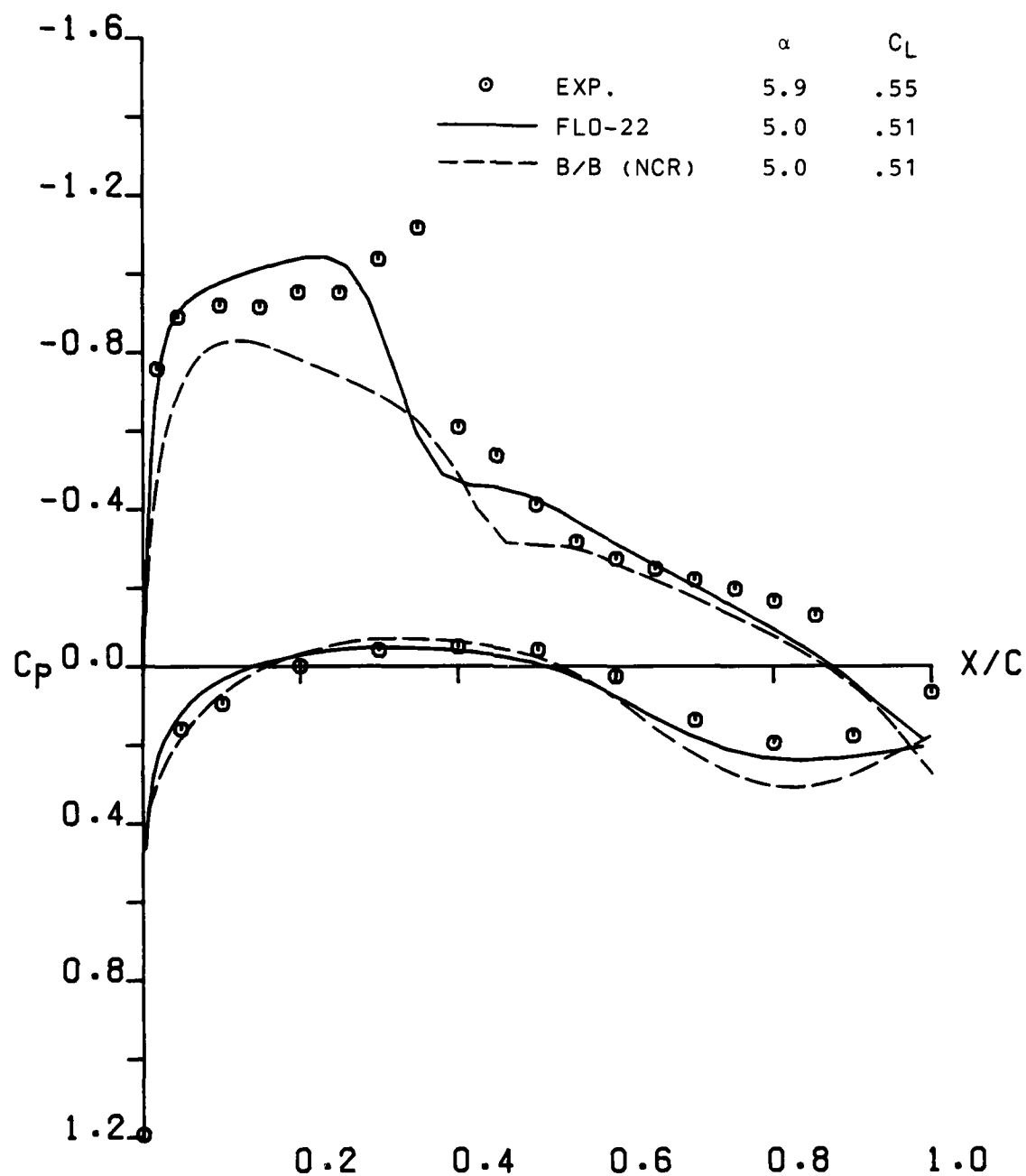
(c)  $\eta = .50$

Figure A-7. - Continued



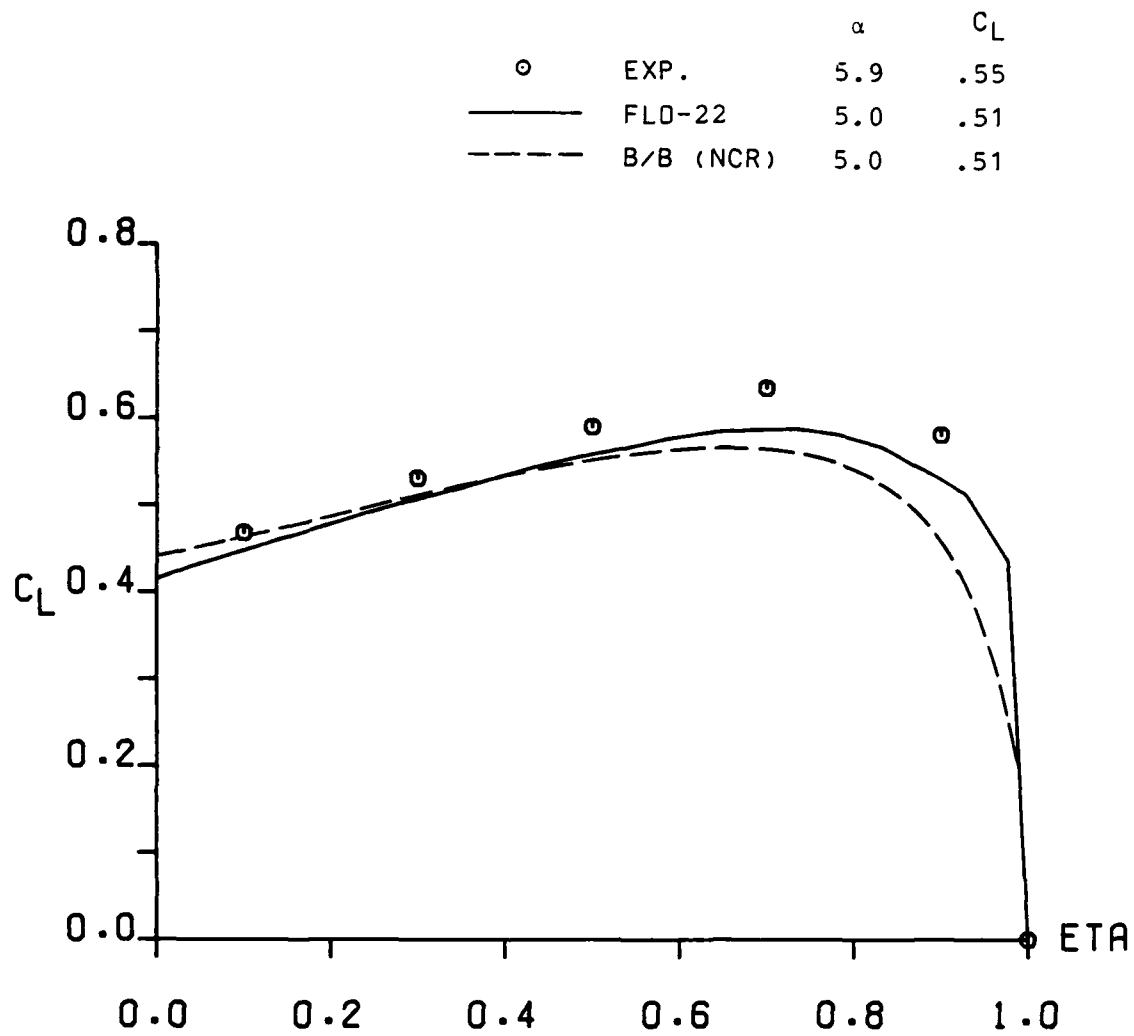
(d)  $\eta = .70$

Figure A-7. - Continued



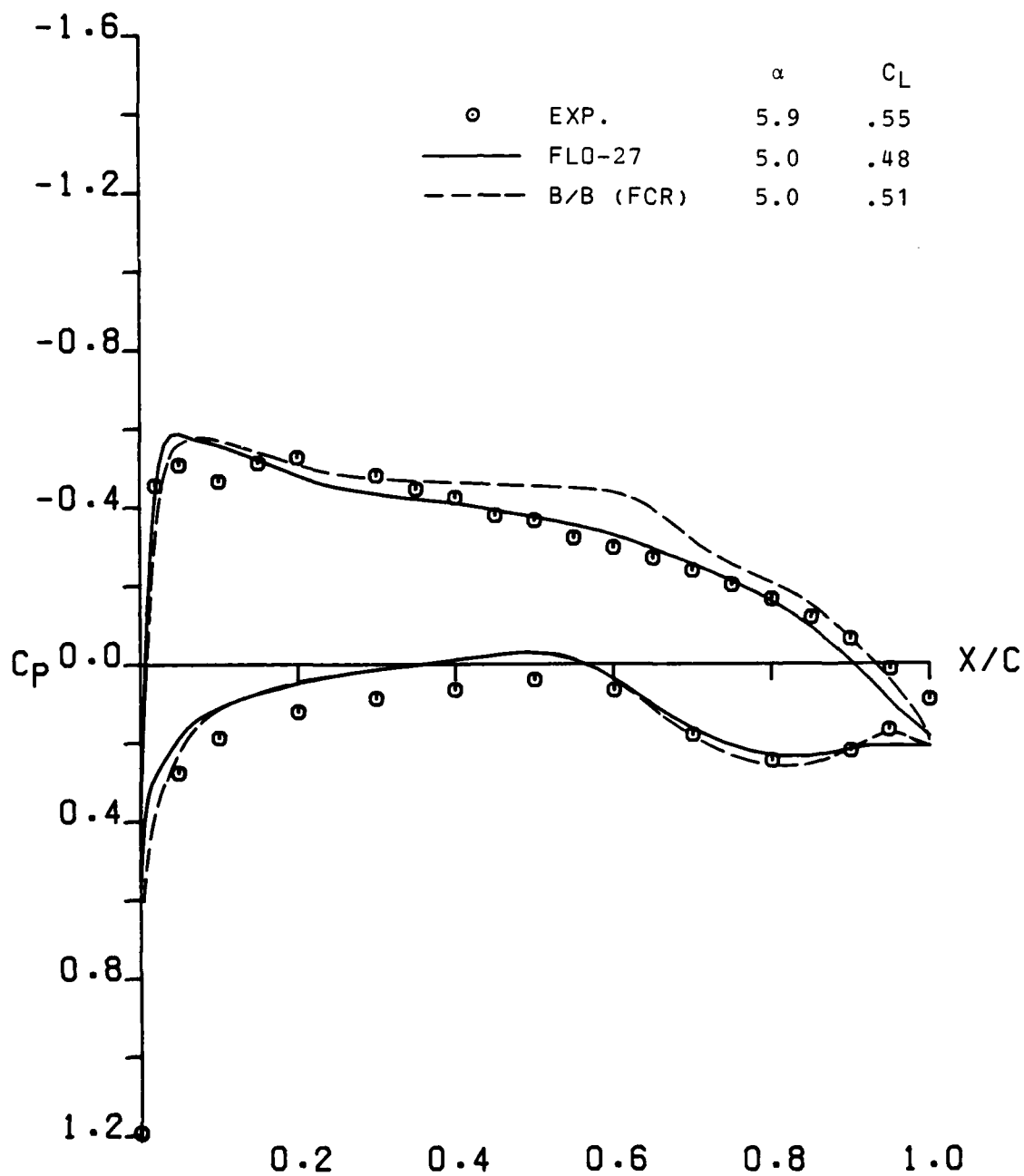
(e)  $\eta = .90$

Figure A-7. - Continued



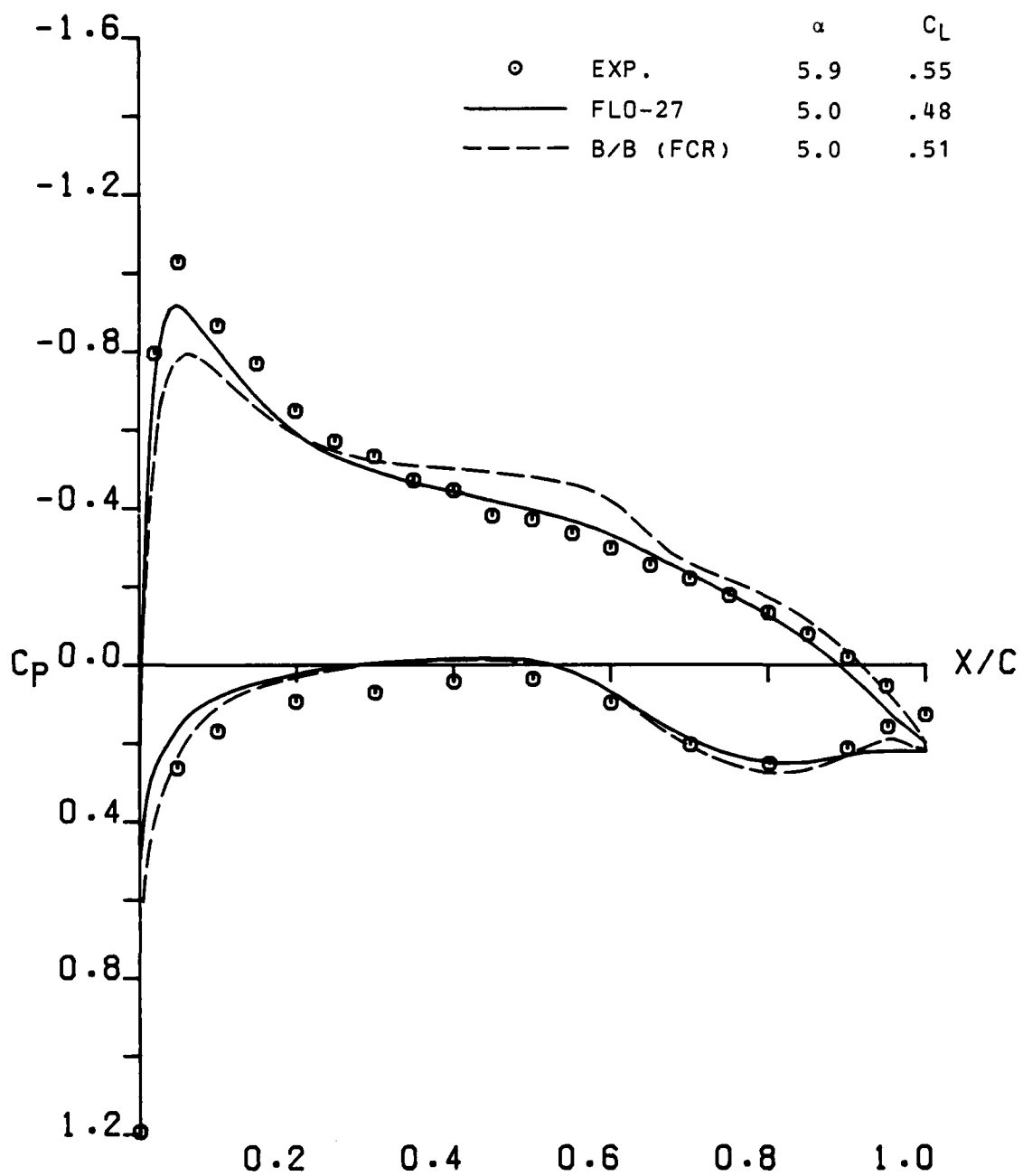
(f) Span load distribution

Figure A-7. - Concluded



(a)  $n = .10$

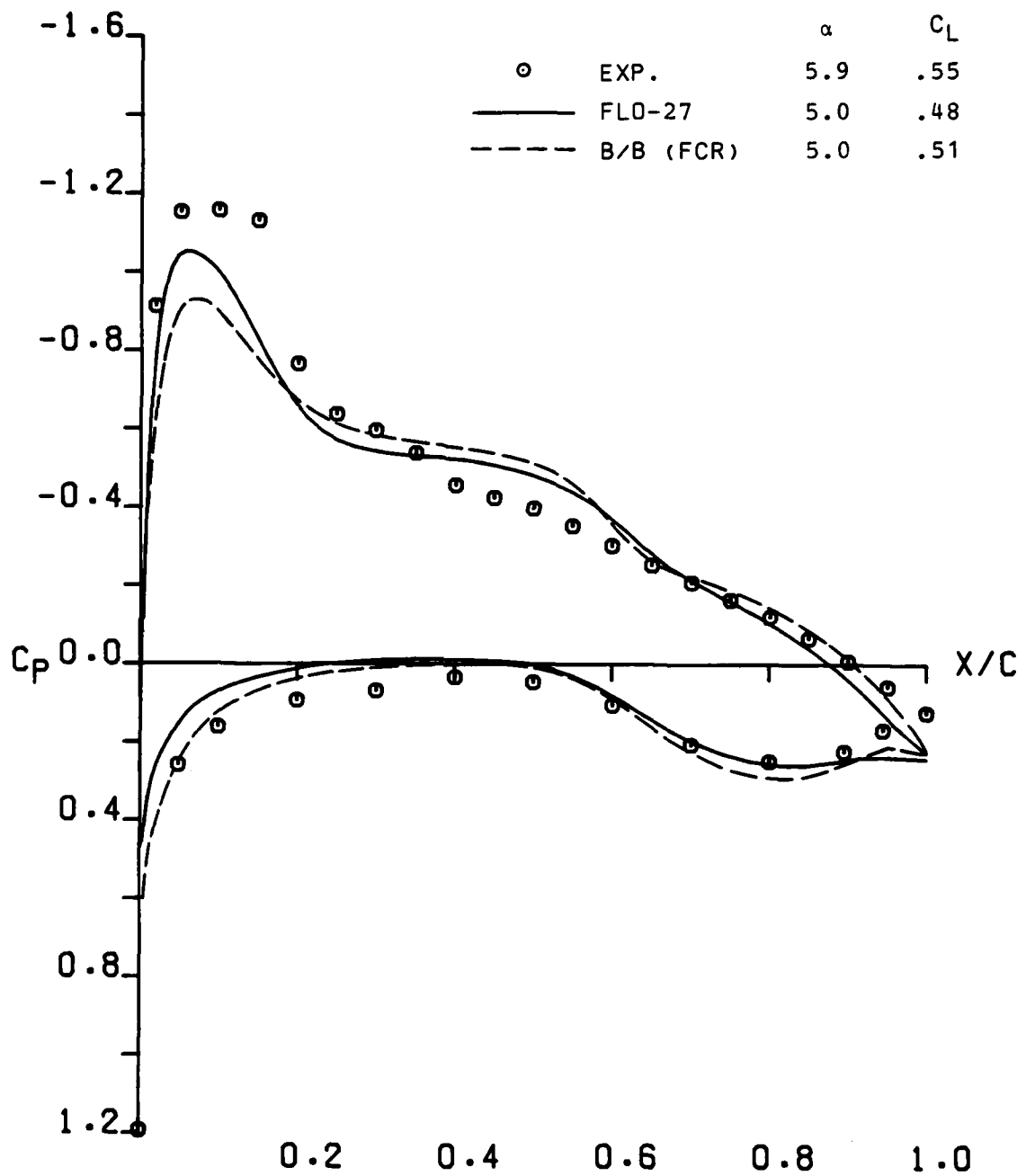
Figure A-8. - Correlation of conservative codes using Wing C experimental data at  $M = .85$ ,  $C_L \approx .5$



(b)  $\eta = .30$

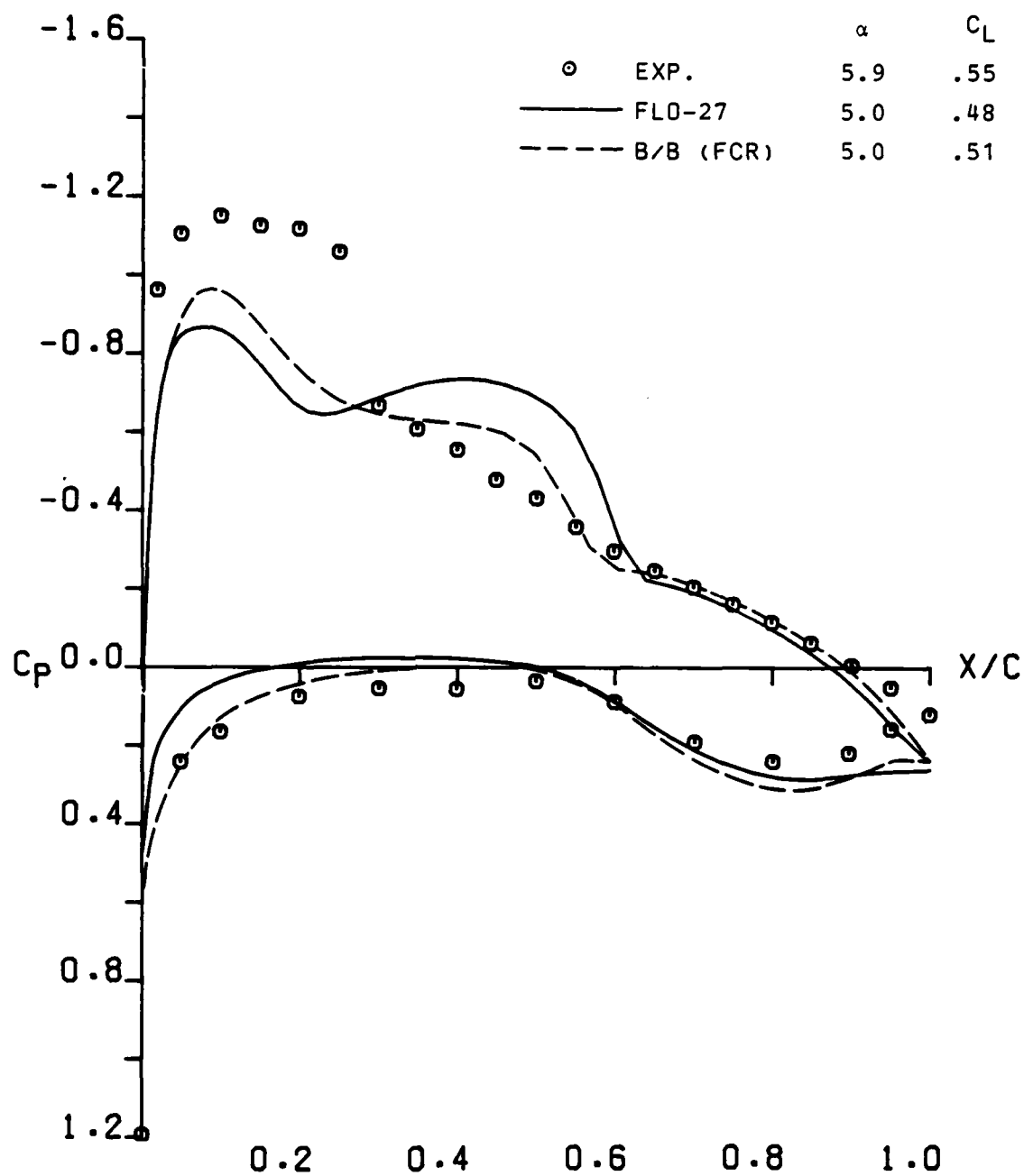
Figure A-8. - Continued





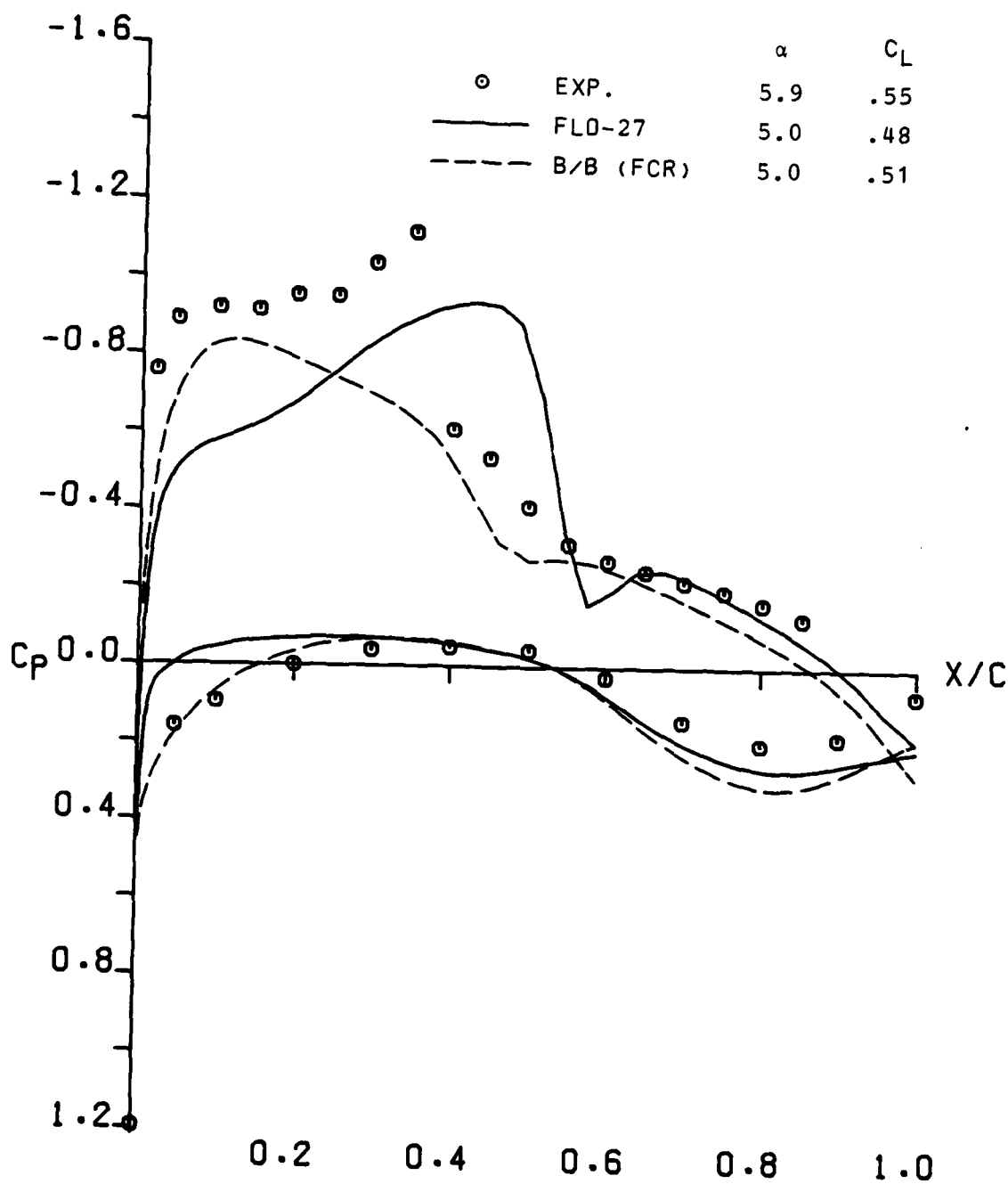
(c)  $\eta = .50$

Figure A-8. - Continued



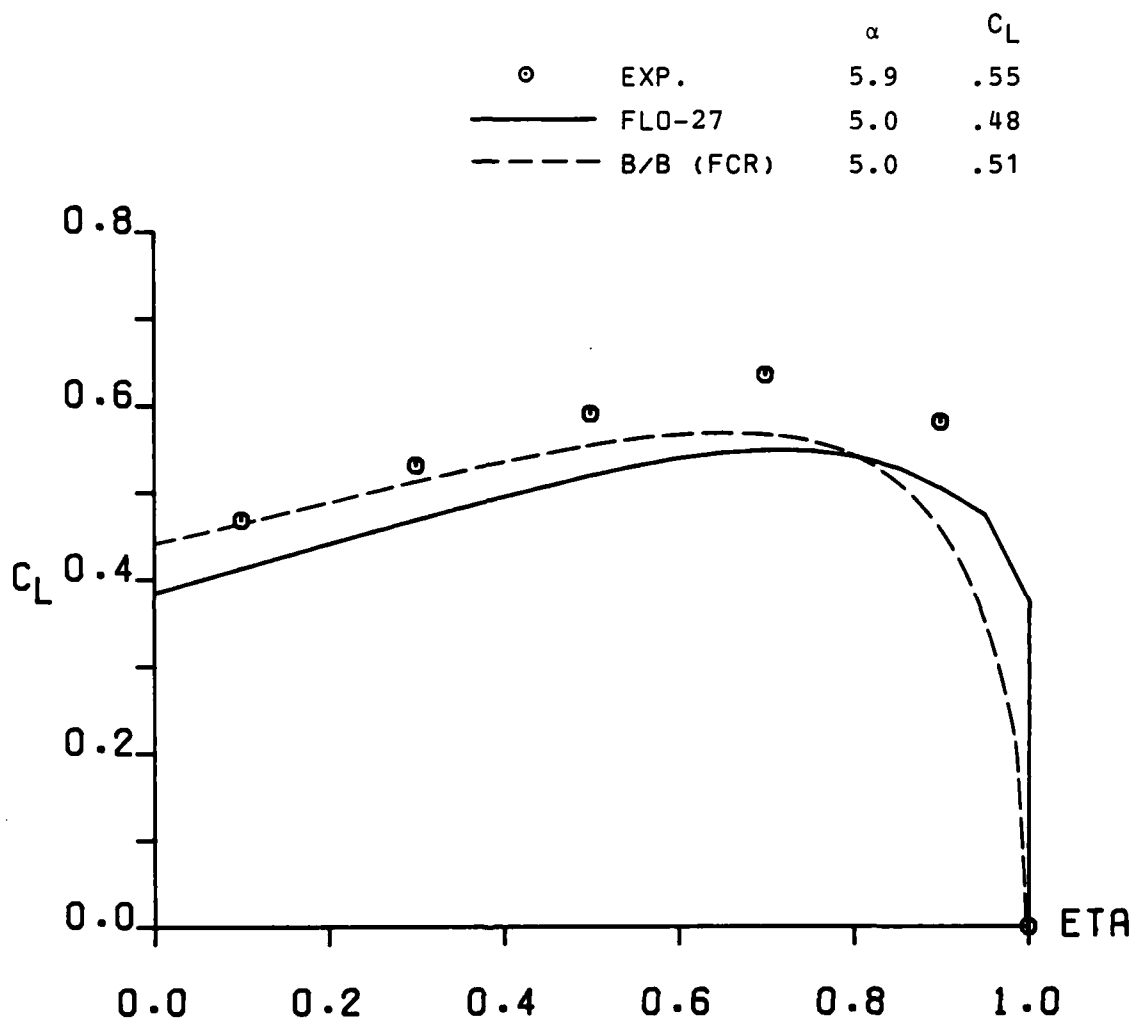
(d)  $\eta = .70$

Figure A-8. - Continued



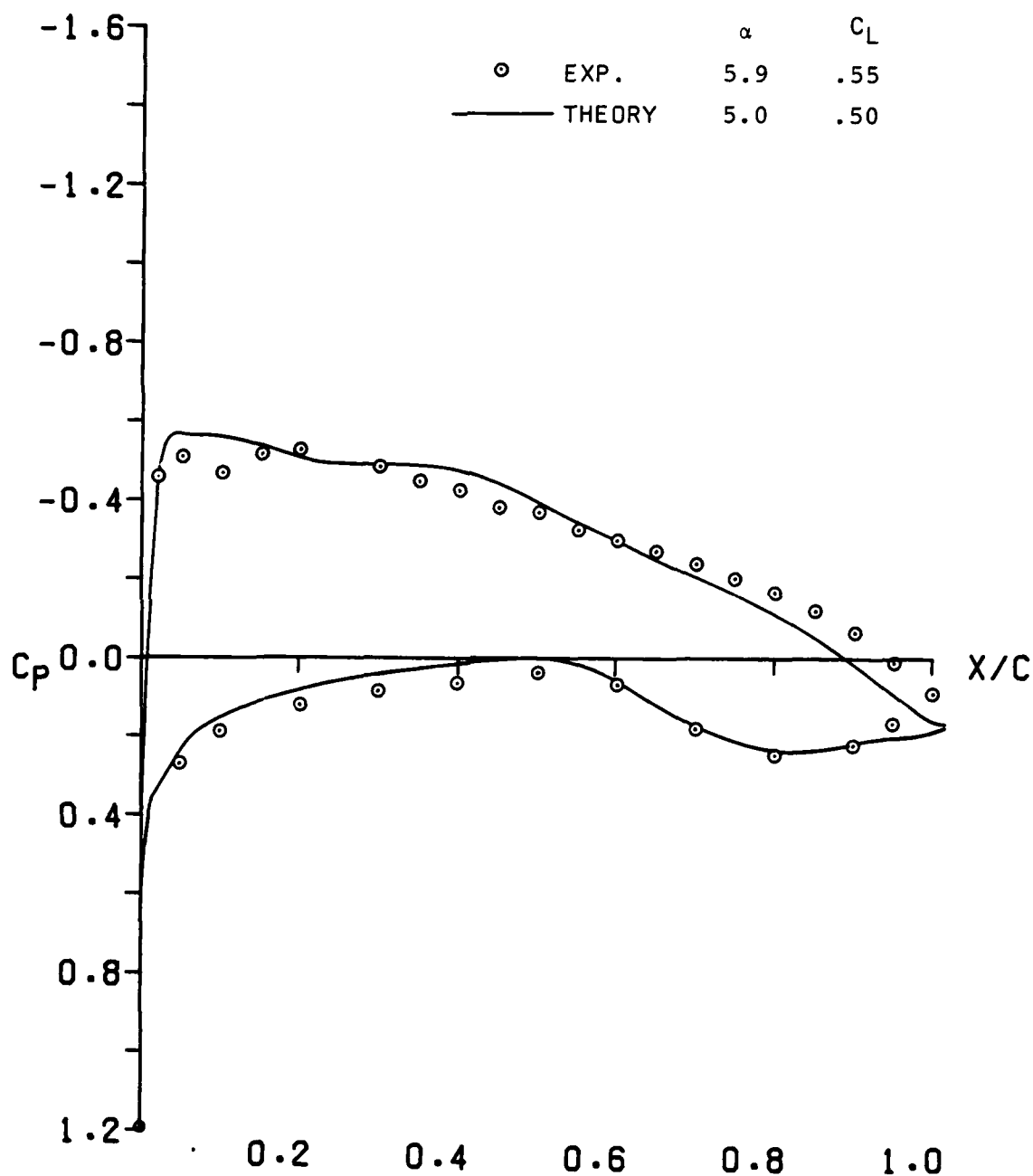
(e)  $\eta = .90$

Figure A-8. - Continued



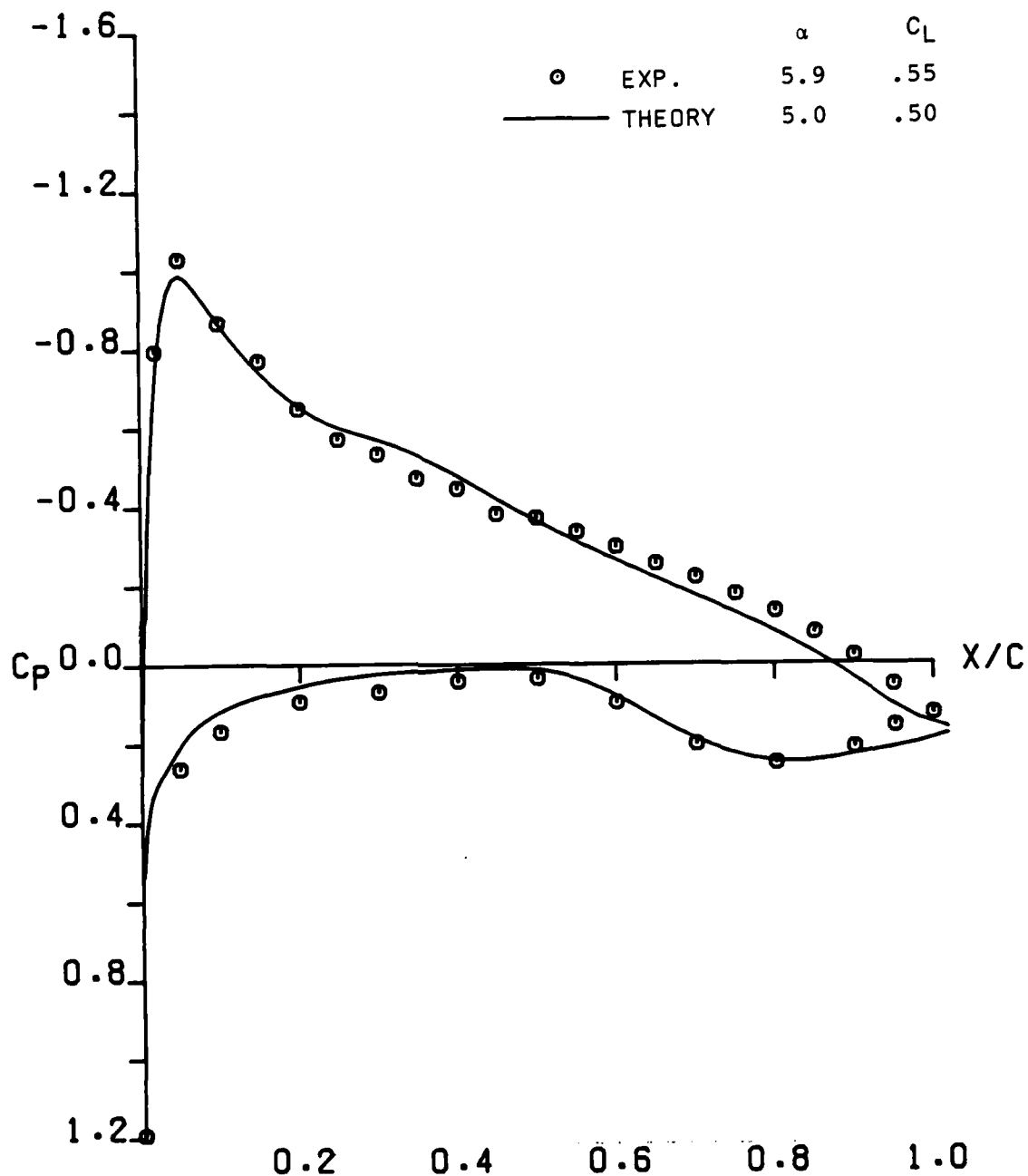
(f) Span load distribution

Figure A-8. - Concluded



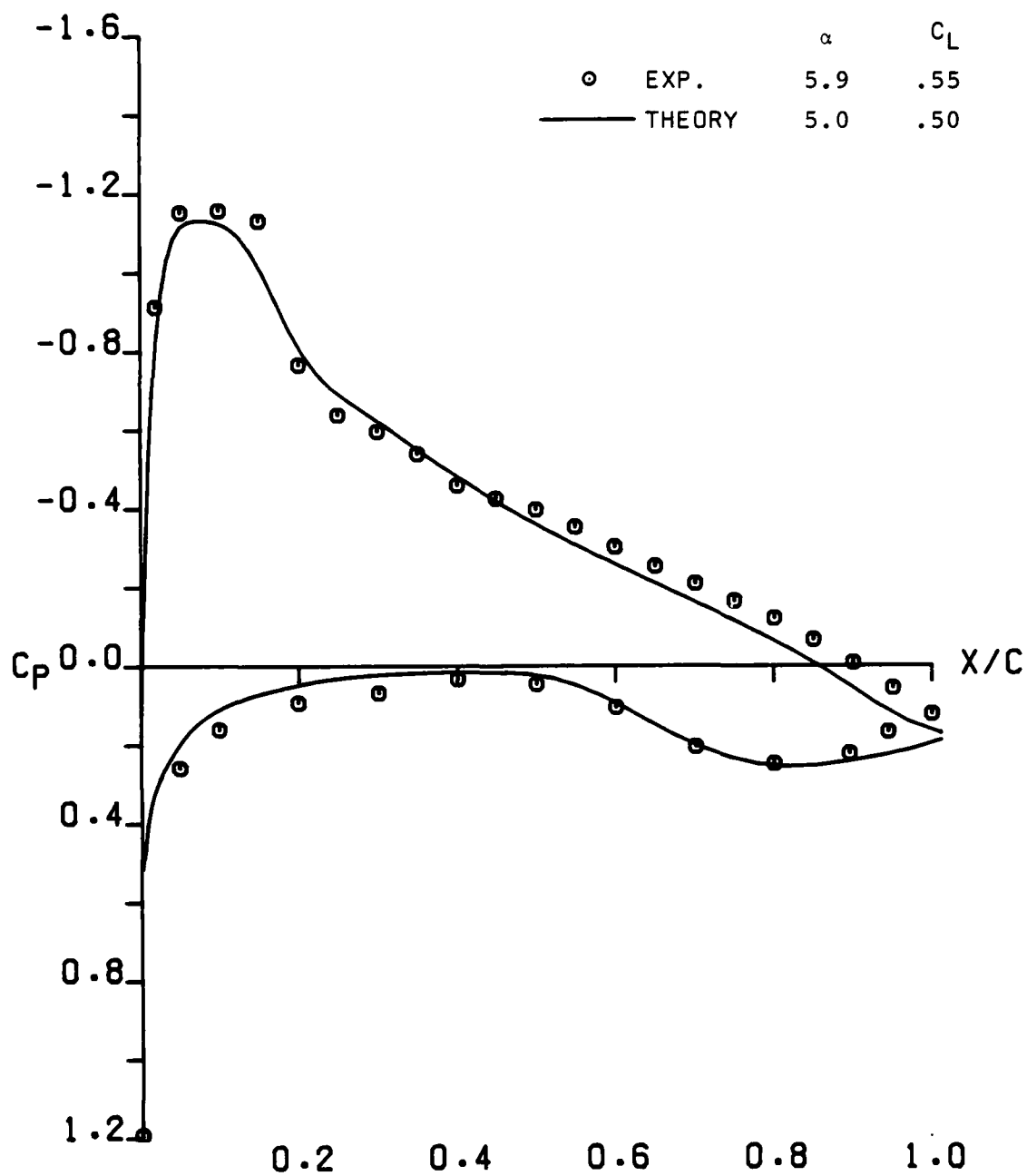
(a)  $\eta = .10$

Figure A-9. - Comparison of FLO-22 results with experiment when viscous corrections are included;  
Wing C,  $M = .85$



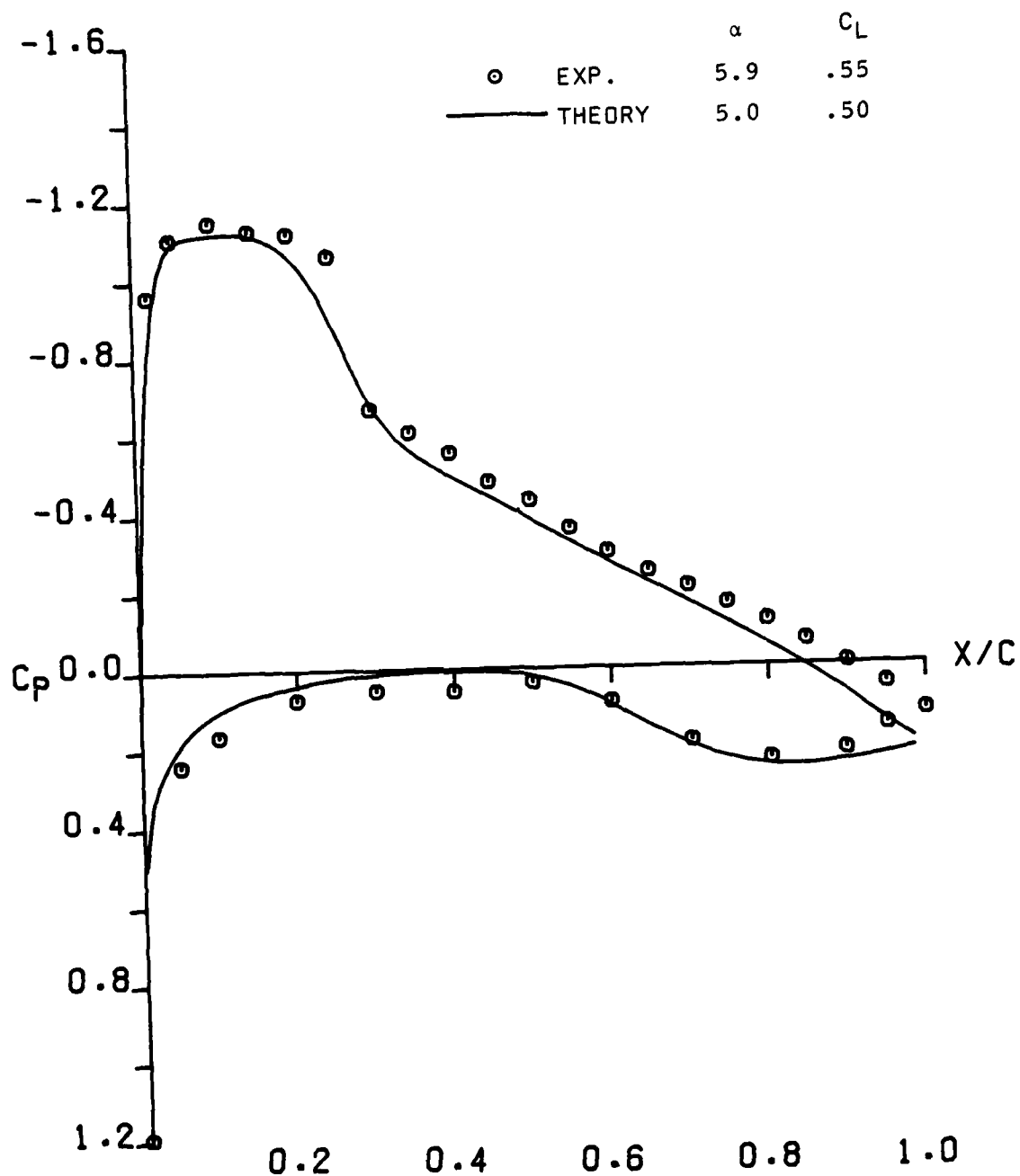
(b)  $\eta = .30$

Figure A-9. - Continued



(c)  $\eta = .50$

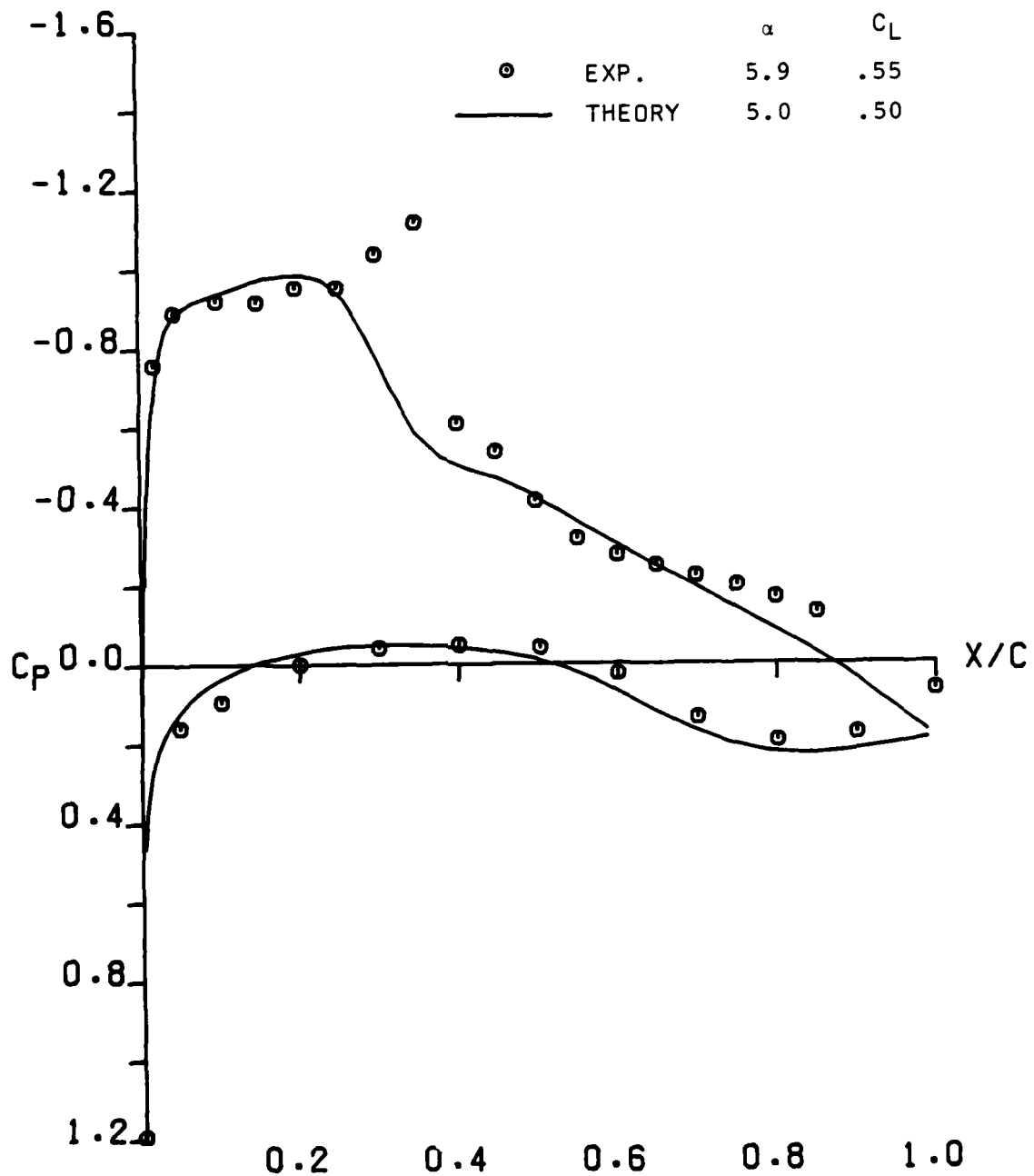
Figure A-9. - Continued



(d)  $\eta = .70$

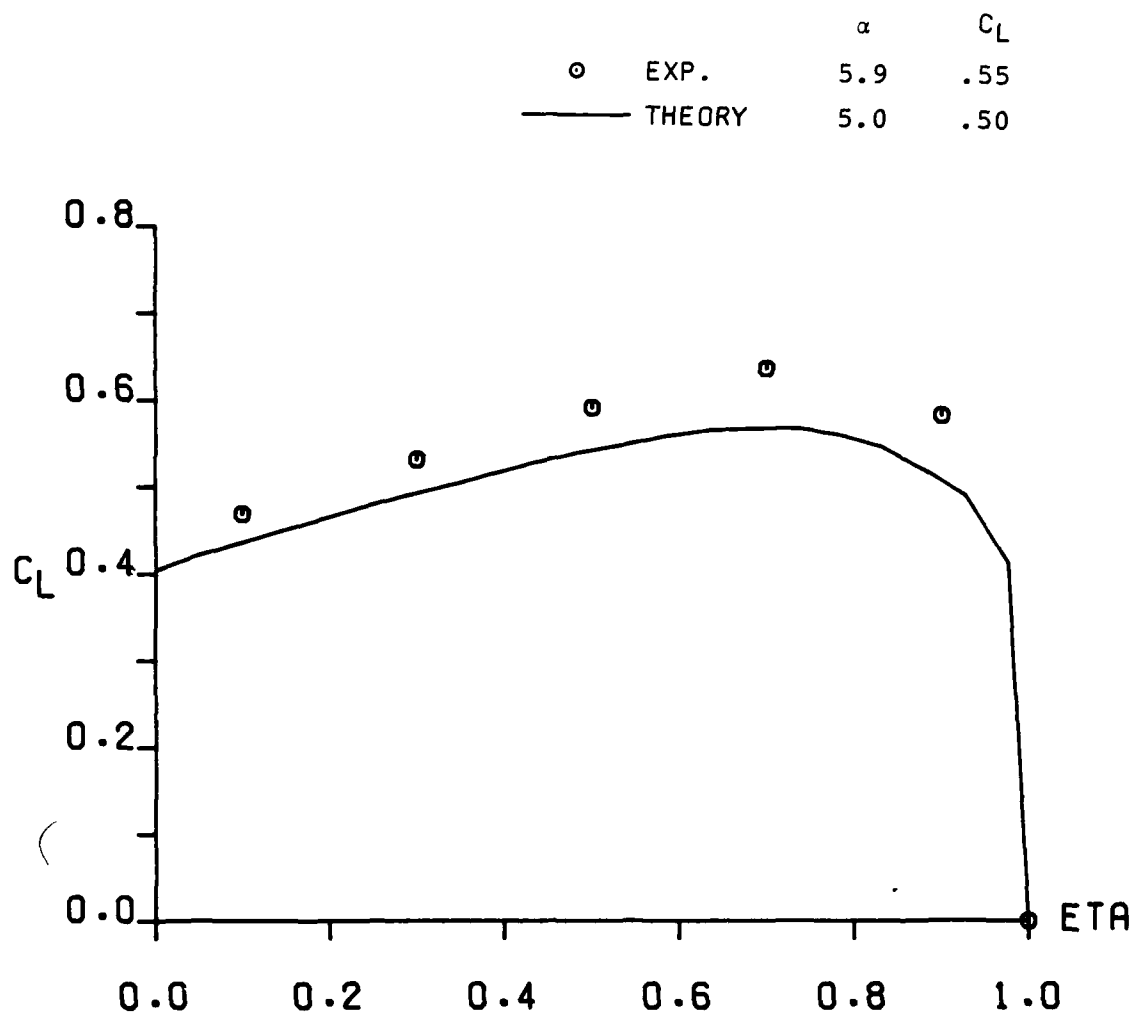
Figure A-9. - Continued





(e)  $n = .90$

Figure A-9. - Continued



(f) Span load distribution

Figure A-9. - Concluded

## APPENDIX B

### EXPERIMENTAL DATA

*(Appendix B - Experimental Data is contained  
in a separate volume to this report.)*